warwick.ac.uk/lib-publications

ENGINEERING DOCTORATE PROGRAMAME
Submission of Work to the Portfolio

Name: Lorena Amoroso

Company: Honeywell

Title: Development and characterisation of MWCNT filled HDPE foams for acoustic transducer applications

The attached document is submitted as part of my Engineering Doctorate Portfolio. Except where acknowledged it is my own work.

Signature

Date: 03/05/2021

I have read the attached work and agree to it being submitted towards the portfolio.

Academic Mentor: Prof Tony McNally   **Date:** 05/05/2021

Industrial Mentor: Dr Christoph Klieber   **Date:** 05/05/2021

This form and the document should be returned to the Research Degrees Office, WMG, International Manufacturing Centre, University of Warwick, Coventry, CV4 7AL.

A scanned copy can be sent to wmgresearchdegrees@warwick.ac.uk

"Development and Characterisation of

MWCNT filled HDPE foams

for

Acoustic Transducer Applications"

By **Lorena Amoroso**

Engineer Doctorate (EngD) Dissertation

Sustainable Materials and Manufacturing (SMM CDT)

University of Warwick

WMG

International Institute for Nanocomposites Manufacturing (IINM)

May 2021

ABSTRACT

The determination of the flow rate of fluids pumped through pipelines is an engineering problem of considerable practical interest. Over other more traditional flow measurement techniques (e.g. orifice, turbine or vortex meters), UFM technology is widely used in large diameter pipelines for measuring flow. Ultrasonic signals are transmitted through the medium of interest by means of electromechanical conversion, with the resultant backscattered energy being detected and converted into an electrical format (transmission and detection of ultrasonic energy). Air-coupled ultrasonic transducers sent and received the ultrasound, determining the performance of the flowmeter. For the purpose of custody transfer of natural gas, one of the most important applications of measurements of gas flow rate in large gas pipelines, a high degree of reliability and accuracy are of paramount importance. Both researchers and manufacturers of measuring equipment must reduce measurement errors. It is essential to optimise the sensor device. The use of new materials for passive MLs within the sensor assembly together with the study/implementation of advanced manufacturing methods for their manufacture is a route to optimizing ultrasonic transducers and their efficiency for enhancing energy transfer and so reducing measurement errors in UFM applications.

In the present work, the concept of using lightweight composite foams based on HDPE and non-functionalised MWCNTs for sound absorption in ultrasonic flow metering (UFM) applications is described for the first time. Materials with suitable acoustic properties (i.e. very low acoustic impedance and attenuation) are not readily available for ML fabrication. The study of new acoustic materials as alternatives to conventional materials for the ML within the sensor assembly has been addressed and is the scope of this EngD project.

A number of methodologies were here employed for the foaming of HDPE, with and without inclusion of MWCNTs using chemical and physical BAs. The key objective was to assess whether foamed HDPE and HDPE-MWCNT composite parts had the required properties to function as passive layers within acoustic sensors. For this purpose, a number of foamed samples with different cellular structures were produced by varying the processing conditions, concentration of BAs and MWCNT content during foaming, using industrially relevant polymer processing methods such as extrusion and IM. Controlling the cellular structure and thus, the resulting properties of the parts is challenging, especially when foaming a semi-crystalline polymer, such as HDPE which also has a very high melt viscosity and rapid crystallisation kinetics. On one hand, the composite foams produced by chemical foaming had acoustic properties comparable to those of *syntactic foams* commonly used in the target application, i.e. acoustic impedances of the order of 1 MRayl. On the other hand, the use of physical foaming allowed for even lower acoustic impedance by a further order of magnitude, ≤0.4 MRayl for unfilled HDPE foams and to a minimum of 0.57 MRayl for the

HDPE-MWCNT composite foams, for a MWCNT content of 0.5 wt%. Physical foaming produced highly foamed parts capable of achieving lower acoustic impedances than materials currently used as commercial layers in the sensor industry (e.g. *ML-Trelleborg* and *Commercial ML*).

Foams of HDPE and HDPE-MWCNT composites are suitable for use as matching layers (MLs) in ultrasonic transducers. The low values of the speed of sound, acoustic impedance and acoustic attenuation, low cost and the possibility of manufacturing these lightweight layers at scale and in high volumes make them a viable alternative to the benchmarking materials.

Acknowledgements

Table of Contents

List of Figures

List of Tables

List of Abbreviations

Z	Acoustic impedance
Z_{AIR}	Acoustic impedance of air
Z_{ML}	Acoustic impedance of the matching layer
Z_{PIEZO}	Acoustic impedance of piezoelectric layer
ACU	Air-coupled ultrasound

BAs	Blowing agents
$X_{c(DSC)}$	Bulk crystallinity
ρ_f	Bulk density of the foam
ρ_p	Bulk density of the un-foamed polymer
CO_2	Carbon dioxide
CNT	Carbon nanotubes
CBA(s)	Chemical foaming agent(s)
T_c	Crystallisation temperature
ρ	Density
DSC	Differential scanning calorimetry
DMTA	Dynamic mechanical thermal analysis
T_g	Glass transition temperature
HDPE	High-density polyethylene
IM	Injection moulding
ML(s)	Matching layer(s)
T_m	Melting temperature
MWCNT	Multi-walled carbon nanotubes
MIM	Microcellular injection moulding
$\tan \delta$	Loss tangent
E"	Loss modulus
NHSK	Nanohybrid shish-kebab
PBA(s)	Physical foaming agent(s)
PE	Polyethylene
SEM	Scanning electron microscopy
SAXS	Small-angle x-ray scattering
SNR	Signal-to-noise ratio
c	Speed of sound
E'	Storage modulus
SCFs	Supercritical fluids
SCF-CO2	Supercritical carbon dioxide
TGA	Thermo-gravimetric analysis
ToF	Time of flight
UFM	Ultrasonic flow metering
XCT	X-ray computed tomography
WAXS	Wide-angle x-ray scattering

CHAPTER 1: INTRODUCTION

1.1 Background

Measurements of gas flow rate in large gas pipelines has had increasing demands over recent years especially with the widespread use of natural gas in both domestic and industrial settings due to rich natural gas resources as well as lower emissions of greenhouse gases than for other fossil fuels [1]. Before reaching its end users, natural gas is processed and transported. Concurrently, with the increased interest in such resources, there is a need to measure large volumes of natural gas in transportation networks accurately [2]. Measuring natural gas flow is costly and may not be effective, especially for custody transfer of natural gas which represents one of the most important applications for flow measurements which also requires an accuracy of 0.5% over most of the flow range [3]. Of fundamental importance is the precision in measuring the flow velocity despite the uncertainty in the flow profile due to the complex mixture of hydrocarbons and inorganic compounds of which natural gas is composed [3]. The enormous value of gas involved makes accuracy crucial, since at current gas prices, an error of 1% in measuring 300 million ft^3 of gas per day can lead to a difference of about $2 million per year [4]. Consequently, designing appropriate processes and equipment is essential.

Different flow measurement technologies can be employed for custody transfer applications, including ultrasonic flow-meter technology (UFM) which presents several advantages over other more traditional flow measurement techniques (e.g. orifice, turbine or vortex meters) [1-3]. Its applicability in large diameter pipelines with a rather high accuracy as well as the fact that it allows bidirectional flow measurements make this technique widely adopted. As part of the ultrasonic technology, ultrasonic flowmeters are commonly used to measure volumetric flow rates, in particular the speed of sound in flowing gases [4]. An ultrasonic flow meter is an inferential measurement device that consists of ultrasonic transducers typically located along a pipe`s wall (see Figure 1.1(A-B)). Inside the UFM, a pair of sensors (ultrasonic transducers) are fitted across from each other in the measuring tube (see Figure 1.1(C)). Each sensor can alternately transmit and receive ultrasonic signals/pulses so that the flow measurement is based on the differential transit time method using ultrasound. Each signal measured by the sensors is directly proportional to the gas flow velocity in the pipe. Hence, the UFM based on the transit time method uses correlations developed on the basis of measurable real time properties, such as the differential propagation times (i.e. time of flight, TOF) of ultrasonic waves, propagating in flow and reverse directions, to calculate the gas path velocity. The accurate measurement of TOF is critical to the accuracy of the flow rate measurement. The error in TOF measurements is mainly related to the amplitude attenuation and

the inertia delay of the received signals [5]. A promising approach to solving the problems of flow measurement errors is based on so-called multipath measurements, in which a number of measurements are performed so as to estimate the flow characteristics in several measuring planes parallel to the longitudinal axis of the pipe [6]. In multipath ultrasonic gas flow-meters, pairs of transducers facing each other are applied in the gas pipeline so that transducers on the same acoustic path alternately send and receive ultrasound, allowing for evaluation of the average velocity on each acoustic path [1]. Each path of ultrasound needs to be analysed and the use of integration algorithms can transform the velocities of multiple paths into the average cross-section velocity [1]. It is the ultrasound signal sent and received from the transducer that directly determines the performance of the flowmeter [5].

Ultrasonic transducers can be considered as the heart of the flowmeter [2]. In ultrasonic transducers, an electrical signal can be produced by taking advantage of the piezoelectric effect in response to the incident ultrasound waves [7]. Since transducers are the devices used for electroacoustic conversion [8] [a], they are the most important component in ultrasonic flowmeter systems and, at the same time, the limiting factor for flow measurement errors [b], as the quality of emitted and received ultrasonic signals greatly affects the calculation of TOF. Consequently, it is essential to optimize this main device.

An ultrasound transducer is made of various components, including an active layer (piezoelectric crystal), two passive layers (a damping material or backing block and one or multiple matching layer/s) as shown in Figure 1.1(D), as well as the electrodes, housing, and an insulating cover [10].

A number of parameters are critical when selecting a suitable transducer for the flow measurement including bandwidth, sensing range, maximum driving voltage and peak frequency that mainly influences the sound attenuation and the signal to noise rate (SNR) [2, 5]. The optimal performance of ultrasonic transducers are achieved only with high efficiencies that ensure a maximum energy transmission. The efficiency of a transducer is indeed defined as the fraction of the applied energy that is converted to the desired energy mode [7, 10]. The performance of ultrasonic transducers is decided by many factors. In addition to the external mechanical and electrical load conditions and structure designs (including radiation surface area, mechanical damping, housing and connector),

---

[a] The main component for generating sound wave and receiving an incoming signal is the piezoelectric resonator. In the transmission mode, it converts an electric signal into a sinusoidal mechanical wave, while in receiving mode, it will generate voltage across it when acted upon by a mechanical pressure. [9] . The magnitude of the electrical signal will vary directly with the wave pressure of the incident ultrasound.

[b] Other components, such as electronics and signal processing, are already well developed and do not need further optimisation.

the selection of the materials and their properties of each component inside the sensors play a critical role [9].
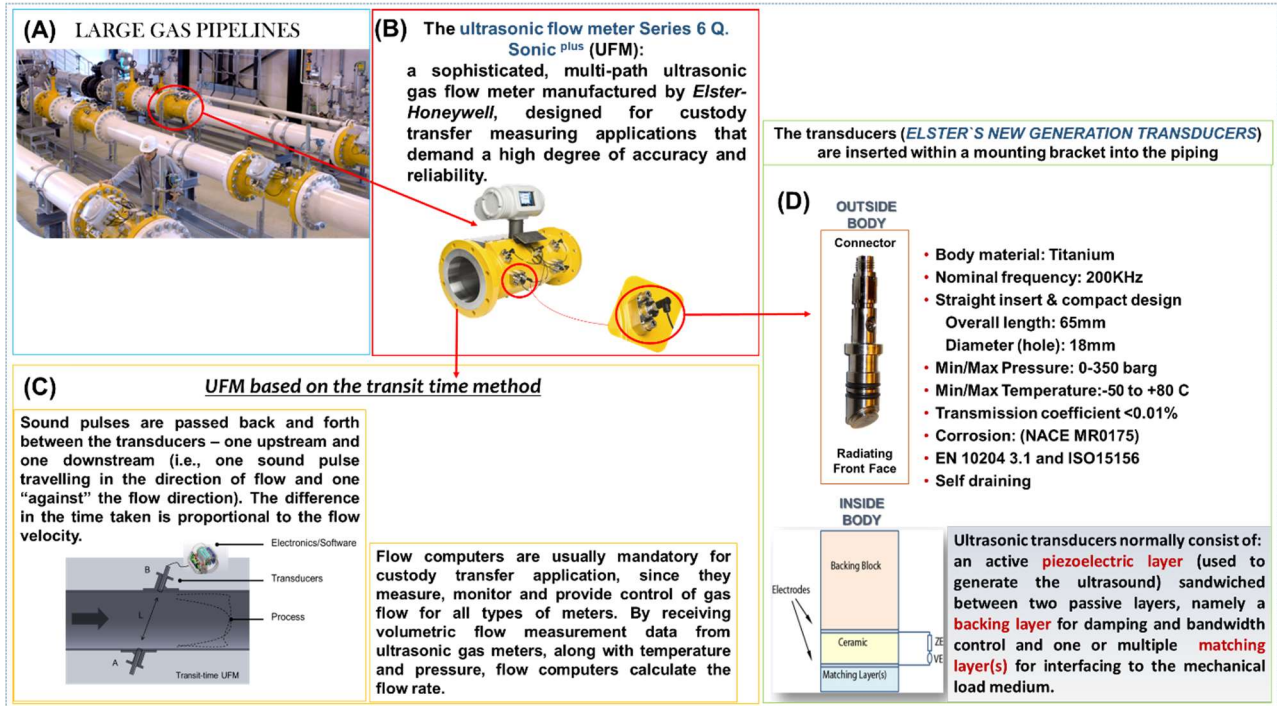
Figure 1.1. Equipment used in industry (specifically by the industrial sponsor, Honeywell) in gas flow rate measurements in (A) large gas pipelines, through (B) ultrasonic flow meters based on the (C) UFM transit time method in which (D) ultrasonic transducers are the primary device in the generation of ultrasound.

1.2 Research Questions and Investigation

Over the years research has focused on developing air-coupled transducers, efficient and reliable for use in practical industrial applications for flow detection [11] and many other measurement applications (e.g. object detection, distance measurement, range sensing, etc.) [12]. Although air-coupling is very attractive for its main advantage of transmitting ultrasonic waves into air and detecting reflected waves from an object [11], there are some difficulties to overcome, such as the high attenuation coefficient of air which increases tremendously as frequency is increased, and the high impedance mismatch between the transducer and air [13].

Attenuation of ultrasonic waves always occurs in large gas pipelines due to the acoustic and thermodynamic properties of the gas. Flow viscosity and heat exchange are the principal reasons for attenuation and distortion of the ultrasonic wave waveform in a gas. In addition, the presence of other factors such as vortices and/or noise in the pipeline affect the propagation of the ultrasonic wave, having thus a great impact on flow rate measurements [1]. Disturbances in gas networks (e.g., noise generated by mechanical vibrations due to pressure drop and/or by gas turbulence and expansion inside the pipeline) adversely affect ultrasonic signals [2]. In particular, the noise level, known as signal-to-noise ratio (*SNR*), increases with flow rate and decreases when expansion

decreases. In the worst case scenario, ultrasonic signals can be completely buried in surrounding noise, making it impossible to complete the measurement [2]. Therefore, the transducer response has to be sufficiently high to always provide a good signal-to-noise ratio, regardless of the frequency, and remain insensitive to attenuation losses. Passive materials have an important role in the performance of transducers in addition to the active material for enhancing energy transfer and preventing unwanted resonances in the transducer [14]. Attenuation and acoustic impedance are the most important material parameters for passive materials [15].

Acoustic impedance is a crucial parameter in designing ultrasonic sensors and sensing systems as it determines the acoustic transmission and reflection at the boundary of two media having different material properties [13]. The acoustic impedance of air is normally many orders of magnitude smaller than the impedance of most sound generating materials (e.g. the acoustic impedance of piezoelectric ceramics is 26 MRayl, while that of air is 4.3×10^{-4} MRayl) [12]. Acoustic waves cannot be sent with the maximum energy transmission into the radiation medium (air) when there is a large difference between the two media (piezoelectric material and air) [9]. A large impedance mismatch causes large loss in the vibrating radiating surface of piezoelectric ceramics and implies that ultrasonic transducers are inherently inefficient, the reason why the generation of ultrasound in air is highly challenging [11]. The common solution for air-coupled ultrasonic measurements is the impedance matched matching layer (ML) for acoustically coupling the active layer to the radiation medium. Bonding a special material to the piezoelectric ceramic as front layer (i.e. matching layer) aims to improve the energy transmission between the active layer and the load medium compensating for their acoustic impedance mismatch [15].

Without one or multiple proper MLs [c], the huge acoustic impedance mismatch will cause most of the ultrasound energy to be reflected at the interface with the load medium [13], greatly reducing the power efficiency and sensitivity of the device, particularly for single frequency transducers (e.g. *Elster/Honeywell's new generation transducers* have a nominal frequency of 200 kHz). The presence of a front ML with an appropriate acoustic impedance will necessarily increase output or sensitivity of the transducer, since the electric power output is only maximized when the load impedance is matched to the source impedance [16, 17]. A ML that provides the required acoustic impedance transition will allow the acoustic energy to be efficiently sent from the piezoelectric resonator through air into the piping, and vice versa allowing the reflected signal to be returned to

---

[c] Dual (or multiple) matching layers structure can provide a further reduction of impedance. Gradient acoustic impedance matching is another technique employed for improving the matching layer design through multilayer structure, in terms of transducer sensitivity, transmission efficiency and improved bandwidth [9].

the transducer for detection, without too much loss. Only the matching of the acoustic impedances can increase the energy transmitting efficiency from the front end of the transducer and maximise the performance and sensitivity of the sensors so to eliminate, or at least minimise, the error in the gas flow measurements discussed in section 1.1. For conventional impedance matching condition, an ideal ML has an acoustic impedance equal to the geometrical mean value of the impedances of the transducer material and radiation medium [16] and a thickness that is one-quarter of the wavelength in the material (thickness = ¼ λ) [10]. This represents the best matching condition (optimum) at which it is believed that there is no reflection from the transducer surface, the output wave amplitude is the highest and thus the energy transfer from the transducer is maximised [16]. Such principle requires very low impedance materials that are not available in pure form or as a single phase. The state of the art for MLs with adjustable acoustic impedance is the mixing of micro- or nano-scale powders into a polymer and adjust the powder content so as to adjust acoustic impedance [18-20]. Materials made of epoxies loaded with suitable fillers are commonly used as passive layers [11]. Powder-loaded epoxy, vacuum-deposited thin-films of glass and parylene are extensively employed as ML materials, whose acoustic impedance may be tailored by the volume fraction of solid powder. Silver epoxy and parylene are commonly used for matching [21] but alumina-filled epoxy as well as other polymer materials (e,g. silica gel) have also been reported for use in matching applications [17]. Dispersed microspheres with air inclusion are commonly preferred for this purpose [22]. Nonetheless, the problem of air dispersion is the non-uniformity in its distribution, which causes scattering of waves leading to an increase of propagation loss and the cost of the product [22]. In material selection for transducer design, there are several material properties to take into consideration, including elastic constants and density on which the speed of sound depends, and machinability, in addition to cost [15].

The design of new ultrasonic transducer assembly process involving advanced manufacturing methods is essential for cost effective and reliable manufacture of ultrasonic devices. More efficient and consistent signal shape with minimal energy loss could be achieved by substituting the materials used currently in MLs while obtaining a wider bandwidth operating range. Investigating/implementing advanced manufacturing methods to fabricate novel composite materials for use in UFM applications would enable cost effective, accurate and reliable fabrication of ultrasonic transducers, yielding higher performance.

1.3 Focus and Innovation of Proposed Research

The desired acoustic impedance values for passive layer components depend on the acoustic impedance of the active material to be matched [21]. Bonding a special material to the piezoelectric ceramic as an acoustic ML can enable the ultrasonic sensor to work in frequencies of up to several

hundred kHz [12]. The *Elster`s new generation transducers* (i.e. target application of this project) need a ML material that has an acoustic impedance in between that of air and the piezo-ceramics of just 0.11 MRayl. Syntactic foams made of epoxy resin and glass micro-balloons are the materials currently employed in the construction of such air-coupled ultrasonic transducers manufactured by the industrial partner Honeywell, which far exceed the required acoustic impedance value. A new design of the front ML can make the ultrasonic transducer wide band and enhance its receiving sensitivity as well as the output power acoustic signal, while guarantying a convenient and low-cost fabrication process. More efficient and consistent signal shape could be achieved by substituting the currently used syntactic foam in the matching layer.

The optimisation of the *Elster-Honeywell`s New Generation Ultrasonic Transducers* through the insertion of novel materials (e.g. polymeric composite foams) never employed before in MLs within the sensor assembly is the main aim as well the innovation of this EngD project. Specifically, foams of high-density polyethylene resin (HDPE) and multi-walled carbon nanotubes (MWCNTs) were selected as potential passive layer candidates for the specific target devices produced by Honeywell. The development, fabrication and evaluation of thermoplastic foams, specifically foams of HDPE and HDPE-MWCNT composites for use in ultrasonic flow metering applications, could lead to improved passive layers for ultrasonic transducers, while meeting the strong desire for low-cost, thin, and lightweight composite materials able to absorb sound waves in a wide frequency range [23].
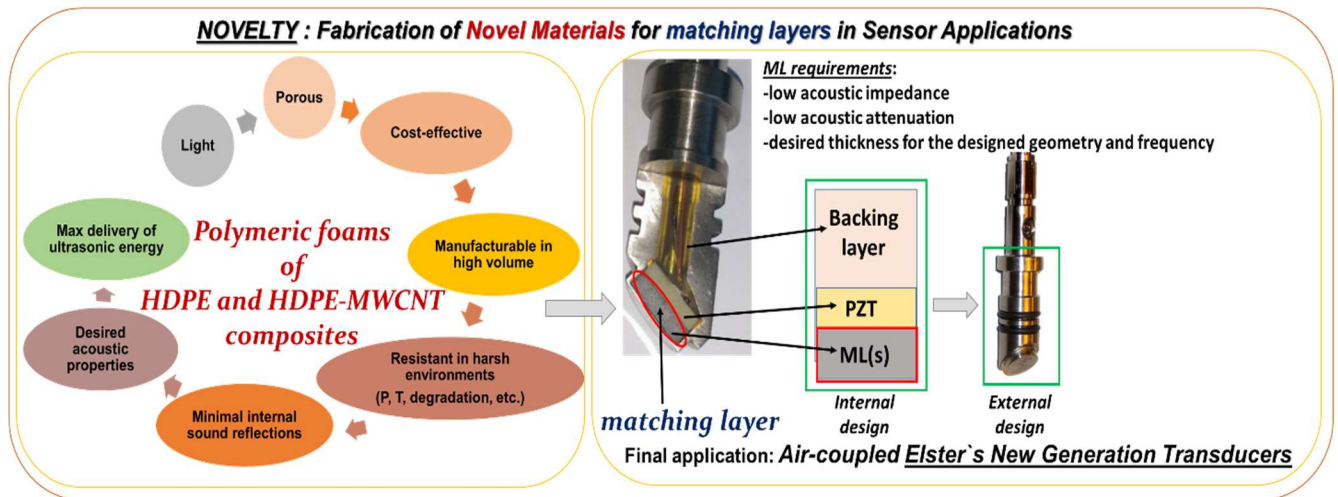
Figure 1.2. Novelty behind the project: Fabrication of novel materials for matching layers in sensor applications.

Foams of composites of MWCNTs and HDPE represent a novel approach to fabricate lightweight foams having the desired combination of properties for application in acoustic sensors. Clearly, there are several technical challenges that need to be overcome in order to prove the novelty behind this solution. The main challenges involved in this research proposal are summerised as following and

will be discussed more in detail in the next sections of this innovation report:

CHALLENGES INVOLVED IN THE RESEARCH SOLUTION

❖ *High crystallinity of the polymer matrix selected*

- Rigidity of the crystalline phase (semi-crystalline polymer)
- Low solubility of gases in polymers (negligible solubility of gases in crystallites of PEs)
- High (melt) viscosity which prevents cell growth
- High stiffness which suppresses cell expansion and increases velocity of sound

❖ *Rapid crystallization kinetics of HDPE which disturbs the cell growth process*

❖ *Tendency of semi-crystalline polymers to form non-uniform cell structures*

❖ *Ensure homogeneity in the system*

❖ *Ensure highly porous structures for low values of acoustic impedance and attenuation*

❖ *Find appropriate conditions for foaming*

❖ *Fabrication issues for thin & uniform ML thicknesses (geometrical accuracy)*

The foams were prepared in a two-step process via both chemical and physical foaming and parametric studies were conducted to investigate the different approaches to manufacturing and processing, as well as the effects of MWCNT loading on foaming behaviour of HDPE. In particular, the foaming behaviour of a number of injection moulded samples was characterised in terms of final foam densities, expansion ratio, cell structure and acoustic properties, to test if the material specifications required for the final application were met. Furthermore, as none of the studies reported to date have investigated the acoustic properties of these foams, a lack of understanding had to be addressed, allowing this study to make a further contribution to scientific knowledge. Furthermore, the use of conventional polymer processing technologies, extrusion and injection moulding, provide a route to the manufacture of the MLs in a cost effective manner, in high volumes and at scale.

1.4 Project Strategy and Sustainability Goals

The main goal of this EngD project is the discovery and use of new foam materials within the sensor assembly together with the study and development of advanced manufacturing methods for their manufacture. In doing so, this will enable the optimization of ultrasonic transducers for use in ultrasonic flow metering applications. In the meantime, the study of new acoustic materials as alternatives to conventional materials can also provide valuable solutions for current and future applications in various other engineering fields [24, 25].

Matching layer designs require ultra-thin MLs layers of micro-size features [15] and fabrication processes that are convenient, reliable and low-cost [9]. Furthermore, adherence to accuracy and

repeatability is extremely important along with size, cost, weight and versatility, the reason why new solutions are essential to satisfy many future demands [4]. The use of automated manufacturing such as injection moulding (IM) can offer numerous benefits including high repeatability in moulding foamed parts, as well as fast production speeds and little post-moulding finishing.

Special injection moulding (IM) processes capable of reducing material consumption are highly desirable, both for reducing production and transportation costs, and for the sustainability of natural resources, as well as for saving the environment [26]. Among the various special IM processes, microcellular IM (MuCell) has proven to be successful in saving on material costs and energy consumption while improving product dimensional stability and production efficiency [27]. It continues to attract attention by producing lightweight parts with advantageous properties as well as additional degrees of freedom in product design and part thickness variation, while requiring less material, lower injection pressures and energy, and shorter cycle times. The direct utilization of foaming (blowing) agents is the most commonly used method for large-scale production [28], and microcellular polymer processing technology has the advantage of using environmentally friendly blowing agents, such as carbon dioxide and nitrogen [29].

Among the wide variety of thermoplastics that have been tested using foam processing techniques, polyethylene (PE) is one of them [30], mainly due to its useful mechanical properties and affordable price, as well as its high chemical resistance and temperature stability. The great balance of toughness, flexibility and resistance to chemicals and abrasion make PEs excellent candidates for foamed products [31]. The addition of a small amount of nanoparticles (e.g. MWCNTs) can significantly improve a variety of properties including sound absorption [23, 32], while still preserving the lightweight of polymer matrices [33].

Polymer nanocomposite foams have increasingly received attention in industry and academia, mainly due to lightweight, high strength and multifunctional properties, but also with regards the relatively low investment costs and simple and convenient moulding process [33]. Polymers offer low density and ease of processing and when on addition of a filler are able to provide a unique combination of properties [33]. To make nanocomposites economically viable, their production must use common processing equipment and avoid additional processing steps. Melt compounding and injection moulding processes are among the most convenient and preferred processing methods for industrial applications, due to their industrial and economic advantages linked to the simplicity, low cost, no need for solvents and environmental friendliness of these techniques. Potential advantages can arise by using nanocomposites in foaming processes as the high aspect ratio and large surface area of nanofillers are extremely beneficial for reinforcing foam materials. Nanofillers

can improve the properties of the matrix (e.g. sound absorbing properties [34]) by providing additional functionality to the neat polymer foams and by changing the structure of the foams through heterogeneous nucleation [34]. The acoustic impedance properties of porous nano-structured materials can be thus adjusted by controlling the total volume fraction of voids. The inclusion of microscopic air pockets in the plastic resin makes polymer foams much lighter and cost-effective than their solid counterparts [35] as well as more sustainable for the reduced amount of plastic needed. Beyond the weight reduction and material savings, there are other sustainability benefits such as those related to the reduced fuel consumption to transport foams, as it is easier transporting lighter weights [36].

1.5 Project placing in the market for the industrial sponsor

Developing, fabricating and evaluating polymer and composite foams of HDPE and MWCNTs with very low acoustic impedance and attenuation could lead to improved passive layers, in terms of efficiency, signal bandwidth, safety, size, and above all cost. Improving the performance of ultrasonic devices through the insertion of such foam composite materials would mean reducing the error in gas flow measurements, enabling the industrial sponsor (Honeywell) to gain significant economic benefits in a highly competitive global market.

In the industries of gas measuring, safety and regulation, Elster-Honeywell is well positioned in the field of gas distribution and gas transmission businesses in various markets worldwide. Meeting the requirements and needs of gas distribution and gas transmission companies is the main target for the organisation (Honeywell) whose market is principally based on the extensive global sales for products (e.g. measuring devices, regulation equipment, electronics and stations) and service network customized solutions to tailor the specific needs of its clients. Honeywell has established a global distribution network and operates in ca. 38 countries mostly focused in North and South America, Europe and Asia, with the major gas markets situated in Germany, Spain, Italy, China, England and Latin America. The main clients are the pipeline companies, gas utilities, gas distribution companies, power plants, chemical and industrial industries, laboratories and solution providers.

Specifically, in the Honeywell business the Elster group represents a leading global provider of gas, electricity and water meters and related communications, networking and software solutions. Its market size involves more than 130 countries and include numerous large, medium and small utilities, distributors and industrial customers across gas, electricity, water and multi-utility organizations for use in residential and commercial and industrial settings.

As the UFM covers gas transmission (big pipelines), distribution (state/city level), and residential (in the basement of each household), the novel product presented in this work would initially fit in the residential market, whose size would be several tens of million units per year, provided that the cost of each individual UFM device is ~50$ (the price includes smart electronics).

1.5 Portfolio Structure

The EngD portfolio is structured as a series of submissions (reports) describing different stages of the EngD project from the identification and investigation of the problem to the detailed stages of developing the most suitable solution and related testing and implementation phases, in addition to the statements of innovation and personal development. In particular, the *Personal Profile* describes a summary of the many competencies developed by the EngD candidate during the course of the degree, whereas the *International Collaborations Report* describes the key international collaborations made during the entire EngD training program.

The list of reports written by the author are outlined in Table 1.1.

Table 1.1. List of titles of the Portfolio Submissions written by the author and submitted as part of the EngD Portfolio during the EngD program.

Submission No.	Title
1	*Ultrasonic transducers for Ultrasonic Flowmeters Applications in Large Gas pipelines*
2	*Polymer Materials for Acoustic Absorption*
3	*Characterisation of Composites of HDPE and MWCNTs prepared by Extrusion and Injection Moulding*
4	*Crystallisation behaviour of Composites of HDPE and MWCNTs: The effect of nanotube dispersion, orientation and polymer deformation*
5	*Preparation and Characterisation of foamed HDPE by addition of chemical foaming agents in Extruder*
6	*Characterisation of Foamed composites of HDPE and MWCNTs prepared by addition of chemical foaming agents during extrusion*
7	*Characterisation of foams of HDPE and HDPE-MWCNT composites prepared by Physical Foaming with SCF-CO_2*
8	*Personal Profile*
9	*International Collaborations Report*

CONTENT OF PORTFOLIO SUBMISSIONS

Research Questions	Submission Portfolio	Novelty	Research Impact: Publications
Problem identification	Submission No.1	The document provides a general overview of the novel research topic interrelating the UFM technology with the material properties and requirements for the final target application.	-
Problem investigation	Submission No.2	The document is the first comprehensive study that addresses both fields of the physics of sound and ultrasonics and polymer science.	*"Polymer Materials for Acoustic Absorption".* Submitted in the journal *Progress in Materials Science*.
Developing the solution	Submission No.3	This study focused on non-foamed HDPE and HDPE-MWCNT composites manufactured by extrusion and injection moulding helped tailor the properties and structures of the novel materials (polymer foams) required for application in acoustic sensors.	Amoroso, Lorena; Heeley, Ellen L.; Ramadas, Sivaram Nishal; and McNally, Tony. *"Crystallisation behaviour of composites of HDPE and MWCNTs: the effect of nanotube dispersion, orientation and polymer deformation".* Published in the journal P*olymer*, 201, (2020), 122587. doi: 10.1016/j.polymer.2020.122587.
Developing the solution	Submission No.4	This study aimed at better understanding the crystallisation behaviour of the HDPE-MWCNT composites since crystallinity and orientation of the crystallites affect both density and elastic properties, which in turn, affect the speed of sound and the direction of acoustic waves propagating in such materials.	
Developing & testing the solution	Submission No.5	This work focused on foaming chemically the neat HDPE with selected chemical blowing agents (CBA_1 and CBA_2), in the course of the extrusion process followed by a further mini- IM step. Different processing conditions, including temperature, pressure and CBA content were studied, and the effect of each on the structure of the HDPE and composite foams on physical and acoustic properties.	*"Morphology and Properties of MWCNT filled HDPE foams prepared with chemical blowing agents".* Intended submission in the journal *Polymer Engineering & Science*.
Developing & testing the solution	Submission No.6	This work is a complimentary study to the previous one conducted on unfilled HDPE foams but with the inclusion of MWCNTs. It elucidates the processing-structure-property relationships of HDPE-MWCNT composites foams prepared by chemical foaming, emphasizing the effects of varying the processing and MWCNT loading (between 0.01 wt% and 5 wt%) on foam morphology and final properties of the moulded composite foam samples.	
Developing & testing the solution + Preliminary implementation	Submission No.7	This work focused on the physical foaming of HDPE and HDPE-MWCNT composites, using MuCell moulding technology, aimed at achieving larger weight reductions and higher porosities of the final foamed parts when compared to composites foams prepared by chemical foaming. The use of $SCF-CO_2$ as PBA allowed to significantly reduce the polymer viscosity, enabling production of very porous parts with very low acoustic impedance.	*"Acoustic Properties of MWCNT filled HDPE foams prepared with physical blowing agents".* Intended Submission in the journal *ACS Applied Materials & Interfaces*.

Finally, the *Innovation Report* (Thesis) is a collation of the most significant outcomes of the project, condensing the entire work in seven chapters structured as follows.

CHAPTER 2 → provides a comprehensive literature review addressing both the physics of sound and material properties as well as a description of the methods used to manufacture cellular polymeric materials with sound absorption properties.

CHAPTER 3 → provides a description of the experimental methodology and procedures used in this work.

CHAPTER 4 → provides a discussion on the characterization with a focus on the crystallisation behaviour of non-foamed HDPE and HDPE-MWCNT composites.

CHAPTER 5 → provides a discussion on the characterization procedure followed and the results obtained from the study focused on foamed samples of HDPE and HDPE-MWCNT composites prepared via chemical foaming.

CHAPTER 6 → provides the discussion on the characterization procedure followed and the results obtained from the study focused on foamed samples of HDPE and HDPE-MWCNT composites prepared via physical foaming, followed by the discussion on the final outcomes obtained from the implementation of the candidate materials in gas pipeline sensors.

CHAPTER 7 → highlights the most important conclusions from the study and gives some recommendations for future work.

1.6 Contribution to Innovation, Knowledge and the Industrial Sponsor

The main innovative aspect of this research is the fabrication of HDPE-MWCNT composite foams, which outperform other polymers and existing materials used commercially as passive layers (e.g. syntactic foams) in terms of acoustic properties. Furthermore, these new composite foams can be prepared at scale and in large volumes using conventional and/or slightly modified polymer processing technology. These novel materials are the product of combining functional nanoparticles (MWCNTs) and foaming technologies (chemical and physical foaming) which resulted in composites having multifunctional desirable characteristics, including lightweight, high specific strength, rigidity, dimensional and thermal stability, and low cost.

Moreover, thermoplastics are favoured over other materials, because easy to process and reprocess when molten, as they have the potential to be recycled by being re-melted to form new articles or burnt to generate electrical energy.

The present thesis provides a significant contribution to knowledge in the field of un-foamed and foamed polymeric nanocomposites. The research conducted is important as it provides an understanding of the chemical and physical forming of composites of polymer and 1D

nanomaterials, such as MWCNTs and their significant applications in areas such as light weighting and packaging, but also in sensors for improving the performance of the measurements of gas flow rate in large gas pipelines. The uniqueness of the system investigated, very different to existing MLs, is highly novel and provides a route to low cost, low weight, stiff and durable materials, while offering an optimal balance of low acoustic impedance and attenuation with reduced density, desired acoustic transmission/absorption, strength, suitable size and shape.

There is limited knowledge about the structure and properties of nanocomposite foams (primarily acoustic properties) given the technical challenges of incorporating un-functionalised MWCNTs and chemical blowing agents into a highly crystalline matrix and high melt viscosity polymer like HDPE.

The processing-structure-property relationships for such foams are poorly understood and this work has made a contribution to the knowledge in this area. Specifically, gainful insights in to the role of gas diffusion, nucleation of cells, cell growth, the role of MWCNTs in the nucleation process and the many processing parameters required to produce useful foams has been achieved. Fundamentally, a significant understanding of the role MWCNTs play in altering the crystallisation behaviour and kinetics of HDPE has been obtained. The structure and properties of theses foams has also been studied in detail using a range of techniques.

The outputs from the research project, both academic and applied are considerable and are considered significant by Honeywell. Firstly, Honeywell nor none of their industrial competitors in the sensor industry have previously employed filled polymer foams as MLs. Not only have HDPE-MWCNT composite foams not been used in sensors before, but the degree of porosity developed in the moulded parts in this work enabled the production of highly expanded materials with significant potential for other application areas, as they have similar (if not better) acoustic impedances of existing commercial ML materials. The introduction of such material products combined with the relative ease of manufacture for an established industrial sector such as that of ultrasonic transducers, could provide Honeywell with new business opportunities leading to increased sales and revenues in what is the global market for sensors and related technologies.

1.7 Aims and Research Questions

The <u>aims</u> of this project are to;

i. Identify novel materials for use as improved passive layers in ultrasonic transducers as well advanced manufacturing methods for their production.

ii. Prepare composites of HDPE and MWCNT by industrially relevant and cost-effective processing techniques, i.e. extrusion and IM and determine the role of MWCNT on the crystallization behaviour of un-foamed HDPE.

iii. Prepare foams of HDPE and HDPE-MWCNT composite by addition of CBAs in extruder prior to foaming during IM and investigate the role of varying processing conditions and MWCNT and CBAs loading on the final properties of as prepared foams. Therefore, determine the foaming behaviour of the foams produced, determine their void content, and measure foam density, expansion fraction, void fraction, cell structure, acoustic and mechanical properties.

iv. Prepare microcellular foams of HDPE and HDPE-MWCNT composite by means of $SCF-CO_2$ (i.e. PBA) during IM assisted via MuCell technology. Therefore, determine foam density, expansion and void fractions, cell structure, acoustic and mechanical characteristics of foams prepared with the MuCell process and correlate foam morphology with the final acoustic properties.

v. Identify the most promising HDPE and HDPE-MWCNT composite foams for the application of interest and test the performance and transmit acoustic response of the sensor incorporating the foams produced.

The <u>objectives</u> of this project are to;

i. Prepare composites of HDPE and MWCNT at various MWCNTs loadings (0.01wt%, 0.1wt%, 0.3wt%, 0.5wt%, 1wt%, 3wt% and 5 wt%) via extrusion and micro-IM.

ii. Assess the morphology and thermal characteristics of the two CBAs (CBA_1 and CBA_2) by SEM, TGA and DSC to establish the most suitable conditions for the chemical foaming process. Therefore, prepare foams via chemical foaming of HDPE and composites of HDPE and MWCNTs with between 0.01 wt% - 5wt% MWCNTs and CBAs content between 1 and 4wt% using a 16mm co-rotating twin-screw extruder and micro-injection moulding.

iii. Characterise the morphology and structure of each foam sample by SEM analysis and investigate the processing- structure relationship of the as fabricated samples. Therefore, determine the reduction in density, porosity, acoustic and mechanical properties by means of analytical balance measurements, void fraction, ultrasonic measurements through transmission in either air or water and compression testing, respectively.

iv. Compound composites of HDPE with MWCNT at 0.1, 0.5 and 1 wt% loadings using twin-screw extrusion and prepare foams via physical foaming of HDPE and HDPE-MWCNT composites using MuCell moulding technology.

v.   Characterise the morphology and structure of each foam sample by SEM analysis and investigate the processing- structure relationship of the as fabricated samples. Therefore, determine the reduction in density, porosity, acoustic and mechanical properties by means of analytical balance measurements, void fraction, ultrasonic measurements through transmission in either air or water and compression testing of forma prepared by physical blowing process.

vi.   Compare the acoustic impedance characteristics of the fabricated foamed samples and benchmark against current commercial ML samples. Therefore, select promising foam samples from those fabricated using both methods (chemical and physical foaming) by examining their potentials to act as passive layers in acoustic sensors.

vii.   Implement the most promising foam samples identified in the previous steps within a full sensor assembly and test performance using optical microphone measurements.

References

[1] H. Zhou, T. Ji, R. Wangb, X. Ge, X. Tang, S. Tang., Multipath ultrasonic gas flow-meter based on multiple reference waves, Ultrasonics, 82, 2018, pp. 145-152.

[2] P. Brassier, B. Hosten, F. Vulovic, High-frequency transducers and correlation method to enhance ultrasonic gas flow metering, Flow Measurement and Instrumentation, 12(3), 2001, pp. 201-211.

[3] L.C. Lynnworth, Y. Liu, Ultrasonic flowmeters: Half-century progress report, 1955–2005, Ultrasonics, 44 (Suppl 1), 2006, pp. e1371-e1378.

[4] D. Hackett, Selecting flowmeters for natural gas, Applied Automation, 2016, pp. A10-A14.

[5] Q. Chen, W. Li, J. Wu, Realization of a multipath ultrasonic gas flowmeter based on transit-time technique, Ultrasonics, 54(1), 2014, pp. 285-290.

[6] S.A. Tereshchenko, M.N. Rychagov, Acoustical multipath flow measurements based on quadrature integration methods, Acoustical Physics, 50(1), 2004, pp. 100-106.

[7] W.R. Hendee, E.R. Ritenour, Ultrasound Waves, in: Medical Imaging Physics, Wiley-Liss Inc, Chapter 19, fourth edition, 2002, pp. 303-316.

[8] X. Dongyu, C. Xin, H. Shifeng, Investigation on fabrication and property of acoustic gradient composites, Composites Science and Technology, 122, 2016, pp. 90-96.

[9] J. Zhu, Optimization of matching layers design for medical ultrasonic transducer, Doctoral Thesis, Intercollege Graduate Program in Materials, The Pennsylvania State University, 2008.

[10] W.R. Hendee, E.R. Ritenour, Ultrasound Transducers, in: Medical Imaging Physics, Wiley-Liss Inc, Chapter 20, fourth edition, 2002, pp. 317-329.

[11] V.K.R. Kommareddy, Air-Coupled Ultrasonic Measurements in composites, MSc Thesis, Retrospective Theses and dissertations, Iowa State University, 2003.

[12] Ultrasonic Sensor (catalog), Cat.No.S15E-5, Murata Manufacturing Co., Tokyo, Japan, 2008, pp. 1-13.

[13] I. Ihara, Ultrasonic Sensing: Fundamentals and Its Applications to Nondestructive Evaluation, in: Sensors: Advancements in Modeling, Design Issues, Fabrication and Practical Applications, Springer, PART V, 2008, pp. 1-20.

[14] G. Kossoff, The Effects of Backing and Matching on the Performance of Piezoelectric Ceramic Transducers, IEEE Transactions on Sonics and Ultrasonics, 13(1), 1966, pp. 20-30.

[15] Q. Zhou, S. Lau, D. Wu, K.K. Shung, Piezoelectric film for high frequency ultrasonic transducers in biomedical applications, Progress in Materials Science 56(2) (2011) 139-174.

[16] M. Toda, Ultrasonic Transducer having Impedance Matching Layer, U.S. Patent Documents, Measurement Specialities Inc.,Lawrenceville, NJ (US), application no. 09/360,305, 2001, pp. 1-16.

[17] H. Wang, T. Ritter, W. Cao, K.K. Shung, Passive materials for high frequency ultrasound transducers, SPIE Proceedings, 1999, pp. 35-42.

[18] S.X. Wang, J. Carlier, A. Ndieguenea, P. Campistrona, D.C. Debavelaerea, C. Soyera, B. Nongaillarda, X.-Z. Zhaob, Stiffness controlled SU-8-based nanocomposites: Application for 1 GHz matching layer conception, 2008 IEEE Ultrasonics Symposium, 2008, pp. 678-681.

[19] Q. Zhou, J.H. Cha, Y. Huang, R. Zhang, W. Cao, K.K. Shung ound transducer application, IEEE Transactions on Ultrasonics, Ferroelectrics, and Frequency Control, 56(1), 2009, pp. 213-219.

[20] F. Tiefensee, C. Becker-Willinger, Nanocomposite materials for high frequency ultrasound matching layers, 2009 IEEE International Ultrasonics Symposium, 2009, pp. 1719-1721.

[21] R.A. Webster, Passive Materials for High Frequency Piezocomposite Ultrasonic Transducer, Doctoral Thesis, Department of Metallurgy and Materials, University of Birmingham, 2009.

[22] M. Toda, New type of matching layer for air-coupled ultrasonic transducers, IEEE Transactions on Ultrasonics, Ferroelectrics, and Frequency Control, 49(7), 2002, pp. 972-979.

[23] R. Gayathri, R. Vasanthakumari, C. Padmanabhan, Sound absorption, Thermal and Mechanical behavior of Polyurethane foam modified with Nano silica, Nano clay and Crumb rubber fillers, IJSER, 4(5), 2013, pp. 301-308.

[24] A. Nick, U. Becker, W. Thoma, Improved Acoustic Behavior of Interior Parts of Renewable Resources in the Automotive Industry, Journal of Polymers and the Environment, 10(3), 2002, pp. 115-118.

[25] M.R.G. Ravandi, H. Mardi, A.A.A. Langari, M. Mohammadian, N. Khanjani, A Review on the Acoustical Properties of Natural and Synthetic Noise Absorbents, Open Access Library Journal, 2(8), 2015, pp. 1-11.

[26] X. Sun, H. Kharbas, J. Peng, L-S. Turng, A novel method of producing lightweight microcellular injection molded parts with improved ductility and toughness, Polymer, 56, 2015, pp. 102-110.

[27] S.P. Nalawade, F. Picchioni, L.P.B.M. Janssen, Supercritical carbon dioxide as a green solvent for processing polymer melts: Processing aspects and applications, Progress in Polymer Science, 31(1), 2006, pp. 19-43.

[28] C. C. Ibeh, M. Bubacz, Current Trends in Nanocomposite Foams, Journal of Cellular Plastics, 44(6), 2008, pp. 493-515.

[29] S. Doroudiani, C.B. Park, M.T. Kortschot, Effect of the crystallinity and morphology on the microcellular foam structure of semicrystalline polymers, Polymer Engineering & Science, 36(21), 1996, pp. 2645-2662.

[30] M. Altan, Thermoplastic Foams: Processing, Manufacturing, and Characterization, in: Recent Research in Polymerization, Intech Open, Chapter 6, 2018, pp. 117-137.

[31] Y. Zhang, Polyolefin Formulations for Improved Foaming: Effects of Molecular Structure and Material Properties, Doctoral Thesis, Department of Chemical Engineering, Queen's University, Kingston, Canada, 2013, pp. 1-133.

[32] D. de Mello, S.H. Pezzin, S.C. Amico, The effect of post-consumer PET particles on the performance of flexible polyurethane foams, Polymer Testing, 28(7), 2009, pp. 702-708.

[33] L.J. Lee, C.C. Zeng, X. Cao, X. Han, J. Shen, G. Xu, Polymer nanocomposite foams, Composites Science and Technology, 65(15-16), 2005, pp. 2344-2363.

[34] L.M. Chen, D. Rende, L.S. Schadler, R. Ozisik, Polymer nanocomposite foams, Journal of Materials Chemistry A, 1(12), 2013, pp. 3837-3850.

[35] D. Klempner, K.C. Frisch, Handbook of Polymeric Foams and Foam Technology, Hanser, 1991, pp. 1-408.

[36] Hydrocerol Chemical foaming agents, 2013. www.MASTERBATCHES.CLARIANT.COM. (Accessed 20/04/2020).

CHAPTER 2: LITERATURE REVIEW

Polymer Materials for Acoustic Absorption

2.1 Introduction

In order to successfully develop materials for acoustic absorption and transmission applications, it is necessary to understand the relevant properties of both materials and acoustics [1].

Acoustics is a branch of physics focused on the study of sound, particularly its production and transmission in the form of pressure waves through media with any other phenomenon induced by this propagation [1-3]. Sound itself is a physical phenomenon that can be described as a disturbance in the medium, generated by the passage of pressure fluctuations (mechanical waves) through an elastic medium (e.g. air molecules) resulting from vibrations acting on the medium [4]. The presence of certain prerequisites, such as a source of energy (e.g. a force), a vibrating object that generates the pressure wave and a medium of transmission (e.g. air), is essential in the production of sound and thus acoustic signals. When a force is applied to the medium by a moving object (e.g. the movement imparted from an ultrasound transducer), the air molecules travel as a consequence in the same direction as the force, for a distance that is proportional to the magnitude of the applied force [5]. The transmission of acoustic energy in air is caused by collisions between the air molecules that pass the energy allowing pressure waves to move and propagate in it [5, 6].

Increasingly, research has focused on developing materials suitable for absorbing sound and reducing noise [7]. The control of the propagation of sound waves is of primary relevance in an increasing numbers of applications [8]. New acoustic materials as alternatives for conventional materials for current and future applications are urgently required. The trend towards sound-absorbing materials with low weight and effective damping properties is in the main driven by demands for higher load capacity and reduced fuel consumption for cars, trucks and aerospace vehicles [9, 10]. Vibration damping is also gaining increased attention for improved vibration and noise control, dynamic stability, fatigue resistance and impact resistance in advanced engineering systems [11]. The strong desire for low-cost, thin, and lightweight materials able to absorb sound waves in a wide frequency range [7] has directed focus on polymer foams. Excellent acoustic absorption and damping properties in reducing noise levels have been found in polymer foams [12]. The foam structure is a determinant factor in affecting the sound absorption efficiency [13]. Sound waves can be greatly absorbed during propagation in foam structures through internal reflection, refraction and dissipation of the sound waves in a cellular structure [14]. Furthermore, the presence of voids or discontinuities in the polymeric matrix of foamed polymers and composites results in a reduction in material consumption through the reduction in weight and density. Therefore, the fabrication of polymer foams results in an advantageous reduction in the total production cost,

provided that the material consumption consists of up to 70% of the total cost of a plastic product [15]. Microcellular materials can reduce material consumption even more significantly with their characteristic microscopic cell size and large number of cells, which in turn translates into further reduction in the costs of plastics, process energy and ultimate transportation of cellular plastics [16]. The inclusion of nanoparticles in the formation of polymer nanocomposite foams offer alternative exciting advantages for improving foam properties as well as the potential of creating novel nanocomposite foams for new applications [17]. Increased cell density and reduced cell size are both effects of the addition of nanoparticles and their high nucleation efficiency [18].

2.2 Physics of Sound

Sound waves are, by definition, longitudinal waves characterised by regions of compression and rarefactions that travel in the same direction as that of the collisions between the medium molecules [5]. A schematic diagram of how a longitudinal acoustic wave propagates in a medium is shown in Figure 2.1.
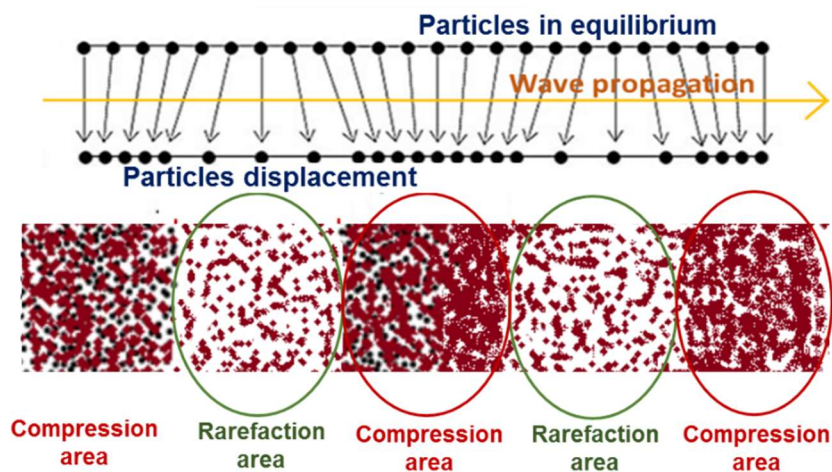
Figure 2.1. Schematic diagram showing the propagation of a longitudinal acoustic wave.

As the propagation of the wave occurs (from left to right in Figure 2.1), displacement of particles around their equilibrium positions are generated which results in the motion of periodic change in air pressure, thus alternating zones of high compression and low rarefaction in the material.

For a complete description and hence understanding of the propagation of sound in a medium, it is important to refer to the main characteristics of an ultrasound wave, summarised below:

- The wavelength (λ) → it denotes the length of one complete wave cycle or, in other words, the distance travelled through one complete cycle of vibration.
- The *frequency* (*f*) → a physical characteristic that describes the number of cycles introduced into the medium per unit time (cps, or sec^{-1}). It can be expressed in units of hertz, kilohertz, or megahertz, with 1Hz=1cps and depends on the mass and overall size of the vibrating object. The frequency range at which sound waves propagate determines the type of acoustic wave. A

frequency that is comprised between 20Hz and 20,000Hz is defined as a *sound wave*. An *infrasonic wave* is a low frequency acoustic wave (not audible to the human ear) characterised by a frequency value typically below 20Hz. Finally, an *ultrasound* (or *ultrasonic*) *wave* propagates at frequencies above the range of human hearing (conventionally defined as being above 20 kHz) [6].

- The *amplitude* (A) → it is the maximum height of the wave cycle (i.e. maximum displacement of vibrating particles in the medium from the mean position) and corresponds to the intensity of the pressure change.

- The *intensity* (*I*) → a physical property that describes the amount of acoustic energy transmitted per unit time and per unit area (usually 1s and 1cm², respectively) in the direction normal to the considered area. The acoustic energy is directly related to the acoustic intensity (*I*) which represents the power a sound wave transports travelling in a medium per unit area (or energy transported per unit time).

- The *phase* → it is a very important factor in the interaction of one wave with another while travelling in a medium. It is measured as an angle in degrees. The result of the combination of two waves "in phase" is constructive interference (the waves add their amplitudes, generating a sound wave of increased intensity). In contrast, two waves that are "out of phase" combine in a destructive interference (amplitudes of the waves add together to cancel each other, resulting in no sound).

For ultrasound waves travelling in a medium, there are two key values, both dependent on the type of medium, which must be taken into consideration:

1. The *speed of sound* (*c*) → it is the velocity at which sound waves travel in a medium like air. Also termed as wave propagation velocity or sound velocity, it depends on the type of medium through which it is moving, and varies with the physical properties of the medium, particularly with density and elastic properties [6]. The acoustic velocity of a longitudinal wave in a material is directly proportional to the elastic modulus and inversely proportional to density of the material [19]. A high compressibility of the medium implies a slow ultrasound velocity. Moreover, the temperature of the medium also influences the speed of sound [20]. The way the speed of sound is related to the frequency and wavelength of the waves can be expressed by the following Equation 2.1 [6]:

$$c = \lambda f \qquad\qquad\qquad\qquad (2.1)$$

where, *c* is the speed of sound in air (m/s), λ is the wavelength (m) and *f* is the frequency (Hz) of the wave. Equation 2.1 describes the propagation of a monochromatic wave in space and time through the characteristic variables λ and *f* used in basic physics [6].

2. The *specific acoustic impedance* (Z) → it denotes the characteristic resistance of the medium and it is the real part of the complex characteristic impedance [1]. The product of the medium density (ρ) multiplied by the velocity of ultrasound in the medium (c) defines the specific acoustic impedance (Z) of that medium.

$$Z = \rho c \qquad (2.2)$$

It may be expressed in units of *rayls*, where 1 rayl = 1 Pa·s·m^{-1} = 1kg·m^{-2}·sec^{-1}. A lower specific acoustic impedance of the medium (Z) will ensure a higher intensity of the sound wave, according to the relationship existing between the intensity of a sound wave (I) with the maximum sound pressure (P_m) in the medium shown in Equation 2.3 [5]:

$$I = \frac{P_m^2}{2\rho c} = \frac{p_m^2}{2Z} \qquad (2.3)$$

An ultrasound beam (i.e. summation of ultrasound waves) that penetrates a medium loses part of the beam energy [5]. The rate at which the beam energy decreases in penetrating a medium is related to the attenuation properties of the medium. The mechanisms governing this reduction in energy (i.e. decrease in ultrasound intensity) are discussed in the following section.

2.3 Mechanisms for Absorption and Dissipation of Sound Energy

The term *attenuation* denotes any mechanism causing a reduction of the energy transported by an ultrasonic beam. As the traveling distance (z) increases, ultrasound attenuation is characterized by an exponential decrease of the wave's pressure amplitude (p) as shown in Equation 2.4 [6].

$$p = p_0 e^{-\alpha z} \qquad (2.4)$$

in which, p_0 is the pressure at the distance $z = 0$ and the quantity α is the pressure frequency-dependent attenuation coefficient given by the sum of the individual coefficients for scatter and absorption [5]. The *attenuation coefficient* (α) (in units of dB/cm) describes the attenuation of ultrasound in a material. Little attenuation in a medium makes it a very good transmitter of ultrasound energy (e.g. water) [5].

The attenuation of ultrasound energy increases approximately linearly with frequency [5]. A higher frequency ultrasound wave is less penetrating and attenuated more readily than a lower frequency ultrasound wave. The exponential decrease of the acoustic intensity (*I*) with the increasing traveling distance (z) is given by Equation 2.5 [6]:

$$I = I_0 e^{-2\alpha z} \qquad (2.5)$$

where, I_0 is the intensity at $z = 0$. A factor of *2* in the exponential term of Equation 2.5 is the result of transforming pressure into intensity, since the intensity is proportional to the square of pressure (see Equation 2.3).

Diverse mechanisms contribute to the total wave intensity attenuation. The processes of relaxation, such as removal of energy from the ultrasound beam and eventual dissipation of this energy mainly as heat are the primary mechanisms of energy dissipation for an ultrasound beam [5]. Scattering, viscous friction and mode conversion (i.e. the transformation of longitudinal waves into shear waves and subsequent absorption of these shear waves) contribute to the overall attenuation, with further important factors such as absorption, diffraction, reflection and refraction [6]. Specifically, absorption and scattering are the two main mechanisms of ultrasound attenuation [6]. Ultrasound energy is "absorbed" by the medium when converted into other forms of energy.

-*Absorption* (expressed in units of decibel/cm) is a material property which measures the energy removed from the sound wave by conversion to heat as the wave propagates through a given thickness of material [21]. Absorption is in contrast to attenuation, which includes energy loss due to scattering and reflection as well as absorption and depends on experimental configuration and sample size [22].

-*Reflection* (as well as refraction) losses at interfaces depend on the impedance mismatch occurring between the two media at the interface [6]. When two media have different characteristic acoustic impedances, phenomena such as reflection and refraction occur at the boundary between the two media [5]. Ultrasound is "reflected" when an orderly deflection of all or part of the beam occurs. When a pressure wave travels in a medium and encounters a second medium, if the surface of the latter is normal to the direction of propagation of the wave, a portion of the wave is reflected at the interface while the rest is transmitted into the new medium [1]. The transmitted energy will then be partly absorbed and partly transmitted through the rest of the material. The ratio between the intensities of the reflected wave and the incident wave can be expressed by Equation 2.6 [1].

$$\frac{I_r}{I_i} = \left(\frac{\rho_1 c_1 - \rho_2 c_2}{\rho_1 c_1 + \rho_2 c_2}\right)^2 \qquad (2.6)$$

where, I_r is the intensity of the reflected wave (W/m^2), I_i is intensity of the incident wave (W/m^2), ρ is density of the medium (kg/m^3) and c is the speed of sound in the medium (m/s). The indexes 1 and 2 in the equation refer respectively to media 1 and 2 through which the sound wave travels. Equation 2.6 can be rewritten to define the reflection coefficient α_R [5] that expresses the ratio of the reflected to the incident acoustic intensity.

$$\alpha_R = \left(\frac{Z_2 - Z_1}{Z_2 + Z_1}\right)^2 \qquad (2.7)$$

For an ultrasound wave that strikes perpendicularly to an interface, the coefficient α_R (dependant on the acoustic impedances of the two media Z_1 and Z_2) represents the fraction of the incident energy that is reflected from the interface. A larger difference in the acoustic impedances of the two media at opposite sides of an interface corresponds, for an incident ultrasound wave, to more reflected

energy [5]. Therefore, when there is a large impedance mismatch at an interface, only a small amount of energy is transmitted across the interface. Conversely, a transmission coefficient α_T describes the fraction of the incident energy that is transmitted across the interface. It is defined by Equation 2.8 as the ratio of the transmitted to the incident acoustic amplitude [5].

$$\alpha_T = \frac{4\,Z_1 Z_2}{(Z_1 + Z_2)^2} \tag{2.8}$$

The terms Z_1 and Z_2 of Equation 2.8 again denote the characteristic acoustic impedances of the first and second medium for longitudinal waves. Clearly, the sum of the two coefficients expressed in equations 2.7 and 2.8 equals unity ($\alpha_T + \alpha_R = 1$), corresponding in the lossless case to the conservation of energy equation. The efficiency of sound transmission into a solid material from air is unlikely to be high, since the densities of solids are much higher than that of gases, unless the speed of sound in the solid can be decreased dramatically.

-*Refraction* can occur when an ultrasound beam changes in direction and is bent after impinging obliquely on an interface between two media [5]. Two conditions are required for refraction to take place: the sound beam must strike the interface at an angle different from 90° and the speeds of sound must be different on opposite sides of the interface. In particular, the condition for the beam entering a second medium at the interface at a more oblique (less steep) angle is that the velocity of ultrasound is higher in such a medium. In certain cases, according to the angle of incidence, an ultrasound beam may be refracted so that no ultrasound energy enters the medium. The angle of incidence at which refraction causes no ultrasound to enter a medium is termed the *critical angle* (θ_c) [6]. The existence of a certain value of θ_c, with an angle of refraction of 90 degrees, determines if the longitudinal wave is transmitted into a solid medium or not. For an incidence angle equal to θ_c, refraction causes a transmission of the sound along the surface of the material, whereas for incident angles greater than θ_c, sound transmission across the interface is prevented by refraction [6]. However, since the propagation of sound waves in solids is complicated, several critical angles may exist [23, 24].

-*Scattering* phenomena can occur in the presence of in-homogeneities like particles in the medium.

Scatter happens when part of an ultrasound beam changes direction in a disorderly fashion [5]. Particles of different nature present different physical properties from those of the surrounding medium (e.g. density or elasticity). As a consequence, interactions between a primary ultrasonic wave and the boundaries of these particles takes place and a secondary wave, denoted as a scattered wave, is emitted [6]. The way a sound beam behaves when encountering an obstacle is related to the size of the obstacle compared with the wavelength of the sound. A scattered wave is generated only when the dimensions of the heterogeneities are lower than (or at least comparable to) the wavelength of sound (λ). The obstacle must be of a size that is comparable or smaller than the wavelength of the ultrasound for the obstacle to scatter energy in various directions. An obstacle's size larger than λ

(relatively smooth obstacle) denotes the integrity of the beam in the change of direction. The sound beam may be partly reflected and the remainder transmitted as a beam of lower intensity through the obstacle [5]. The energy remaining in a sound beam that encounters an obstacle, such as an interface between structures in the medium, decreases approximately exponentially with the depth of penetration of the beam into the medium [5]. Increasing the surface area at the interface between two media can promote energy transfer from one medium to the other [25].

2.4 Acoustic Absorptive Materials

Sound absorptive materials are materials that reduce the acoustic energy of a sound wave by the phenomenon of absorption as the wave passes through it [26]. Acoustic absorption occurs when acoustic energy is transmitted indirectly through the air, interacting with a solid structure [1]. The way the energy interacts with the air critically depends on the morphology of the material. An enhancement of the transfer of energy from the air into the structure and the dissipation of that energy in the structure can enhance the performance of the solid matrix material as an acoustic absorber [1].

In order to absorb sound efficiently, a high number of internal reflections (scattering) has to occur in the material performing as an acoustic absorber. The internal reflections can transfer acoustic energy to a solid structure through frictional losses [1]. The energy in a sound wave is reduced by an absorber by converting the mechanical motion of the air particles into low-grade heat [26]. Heat and acoustic energy are thus closely related [25]. At the molecular level, heat and acoustic energy differ only in the vector direction of molecular displacements. A random motion of the molecules is typical of heat energy, whereas molecular displacements of acoustic and vibrational energy occur at the same time and in the same direction [25]. Acoustic pressure waves must penetrate deeply enough into the material for achieving a large number of interactions with the structure and absorb a substantial fraction of the energy, otherwise it will be immediately reflected back into the surrounding air [1].

Materials with a high sound absorption coefficient are usually porous [27]. Therefore, most sound absorptive materials are highly porous in structure [28]. Porous materials are materials well known for their promising applications in many emerging areas of science and technology (e.g. automotive and aeronautics) [12]. They present a low relative density, low thermal conductivity and good thermal barrier effect, besides a large specific surface area, high specific strength, excellent sound insulation and good energy absorption properties [29]. In particular, porous sound-absorbing materials have found wide application, including with natural fibres, in new composites, recycled materials, porous metals, and smart materials [30]. A porous absorbing material is a solid that contains cavities, channels or interstices in which the sound waves can enter through. Its surface allows sound waves to enter the material through a multitude of small holes or openings [27]. Sound

propagation then takes place in a network of interconnected pores throughout the material. Sound waves that pass through a porous/fibrous material are trapped inside the material and forced to change direction several times. Part of the sound energy is absorbed by conversion to heat in each change in direction. Before passing completely through the absorbing material, sound waves have to travel long distances, reaching reflective surfaces at which, they are reflected back to move towards a new way to exit the material [31, 32]. Viscous and thermal interactions cause the acoustic energy to be dissipated and converted into heat energy [7]. In solids, in addition to the frictional and viscous losses between the solid ligaments and the air in the pores that convert the acoustic energy into heat, dissipation of acoustic energy occurs also from the impact of an acoustic pressure wave on a solid structure [1]. When a porous material is exposed to incident sound waves, the air molecules at the surface of the material and within the pores of the material are forced to vibrate with frequency, losing some of their original energy in the process [20]. Part of the energy of the air molecules is thus converted into heat because of the thermal and viscous losses at the walls of the interior pores and tunnels within the material. Friction between the air molecules and the surfaces of the pores reduces the amplitude of sound waves entering the porous material [28].

The high compressibility of porous materials, due to the presence of a large proportion of gas, results in low speed of sound. Consequently, porous materials are characterized by lower speeds of sound than non-porous materials [8]. The acoustic performance of a sound absorbing material is estimated by the sound absorption coefficient, which varies in dependence on the incident sound frequency [32]. For most common materials, sound absorption coefficients are low at low frequencies. On a microscopic scale, sound propagation in porous materials is generally difficult to study due to the complicated geometries of the frames. According to their frame state, porous materials can be classified as elastic (e.g. polymer foams), rigid (e.g. fibre layers) or limp (e.g. metallic foams) [12]. The fact that sound also excites and moves the frame of certain materials can complicate the description of sound propagation in porous material even further [33]. In poroelastic media for example (i.e. a porous material with elastic structure), waves can propagate in both solid and fluid phases since the solid matrix material, which is both porous and elastic, also contributes to the energy transfer [12]. Compression and shear waves are the two categories of waves that propagate at a time across the solid skeleton and in the saturating fluid inside the pores of poroelastic media. Longitudinal wave types propagate in the fluid phase, while both longitudinal and transversal [a]type propagate in the solid phase [12].

---

[a] A *transverse wave* occurs when its amplitude varies in the direction normal to the direction of the propagation, so that the propagation of the wave is perpendicular to disturbance of the medium [4]

2.4.1 Properties of Acoustic Absorbers

-**Materials** → Porous materials tend to be light in weight and most effective as sound absorption at short wavelengths (e.g. high frequencies). However, their structural strength is limited, unless they form part of a layered or constrained composite with a denser, less porous material [28]. Very high sound absorption coefficients can be achieved by using a number of sound absorbing layers of different materials [34]. Recent advances in material science, chemistry and nanotechnologies are producing significant improvements in design, production and performance of acoustic materials [30]. Their absorption properties depend upon composition, frequency, thickness, surface finish and method of mounting. Commonly, most absorbers are *homogenous* (uniform properties in space) and *isotropic* (properties independent of direction) [1]. Inhomogeneity sometimes can arise from a change in composition or the inclusion of regions of a second material, generating very often a change in the properties to an anisotropic behaviour. Finally, the pore size is of main importance for a material to be considered a good acoustic absorber. As the pore size decreases, less energy is transferred into the solid structure and more is reflected from the surface, making the material less useful as an acoustic absorber. In order to maintain a good performance of an absorbing material, any increase in density must be compensated by a decrease in the speed of sound or an increase in porosity [1]. The sound absorption coefficient of a porous material can be defined by a number of critical features, namely porosity, tortuosity and flow resistivity, which are all linked to the inner microstructure of the porous network [35]. For a sample of porous material, *porosity* is given by the ratio of the volume of air in the sample void space to the total sample volume and represents the percentage of interconnected void space with respect to the bulk volume. The *airflow resistivity*, one of the most important porous material properties governed by the geometry and interconnection of the open cells, is caused by the forces of friction which are opposed to the flow of air passing through open pores in the material [27]. Finally the *tortuosity*, or shape factor, is a measure of the shape of the air void passages and its effect on the material sound absorption properties, as it describes the complexity of the path followed by the acoustical wave inside the skeleton network [27]. The tortuosity of a porous material is essentially determined by the way the open pores are oriented and interconnected. An increase in tortuosity (i.e. more complex path for the acoustic wave) allows to for better sound absorption in the porous material. Additionally, thermal and viscous losses also affect material sound absorption characteristics with respect to the average macroscopic dimensions of the pores. In particular, thermal losses are significant in pores of large size, whereas, by contrast, the high air particle velocity in the smaller pores reflects the importance of airflow and thus viscous losses.

-**Porosity** → In order to be efficient, an acoustic absorber must have an acceptable range of porosity that allows sound waves to penetrate far enough into the structure [1]. The porosity must neither be

too fine nor too coarse. If the porosity is too fine, the majority of the energy will reflect back into the environment never entering deeply enough to allow multiple interactions with the structure. In contrast, if the porosity is too coarse, the pressure wave passes through but with minimal interaction with the structure [1]. Although all materials absorb some incident sound, a wide range of sound-absorbing materials exist to absorb most of the sound energy striking them and reflect very little. The high values of absorption makes such materials very useful for the control of noise in many applications (e.g. aircraft, spacecraft and ships) because of their low weight and effectiveness [30]. Porosity is expressed as the ratio between the pore volume V_{pore} (m³) within the material (voids volume) and the total volume of the material V_{tot} (m³) and is defined by [1]:

$$\Phi = \frac{V_{pore}}{V_{tot}} = 1 - \frac{\rho_a}{\rho_m} \qquad (2.9)$$

Analogously, porosity can be defined in terms of the density (kg·m⁻³) of the porous material (ρ_a) and the solid portion of the material (ρ_m).

-**Pore Structure** → An efficient absorption of sound from air depends on pore structure [36]. According to their availability to an external fluid (e.g. air), porous materials can be classified as having closed or open pores [30]. *Closed pores* are totally isolated from their neighbours and affect some macroscopic properties of the material (e.g. bulk density, mechanical strength and thermal conductivity). *Open pores* are substantially more efficient than closed pores in absorbing sound energy, by presenting a continuous channel of 'communication' with the external surface of the body. The open pore structure can thus ensure interconnected paths for the air that reaches the surface [36].

An acoustic pressure wave that encounters a closed pore will reflect from the outer surface, rather than penetrating into the foam, so the volume of closed pores does not contribute to the total pore volume in determining the acoustic properties of foams [1]. A further distinction can be made between *blind pores*, open only at one end, and *through pores*, open at two ends [30]. Additionally, porous absorbing materials can be further classified as *cellular*, *fibrous,* or *granular* based on their microscopic configurations [37]. In this case, interconnecting voids separate the solid structure (granules, fibres or cells) and contain the air whose viscosity produces the absorption of sound.

-**Flow Regime** → The flow regime in a porous solid gives an indication of how easily pressure waves can penetrate the material, being directly related to the pore size of the material [1]. Pressure waves cannot efficiently penetrate the material if the mean free path of air and the mean distance between pore walls are on the same order. The dimensionless Knudsen number (K_n) is used as a measure of the flow regime of air through a pore. It is defined by the ratio [1]:

$$K_n = \frac{l_{mfp}}{l_{char}} \qquad (2.10)$$

where, l_{mfp} (m) is the mean free path of air molecules and l_{char} (m) is the characteristic length. The characteristic length often refers to the mean distance between pore walls. In the specific case of spherical pores, the characteristic length equals the pore diameter, while the mean free path for spherical solid particles is defined as [1]:

$$l_{mfp_{porous}} = \frac{1}{\sqrt{2}\,n_g \pi d_g^2 + \frac{S_s \rho_s}{\Phi}} \tag{2.11}$$

and is dependent on the number density of gas molecules n_g (molecules/m³), the diameter of gas molecule d_g (m), the specific area of solid S_s (defined as the ratio surface area/mass, with diensions of m²/g), the solid density ρ_s (kg/m³) and porosity Φ (dimensionless).

In a porous solid, three types of flow regime can exist, viscous flow, molecular flow or a combination of both, in which viscous and molecular flow are both important [1].

➢ *Viscous flow* dominates when $K_n \ll 1$. As l_{mfp} is much smaller than l_{char}, gas molecules move in a free space under this flow regime. Viscous flow has to dominate for a material being useful as an acoustic absorber [1]. When the dominant flow regime is viscous, pressure waves can penetrate significantly into the material to a degree that allows enough internal reflections.

➢ *Molecular flow* in contrast dominates for values of $K_n \gg 1$. When molecular flow dominates, pressure waves are not able to penetrate the material deeply enough. As a consequence, most of the acoustic energy is reflected off the surface.

➢ Knudsen numbers on the order of one ($K_n \approx 1$) indicate that the mean free path of air is similar to the average pore diameter in the material. Collisions between gas molecules and the solid portion (frame) of porous material inevitably occur for values of the mean free path of gas molecules of the same order of the mean distance between pore walls. Consequently, it is unlikely in such a case that acoustic waves can penetrate far into the material and dissipate acoustic energy efficiently.

-**Frequency Sound Dependent Behaviour** ➔ Some materials exhibit a frequency sound dependent behaviour [1]. The characteristics of frequency dependence of a material are generally obtained from an experimental measurement of its acoustic impedance, which varies with frequency and with the angle of incidence of the sound wave upon the surface [35]. From exposing a material to sound at various frequencies, it is possible to measure the acoustic impedance, measuring the reflection and attenuation of that sound [1]. Porous materials that are fluid-saturated, in conditions of homogeneity and isotropy, may be completely described by the characteristic impedance (Z_c), wavenumber (k), and other quantities derived from these two [1]. A number of techniques have been developed for determining the characteristic impedance and wave number of a plane wave in the absorbing material as functions of non-acoustic properties, in order to interpret the acoustic behaviour of

porous absorbing materials [27]. Material properties such as density, tortuosity, and porosity are key features in impacting the absorption performance of a material. Additionally, the total thickness, the surface and the presence of layers also contribute to the absorption of sound. In particular, any increase in density, thickness, porosity, and air flow at higher frequencies result in increased levels of absorption performance, as shown from the trend of the curves in Figure 2.2 [35].
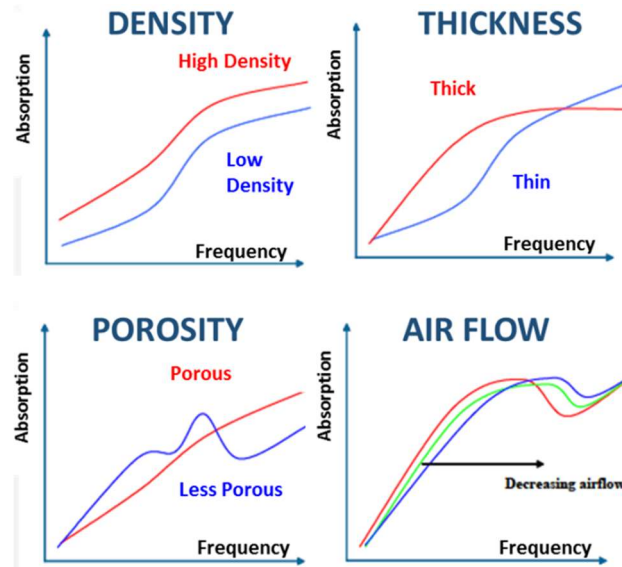
Figure 2.2. Trends in the key features driving the absorption coefficient dependence as a function of frequency. Figure adapted from Ref [35].

Figure 2.2 schematically describes the impact of these key features on sound absorption performance. For simplicity, the effect of each feature is plotted separately to better understand each contribution but in fact the effects are linked [35].

i) *Effect of density on the sound absorption coefficient* →The density of the material is an important factor in governing the sound absorption of any material. An increase in material density results in an increase in sound absorption at medium and high frequencies [32]. Furthermore, the cost of an acoustic material is related directly to its density. High cross-link density leads to low absorption [21].

ii) *Effect of material thickness on the sound absorption coefficient* → The thickness of the porous absorber is important in sound absorption [36]. Numerous studies on the absorption of sound in porous materials reported a dependence of the sound absorption coefficient with material thickness at low frequencies [32]. In order to achieve good sound absorption in the low frequency region, materials with greater thickness are required [38]. A porous material is effective in terms of sound absorption when its thickness is approximately one-tenth of the wavelength of the incident sound [32]. Accordingly, absorbers need to be a minimum of a tenth of a wavelength thick to significantly absorb incident sound and about a quarter of a wavelength to absorb all sound [36]. Ibrahim et al. [39] reported that material thickness had a less effect on sound absorption at high frequencies

(>2000Hz) but a more prominent effect at lower frequencies. The trend shown in Figure 2.2 confirms this observation.

iii) Effect of porosity on the sound absorption coefficient → Number, size and pore type are crucial factors governing the mechanism of sound absorption in porous materials. As previously discussed, enough open pores must be present at the surface of the material for sound entering the porous material. Materials with open pores have superior sound absorption coefficients to materials with closed pores. Moreover, higher density materials with open pores have better sound absorbing properties than lower density materials with open pores [32]. Conversely, in vibration damping applications materials are generally optimised for attenuating at lower frequencies. As a result, these materials have higher densities and thicknesses than absorbers, with a stronger dependency on the internal damping of energy penetrating the material rather than the capture of acoustic energy through a porous architecture [28].

iv) Effect of air flow resistivity on the sound absorption coefficient → Airflow resistivity is a major parameter dominating the acoustic behaviour of porous materials for sound absorption [40]. It was found to be the most influential parameter when considering acoustic absorption and surface impedance of porous materials such as, fibrous and plastic foams or granular materials with rigid frames [41, 42]. Specifically, the use of flow resistivity and porosity empirically allows for the calculation of quantities that specify the acoustic properties of a material, such as the impedance and wavenumber of that material [36]. Experimental determination of flow resistivity and characteristic impedance allows for the description of the performance of an acoustic absorbing material for various applications [1]. In order to define the flow resistivity of a material, it is important to firstly define *flow resistance* (or airflow resistance). This property is a measure of the resistance that airflow meets within the structure, or in other words, how easily air can enter a porous structure, since the sound`s amplitude is decreased by friction as the waves enter the material and move through tortuous passages [26]. This friction quantity converts acoustic energy to heat and thus describes the resistance of the material to airflow. The flow resistance can be sufficient for characterizing the acoustic performance (e.g. sound absorbing and transmitting properties) of a material for many applications with open cell foam products [43]. The ratio between the specific flow resistance and thickness of the material represents the flow resistivity.

As discussed, hitherto porous materials are used in many vibroacoustic applications and behave according to the material intrinsic characteristics [41]. However, not all highly porous materials are suitable as acoustic absorbers [1]. Nonetheless, a material that it is not a good acoustic absorber can still perform well for vibration damping since the mechanism of acoustic absorption differs from the mechanism of vibration damping [1].

2.5 Acoustic Damping Materials

Damping of vibrations in machinery, automobiles and aircraft constitutes an important task for both the reduction of noise and the prevention of fatigue failure of materials [21]. Numerous methods are currently in use for the control of acoustic noise and vibration [28], including vibration damping and the common alternatives to damping, isolation and/or alteration of the mechanical input impedance [44]. All these methods may be used singly or in combination. The source of vibration can be isolated from the body of the noise-radiating structure by means of flexible couplings or mounts or, alternately, another form of vibration control is through the modification of the dynamic characteristics of materials by changes in stiffness or mass [44].

The dissipation of vibrational energy in a structure by means of vibration damping that converts mechanical energy into heat is one of the most common forms of vibration control and is usually achieved by use of some form of damping material [44]. Vibrations are waves similar to sound pressure waves that are transmitted through solid objects as a form of energy. While acoustic absorption occurs when acoustic energy is transmitted indirectly through the air, interacting with a solid structure, vibration damping is related to the direct transmission of acoustic energy through the contact between two solids [1].

Internal or material damping refers to inherent energy dissipation occurring during cyclic motion or deformation of a material [45]. Internal damping is an aggregate of energy dissipation produced by various microscopic sources and mechanisms taking place in a material. Mechanisms that are associated with the internal structure of a material across different length scales are responsible for irreversibly converting kinetic energy into thermal energy [45]. Thermodynamic damping is the paramount internal damping mechanism that develops without the presence of in-homogeneities in the material. Otherwise, all the mechanisms associated with dislocations, grain boundaries, or atomic motion within the material, as well as those dissipations resulting from thermal, electronic and magnetic fields in the material are included in internal damping [45].

In porous materials with fluid-filled pores, damping is the result of a combined damping from the solid porous structure, the fluid, and the interface, due to the relative motion of the two media [45]. Two surfaces in contact generate contact stresses that is the cause of friction or contact damping. Contact stresses lead, in turn, to temperature gradients (on and near the two surfaces) which can be transported from the contact areas [45]. Therefore, the kinetic energy associated with the relative motion of the surfaces is converted into thermal energy.

Normally, internal damping in engineering is characterised by a single frequency and temperature dependent value, since its effectiveness varies over different temperature and frequency ranges. Enhancements of internal damping properties of materials are realised by the use of viscoelastic

materials and changes in the molecular structure of these. Composites and foam-type materials are a typical example of damping materials [45].

2.5.1 Parameters affecting Damping in Polymers

Application of polymers to the surface of a vibrating substrate can increase damping. Commercially, many polymers are used for damping. The basis for damping with polymers is the absorption of vibrational energy in the form of heat in presence of mechanical vibrations [46]. In the polymer structure, sound absorption is related to various molecular mechanisms like the glass transition and it is a measure of the dissipative energy loss as the sound wave travels through the polymer, due to the conversion to heat. Transitions correspond to peaks in the absorption (i.e. high values of the attenuation coefficient α defined in paragraph 2.3). Accordingly, the highest acoustic damping is obtained in transition zones [21].

Temperature and frequency range requirements are distinctive in selecting polymers for damping [46]. For a given polymer, acoustic damping depends on the temperature and frequency of the measurements and is dominated by the glass transition occurring in the amorphous phase of the polymer [47]. The speed of sound and absorption are pressure dependent, due to the pressure dependence of free volume in the polymer [21].

Temperature Dependence of Polymer Acoustic Properties → Acoustic properties of polymers are strongly dependent on temperature [21]. In general, major changes in numerous physical properties of polymers (e.g. acoustic properties) occur going through the glass transition process [47]. A distinction must be made between polymers that are non-crystalline (amorphous) and exhibit only a T_g and semi-crystalline polymers that in addition present a melting transition. There may be other transitions (e.g. β-transition) at temperatures that are above or below the glass transition region [46]. However, secondary transitions are not usually considered important in damping applications [47]. The largest change in acoustic properties of polymers occurs in the transition from a hard glassy solid state to the rubbery plateau, namely across the *glass transition temperature*, T_g [22]. The glass transition temperature, a fixed number, is different from the glass transition. The *glass transition* denotes a process occurring over a temperature range, dependent on the frequency of the measurement, only in the amorphous regions of the polymer [47]. At the glass transition of an amorphous polymer, a number of repeat units (from 10 to 50) in the polymer chain are involved in conformational rearrangements of the chain backbone on a bulk scale. The repeat units become free to move, resulting in cooperative thermal motions of individual chain segments. These large scale motions cannot occur below the glass transition because the chains are frozen. A theoretical interpretation of the glass transition is provided by the *free volume theory*, according to which, the occupied volume increases linearly with temperature [47]. Since a certain free volume must be available for large scale molecular motions to happen, and thus for the glass transition to occur, a

reduction in free volume will raise the T_g of polymers. The glass transition marks the onset of long-range coordinated molecular motion and it is directly related to damping. Polymers damp significantly near their glass transition temperature [21]; the moduli and speed of sound drop above T_g while absorption increases until reaching a maximum [22]. In the vicinity of the glass transition, polymer damping shows a peak which is of extreme importance in damping applications and, correspondingly, the modulus drops by as much as three orders of magnitude [47]. At $T < T_g$, the speed of sound is a relatively high value that rapidly decreases to a relatively low value for $T > T_g$ [21]. At temperatures above the glass transition, melting lowers the modulus, therefore polymers are not generally used in the molten state for damping applications, even though values of loss factor can be very high in this region [47]. Polymers become highly attenuating materials above T_g, at all frequencies [22]. The glass transition temperature for a given polymer depends on a number of variables, such as flexibility of the backbone, pendant groups, steric effects, polarity, crystallinity[(b)], plasticizers, crosslink density, and co-polymer composition [47]. The presence of crosslinks and pendant groups contribute to the glass transition process of polymers by acting as an internal plasticizer to decrease the free volume lowering T_g. Conversely, aromatic pendant groups raise T_g [47]. Plasticization, the addition of liquids to polymers and copolymerization are common strategies to tailor the T_g of polymers [46].

Relationship between Viscoelastic Properties and Damping → There is a frequency dependence of the acoustic properties of polymers due to the dependence of viscoelastic properties on the relationship between frequency and temperature (or analogously time and temperature) [21]. In particular, the dependencies of polymer acoustic properties with frequency and temperature are inversely related. A decrease in temperature corresponds to an increases in frequency and both velocity and attenuation are sensitive to changes in temperature since through the T_g, the velocity decreases while the attenuation shows a peak [22]. When the frequency of sound waves equals the natural resonant frequency of the polymer chain, an absorption peak occurs and the energy is converted into molecular motion (heat). Higher frequencies make molecules move faster so that at higher frequencies, T_g is higher [46].

For dynamic data, the T_g is taken as the temperature of the loss modulus peak or the temperature of the loss tangent peak [46]. Sperling et al. [21] discovered that a quantitative measure of damping behaviour is given by the area under the linear loss modulus versus temperature curve, termed as loss area [21]. The two viscoelastic quantities loss tangent (tan δ) and loss modulus [(c)] (E'') are

---

[(b)] To some extent, crystallinity can result in an increase in T_g by limiting the mobility of polymer chains of the amorphous phase [47]. However, as the degree of crystallinity increases, the T_g tends to be masked and difficult to determine (e.g. polyethylene).

[(c)] The loss modulus is a measure for the conversion of mechanical energy into molecular motion during the transition [21].

usually the prime parameters affecting damping. If these two quantities are small, for given temperature and frequency, damping is accordingly small and vice versa. Increasing the crystalline content can contribute to lowering the maximum value of the loss factor [21].

Both longitudinal and shear wave absorption often increase linearly with frequency [d], with shear absorption always much higher than longitudinal absorption, at any frequency [21]. Since absorption is directly proportional to frequency, the absorption per wavelength ($\alpha\lambda$) results in a constant that is directly proportional to the loss factor tanδ [47]. By using the approximation of tanδ, Ferry concluded that the acoustic absorption α, is related to the loss factor, $tan\delta$, through the following relationship [21]:

$$\alpha \cdot \lambda = 8.686 \cdot \pi \cdot tan\delta \qquad (2.12)$$

Therefore, in acoustic terms, absorption can be expressed as absorption per wavelength, $\alpha\lambda$ (in dB or Np (neper) with 1Np= 8.686 dB), as defined by Equation 2.12, which in terms of modulus absorption can be expressed as tanδ [47]. Molecular structures and mobility thus contribute to both absorption of ultrasonic energy and ductility. In particular, low attenuations are usually offered by hard, glassy and brittle thermoplastics, such as the amorphous polymers PS and PMMA (of the order of 6-10 dB/cm at 10 MHz) [22]. Many polyolefins and PC, as more ductile polymers, generally present high absorption coefficients in the range of 20-40 dB/cm.

2.5.2 Polymer Composites for enhancing Acoustic Attenuation and Vibration Damping

Polymer composites have received increased attention in the development of structural materials with damping properties due to their low density, excellent stiffness and damping characteristics [11]. Compared to pure polymers (i.e. macromolecules, or long-chain molecules, with high molecular weights [46]), composite materials are able to provide improved physical and mechanical properties (e.g. stiffness and strength) [48]. Consequently, polymer composites are widely used in many industries, including automotive, aerospace, construction and electronic. The creation of composite materials, or hybrid materials, with distinct regions of different materials dispersed throughout a matrix material, is useful in tailoring the material as an acoustic absorber and/or acoustic damper for a specific task [1]. The careful selection of matrix material and filler particles can create a composite material with an optimal balance of sound and vibration attenuation, with weight, strength and temperature characteristics at low cost [28]. When particles with mismatched characteristic acoustic impedances are embedded within the matrix that can support shearing loads, the propagating acoustic energy that encounters the particles is partially reflected in random

---

[d] This behaviour is shown when absorption is measured not too close to the damping peak in tanδ, otherwise the absorption approaches a frequency squared behaviour [21].

directions and diffused [28]. Since vectors and modes of the acoustic energy propagation are randomized, the probability of localized energy absorption and damping is increased. As reported in literature by Cushman et al. [25, 28], the noise generated by sound, vibration, and shock can be reduced by loading polymers with mixtures of high and low characteristic acoustic impedance particle species. This principle of including multiple particle types within a matrix provided a means of enhancing the acoustic attenuation and vibration damping of the material. In many cases fillers increase damping, probably by the introduction of new damping mechanisms that are not present in the pure polymer [47].

Optimization of Acoustic Damping in Polymer Composites → Optimization of damping in polymer composites can be attained by active and/or passive means at both the macro- and micro-mechanical levels [11]. The inherent capacity of a damping material for dissipating vibrational energy can contribute to the passive control system. Typically, passive damping requires high loss viscoelastic materials and thermal control. The vibrational energy can be dissipated by shearing motion (deformation) of the viscoelastic material. It is unusual for a material to possess both high damping properties and high rigidity [11]. Increases in damping and impact resistance usually cause corresponding reductions in stiffness and strength of the material [11]. Nevertheless, combinations of improved damping of composites with high stiffness and strength can be achieved by controlling geometrical and mechanical properties on several levels. Hybrid composites are an interesting compromise to obtain improved damping without a great loss of stiffness [11]. Special coatings can also provide alternatives to enhance composite damping, still guaranteeing acceptable reductions in other important properties like strength and stiffness [11, 49-54]. Nonetheless, increasing the shear deformation has commonly showed to improve significantly the internal damping properties of viscoelastic polymers such as composites [55, 56]. The damping increases through a shear mechanism because of the stress transfer at the filler/matrix interface [11]. In addition to the viscoelastic behaviour of both filler and matrix, the role of the interphase region in governing damping in polymer composites is notable where high shear strain energy is stored. The filler/matrix interphase region is characterized by a complex state of stress, caused by geometric and material discontinuities existing between the filler and the matrix and the mismatch in their properties [11].

From what has been discussed so far, the material microstructure highly influences the propagation of ultrasonic waves within it. A peculiar acoustic material can be achieved by dispersing gas bubbles in a fluid to create a 'foam' [57]. Foams are already observed in nature in bones, natural sponges, corals and natural cork [17]. Polymer foams, previously highlighted in paragraph 2.4 as examples of highly porous elastic materials, are solid materials containing a large number of gas bubbles trapped throughout the volume [1]. Due to the internal structure, the acoustics of a foam is different to the sound propagation through a pure liquid or gas. The energy of an incident sound wave is

partially dissipated in the foamed material as air friction inside polymeric cells and viscous friction between adjacent polymer chains leads to its dissipation as heat [58]. Since polymer foams have been used as sound absorbing materials, the relevant characteristics of polymer and nanocomposite foams discussed below.

2.6 Polymeric Foams

Polymer foams (also known as cellular polymers, polymeric foams, plastic foams, or expanded plastics) can have excellent ability in sound absorption, especially for intermediate and low-frequency noise, as well as relatively low costs and can be conveniently moulded into different shapes [7, 38]. These materials contain gaseous voids (air) surrounded by a denser matrix and consist of a solid porous polymer matrix and a gaseous phase derived from a blowing agent, where the polymer matrix (thermoplastic or thermoset) incorporates bubbles in an opened-cell or closed-cell structure [59]. Properly selected processing conditions make it possible to manufacture cellular products with new, modified physical and technological properties, characterized by reduced weight and density as well as improved damping and insulation properties [60]. Foamed polymers offer distinctive advantages over non-foamed polymers [61], e.g. light-weight, low density, flexibility, low dielectric constant, impact-damping properties and low heat transfer making them useful in a wide variety of applications. Common applications of polymeric foams include tissue engineering, acoustic/ electrical/ thermal insulations, membranes in separation process, scaffolds, construction, transportation, protective equipment, packaging materials and cushioning in furniture [61, 62]. The lightweight nature of their porous structure lends foams to be used also as barriers (e.g. thermal and sound barriers), shock absorbers, absorbents and cushions, acting as excellent substitutes for various functional materials [63, 64].

The properties of polymer foams depend on both the intrinsic properties of the polymer and the foam morphology derived from cell density, cell size and cell size distribution [65]. As a result, the properties of polymeric foams can be tailored to meet a vast array of applications by simply varying the manufacturing conditions and/or the polymer matrix composition [66]. The procedures and conditions of foam synthesis crucially influence the size, distribution, number and shape of the pores of the final porous products obtained, thus deciding their final application [61]. The processing methodology mainly depends on the type of mixing and pressure applied during processing [67]. Unless reactions and processing conditions are carefully monitored and controlled, the resulting foam may have undesirable cell density and/ or cell size distributions.

2.6.1. Synthesis of Polymeric Foams

Processing of polymer foams has received considerable attention [17, 68]. Polymer foams can be produced at low cost using conventional polymer processing equipment. The technology of foaming

by means of extrusion or injection moulding is widely used because gas diffusion in molten polymers is fast and it is facilitated by mixing [69]. Extrusion is one of the most industrially relevant methods for plastics processing because it is a simple technique, low cost, solvent free and environmentally friendly [70, 71]. On the other hand, injection moulding is one of the widely used processing methods for mass production of plastics products [72], very often used in combination with extrusion. The short cycle time, excellent dimensional tolerance and the no-post or at least minimal finishing required are among the advantages that enable injection moulding to account for the 32% by weight of all the polymers processed among all processing methods employed [73]. Foams can be produced in the liquid, melt or solid state, by continuous, semi- and non-continuous processes. Extrusion, injection moulding and compression moulding are common methods adopted to produce liquid/melt foams, while to produce foams in solid state, the gas is forced into a solid polymer followed by depressurization [48].

Non-Continuous Foaming → Batch foaming is the typical non-continuous process, commonly used in foaming research [74]. In a batch foaming process, the polymers are first saturated with the foaming agent, in a pressurized vessel, under predetermined conditions of temperature and pressure [48, 74]. The release of pressure leads to the super-saturation state and cell nucleation and growth, for temperatures higher than the glass transition temperature of the polymer matrix. Cell structure is usually fixed by a *pressure quench technique*, that is a cooling of the material below T_g. The cell is unable to nucleate and grow after the release of pressure when the saturation temperature is lower than T_g. Productivity is limited because of the very long saturation times related to the diffusivity that can last from hours to days [48, 74].

Continuous Foaming → Continuous extrusion foaming is a continuous process and represents the most common technology adopted in the foam industry [74]. The extrusion process includes steps of mixing, extruding and cool moulding [75]. Both single- and twin- screw extruders can be used in foaming of plastics and extrusion foaming is performed via injection of a foaming gas into an extrusion barrel. In order to realise a cellular structure of the polymer completely inside the extruder there are specific criteria to be respected (e.g. pressure, cooling conditions, geometrical dimensions of the die, different types of extruder heads) which enable the gas to expand immediately upon exiting the die foaming the extrudate. The homogeneous polymer/gas mixture passes through a die, where a rapid pressure drop (i.e. primary driving force for cell nucleation [76]) induces phase separation and cell nucleation [74]. The use of a shaping die can control the product shape and foam expansion [74]. Extruder dies with fixed section channels should not be used in cellular plastic extrusion but, conversely, the die should be relatively short providing for large pressure decreases while the cross-sectional areas of extruder head channels should be relatively large to avoid considerable decrease in pressure (e.g. straight mandrel and direct flow extruder heads are among the most common [60]) [77]. The materials are foamed and moulded after being extruded into the

mould [75]. The physical evolution of the polymer-gas system depends highly on the pressure and temperature of the system, in addition to the extrusion time. Both head pressure and die pressures need to be kept as high as possible to minimize expansion inside the die [78]. More pressure results in an increase in pore numbers and a decrease in pore size and foaming density. In terms of extrusion temperature, there is an optimal temperature for the process, above which a low melt strength leads to an easy breakage of bubbles, whereas lower temperatures result in high melt viscosity which makes bubble growth difficult [75]. The process of cellular extrusion of thermoplastic materials has been one of the fastest growing processing methods in recent years [8]. The aim is to obtain cellular structures not only with reduced density but with minimum shrinkage while maintaining similar properties to those of products extruded by means of conventional methods [60].

Semi-continuous Foaming → Foaming using injection moulding can be seen as example of semi-continuous processing [18]. It can produce parts with complex geometry. Currently, injection moulding and foaming, based on the use of CO_2 as foaming agent, is in use to produce lightweight products with high mechanical strength [48]. It is a one-time mould process with high productivity and good product quality [75]. The most common method used for large-scale production of foams is the direct utilization of foaming (or blowing) agents to form the gaseous phase during the foaming process [e] [48].

2.6.1.1. Foaming Agents

A foaming agent can be either a non-reactive gas, a solvent or a supercritical fluid [18]. Classifiable as chemical blowing agents (CBAs) or alternatively physical blowing agents (PBAs) [75], foaming agents, are a source of gas which diffuses into the polymer and creates the cellular structure by cell nucleation and growth of bubbles in the polymer matrix [60, 79]. In order to achieve a porous material of appropriate structure and characteristics, blowing agents must be selected with care, depending on the desired properties of the final products, polymer type, and process conditions. The amount and type of blowing agents added strongly affect the final density of the porous material and determine the choice of foaming method utilised, while preserving stiffness which depends predominantly on the type and properties of the polymer material [60, 77]. The size of a foaming gas particle is also important in foaming technology [69]. Generally, the lower the molecular weight of a blowing agent, the higher the gas volume that can be generated per unit weight of blowing agent [80]. The concentration of the foaming agents governs the foam cell density, and accordingly, the size and number of bubbles.

---

[e] Alternatives to blowing agents, there are also other methods to prepare porous polymeric materials. For example, phase inversion, leaching and thermal decomposition. However, most of these methods are only suitable for the preparation of thin film products [48].

Blowing agents may show exothermic or endothermic decomposition characteristics. In the first case, exothermic decomposition proceeds automatically and progresses even after energy cut-off, generally causing local overheating and generation of irregular cellular structures, so that products extruded with the use of such agents must be intensely cooled for a long time to prevent stress build-up and maintain the cellular structure. Conversely, in the case of blowing agents with endothermic decomposition characteristics, the generation of gas during processing is rapidly stopped when the energy flow is cut off, so that the application of such blowing agents considerably shortens cooling times [81]. In general, bubbles obtained with CBAs are larger than that obtained with PBAs, leading in principle to lower mechanical properties [79].

➤ **Chemical Foaming Agents** ➔ A chemical blowing agent is a reactive species, often in the form of porous solids or liquids, which releases gaseous substances only under certain processing conditions either via chemical reaction or thermal decomposition [79]. CBAs make improvement of properties possible for processes like extrusion and injection moulding, enabling both engineering polymers and commodity plastics to be processed more easily [82]. Their use requires little modification to an existing thermoplastics processing line [80]. The injection moulded plastic parts foamed with CBAs are easy to process and show reduced density and reduction in sink marks [79]. The essence of this process is the introduction of CBAs in the plastic material in the form of concentrated master-batches (e.g. 5-70% concentration) or as powders [60]. The majority of studies reported in literature preferred the use of CBAs in the form of concentrated master-batches in polymers for easier handling and proper dispersion in the host polymer [83]. The gas release can be due to either thermal decomposition (which generates gases such as carbon dioxide (CO_2) or nitrogen (N_2) according to the CBA type) or a chemical reaction (endothermic or exothermic, according to the reaction type that either absorbs energy or releases energy, respectively) [60, 82]. The quantity of gas released to foam the polymer and the decomposition temperature are the main selection criteria for CBAs [75]. The CBA must release the gas at a controllable as well as rapid rate, with a gas yield corresponding to the target density [80]. Consistent process control is an important processing benefit of using CBAs [72]. Solubility limits of the gas in the polymer are highly dependent on the temperature and pressure conditions. Furthermore, a correct decomposition temperature is a requirement. If the decomposition temperature of the CBA is considerably above the polymer process temperature, little or no foaming will occur. The consequences of a decomposition temperature considerably below the temperature of the melting processing of the polymer are a poor surface skin quality and an overblown and ruptured cell structure [80].

CBAs can be inorganic (e.g. sodium bicarbonate, ammonium carbonate, ureaoxalic acid, sodium borohydride) or organic (e.g. azo type, nitroso group, sulfonyl types) types. Commonly, organic CBAs are widely used in industry to form plastic foams, whereas inorganic CBAs are more used to assist foaming rather than as blowing agents because they are characterised by a wide decomposition

temperature range that complicates the control of the foaming process [75]. CBAs are usually used to make high and medium density foam plastics and rubbers, with typical foam density in the range of 400-800 kg/m^3 corresponding to a density reduction of about 20-45% from the density of the un-foamed polymer [80]. Although physical foaming techniques produce lower foam density than chemical ones, with density reductions up to 80%, the use of CBAs do not require any modifications to processing equipment (e.g. extruder) [84, 85]. Therefore, CBAs are preferred where it is necessary to maintain low levels of capital expenditure on equipment and machinery [77]. However, when aiming to produce foam with densities below 400 kg/m^3, the high cost of employing CBAs rather than PBAs discourages their use [80].

➢ **Physical Foaming Agents** ➔ Physical foaming agents are substances that gasify under certain foaming conditions [75]. They generate gases through irreversible physical changes in their conditions to foam the polymer, passing from a dense phase to a gas phase. Finally, volume expansion of the gas leads to the formation of bubbles inside the polymer matrix [17]. Commonly, PBAs are used to produce all types of foamed plastics, both thermoplastics and thermosets, over the full range of density [80]. When the foam density is low, less than 50 kg/m^3, PBAs are almost the only type of foaming agent suitable. Common PBAs include low-boiling-point liquids (e.g. propane, butane, pentane, iso-pentane, dichloromethane, Freon), hollow-sphere solids (e.g. inorganic type such as glass, alumina, magnesium oxide, zirconia, ceramic, silicon dichloride, charcoal, borate, phosphate, or organic type as natural cellulose derivative, natural emulsion, synthetic phenolic resin, urea resin) and inert gases (nitrogen, carbon dioxide, argon, water) [75]. In recent years, the foaming industry has preferred inert gases as blowing agents rather than volatile chemicals (e.g. chlorofluorocarbons (CFC)), volatile hydrocarbons and alcohols to ensure safety and avoid chlorine atoms and emissions of volatile organic compounds, VOCs, that contribute to ozone formation) [48]. Under standard atmospheric pressure, the inert gas is mixed with the molten polymer to form the foamed body directly [48, 75]. PBAs are relatively low in cost but sometimes their use requires special equipment [80]. Nevertheless, physical foaming is generally the preferred method to produce polymeric foams, primarily because the lack of hazardous chemical solvent use can avoid the challenges in the removal of side-products [17]. Inert gases such as carbon dioxide (CO_2) and nitrogen (N_2) are among the most conventionally used blowing agents. When using inert gases, the physical properties of the polymer remain unaffected, unlike in the case of CBAs which react to generate decomposition products and often residues that can affect the material properties negatively (e.g. embrittlement) [86]. N_2 is the most environmentally acceptable blowing agent, since it comes from the atmosphere, it is abundant and cheap [80]. On the other hand, solubility of CO_2 in several polymers is higher than that of N_2 and therefore potentially able to generate more cell nuclei essential to foam a polymer. CO_2 is inexpensive, non-toxic and environmentally benign and is considered as 'greenhouse neutral' when obtained by extraction from air or other natural resources, or as a by-

product of fermentation processes or ammonia manufacture. Molecules of CO_2 are small, and can diffuse fast through a polymer. The high diffusivity of CO_2 in the polymer melt due to its small size ensures a fast mixing process [48], leading to high cell growth rates but, at the same time, to a higher possibility of gas escape to atmosphere (i.e. the cause of foamed structure collapse [69]). From the data of the solubility of carbon dioxide in molten HDPE measured experimentally by Sato and co-workers [87], a solubility value of 407 g-gas/ g-polymer was obtained at 160 °C and 70 bar, whereas a lower value of 350 g-gas/ g-polymer was reported for a temperature of 180 °C at the same pressure of 70 bar. The solubility of $CO_{2,gas}$ is influenced not only by the pressure and temperature of the system, but also by the total amount of crystalline content of the polymer [88].

➢ **Supercritical fluids** → Supercritical fluids (SCFs) have also become very attractive physical blowing agents in polymer foaming processes [17]. Such fluids are added in an overcritical state directly into the polymer melt in the injection unit during plasticization when a high density reduction is the goal [86]. Due to the high pressure and high temperature in the plasticization unit, the mixing of blowing agents in a supercritical state into the polymer enables a high degree of solubility in the polymer melt. A fluid in a supercritical state possesses low viscosity, low surface tension and good diffusion properties, which translate into quick wetting and high solubility in the polymer and therefore, into a high nucleation density yielding a homogeneous foam structure. Foaming is induced by an expansion of the blowing agent caused by a rapid pressure drop and the subsequent transition of the aggregate state into a gaseous state, which increases the volume in the polymer to create the foam structure [86]. Supercritical carbon dioxide, SCF-CO_2, is the most attractive choice because of its low cost, non-toxic and non-flammable properties, and relatively high solubility in many polymers [48]. It is also easily recyclable, stable, and easy to obtain from air and recycle [17, 89, 90]. SCF-CO_2 has tremendous potential as a plasticizer in polymer processing [91] and allows for low-energy and low-cost polymer processing protocols, since it can be removed from the reaction system through simple depressurization at ambient temperatures [17]. In recent years, supercritical CO_2 has been used to foam various polymers, such as poly(methyl methacrylate), poly(styrene), poly(ethylene), and poly(urethane) [17]. The relatively moderate critical temperature (31.1 °C) and pressure (73.8 bar) of CO_2 make carbon dioxide the most favourable choice of blowing agent in many applications [86]. Dissolved CO_2 causes a considerable reduction in the viscosity and surface tension of the polymer melt due to an increase in free volume [91]. Moreover, it alters physical properties of polymers such as density, diffusivity and swollen volume.

2.6.2. Principle of Foaming: Process and Mechanisms of Foam Formation

In foaming processes, bubble nucleation and growth are the two basic steps involved [48]. In the *nucleation process*, a homogeneous polymer-gas mixture generates a new distinct thermodynamic phase (bubble phase) [18]. The following *growth process* leads bubble nuclei to grow into final

bubbles [48]. Both processes are effected by different physical properties (e.g. viscosity, gas solubility, surface tension, and polymer T_g) that are inter-related and often are a function of the temperature and pressure of foaming [18]. A typical polymer foaming process involves four main steps, which can be summarized as follows, see Table 2.1. [79].

Table 2.1. Main steps of a typical polymer foaming process.

Step 1.	**Dissolution of the gas blowing agent in the molten polymer** at elevated pressure, which ensures the formation of a polymer-gas solution (i.e. single-phase supersaturated solution characterised by a molecular level dispersion) once the polymer is saturated. The polymer is impregnated (in foam extrusion and injection moulding processes) or saturated (in batch foaming) with a blowing agent under certain conditions of high pressures and defined temperatures **[18]**.
Step 2.	**Nucleation of a population of gas clusters** in the supersaturated solution upon submitting the polymer-gas solution to a thermodynamic instability that nucleates microcells. Nucleation is the step of generating gas bubbles (i.e. billions of microcells) in the polymer melt through a reversible thermodynamic process. The rate of cell nucleation is a critical factor for a foaming process, as it is related to a change in the thermodynamic state of the system and phase separation [69]. The number of cells nucleated in the polymer depends on the pressure difference in the melt and atmospheric pressure. A rapid pressure drop usually yields a high nucleation rate in the polymer matrix. An increase in temperature in the system is the alternative route to lower the solubility of the solution and achieve nucleation. A change in the processing parameters or equipment configuration can facilitate the generation of high cell density and small cell sizes.
Step 3.	**Growth of nucleated bubbles in the polymer** to their ultimate equilibrium size. The diffusion rate and the rheology of the polymer-gas solution control and limit the rate at which the cells grow. Specifically, in semi-crystalline polymers the cell growth is controlled by the viscoelastic properties of the polymer matrix, as opposed to amorphous polymers where the cell growth is controlled by gas diffusion rate [92]. While the cells continue to expand by diffusion of the dissolved gas from the polymer melt into the bubbles (i.e. nucleated cells), the density of the polymer is reduced. In order to realise the control of the growth rate and size of bubble formation during the foaming processes, the conditions of temperature, pressure and humidity of the selected polymer-gas system must be carefully monitored and controlled [67]. The presence of other bubbles and the time allowed for the cells to grow before solidification are other factors controlling the cell growth process [79].
Step 4.	Finally, the **stabilization of the cell structure** is realised via cooling. The stabilisation depends on the cell growth stresses and melt-strength [18].

2.6.2.1. Classical Nucleation Theory

The classical nucleation theory is the empirical theory still most frequently used to describe the mechanisms of cell nucleation and growth in polymeric foams [18, 93].

During nucleation, stable nuclei are generated from molecules that overcome an energy barrier and gather together to form 'embryos' of a new phase [48]. An ensemble of atoms termed *nucleus* can grow irreversibly into a larger sized nucleus within the body of a metastable parent phase (polymer melt). The difference in free energies between the two systems is the basic driving force for such transformation, since the new phase (bubble/foam cell of the polymer foaming) presents a lower free energy than the parent phase [18]. A nucleus has a minimum size, the *critical radius*, at which the free energy barrier reaches a high-energy maximum. Below this radius, the nucleus collapses into the melt, while above this critical size, a stable nucleus is formed and continues to grow becoming a stable bubble [18]. In particular, when the nucleus size is smaller than the *critical radius size*, an increase in the nucleus size corresponds to an increase in free energy, (i.e. the growth of the nucleus requires energy). In contrast, for nucleus sizes above the critical size, further increase of embryo sizes leads to a reduction in free energy. Therefore, any nucleus with size greater than the critical radius will continue to grow, being energetically favourable and stable [17], as showed in Figure 2.3.
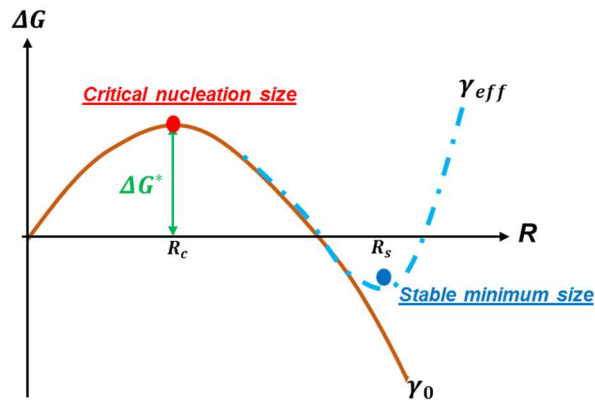
Figure 2.3. Graph of Gibbs free energy (ΔG) versus nuclei size (radius R). A reduction in free energy is shown for growth of the nuclei with sizes above the critical size, R_c.

A fine dispersion of particles, defined *nucleation agents*, can facilitate the formation of nucleation centres for a gaseous phase by reducing the nucleation free energy [59]. As a result, foam cells with a controlled structure and uniform distribution can form based on the amount and uniform distribution of the nucleation agents [94].

Homogenous and heterogeneous nucleation are the two types of cell nucleation that can arise [18].

Homogeneous nucleation: In homogenous nucleation, there is a spontaneous and random formation of bubbles (foam cells) characterised by the absolute absence of foreign bodies, additives or pre-existing cavities in the nucleus formation stage. Changes in temperature or pressure, or random

fluctuations can usually cause this event to occur [18]. The bubble stability depends on the competition between the interfacial energy (surface energy) and the pressure difference ΔP between the internal bubble and its surrounds. The rate of homogenous nucleation can be calculated from equation 2.13, as [18]:

$$N_o = C_0 f_0 \exp\left(-\frac{\Delta G_{crit}}{K_b T}\right)$$ (2.13)

where, the steady state nucleation rate N_0 is given by, the concentration of gas molecules, C_0, a kinetic pre-exponential factor f_0, which varies with the surface area of the nucleus (frequency factor of the gas molecules joining the nucleus), the free energy of critical nucleus formation, ΔG_{crit}, that represents the energy barrier for nucleation, the Boltzmann constant, K_b, and the absolute temperature, T [18, 48]. As seen in equation 2.13 from the exponential dependence, the impact of the factor ΔG_{crit} on the foam quality is quite strong. In classical theory, the expression of the free energy ΔG_{crit} of the critical nucleus formation is given by equation 2.14 [18]:

$$\Delta G_{crit} = \frac{16\pi\sigma^3}{3\,\Delta P^2}$$ (2.14)

where, the term ΔP denotes the difference in pressure between the nucleating and the metastable phases. This same ΔP equals the difference between the pressures inside and outside the nucleating bubble when the polymer is fully saturated with the gas (e.g. CO_2) and the gas` partial molar volume in the polymer is zero. In such a case, it can be considered as the pressure drop required to induce nucleation (ΔP = $P_{initial}$–P_{final}). The value of σ in equation 2.14 depends on the size of the critical bubble (nucleus) and it is an inaccessible quantity [18]. Classical nucleation theory replaces this term by approximating with a measurable quantity like the surface tension of the bubble/polymer interface. Overall, homogeneous nucleation is characterized by a wide cell size distribution of the final microcellular structure [17].

Heterogeneous nucleation: Heterogeneous nucleation is characterised by the presence of additives that act as nucleation centres and does not occur spontaneously [18]. In heterogeneous nucleation, the initiation of cell growth is supported by the existence of foreign particles or surfaces, promoting simultaneous growth of cells inside the polymer matrix [17]. The classical equations change slightly because surfaces promote wetting [17]. The nucleation rate can in this case be expressed as [18]:

$$N_1 = C_1 f_1 \exp\left(-\frac{\Delta G_{crit}^{het}}{k_b T}\right)$$ (2.15)

and, it depends on the concentration of heterogeneous nucleation sites, C_1, the frequency factor of gas molecules joining the nucleus, f_1, the Boltzmann constant, K_b, the absolute temperature, T, and the free energy or work needed in forming a critical nucleus in a heterogeneous system, ΔG_{crit}^{het}. The type of particle and surface topography (expressed by the shape factor S) were found to influence nucleation [18]. The introduction of additives can lower Gibb's free energy maximum if plate-like

additives with a planer surface and low activation energy are assumed. In a comparison between flat surfaces and tubular particles, the former offer better nucleation rates [95]. Heterogeneous nucleation is most favourable on flat surfaces since they provide the lowest energy barrier to nucleation. As a consequence, atoms and molecules tend to aggregate at the foreign surface [17]. The term ΔG_{crit}^{het} in a heterogeneous system is proportional to the work ΔG_{crit}^{hom} in a homogeneous system by a factor defined as shape factor (S) [18]:

$$\Delta G_{crit}^{het} = \Delta G_{crit}^{hom} \cdot S(\theta) \qquad (2.16)$$

The shape factor (S) depends on the wetting or contact angle (θ) between the bubble and the surface of the additive. Its expression is reported in equation 2.17 [18]:

$$S(\theta) = \frac{1}{4}(2 + 3\cos(\theta) - \cos^3(\theta)) \qquad (2.17)$$

As can be deducted from equation 2.17, the shape factor decreases as the contact angle increases, leading to a further reduction in ΔG_{crit}^{het}. The surface has no effect for a value of $\theta=180°$, so that is $\Delta G_{HET} = \Delta G_{HOM}$ [17]. No nucleation will take place if $\theta = 0°$, since the attraction to the surface is so strong that atoms and molecules prefer to adsorb to the surface rather than interact with each other. At any other intermediate value of θ, $\Delta G_{HET} < \Delta G_{HOM}$, therefore nucleation is promoted by the foreign surface. The energy-barrier required for cell nucleation in this case is lower than the energy-barrier needed in homogeneous nucleation. Qualitatively, a small contact angle and a large surface curvature of the nucleant offer a higher reduction in critical energy, which leads to an increase in the nucleation rate [95]. A narrow cell size distribution is typical of heterogeneous nucleation [17]. While for homogeneous nucleation, initiation and growth of cells are concurrent and lead to a wide cell size distribution in the final microcellular structure. For heterogeneous nucleation, the initiation of cell growth, supported by the existence of foreign surfaces, promotes simultaneous growth of cells inside the polymer matrix, resulting in a narrow cell size distribution [17].

Overall, in the production of cellular plastics, it is believed that both homogeneous and heterogeneous nucleation occur in relative amounts that depend on the specific processing conditions (e.g. the number of heterogeneous micro-voids may increase with saturation gas pressure due to the volumetric changes associated with large decompressions) and may occur simultaneously [92]. In most foam processing techniques, one would expect always some degree of heterogeneous nucleation due to inherent impurities in the polymer matrix [96]. A population of micro-voids in fact exists within the polymer matrix promoting heterogeneous nucleation, which implies that the heterogeneous domain size strongly influences the nucleation process, resulting in the preferential growth of heterogeneously nucleated cells over the homogeneous nucleation of additional cells. Nucleation and growth control of bubbles can attain various desirable cell morphologies of the foamed products with small or large, open or closed foam cells [18].

2.6.2. Cell Morphology of Polymeric Foams
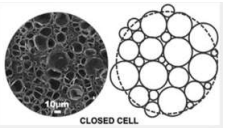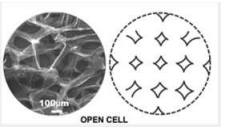
The number of cells per unit volume defines the *cell density* [17]. Cell density as well as cell size and cell size distribution determine the morphology of a foam and are governed by cell nucleation and cell growth mechanisms, contributing to the final bulk density and foam properties [17]. In particular, the foaming conditions of pressure, temperature, and time mainly determine the final morphology of polymer foams by affecting both the kinetics of nucleation and bubble growth processes [17].

A decrease in the cell density is observed at low pressures [97]. In contrast, high pressures increase the driving force to initiate cell growth resulting in a high cell density. The higher the pressure, the lower the polymer melt strength and interfacial tension, which will generate larger cells. Therefore, the cell size depends predominantly on the pressure within the cells [69]. However, as reported by Dai and co-workers, at constant saturation conditions of pressure and time, cell size increases with increasing temperature while cell density and mass density of the polymer foam decrease [97]. The temperature is defined in relation to the glass transition temperature for amorphous polymers and to the melting temperature for semi-crystalline polymers [18]. The highest cell density is observed in the vicinity of the T_g, at which viscosity is notably high to prevent the coalescence of bubbles but not their growth [97]. At foaming temperatures below the T_g of the polymer, the high viscosity (resistance) of the polymer bulk prevents the nucleated bubbles from growing. On the other hand, at higher temperatures above the T_g, the low polymer viscosity makes bubble growth easier.

2.6.2.1. Classification of polymeric foams

Polymer foams can be classified on the basis of cell structure, wall stiffness, volume expansion ratio and cell size, see Table 2.2. [18].

Table 2.2. Main classification of polymer foams.

Cellular structure	Closed-cell structure	
In accordance to processing methodology, two distinct structures can be achieved in the final foamed polymer.	 **(Figure adapted from Ref.[17]).**	The cellular structure refers to the type of connection among the cells within the foam **[18]**. Separate and discrete cells are considered closed-cell and characterise closed cell foams (e.g. *syntactic foams*). Foam cells are isolated from each other and the volume of individual bubbles do not communicate since the cavities are surrounded by complete (intact) cell walls. Since air cannot penetrate into a closed pore, closed-cell foams are not typically useful as acoustic absorbers. Thereby, better insulation and lower permeability characterise these foams **[1, 59]**.
	Open-cell structure (Figure adapted from Ref.[17]).	Conversely, cell walls are broken in open cell foams, whose structure consists of mainly ribs and struts, with interconnected cells through holes. The pores formed by the gas bubbles can interconnect between them without any barriers, and between the individual bubbles the solid structure is in the form of ligaments. In terms of properties, open cell foams differ from the closed cell foams in ensuring absorptive capability [18]. It is important to note that a small volume of closed-cells is always present in foams that are considered to be open-cell [1]. Interaction between open and closed cell structures determines the final properties and end use of foams. It plays a key role in the final microstructure of the foam [17]. The final foam with closed cell morphology is more rigid than open cell foams, while materials with an open cell morphology are softer [17].
Wall stiffness Different foams can be obtained by changing the chemistry, structure, density & raw materials applied during foaming [61].	**Flexible foams**	The wall stiffness can differentiate flexible foams from rigid foams [18]. While flexible foams present cell walls that collapse when pressed, rigid foams are characterized by stiff cell walls [18]. The two forms of polymer foams differ in composition, cell morphology and physical properties [59]. This distinction makes them applicable in different fields. Flexible foams are preferred in applications such as furniture, transportation, shoes, bedding, textile, sports applications, shock and sound attenuation.
	Rigid foams	Rigid foams on the other hand, besides their use in furniture and transportation, are preferably employed in building insulation, appliances, packaging, flotation and cushion, food and drink containers [67].
Volume expansion ratio **(VER)**	**High-density** **Medium-density** **Low-density**	A further classification of foams can be based on the volume expansion ratio, defined as the ratio between the bulk density of the pure polymer and the bulk density of the foamed sample [18]. The volume expansion ratio is the inverse of the relative density. Thereby, polymer foams can be distinguished as high-density (VER$\leq$ 4), medium-density (VER$\geq$4–10) and low-density (VER$\geq$10–50).
Cell size The main cell size distinguishes polymeric foams in terms of pore size [98, 99].	**Macro-cellular foams** (cell size $\geq$ 50 µm) **Micro-cellular foams** (cell size $\leq$ 10 µm) **Nano-cellular foams** (cell size $\leq$ 100 nm)	Conventional foams usually have a cell size of around 100µm and cell density of $<10^6$ cells/cm^3 [48]. Advancements in foam processing technology led to the development of new foams: fine-celled foams (cell size between 10µm and 100µm), micro-cellular foams (cell size of $\leq$10µm and cell density of $>10^9$ cells/cm^3) and nano-cellular foams (cell size of <1µm and cell density $>10^{15}$ cells/cm^3) [18]. Compared to conventional foams, microcellular foams of the same density have shown many promising/improved properties, particularly mechanical, due to smaller cell sizes and cell size uniformity [16, 18, 48]. Properties of nano-cellular foams can be further improved over micro-cellular foams due to the increase in surface area.[18].

2.6.3. Microcellular Foams

Microcellular foams are attractive materials and offer a solution to reducing significantly the amount of plastics used while offering properties not possessed by conventional foams and non-foamed polymers [100, 101]. Compared to conventional foams in which weight reduction leads to reductions in mechanical properties, these materials exhibit enhanced impact strength, toughness, fatigue life, and thermal stability [102]. Considered as lightweight and high strength materials, microcellular foams can be used for both structural applications and many others such as insulation, packaging, structures, and filters [18, 59, 103]. The unique multi-functionality and superior properties of these polymer foams at low density results in them being utilized in various applications [17]. Foam density[(f)] is the most important property next to cell size in marking different foams [18]. Microcellular and ultra-microcellular foams exhibit specific density reductions (relative to the non-foamed plastic) from 5% to 95%, with cell diameter sizes from 0.1 to 10 microns, and cell densities from 10^9 to 10^{15} cells/cm^3 [103]. The microscopic cell size and large number of cells in microcellular polymer materials can significantly reduce material consumption, which in turn results in product weight reduction and at the same time reduced costs of plastic required, process energy and ultimate transportation of cellular plastics [16]. This is one of the advantages of microcellular polymers over conventional foams, in which the weight reduction is generally achieved at the expense of reduced mechanical properties [103], so limiting their potential as lightweight structural materials [104]. Compared to macro-cellular foams, microcellular foams can offer unique characteristics due to their finer cellular structures which is able to bear greater loads before failing [103]. This explains the enhanced mechanical properties of these materials [105]. Different studies in fact have demonstrated that extremely fine cellular structures of microcellular and ultra-microcellular or nano-cellular foams result in substantial improvement in any property that requires the polymer to be stressed to the limit, such as impact strength or toughness, flexural fatigue failure, and elongation at break [105-107].

As stated above, microcellular plastics are commonly produced in foaming processes such as extrusion or foam injection moulding of polymers, by means of blowing agents [108], but very stringent conditions are required for their production (e.g. extremely high pressure and high pressure drop rate) [18, 48]. Nevertheless, the use of MuCell moulding technology, defined as the most significant plastic processing innovation in the last 35 years [109], allows to reduce significantly the injection pressures and shear heating due to the use of SCFs that decrease the material viscosity [110]. This foam process is known as microcellular foaming, since the bubbles obtained can in principle have micron sizes [109]. What differentiates this technology from the other foaming

---

[(f)] Foam density is determined by three different contributions, namely porosity, density of the gas inside the pores and the density of the solid matrix material [1].

processes is the massive weight reductions in cross sections as well as the possibility offered to foam all materials, including high melt temperature materials. Foaming during injection moulding presents important advantages over other processes of foaming, including increased melt flow, lower injection pressures, faster cycle times, smaller shot size, greater dimensional stability, and weight savings in moulded parts.

2.6.3.1. Microcellular Moulding Technology

MuCell moulding technology, invented by Suh et al. [111], has been successfully commercialized by Trexel [112] of the United States to injection mould microcellular foamed plastics. Microcellular injection moulding has already impacted significantly the worldwide plastics industry [113]. It is able to produce large weight reductions in thin parts and microcellular foams with uniform cell distribution [110]. The technology enhances product design, reduces product costs and improves processing efficiency, permitting at any rate the production of strong and lightweight products with a reduced consumption of the raw materials [110]. The MuCell moulding technology is suitable for injection moulding and structural foam moulding and does not require typical chemical or physical blowing agents, either nucleating agents or reactive components. The use of supercritical fluids (SCFs) of atmospheric gases (e.g. N_2 or CO_2) enables the creation of microscopic cells uniformly sized and equally distributed in the polymer [110]. The foam process consists of four steps, namely gas dissolution, homogeneous nucleation, cell growth and shaping [110], After a single-phase solution is reached in the barrel, through injection of the SCF into the polymer, a number of nucleation sites are formed and cells start to expand by diffusion of the gas into the bubbles. The production of microcellular foams through this technology requires a bespoke screw design for better mixing and a sealed barrel with gas injectors [48]. Some components of the standard reciprocating-screw injection moulding machine are modified and a fast injection speed in the injection unit can ensure a high pressure drop rate. Control of the rate of pressure drop is made at the mould gate to ensure a finer cell structure and a more uniform cell size distribution [48]. The part shape is controlled by the mould design, while the processing conditions control cell growth. Among the moulding parameters, the shot size is the most significant in affecting cell size, as well as cell density, and tensile strength [110]. Cycle times can be reduced by up to 50%; pack and hold time are eliminated because of the internal gas pressure, whereas cooling time is reduced by the inherent viscosity reduction of the MuCell process [110]. Millions of microcells can be created, achieving microcellular plastics with cell sizes less than 30µm [113]. Fabrication on this scale can offer a wide array of advantages in controlling and improving material quality. Less-expensive precision parts characterized by consistently high quality and dimensional stability can be thus produced through this technology.

2.6.3.2. Competitive Processes during Microcellular Processing

Competitive processes can occur during microcellular processing that interfere by modifying the mechanisms governing nucleation and growth of the cells and, therefore, greatly influencing the morphology of the resulting foam.

A phenomenon quite common during foam expansion and that highly influences cell morphology is *coalescence* [79]. As the cells grow and the wall thickness decreases, the probability of coalescence between neighbouring cells increases, resulting in a decrease in cell density [97]. Behravesh at al. [114] found that coalescence is facilitated by a high shear stress during processing, nevertheless its probability decreases with low melt temperatures. The melt strength of the polymer is critical in this case. Besides determining the total amount of cells and their size, if the polymer melt strength is low, cell walls may disrupt due to internal gas pressure and coalescence of cells can occur [15].

Obtaining a uniform cell structure with a high cell density is problematic in conventional foaming processes where foaming agents are mixed with the polymer [94]. While the foamability of polymers is influenced by the sorption of gas in the polymer, the mechanisms of cell nucleation and cell growth are affected by the amount of the gas dissolved in the polymer and the rate of gas diffusion [115-118]. As the diffusion process is driven by concentration gradients and the system free energy [119], the gas preferentially diffuses towards the nucleated cells, leaving low gas concentration regions characterised by insufficient gas to nucleate additional cells adjacent to the stable nuclei. The cell density will increase only if the size of the depleted gas regions is less than the characteristic spacing between cells, so that additional cells tend to nucleate between existing cells [119]. The mixing of the polymer/gas system and the formation of a single-phase solution should promote convective diffusion of the gas into the polymer matrix (e.g. through shearing/mixing action of the screws) in order to disperse the gas bubbles uniformly throughout the polymer and thus obtain a uniform distribution of the foam cells [119]. As a result of effective mixing, the diffusion rate is improved, the interfacial area per unit volume is increased, the diffusion distance is reduced and the local gas concentration is redistributed in the polymer matrix.

Another example of a competitive process is *gas-induced crystallization*, namely the crystallization enhanced by gas dissolution [120]. The process of gas dissolution and crystallization process are generally uncoupled at low temperatures with the crystallization kinetics lagging behind the gas diffusion kinetics [120]. However, when processing the polymer melt at high temperatures (100 - 200 °C), the gas diffusion kinetics and the kinetics of crystallization may be on the same time scale, since in the presence of high gas concentrations over a critical gas concentration level, the crystallization kinetics can be enhanced by gas dissolution. A gas dissolved in a polymer results in plasticization, and thus in an increased degree of molecular mobility and a lower T_g [120]. During gas dissolution, the gas molecules occupy the free volume of the polymer, and in some cases, gas and polymer molecules may bind together through secondary bonding. When the gas concentration

increases, the polymer begins to swell indicating a growing mean spacing between polymer chain segments until, at a critical gas concentration, the mean distance between polymer chain segments reaches a critical value. Above this critical spacing, chain segments possess sufficient energy and mobility that molecular relaxation and/or realignment forming crystalline structures is feasible during cellular processing. If secondary bonding occurs and is prevalent in the system, an additional energy contribution is required to sever the secondary bonds and displace the gas molecules prior to molecular alignment and crystallization [120].

A notable factor having a significant impact on the ultimate cellular structure is the degree of crystallinity (i.e. fraction of the polymer that is fully crystalline). As the crystallinity increases, the cellular structure is developed locally [103]. In general, no foaming is observed from highly crystallized samples. Gas molecules trapped in the crystalline domains may tend to act as crystal defects or may play a role in forming new crystalline microstructures [120].The crystallites are also nucleated from the melt at a definite range of temperatures and they grow forming spherulites (i.e. aggregates of crystallites). Controlling the cellular structure of semi-crystalline polymer foams is generally more difficult than that of amorphous polymers because of the high crystallinity and size of crystallites [16, 88]. This explains why most of the research on the microcellular processing of polymers over the past decades has focused on the foaming of amorphous polymers, not semi-crystalline polymers [103]. While in microcellular processing of amorphous polymers, the nucleation of cells takes place homogeneously in the entire bulk polymer with expansion occurring uniformly [103], in highly crystalline polymers the absorption and diffusion take place almost exclusively through the amorphous regions [121, 122]. Therefore, the formed polymer/gas solution is not uniform, resulting in a foam structure highly affected by the crystal morphology of the polymer [103], and usually develops only on the surface of the polymer samples [117].

2.6.4 The Challenge of Foaming Semi-crystalline Polymers

The solubility and diffusivity of the blowing agent in and through semi-crystalline polymers are critical factors in processing microcellular foams [103]. Both crystallinity and morphology have a significant effect on the solubility and diffusivity of the blowing agent in the polymer as well as on the cellular structure of the resulting foams [117]. The gas diffusivity in such polymers is strongly influenced by the crystallinity and precisely, increased crystallinity will result in a decrease in diffusivity because a more restricted pathway for the diffusing gas molecules through the amorphous phase [103]. Small gas molecules can diffuse into the polymer but the presence of crystalline regions complicates the process and leads to a reduction in diffusivity. In a simplistic sense, a semi-crystalline polymer can be imagined as a two-phase model of impenetrable crystallites dispersed in a rubbery amorphous matrix [103]. The presence of crystalline regions may tend to slow the diffusion rate of the displaced gas while restricting the amorphous chain segment mobility (i.e. chain

immobilization) due to the proximity of crystallites which may tend to decrease gas solubility through reductions in free volume. Although cell nucleation can be controlled using the gas saturation pressure, the range of this control method for semi-crystalline polymers is significantly limited by the presence of the additional heterogeneous nucleation contributions at the amorphous/crystalline interfaces [92].

The crystalline microstructure provides three technical challenges for the microcellular foaming of semi-crystalline polymers, as discussed by Colton [123]. These three problems are namely, i) low gas solubility in the crystalline regions, ii) the physical size and structure of the crystals, and iii) the requirement to foam near the melting temperature instead of near the glass transition temperature (as for foaming amorphous polymers) of the polymer. Low gas solubility results due to the tight packing of the polymer chains in the crystalline regions, which leaves little room for the gas and, consequently, a small driving force available for the nucleation process to begin and the subsequent growth of the bubbles. The driving force, which is due to the gas pressure, is not adequate to overcome the attractive forces and entanglements of the polymer chains, thus necessarily foaming above the melting point is the only reasonable approach for producing microcellular structures of semi-crystalline polymers. On one hand, processing above the melting point enables all the crystals to melt leaving an amorphous structure that allows enough molecular motion to accommodate bubble nucleation and growth for the microcellular foams produced. On the other hand, as melting lowers significantly the melt viscosity and thus melt strength, a temperature control is required to avoid an excessive softening of the polymer due to too high a temperature, which will lead to uncontrollable cell growth [123]. Poly(olefin)s usually offer a poor foam structure because of their relatively poor melt strength [15]. The cell morphology of the polymer foam is significantly affected by its viscosity and melt strength [29]. Another major obstacle with the foaming of semi-crystalline polymers is the microstructure of the crystallites, which can physically prevent foaming to occur since the gas does not dissolve in the crystallites [103]. Moreover, as the processing temperature is raised above the melting point of the polymer, to initiate foaming, crystallization begins even before the melting point is reached.

PE Foams → After the first commercial production of polyethylene (PE) foams, which dates back to the early 1940s [124], considerable efforts have been made in developing polyolefin foams with a morphology of controllable cell size and narrow cell size distribution [66]. Generally, crystal growth rates in PE are very fast (typically about 83,000 nm/sec [125]), therefore crystallization occurs faster than foaming, driving any gas in the polymer to concentrate into the inter-crystalline amorphous regions, in a non-uniform manner [123]. This creates several challenges in microcellular processing of semi-crystalline materials. The foaming behaviour of various grades of PE have been investigated, produced using a wide variety of processing methods, ranging from extrusion, to injection or compression moulding, which are commonly employed in the manufacturing of

polyolefin foams. Blends and composites of PE, as well as branched and cross-linked poly(olefin)s have also been investigated, in response to the loss of toughness and ductility caused by the generation of the cells, which is one of the common problems with polymer foams [29]. Historically, both high-density polyethylene (HDPE) and low-density polyethylene (LDPE) are used as foam materials. In particular, HDPE is able to solidify fast enough to sustain thin cell walls, due to its rapid crystallisation kinetics and high crystallinity [66]. It is known that solid-state microcellular foaming of HDPE is very difficult to achieve [126].

In current industry practices, common methods to improve the cell structure during the moulding of parts from semi-crystalline polymer are the addition of fillers or other additives to create more heterogeneous nucleation or, alternatively, the increase of the cooling rate to decrease the crystallinity. As high cooling rates result in less crystallinity and thus reduced strength of the final foamed part, adding fillers is an efficient method to achieve both the necessary crystallinity and cell structure in a microcellular part [127]. Modifying a polymer via heterogeneous nucleation (i.e. a filled polymer) is a major strategy for making acceptable microcellular structures for all PE's. The cell structure can be improved significantly by adding fillers into unfilled HDPE to promote nucleation and increase the number of nuclei in a foaming polymer melt [69, 127, 128].

2.6.5. Advantages of Nanofiller Addition in making Polymer Foams

Enhancing the strength of the foam without compromising light weight is one of the most important aspects of polymer foam research [17]. Properties such as toughness and ductility of neat polymer foams are usually inferior to their solid counterparts because of the inclusion of air bubbles [17]. Although polymer foams have been largely applied in a variety of industries as lightweight materials, they suffer from low mechanical strength, poor surface quality, and low thermal and dimensional stability [48, 65, 97]. Nevertheless, the properties of polymer foams can be enhanced by enhancing the polymer matrix and controlling the foam structure [129-132]. The ability to control cell size is highly important in controlling the properties of foams [17]. Common approaches adopted are the use of fillers to reinforce the polymer matrix and the decrease of the average cell size without decreasing foam density [17]. Microcellular plastics and microcellular polymer nanocomposites have both attracted much attention [133]. The presence of nanoparticles can be extremely beneficial in enhancing mechanical and physical properties of foam materials [18, 48]. Nanofillers have been widely explored to reach a high functionality to weight ratio in polymer foams, as they can reinforce the polymeric matrix, while decreasing cell size [17].

Nano-sized particles (i.e. order of 10^{-9} m) are widely used in the manufacture of nanocomposites as fillers to modify and enhance the properties of the matrix polymer, due to their nanoscale dimensions. In comparison with traditional fillers, the much larger surface area offered by nanofillers leads to a larger three dimensional interfacial region with properties different from those

of the bulk polymer [17]. Their combination of high aspect ratio and large surface area offer the potential for high reinforcing efficiency, good barrier properties, and improved dimensional and thermal stability [100]. The use of inorganic fillers in thermoplastics with the microcellular injection moulding process allows to further exploit the exceptional characteristics of polymer foams by enhancing the polymer matrix properties and controlling the foam structure [113]. Compared to unfilled microcellular samples, microcellular nanocomposites exhibit higher tensile strength as well as more uniform cell distribution and smaller cell size [48]. As fillers of size less than 100nm, in at least one dimension, nanofillers provide an outstanding opportunity to control polymer foam structure and properties, by tailoring shape, size and surface chemistry of the nanoparticles.

Classical nucleation theory describes qualitatively the effect of nanoparticles on cell density as heterogeneous nucleation agents induce heterogeneous nucleation [48]. During the foaming process, nanoparticles behave like nucleating agent that nucleate cells at the boundary between the polymer and the nanoparticle, while foaming agents contribute to the homogenous dispersion of the nanoparticles in the polymer matrix, hence improving the properties of the polymer foams [29]. Adding particles or nanoparticles that act as nucleation agents to reduce the nucleation free energy is an established practice to obtain foam cells with a controlled structure and uniform distribution [17, 100]. The addition of small amounts of well-dispersed nanoparticles in the polymer phase may aid in facilitating the bubble nucleation process [48], so that the cell size is reduced in accordance with the increased nucleation rate, since cell size and number of nucleation sites (cell density) are inversely proportional in foams with the same bulk density [101]. Nanofillers force nucleation to occur at the filler–polymer interface [17]. The effectiveness of a nucleating agent depends on its surface geometry and surface properties [128]. By tailoring the surface chemistry of the nanofillers, dispersion of nanofillers and cell nucleation efficiency can be controlled. The energy barrier for bubble nucleation can be lowered through the contact angle, affecting both structure and density of the foam [17].

The amount and distribution of the nucleation agents are also important factors in determining the quality of a foam [100]. McClurg [134] outlined the qualities of ideal nucleating agents for polymer foaming, suggesting that a high degree of uniformly dispersed particles with uniform size and non-wetting surfaces are suitable nucleants to produce desirable foams with high cell density and small cell size. The large surface area of nano-sized fillers provides many more nucleation sites, tending to lead to a smaller average cell size and a narrow cell distribution because more bubbles start to nucleate concurrently, resulting in less gas available for bubble growth [48]. At a given concentration, more nanofillers are present per unit volume and their small size creates a larger number of potential nucleation sites (i.e. increased nuclei number in the foamed polymer melt) [17]. The foam cell density can be increased by means of filler addition by orders of magnitude depending on the filler size and content which strongly affect the foam cell density [94]. The smaller the filler

particles the higher the nucleation densities, although a certain lower limit of particle size exists [94]. In a study conducted by Goren et al. [135], the authors concluded there is a competing effect between the number of nucleation sites (smaller particles, more sites) and nucleation efficiency (smaller particles, lower nucleation efficiency). Foams with a fine filler size have shown a higher cell density at a high saturation pressure, whereas, at a low saturation pressure, the fine filler results in a lower cell density, becoming nearly the same as the unfilled foam at a certain saturation pressure. At low gas saturation pressure indeed, only relatively large filler particles can create cells because the amount of gas at the polymer/filler interface is small [94]. The increase in viscosity caused by addition of nanofillers to polymers prevents void coalescence with further decreases in the average cell size.

Nevertheless, foam properties are improved only if a fine dispersion of nanoparticles inside the matrix is ensured [100]. On the other hand, the actual nucleant density will be greatly reduced if particle dispersion is poor. The presence of agglomerated nanoparticles act as defects and can have detrimental effects on polymer foam performance due to reduced nucleation efficiency [29].

2.7 Acoustic Properties of Unfilled Polymer and Polymer Composite Foams

Compared with traditional metallic foams, polymer foams have advantages with regard sound absorption due to their light weight and relative ease of processability [14]. Polymer foams are example of materials whose acoustic efficiencies are influenced by elastic and damping properties [136]. A sound wave is generally reflected at the solid-gas interface and dissipated in the cellular structure via propagation [14]. As sound propagates through a porous material, acoustic energy is dissipated by frictional effects at the cell walls, heat transfer through the skeleton structure, and conversion of acoustic energy into internal energy [137]. The viscous friction between polymer chains and air friction inside cells allows the acoustic energy to be absorbed and moved inside the cells, being dissipated as heat [7, 138]. Cells must be interconnected throughout the entire foam body as well as connected to the ambient environment for foams to absorb and dissipate acoustic energy [139].

Theoretical prediction of the acoustic properties of porous materials through finite-element-based numerical formulations and/or modelling is not an easy task due to the complicated cell structure of these materials and more research is still required to understand the relationship between cell morphology and acoustic properties such as the sound absorption coefficient [139].

The acoustic performance of a porous material depends on the relationship between structure properties such as cell morphology, cell wall thickness and pore size, which affect the macrostructure of the material, and acoustic properties. In addition to cell size and cell density, the sound absorption efficiency of polymer foams can also be influenced by the modulus of the polymer [14]. Five macroscopic properties have been identified by the Johnson–Allard model as responsible

for the acoustic performance of a given material, namely: porosity, airflow resistivity, tortuosity, viscosity and thermal characteristics, which are all linked to the inner microstructure of the porous network [139]. The difference in cell size and cell density mainly dominates the reflection and dissipation of the propagation of sound waves [14]. Clearly, as the microstructure of a porous material is determined by the processing parameters used during fabrication, optimization of the fabrication process can be effective at optimizing the sound absorption behaviour of a material [139].

The presence of nanofillers influences acoustic properties of foams by improving sound absorbing properties [17]. Their incorporation leads to an increase in stiffness of the cell wall which leads to a significant improvement in the acoustic damping efficiency of the foams. The increased rigidity of the cell wall is responsible for the greater sound absorption observed in composite foams compared to unfilled polymer foams as a result of the increased dissipation of energy as heat, scattering or reflection of sound waves at the cell walls. In addition, the increase in acoustic absorption by the addition of fillers may be due to the large surface area of the filler at the matrix-filler interface, at which the acoustic energy is dissipated as heat energy [140, 141]. The increase in the filler content normally leads to an increase in the sound absorption coefficient (α) [7]. The filler acts as a nucleation agent and promotes the formation of cells, so that the cell size decreases and the cell density increases [14]. Furthermore, the reduction of cell size resulting from the addition of nanofillers in the polymer contributes to the improvement of sound absorbing properties by increasing tortuosity [33]. The formation of fine morphology by addition of fillers creates more paths for sound waves passing through the foam structure, which allow them to absorb more sound [7].

Mendelsohn et al. [67] studied syntactic foams comprising hollow polymeric microspheres (in particular expanded polystyrene microspheres) dispersed randomly in a poly(urethane) matrix resin. These cellular materials showed utility as sound absorbing and decoupling agents, also having important properties, such as high porosity, low acoustic reflectivity, and high compression strength [67].

Dib et al. [12] studied the acoustic absorption efficiency in a poro-elastic medium, i.e. a poly(urethane) (PU) polymer foam, in which a very good performance in absorbing noise at medium and high frequencies (roughly between 1500 Hz and 10^4 Hz) was reported. On the other hand, small absorption coefficients were obtained at low frequencies (lower than 1 KHz). The analysis of the sound absorption coefficient at different characteristic frequency bands revealed a huge influence of the foam frame rigidity in the vicinity of the resonance frequency [12]. Variations of the absorption coefficient normally occur around the *frequency of resonance* (i.e. the quarter-wave frequency of the foam material) by varying the Young`s modulus and the Poisson coefficient of the skeleton (frame), as these parameters along with the density of the material, play a key role in the acoustic absorption quality of the foams [12]. Lee and co-workers [58] found that the sound absorption ratio

of PU foams increases, over a wide frequency range of 150–1800 Hz, with increasing nano-silica loading. However, at very low frequencies (100–150 Hz), unfilled samples presented a higher sound absorption ratio than nano-silica filled samples, because of the resonance effect [58].

Nanocomposite foams filled with carbon nanotubes (or even carbon nanofibers) have also received increasing attention, mainly due to the improved mechanical properties that enhance the sound absorption properties resulting from the addition of these types of fillers to the polymer foam [142, 143]. Considerable improvements in PU foam sound absorption are reported in the literature by reinforcing poly(urethane) through the use of MWCNTs as well as nanoclay and titania nanoparticles [141]. In particular, sound absorption properties of PU foams showed to be affected by the addition of small amounts of MWCNTs. Significant improvements of the sound transmission loss are seen in comparison with pure PU foams, leading to better sound insulation properties [141]. Verdejo et al. [140] found that the incorporation of MWCNTs to flexible PU foams resulted in a monotonical increase in acoustic damping efficiency. Even a loading fraction of 0.1 wt% MWCNTs was enough to significantly raise the sound absorption ratio. It delivered an increase in the peak absorption coefficient from 70% (value of the pure polymer foam) up to 90% in the high frequency range of 1–7 KHz. The increase in the sound absorption ratio is attributable to the enhanced mechanical energy damping, due to the interfacial sliding and stick-slip behaviour at the polymer–carbon nanotube interface [140]. Furthermore, the acoustic absorption range of polystyrene (PS) composite foams (filled with lignin nanoparticles and MWCNTs) was found to be wider than pure PS foam, with more sound energy dissipated into the polymer in a much broader sound wave frequency band, attributed to the cell size and cell density varied by addition of the fillers [14].

2.8. Polymer Nanocomposite Foams

Foaming of polymer composites and nanocomposites has been recently regarded as a promising fabrication strategy to tailor micro-and nanostructures in order to promote electrical, thermal and mechanical properties of these materials by aligning one-dimensional (1D) and two-dimensional (2D) multifunctional fillers through biaxial stress fields induced by foam expansion. Biaxial stretching of the polymer-gas solution near the bubble surface generates pressure fluctuations around the heterogeneous phase (i.e. the solid filler and crystallites) causing local regions to be subjected to a pressure that is lower than the overall pressure in the system. This translates to local increased super-saturation levels and growth of existing micro-voids, which in turn markedly increase the rate of cell nucleation (i.e. bubble growth-induced cell nucleation under static conditions) [128].

Nano-cellular polymeric foams, or *nanofoams*, are hence expected to be superior to existing foam materials as a consequence of the higher strength-to-weight ratio for use in any applications porous polymers are currently used, but with improved performance [61, 80, 144]. In a blown foam, the cell shape and the characteristics of the cells affect significantly the structural, acoustic, thermal and

electrical properties of the foam [67]. Moreover, the presence of nanofillers influence significantly the mechanical, acoustic, electrical, rheological and thermal properties of polymer foams [17]. Nanofillers add functionality to polymer foams by providing increased strength [145, 146], surface area and damping properties [140] over traditional foams, while not diminishing other properties (e.g. transparency, breakdown strength and ductility of the polymers [17]). By adding nanofillers, it is even possible to achieve multi-functionality in highly conductive transparent polymers or composites with simultaneous improvements in strength and ductility. Micro- and nano-porous foams obtained from polymer nanocomposites have found a wide range of applications [80, 144], from thermal insulation to tissue engineering scaffolds [48]. New application fields see them used also in hydrogen storage, electromagnetic shielding and as sensors [17]. Different types of nanofillers can create different types of nanocomposite foams with specific strengths. Specifically, fillers such as silica, nanoclay and carbon nanotubes are known to be effective particles for obtaining uniform and fine foam structures in many microcellular foaming processes [147].

Carbon nanotube fillers → The low density, good manufacturability, superior chemical resistance and tunable multifunctional properties of composites of polymers and carbon nanotubes (CNTs) continues to arouse wide interest from both industry and academia [148]. Carbon-based nanofillers, such CNTs, add strength and conductivity to foams [17]. They can create a conductive filler network [149] and present a conducting-semiconducting structure-dependent electronic behaviour [150]. The advantage of providing superior electromagnetic wave absorption and pressure sensitivity has resulted in CNT-based nanocomposite foam being applied in the fabrication of high performance piezo-resistive sensing devices and novel EMI (electromagnetic interference) shielding polymer composite foams [151, 152]. Although the influence of CNT properties such as aspect ratio and surface chemistry on the properties of solid (un-foamed) polymer nanocomposites have been extensively studied, their influence on the properties of composite foams are more complex than the solid counterparts and are still not fully understood. To produce polymer nanocomposite foams with desirable properties (e.g. acoustic), a better understanding of the interactions between fillers, bubbles and the matrix in CNT filled polymer composite foams is necessary. Undoubtedly, processing methods influence the foam morphology of nanocomposite foams, and the aspect ratio of the CNTs, which varies with processing, is expected to also alter the foam morphology. The alignment of the nanotubes inside the nanocomposite foams was in fact found to change with bubble density [142]. Nonetheless, the aspect ratio of MWCNTs in the composites has shown to have no significant effects on the solubility of CO_2 in the foamed composites, in agreement with the finding of Taki and co-workers [153], who found that the solubility of CO_2 in nanoclay/polypropylene composite foams did not change with filler content.

Albeit, the mechanism of nucleation in foams is still under investigation, a study by Chen et al. [142], concerning the use of multi-walled carbon nanotubes (MWCNTs) as fillers in nanocomposite

foams, gives interesting insight into this process. A different action between ends and sidewalls of the nanotubes is presented in the number of effective bubble nucleation sites. The differences in geometry and defect structure lead shorter nanotubes and long nanotubes to act as distinct heterogeneous nucleating centres. At low saturation pressures, nucleation was shown to occur mainly at the nanotube ends. The critical free energy of nucleation is lower at the nanotube ends than at the sidewalls, therefore, nanocomposites with shorter nanotubes presented greater bubble density under the same foaming conditions and MWCNT concentration [142]. At high saturation pressures, on the other hand, nucleation at the nanotube sidewalls is feasible and longer nanotubes were shown to increase bubble density in the composites with higher aspect ratio MWCNTs, acting as multiple nucleation sites [142].

2.8.1. HDPE-MWCNT Nanocomposites Foams: Research gaps

The introduction of MWCNTs into the HDPE foam may induce nucleation of a considerable quantity of bubbles, ultimately providing a comparable weight reduction to neat HDPE foams. Any reduction in strength derived from the inclusion of cells could be compensated for by the reinforcement of cell walls with MWCNTs.

From what emerged from this review of the published literature, there have been very few studies conducted on HDPE-MWCNT composite foams. Most of the research is solely focused on other properties of these multifunctional foam types, including electrical [148, 152], thermoelectric [149], mechanical and transport properties [150].

The literature confirms that MWCNTs are efficient nucleating agents but the extent of the enhancement of the physical, mechanical and acoustic absorbing properties of a semi-crystalline polymer like HDPE has not been evaluated yet. None of the studies reported to date investigated the acoustic properties of these foams. The lack of understanding how the morphology and structure of such foams is correlated to their final properties, especially acoustic, needs to be addressed. The role and the importance of the addition of MWCNTs to the HDPE needs further research alongside with the variation of filler content and conditions of foaming.

The focus of the research undertaken in this EngD project can fill the gaps emerged from the literature while providing a new contribute to the knowledge where both routes of chemical and physical foaming are addressed. Fundamentally, foam composites of MWCNTs with HDPE represent a novel approach to fabricating lightweight foams and besides having the desired combination of properties for application in acoustic sensors, could be applied in many other fields. Further to the description of the current state of the literature, there is a significant opportunity to develop novel MWCNT-filled composite foams that could provide the desired combination of properties required for acoustic sensor application.

References

[1] M.A. Kuczmarski, J.C. Johnston, Acoustic Absorption in Porous Materials, NASA/TM, Conference Paper, NASA Glenn Research Center, Cleveland, US, March 2011, pp. 1-20.

[2] K.J. Kushla, Sound and the Ear, in: Fundamentals of Audiology for the Speech-Language Pathologist, Jones & Bartlett Learning, Chapter 2, second edition, 2017, pp. 15-36.

[3] S.W. Rienstra, A. Hirschberg, An Introduction to Acoustics, Eindhoven, 2009, pp. 1-286.

[4] D.R. Raichel, The science and applications of acoustics, Springer, second edition, 2006, pp. 1-649.

[5] W.R. Hendee, E.R. Ritenour, Ultrasound Waves, in: Medical Imaging Physics, Wiley-Liss Inc, Chapter 19, fourth edition, 2002, pp. 303-316.

[6] P. Laugier, G. Haïat, Introduction to the Physics of Ultrasound, in: Bone Quantitative Ultrasound, Springer, Chapter 2, 2011, pp. 29-45.

[7] R. Gayathri, R. Vasanthakumari, C. Padmanabhan, Sound absorption, Thermal and Mechanical behavior of Polyurethane foam modified with Nano silica, Nano clay and Crumb rubber fillers, IJSER, 4(5), 2013, pp. 301-308.

[8] A. Kovalenko, M. Fauquignon, T. Brunetb, O. Mondain-Monval, Tuning the sound speed in macroporous polymers with a hard or soft matrix, The Royal Society of Chemistry, 13(25), 2017, pp. 4526-4532.

[9] A. Nick, U. Becker, W. Thoma, Improved Acoustic Behavior of Interior Parts of Renewable Resources in the Automotive Industry, Journal of Polymers and the Environment, 10(3), 2002, pp. 115-118.

[10] M.R.G. Ravandi, H. Mardi, A.A.A. Langari, M. Mohammadian, N. Khanjani, A Review on the Acoustical Properties of Natural and Synthetic Noise Absorbents, Open Access Library Journal 2(8), 2015, pp. e1598_1-11.

[11] I. C. Finegan, R. F. Gibson, Recent research on enhancement of damping in polymer composites, Composite Structures, 44(2-3), 1999, pp. 89-98.

[12] L. Dib, S. Bouhedja, H. Amrani, Mechanical Parameters Effects on Acoustic Absorption at Polymer Foam, Advances in Materials Science and Engineering, 2015, pp. 1-10.

[13] X. Sun, W. Liang, Cellular structure control and sound absorption of polyolefin microlayer sheets, Composites Part B: Engineering, 87, 2016, pp. 21-26.

[14] Y. Fei, W. Fang, M. Zhong, J. Jin, P. Fan, J. Yang, Z. Fei, L. Xu, F. Chen, Extrusion Foaming of Lightweight Polystyrene Composite Foams with Controllable Cellular Structure for Sound Absorption Application, Polymers, 11(1), 2019, pp. 106-116.

[15] A.H Behravesh, C.B. Park, L.K. Cheung, R.D. Venter, Extrusion of polypropylene foams with hydrocerol and isopentane, Journal of Vinyl and Additive Technology, 2(4), 1996, pp. 349-357.

[16] A.K. Bledzki, J. Kühn, H. Kirschling, W. Pitscheneder, Microcellular Injection Molding of PP and PC/ABS with Precision Mold Opening and Gas Counterpressure, Cellular Polymers, 27(2), 2008, pp. 91-100.

[17] L.M. Chen, D. Rende, L.S. Schadler, R. Ozisik, Polymer nanocomposite foams, Journal of Materials Chemistry A, 1(12), 2013, pp. 3837-3850.

[18] C. Okolieocha, D. Raps, K. Subramaniam, V. Altstädt, Microcellular to nanocellular polymer foams: Progress (2004-2015) and future directions - A review, European Polymer Journal, 73, 2015, pp. 500-519.

[19] D.Y. Xu, X. Cheng, S.F. Huang, Investigation on fabrication and property of acoustic gradient composites, Composites Science and Technology, 122, 2016, pp. 90-96.

[20] L. Istvan, L.L. Beranek, Sound-Absorbing Materials and Sound Absorbers, in: Noise and Vibration Control Engineering, Principles and Applications, John Wiley & Sons, Chapter 8, second edition, 2006, pp. 215-278.

[21] D.W.Van Krevelan, Acoustic Properties, in: Properties of Polymers, Elsevier Science, Chapter 14, fourth edition, 2009, pp. 505–522.

[22] M. Sinha, D.J. Buckley, Acoustic Properties of Polymers, in: Physical Properties of Polymers Handbook, Springer, Chapter 60, second edition, 2007, pp. 1021-1031.

[23] D. Royer, E. Dieulesaint, Elastic Waves in Solids I, Springer, 2000, pp. 1-374.

[24] G.S. Kino, Acoustic Waves: Devised Imaging and Analog Signal, Prentice Hall, 1987, pp. 1-688.

[25] W.B. Cushman, Acoustic absorption or damping material with integral viscous damping, U.S. Patent Documents, Poiesis Research, Inc., 1998, application no. 780,271.

[26] H.S. Seddeq, Factors Influencing Acoustic Performance of Sound Absorptive Materials, Australian Journal of Basic and Applied Sciences, 3(4), 2009, pp. 4610-4617.

[27] M.J. Crocker, J.P. Arenas, Use of Sound-Absorbing Materials, in: Handbook of Noise and Vibration Control, John Wiley & Sons Inc., Chapter 57, 2007, pp. 696-713.

[28] W.B. Cushman, G.B. Thomas, Acoustic attenuation and vibration damping materials, U.S. Patent Documents, Poiesis Research Inc., 1995, application no. 186,058.

[29] M. Altan, Thermoplastic Foams: Processing, Manufacturing, and Characterization, in: Recent Research in Polymerization, Intech Open, Chapter 6, 2018, pp. 117-137.

[30] J.P. Arenas, M.J. Crocker, Recent Trends in Porous Sound-Absorbing Materials, Sound and Vibration, 44(7), 2010, pp. 12-17.

[31] R. Guastavino, Elastic and acoustic characterisation of anisotropic porous materials, Doctoral Thesis, Department of Aeronautical and Vehicle Engineering, KTH Engineering Science, Stockholm, 2008.

[32] A.E. Tiuc, O. Vasile, A-D. Usca, T. Gabor, H. Vermecan, The Analysis of Factors That Influence the Sound Absorption Coefficient of Porous Materials, RJAV, 11(2), 2014, pp. 105-108.

[33] J. Allard, N. Atalla, Propagation of Sound in Porous Media: Modelling Sound Absorbing Materials, John Wiley & Sons, second edition, 2009, pp. 1–351.

[34] M. Bilova, E. Lumnitzer, M. Badida, R. Kralikova, Analysis of Acoustical Properties of mono and multilayer Sound Absorbers, Annals of DAAAM for 2011 & Proceedings of the 22nd International DAAAM Symposium, 22(1), 2011, pp. 1219-1220.

[35] C. Skinner, J. Peters, J. Vandenbroeck, Acoustic Absorbers: A third way for the management of sound in automobiles, Paper for UTECH Europe, 2006, pp.1-15.

[36] T.J. Cox, P. D'Antonio, Acoustic Absorbers and Diffusers, Theory, design and application, Spon Press, 2004, pp. 1-405.

[37] J. Rouquerol, D. Avnir, C.W. Fairbridge, D.H. Everett, J.H. Haynes, N. Pernicone, J.D.F. Ramsay, K.S.W. Sing, K.K. Unger, Recommendations for the characterization of porous solids (Technical Report), Pure and Applied Chemistry, 66(8), 1994, pp. 1739-1758.

[38] C.H. Sung, K. S. Lee, K.S. Lee, S. M. Oh, J.H. Kim, M.S. Kim, H.M. Jeong, Sound damping of a polyurethane foam nanocomposite, Macromolecular Research, 15(5), 2007, pp. 443-448.

[39] M.A. Ibrahim, R.W. Melik, Physical Parameters Affecting Acoustic Absorption Characteristics of Fibrous Materials, Proceedings of the Mathematical and Physical Society of Egypt, 46, 1978, pp. 125-130.

[40] R. Dragonetti, C. Ianniello, R.A. Romano, Measurement of the resistivity of porous materials with an alternating air-flow method., Journal of the Acoustical Society of America, 129(2), 2011, pp. 753-764.

[41] M. Ouisse, M. Ichchou, M. Ichchou, S. Chedly, M. Collet, On the sensitivity analysis of porous material models, Journal of Sound and Vibration, 331(24), 2012, pp. 5292-5308.

[42] N. Sebaa, Z.E.A. Fellah, M. Fellah, W. Lauriks, C. Depollier, Measuring flow resistivity of porous material via acoustic reflected waves, Journal of Applied Physics, 98(084901), 2005, pp. 1-10.

[43] D.A. Bies, C.H. Hansen, Flow resistance information for acoustical design, Applied Acoustics, 13(5), 1980, pp. 357-391.

[44] D.A. Bies, C.H. Hansen, Vibration Control, in: Engineering Noise Control: Theory and Practice, Spon Press, Chapter 10, third edition, 2003, pp. 1-733.

[45] A. Akay, A. Carcaterra, Damping Mechanisms, in: Active and Passive Vibration Control of Structures, CISM International Centre for Mechanical Sciences, Springer, Chapter 6, Vol. 558, 2014, pp. 259-299.

[46] L.H. Sperling, Basic Viscoelastic Definition and Concepts, in: Sound and Vibration Damping with Polymers, ACS Symposium Series, Chapter 1, Vol. 424, 1990, pp. 5-22.

[47] B. Hartmann, Relation of Polymer Chemical Composition to Acoustic Damping, in: Sound and Vibration Damping with Polymers, ACS Symposium Series, Chapter 2, Vol. 424, 1990, pp. 23-45.

[48] L.J. Lee, C.C. Zeng, X. Cao, X. Han, J. Shen, G. Xu, Polymer nanocomposite foams, Composites Science and Technology, 65(15-16), 2005, pp. 2344-2363.

[49] S.J. Hwang, R.F. Gibson, Prediction of fiber-matrix interphase effects on damping of composites using a micromechanical strain energy/finite element approach, Composites Engineering, 3(10), 1993, pp. 975-984.

[50] S. K. Chaturvedi, G. Y. Tzeng, Micromechanical modeling of material damping in discontinuous fiber three-phase polymer composites, Composites Engineering, 1(1), 1991, pp. 49-60.

[51] J. Caruso, C. Chamis, Assessment of Simplified Composite Micromechanics Using Three-Dimensional Finite-Element Analysis, Journal of Composites, Technology and Research, 8(3), 1986, pp. 77-83.

[52] S. Dong, R. Gauvin, Application of dynamic mechanical analysis for the study of the interfacial region in carbon fiber/epoxy composite materials, Polymer Composites, 14(5), 1993, pp. 414-420.

[53] R.F. Gibson, Damping characteristics of composite materials and structures, Journal of Materials Engineering and Performance, 1(1), 1992, pp. 11-20.

[54] I. C. Finegan, R. F. Gibson, Analytical and experimental characterization of damping and stiffness in polymer composites having coated fibres as reinforcement, Proceedings of the ASME Noise Control and Acoustics Division, 24, 1997, pp. 27–138.

[55] S.A. Suarez, R.F. Gibson, C.T. Sun, S.K. Chaturvedi, The influence of fiber length and fiber orientation on damping and stiffness of polymer composite materials, Experimental Mechanics, 26(2), 1986, pp. 175-184.

[56] R.F. Gibson, S.K. Chaturvedi, C.T. Sun, Complex moduli of aligned discontinuous fibre-reinforced polymer composites, Journal of Materials Science, 17(12), 1982, pp. 3499-3509.

[57] I.B. Salem, R-M. Guillermic, C. Sample, V. Leroy, A. Saint-Jalmesa, B. Dollet, Propagation of ultrasound in aqueous foams: bubble size dependence and resonance effects, Soft Matter, 9(4), 2013, pp. 1194-1202.

[58] J. Lee, G.H. Kim, C.S. Ha, Sound Absorption Properties of Polyurethane/Nano-Silica Nanocomposite Foams, Journal of Applied Polymer Science, 123(4), 2012, pp. 2384-2390.

[59] D. Klempner, K.C. Frisch, Handbook of Polymeric Foams and Foam Technology, Hanser, 1991, pp. 1-408.

[60] T. Garbacz, L. Dulebova, Processing Characteristics and Properties of the Cellular Products Made by Using Special Foaming Agents, Scientific Proceedings 2012, STU in Bratislava, Vol. 20, 2012, pp. 74-80.

[61] E. Aram, S. Mehdipour-Ataei, A review on the micro- and nanoporous polymeric foams: Preparation and properties, International Journal of Polymeric Materials and Polymeric Biomaterials, 65(7), 2016, pp. 358-375.

[62] Y. Yang, M.C. Gupta, K.L. Dudley, R.W. Lawrence, Conductive Carbon Nanofiber–Polymer Foam Structures, Advanced Materials, 17(16), 2005, pp. 1999-2003.

[63] D. Klempner, V. Sendijarevic, Handbook of Polymeric Foams and Foam Technology, Hanser, second edition, 2004, pp 1-549.

[64] J.Q. Wang, W.K. Chow, A brief review on fire retardants for polymeric foams, Journal of Applied Polymer Science, 97(1), 2005, pp. 366-376.

[65] M.C. Saha, H. Mahfuz, U.K. Chakravarty, M. Uddin, Md E. Kabir, S. Jeelani, Effect of density, microstructure, and strain rate on compression behavior of polymeric foams, Materials Science and Engineering: A, 406(1), 2005, pp. 328-336.

[66] Y. Zhang, Polyolefin Formulations for Improved Foaming: Effects of Molecular Structure and Material Properties, Doctoral Thesis, Department of Chemical Engineering, Queen's University, Kingston, Canada, 2013, pp. 1-133.

[67] R.B. M. A. Mendelsohn, F. W. Navish, Sound absorbing and decoupling syntactic foam, U.S. Patent, Westinghouse Electric Corporation, Pittsburgh, PA, 1995, pp. 1-26.

[68] M. A. Shafi, K. Joshi, R. W. Flumerfelt, Bubble size distributions in freely expanded polymer foams, Chemical Engineering Science, 52(4), 1997, pp. 635-644.

[69] M. Kozlowski, Lightweight Plastic Materials, in: Thermoplastic Elastomers, InTech, Chapter 14, 2012, pp. 291-318.

[70] D. Liu, X. Li, H. Song, P. Wang, J. Chen, Q. Tian, L. Sun, L. Chen, B. Chen, J. Gong, G. Sun, Hierarchical structure of MWCNT reinforced semicrystalline HDPE composites: A contrast matching study by neutron and X-ray scattering, European Polymer Journal, 99, 2018, pp. 18-26.

[71] V. Pettarin, Injected Polymer-Matrix Nanocomposites: Morphology-Performance Relationship, in: Polymer-Matrix Composites: Types, Applications & Performance, Nova Polymer Science and Technology, Chapter 6, 2014, pp. 129-165.

[72] A.K. Bledzki, O. Faruk, Influence of Processing Temperature on Microcellular Injection-Moulded Wood–Polypropylene Composites, Macromolecular Materials and Engineering, 291(10), 2006, pp. 1226-1232.

[73] L-S. Turng, Special and emerging injection molding processes, Journal of Injection Molding Technology, 5(3), 2001, pp. 160-179.

[74] Y. Li, Z. Chen, C. Zeng, Poly(MethylMethacrylate) (PMMA) Nanocomposite Foams, in: Polymer Nanocomposite Foams, CRC Press, Chapter 1, 2010, pp. 1-33.

[75] P.S. Liu, G.F. Chen, Producing Polymer Foams, in: Porous Materials Processing and Applications, Elsevier, Chapter 7, 2014, pp. 345-381.

[76] C. B. Park, D. F. Baldwin, N. P. Suh, Effect of the pressure drop rate on cell nucleation in continuous processing of microcellular polymers, Polymer Engineering & Science, 35(5), 1995, pp. 432-440.

[77] T. Garbacz, L. Dulebova, Porophors used in the extrusion process, Chemistry & Chemical Technology, 7(1), 2013, pp. 113-118.

[78] J.R. Wagner, E.M. Mount, H.F. Giles, Foam Extrusion, in: Extrusion, William Andrew Publishing, Chapter 53, second edition, 2014, pp. 603-607.

[79] J.A.R. Ruiz, M. Vincent, J-F. Agassant, T. Sadik, C. Pillon, C. Carrot, Polymer foaming with Chemical Blowing Agents: Experiment and modeling, Polymer Engineering and Science, 55(9), 2015, pp. 2018-2029.

[80] D. Eaves, Handbook of Polymer Foams, Rapra Technology Limited, 2004, pp. 1-277.

[81] T. Garbacz, T. Jachowicz, I. Gajdoš, G. Kijewski, Research on the influence of blowing agent on selected properties of extruded cellular products, Advances in Science and Technology Research Journal, 9(28), 2015, pp. 81-88.

[82] A.K. Bledzki, O. Faruk, Effects of the chemical foaming agents, injection parameters, and melt-flow index on the microstructure and mechanical properties of microcellular injection-molded wood-fiber/polypropylene composites, Journal of Applied Polymer Science, 97(3), 2005, pp. 1090-1096.

[83] T. Sadik, C. Pillon, C. Carrot, J. Reglero Ruiz, DSC studies on non-isothermal and isothermal decomposition of chemical blowing agents based on citric acid and sodium bicarbonate, Thermochimica Acta, 659, 2017, pp. 74-81.

[84] Á. Kmetty, K. Litauszki, D. Réti, Characterization of Different Chemical Blowing Agents and Their Applicability to Produce Poly(Lactic Acid) Foams by Extrusion, Applied Sciences, 8, 2018, pp. 1960-1977.

[85] C. Okolieocha, D. Raps, K. Subramaniam, V. Altstädt, Microcellular to nanocellular polymer foams: Progress (2004–2015) and future directions – A review, European Polymer Journal, 73, 2015, pp. 500-519.

[86] M. Rohleder, F. Jakob, Foam Injection Molding, in: Specialized Injection Molding Techniques, William Andrew Publishing, Chapter 2, 2016, pp. 53-106.

[87] Y. Sato, K. Fujiwara, T. Takikawa, Sumarno, S. Takishima, H. Masuoka, Solubilities and diffusion coefficients of carbon dioxide and nitrogen in polypropylene, high-density polyethylene, and polystyrene under high pressures and temperatures, Fluid Phase Equilibria, 162(1), 1999, pp. 261-276.

[88] P. Rachtanapun, S. M. Selke, Strategy to Produce High-Void Fraction in Microcellular Foamed Polyolefins, CMU Journal, 5(1), 2006, pp. 15-31.

[89] I. Ghasemi, A. T. Farsheh, Z. Masoomi, Effects of multi-walled carbon nanotube functionalization on the morphological and mechanical properties of nanocomposite foams based on poly(vinyl chloride)/(wood flour)/ (multi-walled carbon nanotubes), Journal of Vinyl and Additive Technology, 18(3), 2012, pp. 161-167.

[90] A.I. Cooper, Porous Materials and Supercritical Fluids, Advanced Materials, 15(13), 2003, pp. 1049-1059.

[91] S.P. Nalawade, F. Picchioni, L.P.B.M. Janssen, Supercritical carbon dioxide as a green solvent for processing polymer melts: Processing aspects and applications, Progress in Polymer Science, 31(1), 2006, pp. 19-43.

[92] D.F. Baldwin, C.B. Park, N.P. Suh, A microcellular processing study of poly(ethylene terephthalate) in the amorphous and semicrystalline states. Part II: Cell growth and process design, Polymer Engineering & Science, 36(11), 1996, pp. 1446-1453.

[93] V.I. Kalikmanov, Classical Nucleation Theory, in: Nucleation Theory, Springer, Volume 860, Chapter 3, 2013, pp. 17-41.

[94] C. Lee, B. Kent, S. Rich, W. Xiang, Effect of Filler Size on Cell Nucleation during Foaming Process, Journal of Cellular Plastics, 38(2), 2002, pp. 139-148.

[95] N.H. Fletcher, Size Effect in Heterogeneous Nucleation, The Journal of Chemical Physics, 29(3), 1958, pp. 572-576.

[96] N.S. Ramesh, I.A. Kweeder, D.H. Rasmussen, G.A.Campbell, An Experimental Study on the Nucleation of Microcellular Foams in High Impact Polystyrene, Society of Plastics Engineers Technical Papers, 38, 1992, pp. 1078-1081.

[97] X. Dai, Z. Liu, Y. Wang, G. Yang, J. Xu, B. Han, High damping property of microcellular polymer prepared by friendly environmental approach, The Journal of Supercritical Fluids, 33(3), 2005, pp. 259-267.

[98] K.S.W. Sing, D.H. Everett, R.A.W. Haul, L. Moscou, R.A. Pierotti, J. Rouquerol, T. Siemieniewska, Reporting Physisorption Data for Gas/Solid Systems with Special Reference to the Determination of Surface Area and Porosity, Pure and Applied Chemistry, 57(4), 1985, pp. 603-619.

[99] R. Dawson, A.I. Cooper, D.J. Adams, Nanoporous organic polymer networks, Progress in Polymer Science, 37, 2012, pp. 530–563.

[100] C. C. Ibeh, M. Bubacz, Current Trends in Nanocomposite Foams, Journal of Cellular Plastics, 44(6), 2008, pp. 493-515.

[101] W. Zhai, J. Yu, L. Wu, W. Ma, J. He, Heterogeneous nucleation uniformizing cell size distribution in microcellular nanocomposites foams, Polymer, 47(21), 2006, pp. 7580-7589.

[102] P. Rachtanapun, S.E.M. Selke, Strategy to Produce High-void Fraction in Microcellular Foamed Polyolefin, CMU Journal, 5(1), 2006, pp. 15-31.

[103] S. Doroudiani, C.B. Park, M.T. Kortschot, Effect of the crystallinity and morphology on the microcellular foam structure of semicrystalline polymers, Polymer Engineering & Science, 36(21), 1996, pp. 2645-2662.

[104] F. Saint-Michel, L. Chazeau, J-Y. Cavaille´, E. Chabert, Mechanical properties of high density polyurethane foams: I. Effect of the density, Composites Science and Technology, 66(15), 2006, pp. 2700-2708.

[105] D.I. Collias, D.G. Baird, R.J.M. Borggreve, Impact toughening of polycarbonate by microcellular foaming, Polymer, 35(18), 1994, pp. 3978-3983.

[106] A.M. Kraynik, W.E. Warren, The elastic behavior of low-density cellular plastics, in: Low Density Cellular Plastics: Physical Basis of Behavior, Chapman & Hall, Chapter 7, 1994, pp. 217.

[107] B.E. Obi, Foaming Processes, in: Polymeric Foams Structure-Property-Performance, William Andrew Publications, Elsevier, Chapter 6, 2018, pp. 131-188.

[108] E. Bociąga, P. Palutkiewicz, The influence of injection molding parameters and blowing agent addition on selected properties, surface state, and structure of HDPE parts, Polymer Engineering & Science, 53(4), 2013, pp. 780-791.

[109] A. Oprea-Kiss, I. Kiss, About the numerous cost and processing advantages of the microcellular foam injection molding process for thermoplastics materials in the automobile industry, Analecta, 9(2), 2015, pp. 6-14.

[110] K. Jacobsen, D. Pierick, Microcellular foam molding: advantages and application examples, SPE-ANTEC, 2001, pp. 449-453.

[111] J.E. Martini-Vvedensky, N.P. Suh, F.A. Waldman, Microcellular closed cell foams and their method of manufacture, U.S. Patent Documents, Massachusetts Institute of Technology, Cambridge, Mass, 1984, application no. 403,831.

[112] Trexel Inc., MuCell Molding Technology. https://www.trexel.com/en/(Accessed 31/01/2021).

[113] J. Xu, Morphology for microcellular injection molding, Society of Plastics Engineers, 2009, pp. 1-2.

[114] C.B. Park, A.H. Behravesh, R.D Venter, Low density microcellular foam processing in extrusion using CO2, Polymer Engineering & Science, 38(11), 1998, pp. 1812-1823.

[115] M. Shimbo, D.F. Baldwin, N.P. Suh, Viscoelastic behavior of microcellular plastics, Polymeric Materials: Science and Engineering, American Chemical Society Conference, 67, 1992, pp. 512-513.

[116] L.M. Matuana, C.B. Park, J.J. Balatinecz, Processing and cell morphology relationships for microcellular foamed PVC/wood-fiber composites, Polymer Engineering & Science, 37(7), 1997, pp. 1137-1147.

[117] S. Doroudiani, C.B. Park, M.T. Kortschot, Processing and characterization of microcellular foamed high-density polythylene/isotactic polypropylene blends, Polymer Engineering & Science, 38(7), 1998, pp. 1205-1215.

[118] L. Matuana, F. Mengeloglu, Microcellular foaming of impact-modified rigid PVC/wood-flour composites, Journal of Vinyl and Additive Technology, 7(2), 2001, pp. 67-75.

[119] D.F. Baldwin, Microcellular polymer processing and the design of a continuous sheet processing system, Doctoral Thesis, Department of Mechanical Engineering, Massachusetts Institute of Technology, 1994, pp. 1-267.

[120] V. Kumar, D.S. Gebizlioglu, Carbon Dioxide-Induced Crystallization in PET Foams, Society of Plastics Engineers Technical Papers, 37, 1991, pp. 1297-1299.

[121] A.S. Michaels, H.J. Bixler, Flow of gases through polyethylene, Journal of Polymer Science, 50(154), 1961, pp. 413-439.

[122] H. Sha, I.R. Harrison, CO2 permeability and amorphous fractional free-volume in uniaxially drawn HDPE, Journal of Polymer Science Part B: Polymer Physics, 30(8), 1992, pp. 915-922.

[123] J.S. Colton, The Nucleation of Microcellular Foams in Semi-Crystalline Thermoplastics, Materials and Manufacturing Processes, 4(2), 1989, pp. 253-262.

[124] J.C. Salamone, Polymeric materials encyclopedia, Boca Raton: CRC Press, 1996.

[125] B. Wunderlich, Macromolecular Physics, in: Crystal Nucleation, Growth, Annealing, Volume 2, Academic Press New York, 1976, pp. 1-476.

[126] M.M. Khorasani, S.R. Ghaffarian, S.H. Goldansaz, N. Mohammadi, A. Babaie, Solid-state microcellular foaming of PE/PE composite systems, investigation on cellular structure and crystalline morphology, Composites Science and Technology, 70(13), 2010, pp. 1942-1949.

[127] J. Xu, Microcellular injection molding, John Wiley & Sons, Inc., 2010, pp. 1-618.

[128] M. Nofar, C.B. Park, Introduction to Plastic Foams and Their Foaming, in: Polylactide Foams, William Andrew Publishing, Chapter 1, 2018, pp. 1-16.

[129] M.C. Saha, M.E. Kabir, S. Jeelani, Enhancement in thermal and mechanical properties of polyurethane foam infused with nanoparticles, Materials Science and Engineering: A, 479(1), 2008, pp. 213-222.

[130] D-X. Yan, K. Dai, Z-D. Xiang, Z-M. Li, X. Ji, W-Q. Zhang, Electrical conductivity and major mechanical and thermal properties of carbon nanotube-filled polyurethane foams, Journal of Applied Polymer Science, 120(5), 2011, pp. 3014-3019.

[131] M.M.A. Nikje, Z.M. Tehrani, Thermal and mechanical properties of polyurethane rigid foam/modified nanosilica composite, Polymer Engineering & Science, 50(3), 2010, pp. 468-473.

[132] R. Verdejo, C. Saiz-Arroyo, J. Carretero-Gonzalez, F. Barroso-Bujans, M.A. Rodriguez-Perez, M.A. Lopez-Manchado, Physical properties of silicone foams filled with carbon nanotubes and functionalized graphene sheets, European Polymer Journal, 44(9), 2008, pp. 2790-2797.

[133] M. Yuan, A. Winardi, S. Gong, L.-S. Turng, Effects of nano- and micro-fillers and processing parameters on injection-molded microcellular composites, Polymer Engineering & Science, 45(6), 2005, pp. 773-788.

[134] R.B. McClurg, Design criteria for ideal foam nucleating agents, Chemical Engineering Science, 59(24), 2004, pp. 5779-5786.

[135] K. Goren, L. Chen, L.S. Schadler, R. Ozisik, Influence of nanoparticle surface chemistry and size on supercritical carbon dioxide processed nanocomposite foam morphology, Journal of Supercritical Fluids, 51(3), 2010, pp. 420-427.

[136] S. Liu, Designer nanoparticles as efficient nucleation agents in polymer foaming, Doctoral Thesis, Institute for Nanotechnology of the University of Twente, University of Twente, Netherlands, 2017, pp. 1-174.

[137] L. Chen, L. S. Schadler, R. Ozisik, An experimental and theoretical investigation of the compressive properties of multi-walled carbon nanotube/poly(methyl methacrylate) nanocomposite foams, Polymer, 52(13), 2011, pp. 2899-2909.

[138] L.J. Gibson, M.F. Ashby, Cellular Solids: Structure and Properties, Cambridge University Press, 1999, pp.1-532.

[139] S.G. Mosanenzadeh, H.E. Naguib, C.B. Park, N. Atalla, Development, characterization, and modeling of environmentally friendly open-cell acoustic foams, Polymer Engineering & Science, 53(9), 2013, pp. 1979-1989.

[140] R. Verdejo, R. Stämpfli, M. Alvarez-Lainez, S. Mourad, M.A. Rodriguez-Perez, P.A. Brühwiler, M. Shaffer, Enhanced acoustic damping in flexible polyurethane foams filled with carbon nanotubes, Composites Science and Technology, 69(10), 2009, pp. 1564-1569.

[141] W.A. Orfali, Acoustic Properties of Polyurethane Composition Reinforced with Carbon Nanotubes and Silicon Oxide Nano-powder, Physics Procedia, 70(Supplement C), 2015, pp. 699-702.

[142] L.M. Chen, R. Ozisik, L.S. Schadler, The influence of carbon nanotube aspect ratio on the foam morphology of MWNT/PMMA nanocomposite foams, Polymer, 51(11), 2010, pp. 2368-2375.

[143] W. Chen, T. Xiaoming, L. Yuyang, Carbon nanotube-reinforced polyurethane composite fibers, Composites Science and Technology, 66(15), 2006, pp. 3029-3034.

[144] S. Liu, Designer nanoparticles as efficient nucleation agents in polymer foaming, Institute for Nanotechnology of the University of Twente, University of Twente, Netherlands, 2017.

[145] L. Chen, L. S. Schadler, R. Ozisik, An experimental and theoretical investigation of the compressive properties of multi-walled carbon nanotube/poly(methyl methacrylate) nanocomposite foams, Polymer, 52(13), 2011, pp. 2899-2909.

[146] X. Han, C. Zeng, L.J. Lee, K.W. Koelling, D.L. Tomasko, Extrusion of polystyrene nanocomposite foams with supercritical CO_2, Polymer Engineering & Science, 43(6), 2003, pp. 1261-1275.

[147] R. Nobe, J. Qiu, M. Kudo, K. Ito, M. Kaneko, Effects of SCF content, injection speed, and CF content on the morphology and tensile properties of microcellular injection-molded CF/PP composites, Polymer Engineering & Science, 59(7), 2019, pp. 1371-1380.

[148] L. Hoang, M. Aghelinejad, S. Leung, Z.H. Zhu, High Density Polyethylene/Carbon Nanotube Nanocomposite Foams: Electrical Conductivity And Percolation Threshold, CSME International

Congress 2018, Proceedings of The Canadian Society for Mechanical Engineering International Congress 2018, Toronto, Canada, 2018, pp. 1-5.

[149] M. Aghelinejad, S.N. Leung, Enhancement of thermoelectric conversion efficiency of polymer/carbon nanotube nanocomposites through foaming-induced microstructuring, Journal of Applied Polymer Science, 134(28), 2017, pp. 45073_1-10.

[150] M. Antunes, J.I. Velasco, Multifunctional polymer foams with carbon nanoparticles, Progress in Polymer Science, 39(3), 2014, pp. 486-509.

[151] M. Panahi-Sarmad, M. Noroozi, M. Abrisham, S. Eghbalinia, F. Teimoury, A.R. Bahramian, P. Dehghan, M. Sadri, V. Goodarzi, A Comprehensive Review on Carbon-Based Polymer Nanocomposite Foams as Electromagnetic Interference Shields and Piezoresistive Sensors, ACS Applied Electronic Materials, 2(8), 2020, pp. 2318-2350.

[152] L. Xu, L-C. Jia, D-X. Yan, P-G. Ren, J-Z. Xu, Z-M. Li, Efficient electromagnetic interference shielding of lightweight carbon nanotube/polyethylene composites via compression molding plus salt-leaching, RSC Advances, 8(16), 2018, pp. 8849-8855.

[153] K. Taki, K. Tabata, S-i. Kihara, M. Ohshima, Bubble coalescence in foaming process of polymers, Polymer Engineering & Science, 46(5), 2006, pp. 680-690.

CHAPTER 3: MATERIALS AND METHODS

3.1 Materials

➢ **HDPE** → High-density polyethylene resin (HDPE), grade HMA 025, with a melting point of 135 °C, density of 0.964 g cm^{-3} and a melt flow index (MFI) of 8 g/10 min at 190 °C/2.16 kg was purchased from ExxonMobil in pellet form.

➢ **MWCNTs** → Non-functionalised commercially available thin multi-walled carbon nanotubes (MWCNTs) produced by catalytic carbon vapour deposition (CCVD), with an average diameter of 9.5 nm and average length of 1.5 μm (grade NC7000, purity: > 90%) were purchased from Nanocyl S.A., Belgium and used as received. The density of the MWCNTs was reported as 1.75 g cm^{-3} [1], with a surface area of between 250 and 300 m^2/g [2]. The average aspect ratio (length/diameter ratio) of 157 allows these MWCNT to be considered relatively short CNTs.

➢ **CBAs** → Two types of Chemical Blowing Agents (CBAs), which decompose endothermically were used to modify the polymer to generate a foam structure via chemical foaming. Specifically, Hydrocerol Compound (product code: *OXABRG20930*) and Hydrocerol CF (product code: *OXABRB20930*), referred in this thesis as CBA$_1$ and CBA$_2$, respectively, were both purchased from Clariant as pure CBAs in the physical form of white powders and were used as received. Both Hydrocerol(s) are CO_2 based and very similar to each other. The only difference is the particle size of the powder, a variable thought to effect the extent of CBA dispersion in polymers. In particular, CBA$_2$ was ground to have a finer particle size, which eventually provides foams of smaller cell sizes than those with CBA$_1$. The technical product information sheets report a density of approx. 1.7 g cm^{-3}, an activation temperature of 160 °C and a thermal gas yield in the range of 140 cm^3/g gas for both CBAs. A third type of Hydrocerol (trade name ITP 815), also characterised by an activation temperature of 160 °C and endothermic-type decomposition, was used in conjunction with the PBA, SCF-CO_2, to assist physical foaming of unfilled HDPE and HDPE-MWCNT composite parts. It is referred in this thesis to as CBA$_3$.

➢ **SCF-CO_2** → Supercritical carbon dioxide (SCF-CO_2) was employed during the use of MuCell technology for physical foaming in injection moulding. The use of CO_2 in an super-critical state (i.e. conditions of both pressure and temperature above the critical values of 73.84 bar and 31 °C [3]) allows for the special combination of gas-like viscosity and liquid-like density of a supercritical fluid.

➢ **Benchmark Materials:** Three different materials were used as benchmarks in this project, as they are already in commercial use as matching layers for acoustic transducers. Specifically, *syntactic foams* made of epoxy resin (RX771C, from ROBNOR RESINS) and glass micro-balloons (from 3M Microspheres) are the materials currently employed inside the *Elster New Generation*

Ultrasonic Transducers construct. Furthermore, two commercial matching layers based on silicon composites and here referred to as *Commercial ML* and *ML-Trelleborg*, were provided by the industrial sponsor (Honeywell) with no further information provided due to sensitive company data.

3.2 Processing Methods

A typical (nano)composite preparation procedure is given in the schematic shown in Figure 3.1. This general approach was followed for the preparation and realisation of both solid-state and expanded (foamed) samples using the CBAs, neat HDPE and the HDPE-MWCNT composites, further detail is given in sections 3.2.1 and 3.2.3, respectively.
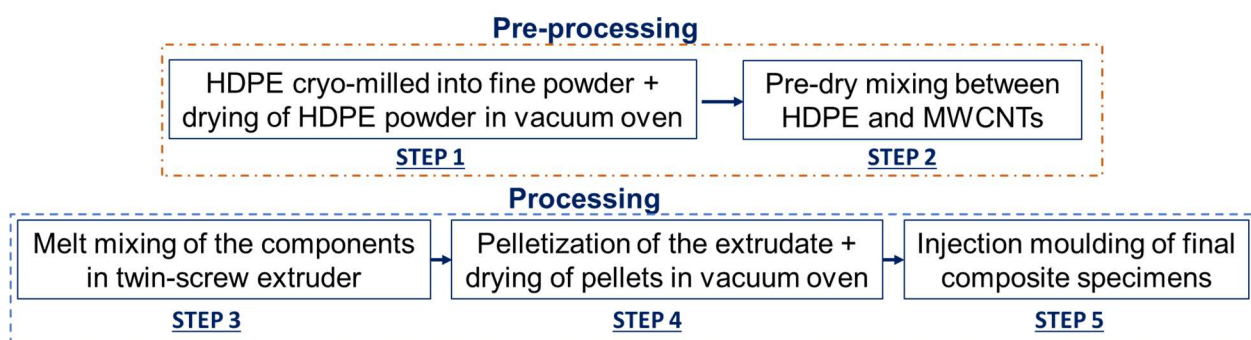
Figure 3.1. Schematic representation of the typical protocol followed for the preparation of composites.

A 16 mm co-rotating parallel twin-screw extruder, PRISM ThermoFischer Scientific, and a micro-injection moulding, Thermo-Scientific Haake™ MiniJet Proto, were the main processing equipment used in this project to carry out steps 3 and 5, respectively.
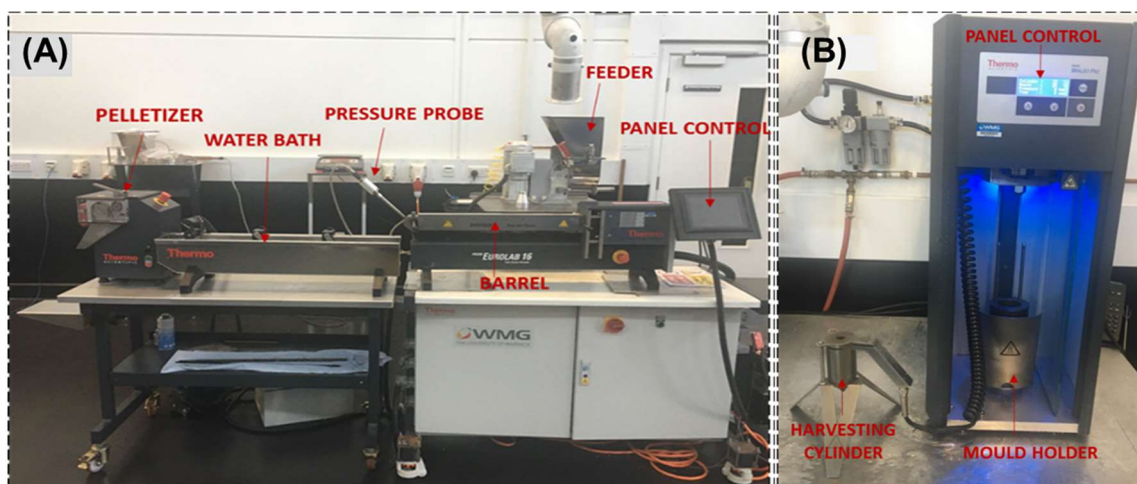
Figure 3.2. Photographs of the main processing equipment used in this project: (A) PRISM Thermo-Fischer Scientific 16 mm co-rotating parallel twin screws extruder and (B) Thermo-Scientific Haake™ MiniJet Proto injection moulding machine.

3.2.1 PART I: Non-foamed Composites of HDPE-MWCNT

STEP 1. HDPE pellets were first ground to a fine powder, using a SPEX® SamplePrep Freezer Mill 6870 (Stanmore, UK) and dried in a vacuum oven at 40 °C for 12 h prior to processing to improve

dry mixing between the polymer matrix and the filler. No HDPE degradation was observed, when examined by FTIR spectroscopy, as a consequence of the grinding process.

STEP 2. Composites were prepared by dry blending HDPE and MWCNTs both in powder form, with MWCNT loadings specified in both percentages by weight and by volume in Table 3.1. The volume fraction of filler was calculated considering a void free structure, using the density values of 0.964 g cm^{-3} and 1.75 g cm^{-3}, relative to HDPE and MWCNT, respectively.

Table 3.1. Loadings of MWCNTs used for HDPE-MWCNT composites.

MWCNT loading /wt%	MWCNT loading /vol%	Sample Acronym
0	0	HDPE
0.01	0.01	HDPE+0.01wt%MWCNT$_S$
0.1	0.06	HDPE+0.1wt%MWCNT$_S$
0.3	0.17	HDPE+0.3wt%MWCNT$_S$
0.5	0.28	HDPE+0.5wt%MWCNT$_S$
1	0.55	HDPE+1wt%MWCNT$_S$
3	1.68	HDPE+3wt%MWCNT$_S$
5	2.82	HDPE+5wt%MWCNT$_S$

STEP 3. MWCNTs were added to the HDPE matrix using a 16 mm twin-screw extruder shown in Figure 3.2(A), with a screw speed of 100 rpm and the following operational temperature profile set along the barrel during the entire extrusion process.

Die	Zone 10	Zone 9	Zone 8	Zone 7	Zone 6	Zone 5	Zone 4	Zone 3	Zone 2
155˚C	155˚C	150˚C	150˚C	150˚C	140˚C	140˚C	140˚C	135˚C	135˚C

Such a temperature profile guaranteed a gradual and uniform melting of the components within the system. Neat HDPE was subjected to the same processing conditions as the composite samples, as a control sample.

STEP 4. The molten extrudate exiting the extruder die in the form of a filament was cooled in a water bath and pelletised immediately after using a laboratory pelletizer. The pellets were then dried (~8 h) at 80℃ prior to injection moulding.

STEP 5. Pellets were injection-moulded using the piston injection moulding system shown in Figure 3.2(B), to produce standard dumbbell-shaped tensile bars conforming to ASTM D638 V, circular disks of 25 mm diameter × 1.65 mm thickness for oscillatory rheology and acoustic measurements,

and 80 mm × 10 mm × 4 mm rectangular bars for DMTA measurements. Specimens of neat polymer and the composites for further testing were prepared at appropriate machine setting conditions of injection temperature, $T_{cylinder}$ (i.e. temperature in the harvesting cylinder); injection pressure, P_1; time of injection, t_1; mould temperature, T_{mould}; post-pressure of injection, P_2 (i.e. holding pressure of injection); time of post-injection, t_2 (i.e. holding pressure time); and pressure drop, ΔP, see Table 3.2.

Table 3.2. Parameters set for micro injection moulding machine for the production of composite samples.

$T_{cylinder}$/ °C	T_{mould}/ °C	P_1/bar	t_1/sec	P_2/bar	t_2/sec	ΔP/bar
160	50	450	10	250	5	200

3.2.2 PART II-A: Foams of HDPE via Chemical Foaming

Two conventional polymer processing techniques, extrusion and injection moulding (IM) were combined with the aim of obtaining a uniform distribution of the CBA throughout the polymer matrix during extrusion prior to production of a cellular structure in a further IM step. The mixture of HDPE and CBA was processed in the plasticizing system (twin-screw extruder), and then shaped in the micro-IM machine where eventually foaming occurred and/or was completed. The extrusion process is still conventional and not a cellular extrusion process. The limitations of the equipment did not allow for the measure and adjustment of torque, screw speed, and pressure distribution in the different heating zones and plasticizing extrusion head during extrusion.

STEP 1. In order to improve dry mixing between the polymer matrix and the CBA powders, HDPE pellets were first ground to a fine powder prior to processing (see step 1 above, section 3.2.1).

STEP 2. Blends were prepared by dry mixing each blowing agent and the HDPE powder. The CBA loadings introduced during mixing are specified in Table 3.3.

Table 3.3. Loadings of CBAs used in this project for chemical foaming trials of HDPE.

CBA loading /wt%	Sample Acronym with **CBA₁**	with **CBA₂**
0.1	HDPE+0.1wt%CBA_1	HDPE+0.1wt%CBA_2
0.2	HDPE+0.2wt% CBA_1	HDPE+0.2wt% CBA_2
0.3	HDPE+0.3wt% CBA_1	HDPE+0.3wt% CBA_2
0.4	HDPE+0.4wt% CBA_1	HDPE+0.4wt% CBA_2
0.5	HDPE+0.5wt% CBA_1	HDPE+0.5wt% CBA_2
1	HDPE+1wt% CBA_1	HDPE+1wt% CBA_2
4	HDPE+4wt% CBA_1	HDPE+4wt% CBA_2
5	HDPE+5wt% CBA_1	HDPE+5wt% CBA_2

STEP 3. The CBAs were incorporated into the HDPE matrix using a 16 mm twin-screw extruder, with a fixed screw speed of 80 rpm and various operational temperature profiles along the extruder barrel. Five different temperature profiles were carefully selected [a] to investigate the effect of temperature on foaming. The five temperature profiles adopted are as follows:

(**Profile 1**):

Die	Zone 10	Zone 9	Zone 8	Zone 7	Zone 6	Zone 5	Zone 4	Zone 3	Zone 2
165˚C	165˚C	165˚C	165˚C	165˚C	165˚C	165˚C	165˚C	165˚C	165˚C

(**Profile 2**):

Die	Zone 10	Zone 9	Zone 8	Zone 7	Zone 6	Zone 5	Zone 4	Zone 3	Zone 2
175˚C	170˚C	170˚C	168˚C	168˚C	165˚C	165˚C	165˚C	160˚C	160˚C

(**Profile 3**):

Die	Zone 10	Zone 9	Zone 8	Zone 7	Zone 6	Zone 5	Zone 4	Zone 3	Zone 2
140˚C	140˚C	150˚C	180˚C	180˚C	175˚C	160˚C	150˚C	145˚C	140˚C

(**Profile 4**):

Die	Zone 10	Zone 9	Zone 8	Zone 7	Zone 6	Zone 5	Zone 4	Zone 3	Zone 2
155˚C	155˚C	155˚C	155˚C	155˚C	155˚C	155˚C	155˚C	155˚C	155˚C

(**Profile 5**):

Die	Zone 10	Zone 9	Zone 8	Zone 7	Zone 6	Zone 5	Zone 4	Zone 3	Zone 2
160˚C	160˚C	160˚C	160˚C	160˚C	160˚C	160˚C	160˚C	160˚C	160˚C

In all the selected profiles the processing temperature was always set above the polymer melting point (135 °C) to both promote gas saturation and allow microcellular foam nucleation to occur [b].

STEP 4. The molten extrudate exiting the extruder die in the form of a filament (i.e. nucleated extrudate) was quenched in a water bath and stabilized to retain the cell density obtained and pelletised immediately after, using a laboratory pelletizer. The pellets were then dried (~8 h) prior to injection moulding.

STEP 5. Pellets of the modified polymer were subsequently processed using the piston IM system to produce foamed parts in the shape of circular disks of 25 mm diameter × 1.65 mm thickness (or alternately larger circular disks of 35 mm diameter × 5 mm thickness as discussed in section 3.1.3 of Submission Portfolio No.5) used as specimens for further testing.

The different process design strategies derived from this study assume independent control, or at least a relative dependence, of the major process functions (i.e. solution formation, cell nucleation,

---

[a] These temperature profiles were extracted from information derived from studies found in literature supported by the Hydrocerol technical datasheets, i.e. CBA_1 and CBA_2 grades. Temperatures similar to those commonly applied in foam extrusion or foam injection moulding have been reproduced, ideally driving the decomposition reaction to take place in the barrel or entirely in the mould cavity of the injection moulding machine. Details with regard the adoption of these specific processing conditions can be found in the Submission Portfolio No.5 (sections 3.1.1 and 3.1.2).

[b] In HDPE the low gas solubility and the physical constraints imposed by the crystallites below the melting point impede microcellular foam nucleation to occur [4].

and cell growth) from the process variables (i.e. saturation time, saturation pressure, foaming time, and foaming temperature).

In order to optimise the conditions applied during the IM step, nine methods were developed and are here summarised in Table 3.4. The assigned nomenclature for each method corresponds to a different combination of machine parameters.

Table 3.4. Parameter settings employed for the production of HDPE foams during IM trials.

Injection Moulding Method	$T_{cylinder}/\,^\circ C$	$T_{mould}/\,^\circ C$	P_1/bar	t_1/sec	P_2/bar	t_2/sec	$\Delta P/bar$
1	165	60	450	10	250	5	200
2	170	60	600	6	250	5	350
3	170	70	450	6	250	5	200
4	170	75	600	6	200	10	400
5	170	80	600	6	250	5	350
6	170	75	600	6	450	10	150
7	180	110	800	1	300	5	550
8	180	180	150	1	0	7	150
9	185	185	150	1	0	7	150

Among the nine methods listed in Table 3.4, Methods 8 and 9 differ from the other methods in that they are characterised by isothermal processes performed by rapid cooling/quenching of the hot mould (containing the molten sample) in a cold water bath. The rapid quenching of the material contained within the mould in cold water allowed the foamed sample to be rapidly cooled and stabilize much quicker than if the cooling was done by the machine, while addressing the issue of high polymer crystallinity. This procedure helped to prevent gas loss from the bubbles and thus the shrinkage and also collapse of the bubbles as well as the formation of a temperature gradient distribution from the wall to the core of the mould since cooling occurred uniformly.

3.2.3 PART II-B: Foams of HDPE-MWCNT Composites via Chemical Foaming

STEP 1. In order to improve dry mixing between the polymer matrix, the filler and the CBA powders, HDPE pellets were first ground to a fine powder prior to processing (see step 1 above, section 3.2.1).

STEP 2. Dry blends of the components were prepared by dry blending each CBA with HDPE and MWCNTs (all in powder form). The loadings of MWCNTs and CBAs introduced during the mixing process are specified in Table 3.5.

Table 3.5. Loadings of CBA and MWCNTs used in this project for chemical foaming trials of composites.

MWCNT loading /wt%	CBA loading /wt%	Sample Acronym (*) (Example with CBA$_1$)
0 (Unfilled HDPE)	1; 4	HDPE+1wt%CBA_1 HDPE+4wt%CBA_1
0.01	1; 4	HDPE+0.01wt%MWCNT+1wt%CBA_1 HDPE+0.01wt%MWCNT+4wt%CBA_1
0.1	1; 4	HDPE+0.1wt%MWCNT+1wt%CBA_1 HDPE+ 0.1wt%MWCNT+4wt%CBA_1
0.3	1; 4	HDPE+0.3wt%MWCNT+1wt%CBA_1 HDPE+0.3wt%MWCNT+4wt%CBA_1
0.5	1; 4	HDPE+0.5wt%MWCNT+1wt%CBA_1 HDPE+0.5wt%MWCNT+4wt%CBA_1
1	1; 4	HDPE+0.1wt%MWCNT+1wt%CBA_1 HDPE+0.1wt%MWCNT+4wt%CBA_1
3	1; 4	HDPE+3wt%MWCNT+1wt%CBA_1 HDPE+3wt%MWCNT+4wt%CBA_1
5	1; 4	HDPE+5wt%MWCNT+1wt%CBA_1 HDPE+5wt%MWCNT+4wt%CBA_1

(*) Although the column with the acronyms listed for the samples with CBA$_2$ is not shown in Table 3.5, the nomenclature followed for each sample is the same as indicated in the table except for the final part in subscript where CBA$_2$ replaces CBA$_1$.

<u>*STEP 3*</u>. CBA and MWCNTs were incorporated into the HDPE matrix using the 16 mm twin-screw extruder, with a fixed screw speed of 80 rpm (sufficiently high to ensure gas absorption) and *Profile 1*.

<u>*STEP 4*</u>. Same pelletizing step as *STEP 4* in section 3.2.2.

<u>*STEP 5*</u>. The pellets were subsequently processed using the piston IM system to produce foamed parts in the shape of circular disks of 25 mm diameter × 1.65 mm thickness used as specimens for further testing. Various processing conditions were investigated during the IM experiments by systematically changing one parameter at a time on the machine settings after processing a new batch of material (i.e. same pellets produced simultaneously by the molten extrudate at the same temperature conditions, MWCNT and CBA loading. In particular, the parameter settings of *Methods 1*, *2*, *4*, *6*, *8* and *9*, defined in Table 3.4., were investigated during the IM trials for the production of composite foams.

3.2.4. PART III: Foams of HDPE-MWCNT Composites via Physical Foaming

The step-by-step approach of the preparation procedure described in Figure 3.1 was altered.

STEP 1. Composites were prepared by dry blending HDPE and MWCNTs both in powder form, with MWCNT loadings of 0.1 wt%, 0.5 wt%, and 1 wt%.

STEP 2. MWCNT were melt mixed into the HDPE matrix, this time using a 24 mm co-rotating parallel twin-screw extruder, Thermo-Fischer Scientific, with a L/D ratio of 40.

The conditions applied during compounding for the composites were similar to those commonly applied in the industry for high volume production of plastics. A screw speed of 750 rpm was set during the entire extrusion process with an operating temperature profile along the barrel as follows:

Die	Zone 10	Zone 9	Zone 8	Zone 7	Zone 6	Zone 5	Zone 4	Zone 3	Zone 2
220˚C	220˚C	220˚C	220˚C	220˚C	220˚C	220˚C	220˚C	180˚C	100˚C

STEP 4. The molten extrudate exiting the extruder die in the form of a filament was cooled in a water bath and pelletised. The pellets were then dried (~8 h) at 80℃ prior to being processed at IKV, Aachen.

STEP 5. The pellets were subsequently processed using physical blowing process during injection moulding.

The trials were conducted on an Arburg Alldrive 520A-400, equipped with a MuCell aggregate (located in the Institute of Plastics Processing (IKV), at RWTH Aachen University, Germany). The MuCell aggregate, with its SCF delivery system, enables the dosage of a precise amount of SCF-CO_2 gas each moulding cycle directly into the polymer melt in the plasticizing unit of the injection moulding machine. A schematic representation of the apparatus is shown in Figure 3.3.
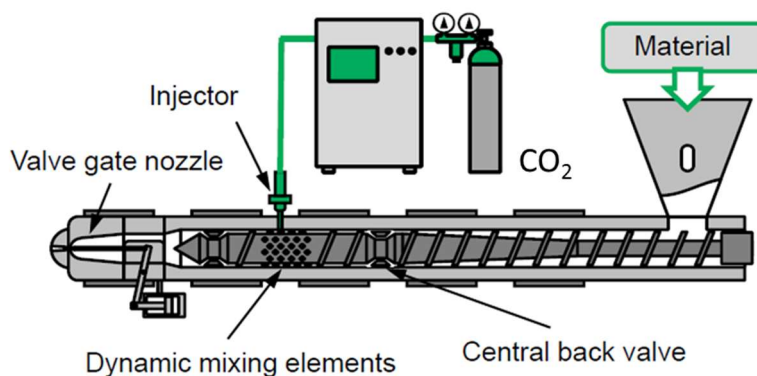
Figure 3.3. Schematic representation of the injector based foam injection moulding, MuCell, used in the trials for physical foaming HDPE and HDPE-MWCNT composites.

The pellets were fed through a hopper into a heated barrel with a reciprocating (bespoke) screw geometry used to achieve better mixing of the physical blowing agent (PBA). In particular, a 40 mm diameter screw (with screw/length ratio = 24) was used to plasticate the compound in the plasticization zone. The operating temperature profile along the barrel of the plasticizer aggregate is shown as follows:

Heating Zones	Zone 1	Zone 2	Zone 3	Zone 4	Zone 5	Zone 6	Zone 7
	200˚C	200˚C	190˚C	185˚C	180˚C	170˚C	30˚C

Plate specimens were injection moulded from pellets of HDPE and HDPE-MWCNT composites, enabling the production of foamed parts characterised by a foamed core and a compact surface layer (i.e. skin layer). The bespoke mould with steps in plate thickness employed in the trials has a plate geometry of 90 x 140 x 3mm³, characterised by two different thicknesses (2 and 3 mm) and is shown in Figure 3.4. This mould allowed for the production of multilayer plaques, which translates in two areas with different values of thicknesses and thus densities.
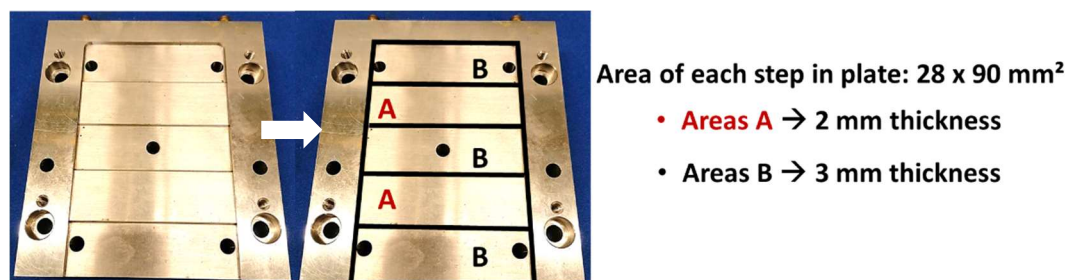
Figure 3.4. Photograph of the mould surface with steps in plate thickness used in the MuCell trials.

Compared to conventional moulds, this type of tool with a decompression opening offers essential advantages for achieving greater weight reduction and a reduced density gradient in the direction of flow, creating the high pressure drop rate needed for a fine-pored structure.

Two approaches to moulding these materials was adopted, namely under-volumetric and negative compression moulding. Differences in density along the flow path as well as in internal structure and surface qualities of the final microcellular injection moulded parts are expected when filling the mould cavity sub-volumetrically or volumetrically in negative compression, varying the dosing volume. Foamed parts made using the latter process can be manufactured with a significant reduction in density and are generally characterised by an even density gradient across the flow path. In under-volumetric moulding, the entire volume of the mould cavity is not filled during the injection of the material so that the expanded part can occupy the free volume available in the mould tool. Conversely, precision mould opening moulds, also referred to as negative compression moulding, core back expansion or breathing tools, are first volumetrically filled with the SCF loaded melt solution and maintained under pressure (i.e. holding pressure) before initiate an enlargement of the cavity volume after a predefined delay time [3]. Once the delay time (i.e. holding time) has passed, the cavity space (i.e. opening distance) is increased by a mould or machine movement, inducing an even pressure reduction throughout the entire cavity, enabling the melt to foam. The opening speed of the tool defines the number of nuclei in addition to the pressure drop rate, whereas the delay time determines the skin layer thickness and the pore diameter of the final foam.

Three trials were conducted during this foam injection moulding, as outlined in Table 3.6.

Table 3.6. Moulding trials employed during foam injection moulding with Mucell technology.

Processing Strategy	Moulding Process	Trials Acronym
1.	Under-volumetric	*TRIAL 1*
2.	Negative compression (or core back expansion)	*TRIAL 2*
3.	Negative compression with additions of 1wt%CBA$_3$	*TRIAL 3* [c]

From the trials, the following list of samples (i.e. plate specimens) were produced:

Table 3.7. List of samples produced in the moulding trials with Mucell technology.

MWCNT loading /wt%	Trial Type	Sample Acronym
0 (Unfilled HDPE)	1	HDPE_UV_A; HDPE_UV_B
	2	HDPE _NC_A; HDPE _NC_B
	3	HDPE+CBA$_3$_NC_A; HDPE+CBA$_3$_NC_B
0.1	1	HDPE+0.1wt%CNT_UV_A; HDPE+0.1wt%CNT_UV_B
	2	HDPE+0.1wt%CNT_NC_A; HDPE+0.1wt%CNT_NC_B
	3	HDPE+0.1wt%CNT+CBA$_3$_NC_A; HDPE+0.1wt%CNT+CBA$_3$_NC_B
0.5	1	HDPE+0.5wt%CNT_UV_A; HDPE+0.5wt%CNT_UV_B
	2	HDPE+0.5wt%CNT_NC_A; HDPE+0.5wt%CNT_NC_B
	3	HDPE+0.5wt%CNT+CBA$_3$_NC_A; HDPE+0.5wt%CNT+CBA$_3$_NC_B
1	1	HDPE+1wt%CNT_UV_A; HDPE+1wt%CNT_UV_B
	2	HDPE+1wt%CNT_NC_A; HDPE+1wt%CNT_NC_B
	3	HDPE+1wt%CNT+CBA$_3$_NC_A; HDPE+1wt%CNT+CBA$_3$_NC_B

The details of the experiments carried out in this work are summarized in tables 3.8 and 3.9. Specifically, the parameters that were fixed for all experiments are shown in Table 3.8.

Table 3.8. Constant parameter settings employed for the production of foamed parts during all MuCell trials.

Clamping force of the injection unit	Mould Temperature	Back pressure	Dosing speed
800 kN	60°C	200 bar	100 min^{-1}

---

[c] A combination of foaming agents were used in *TRIAL 3* to generate the cell structure. Rate of pressure drop and level of SCF are the only contributors to cell nucleation when using PBAs with unfilled materials. Therefore, there is a tendency for a non-uniformity of cell structure with PBAs in unfilled materials, particularly unfilled, semi-crystalline polymers. The practice of adding CBAs to the system, which tend to self-nucleate, to assist physical foaming is quite common. The benefit of self-nucleation with CBAs results in a more uniform cell structure, especially with unfilled HDPE, when compared to PBAs.

Other parameters such as the gas content and injection flow rate, listed in Table 3.9, were varied throughout the trials, to investigate their effects on the degree of mould filling, void fraction, and cell size uniformity.

Table 3.9. Variable parameter settings employed for the production of foamed parts during each MuCell trial.

TRIAL 1: **Under-volumetric Moulding Trials**

MWCNT loading /wt%	Dosing Volume / cm³	Injection Speed / cm³/s	Gas Content / wt%
0 (neat HDPE)	42	100	1.35
0.1	42	125	2
0.5	42	125	1.75
1	42	125	1.75

TRIAL 2: **Negative Compression Moulding Trials without additions of CBA**.

MWCNT loading /wt%	Dosing Volume / cm³	Injection Speed / cm³/s	Gas Content / wt%	Holding Pressure / bar	Holding Time / s	Opening Speed / mm/s	Opening Distance / mm
0 (neat HDPE)	50.5	100	2	600	2	3 - 5	0.5 - 3
0.1	50.5	125	2	600	1.5	1 - 5	0.5 - 3
0.5	50.5	125	1.5	600	0.1	1 - 5	0.5 - 8
1	50.5	125	1.5	600	0.1	1 - 5	0.25 - 8

TRIAL 3: **Negative Compression Moulding Trials with additions of 1wt% CBA₃.**

MWCNT loading /wt%	Dosing Volume / cm³	Injection Speed / cm³/s	Gas Content / wt%	Holding Pressure / bar	Holding Time / s	Opening Speed / mm/s	Opening Distance / mm
0 (neat HDPE)	50.5	100	1.75	600	2	1 - 5	0.5 - 6
0.1	50.5	125	2	600	1.5	1 - 5	0.5 - 3
0.5	50.5	125	1.5	600	0.1	1 - 5	0.5 - 8
1	50.5	125	1.5	600	0.1	1 - 5	0.25 - 8

3.3 Materials Characterisation

A characterisation study of the samples prepared using the various processing conditions described in section 3.2 was subsequently conducted to enable an initial screening of materials in order to assess whether they had the potential for application in acoustic sensors.

Structure-property relationships are the basic step to understanding the relative performance of a material for a given application.

PART I: The properties manifested by the composites in their solid-state (e.g. thermal, physical, rheological, acoustic and mechanical properties) is ultimately reflected in the final properties of the

foamed counterpart. Studying the properties of HDPE and HDPE-MWCNT composites in their solid-state was considered essential for helping to tailor the properties and structures of the corresponding foams particularly given the known nucleating effect that MWCNTs have for semi-crystalline polymers. Initially, the morphology, structure and the degree of dispersion of MWCNTs in neat HDPE were studied using a combination of techniques including oscillatory rheology, scanning electron microscopy (SEM), differential scanning calorimetry (DSC), static mechanical tensile and compression testing, thermo-gravimetric analysis (TGA), density and ultrasonic air-coupled measurements through transmission. Additional analysis using Raman spectroscopy and dynamic mechanical thermal analysis (DMTA) were carried out on composite samples and the relevant detail can be found in Submission Portfolio No.3. Finally, X-ray scattering techniques, both small- and wide-angle X-ray scattering (SAXS/WAXS) measurements, were used to determine the crystalline structure development in the composites.

PARTs II and III: Foamed samples of HDPE and HDPE-MWCNT composites (PARTs II and III) were also characterised so as to investigate the foaming characteristics as well as the effects of varying both the processing parameters and the initial MWCNT loading (between 0 % and 5 % by weight) on selected physical and acoustic properties. A preliminary material screening was completed, assessing density reduction, acoustic characteristics and morphological features of the moulded samples derived from varying processing conditions.

3.3.1 Parallel Plate Oscillatory Rheometry

The rheological behaviour of un-foamed composites was studied using a Thermo Scientific Haake MARS III rheometer equipped with a 25 mm parallel plate geometry using a 1 mm gap between plates in an air atmosphere. Two distinct dynamic mechanical tests were performed. Firstly, oscillatory amplitude stress sweeps were first undertaken over a stress range of 0.1 to 100 Pa at a fixed temperature and frequency of 160 °C and 1 Hz, respectively. This test indicated the region in which the deformation was small enough for the storage modulus (G') to be independent of deformation. Initially, each moulded disk was allowed to acclimatise on the plates at 160 °C allowing the sample to melt before being trimmed to size (from a thickness of 1.65 mm to a thickness of 1 mm) with a sharp blade prior to commencing the test. Second, the sample of 1 mm thickness was then subjected to dynamic oscillation frequency sweeps in the range 0.1-100 Hz, under a controlled stress at 100 Pa and an air atmosphere at room temperature.

3.3.2 Scanning Electron Microscopy (SEM)

In the preliminary work on un-foamed composites, the presence of MWCNTs and their dispersion in the HDPE matrix was examined using a Zeiss sigma field emission SEM fitted with a Gemini column. The same SEM instrument was used to image the final foamed structures produced by foam

processing the unfilled HDPE and MWCNT filled HDPE composites (PARTs II and III) in order to compare them with micrographs obtained for benchmark or current commercial materials. For measurements using the InLens detector, a working distance of 2.5 mm was used and an acceleration voltage of 3 kV. Prior to imaging, the sample disks were cryo-fractured using a hammer, after placing them in a liquid nitrogen bath for ~ 5 hours. The fractured surface was mounted on an aluminium SEM stub and sputter coated (~10 nm) using an Au/Pt metal target (Cressington 108 auto) under a weak argon atmosphere to prevent charging and surface heating.

The powder morphology of CBA_1 and CBA_2 was also examined by applying the same conditions. Prior to imaging, powders of each CBA were stuck on a layer of conductive carbon tape which was adhered on an aluminium SEM stub and then sputter coated.

3.3.3 Differential Scanning Calorimetry (DSC) Measurements

The thermal behaviour of HDPE and un-foamed HDPE-MWCNT composites was studied using a Mettler Toledo (DSC1, model 700, 400W) equipped with FRS5 thermocouple sensor, robotic sample changer and evaluated using a STARe Version 15.01 software package. Non-isothermal scans were performed under nitrogen (20 cm^3 min^{-1}). Samples of 5 ± 1 mg were inserted into aluminium pans with pieced lids and heated from 25 °C to 200 °C at a heating rate of 10 K min^{-1} (first heating) and held at this temperature for 60 s to eliminate any thermal history. Samples were then cooled to 25 °C at 10 K/min (first cooling), held at 25 °C for 60 s, before being re-heated (second heating) and cooled using the same protocol as described above.

At least three samples were subjected to the heat-cooling cycles and the corresponding mean values reported. The crystallinity $X_{c(DSC)}$ was determined by dividing the enthalpy of melting ΔH_m for the sample by a melting enthalpy of 293.6 J/g i.e. for a theoretically 100% crystalline HDPE [5], as shown in Equation 3.1:

$$X_c = \left(\frac{\Delta H_m}{(1-W_f)\Delta H_{100}} \right) \times 100 \qquad (3.1)$$

where, W_f is the weight fraction of filler and ΔH_{100} is the melting enthalpy of a theoretically 100% crystalline HDPE (293.6 J/g).

Additionally, the thermal characterisation of CBA_1 and CBA_2 (employed in PART II) was performed on as received samples, prior to extrusion. Understanding their thermal behaviour was important to evaluate the most suitable conditions for the chemical foaming of the polymer, assisting the optimisation of the foam processing.

3.3.4 Small- and Wide-Angle X-ray scattering (SAXS/WAXS) measurements

The SAXS/WAXS data was collected using a Xenocs Xeuss 2.0 X-ray instrument operating with a Cu-K_α source (λ = 1.54 Å). Simultaneous 2D SAXS/WAXS data were collected on Pilatus 300K

and Pilatus 100K detector systems, respectively, calibrated with silver behenate. The SAXS detector was positioned at a distance of 2.48 m from the sample. An evacuated chamber was placed between the sample and SAXS detector to reduce air scattering and absorption. The WAXS detector was positioned in the evacuated sample chamber at a distance of 162 mm. The undrawn samples were positioned vertically in the instrument's evacuated sample chamber and static 2D SAXS/WAXS data was taken at an acquisition time of 120s (λ = 1.54 Å). 2D SAXS/WAXS data of the drawn samples were taken at the neck section of the sample at an acquisition time of 60 s.

X-ray diffraction (XRD) data were collected using a PANalytical Empyrean diffractometer with a Co-K$_\alpha$ source (λ = 1.79 Å) operating at 40 kV and 40 mA. The samples were mounted in flat circular holders and rotated during measurement (0.5 s^{-1}). Data was collected on a PIXcel detector system (1D mode) with a continuous scanning mode over a scattering angle range of $2\theta = 5° - 60°$.

SAXS/WAXS Data Analysis: All SAXS/WAXS data were normalised for sample thickness, transmission and background scattering. X-ray data reduction and analysis was performed using the Xeuss 2.0 instrument data processing and analysis software. 2D SAXS/WAXS data were reduced to 1D scattering profiles of intensity (*I*) versus scattering vector (*q*) for SAXS and 2θ for WAXS (where $q = (4\pi/\lambda) \sin (\theta)$, 2θ is the scattering angle and λ is the X-ray wavelength), by sector averaging around the beam stop by a fixed angle and radius, *q*. To estimate the relative orientation azimuthal 1D profiles were obtained from the 2D SAXS data, where the angular variation in intensity, $I(q, \varphi)$, was obtained at a fixed radius *q*, over an azimuthal angle, φ, range of 0-360°. The two peaks from the 1D azimuthal profiles were then fitted using Lorentzian functions to obtain the average full-width half-maximum (FWHM). Correlation functions were computed on the 1D SAXS profiles using the Corfunc software [6] incorporated into the SasView SAXS analysis package [7]. The 1D correlation function, $\gamma(R)$, is expressed as:

$$\gamma(R) = \frac{1}{Qs} \int_0^\infty I(q)q^2 \cos(qR)\, dq \tag{3.2}$$

where, $I(q)$ is the scattering intensity and Q_s is the experimental invariant obtained from the 1D SAXS profile between the experimental limits of q_1 (first data point) and q_2 (region where $I(q)$ is constant). The scattering invariant is expressed as:

$$Q_s(t) = \int_0^\infty q^2 I(q)dq \approx \int_{q_1}^{q_2} q^2 I(q)dq \tag{3.3}$$

The 1D correlation functions were obtained from the extrapolation of the 1D SAXS data ($q \rightarrow \infty$) according to Porod's law [8] and a Guinier model back extrapolation ($q \rightarrow 0$) [9]. The correlation function analysis assumes an ideal two-phase lamellar morphology [9, 10] where various parameters including the long period, L_p, crystalline layer thickness H_b, and estimated local percent crystallinity X_c [6] can be extracted.

3.3.5 Thermo-gravimetric Analysis (TGA)

The thermal stability of un-foamed HDPE-MWCNT composites was studied by thermo-gravimetric analysis (TGA) using a Mettler Toledo TGA1-STARe system. Each sample (ca. 4-5 mg) was tested in a nitrogen atmosphere. An inert atmosphere in this preliminary study was satisfactory for simply understand the thermal stability of these materials. The measurements were performed using 70 μL alumina pans, in which the sample was placed before being heated from room temperature to 800 °C at a constant heating rate of 10 K min^{-1}. The curve of the residual weight loss (%) versus temperature was recorded during the heating process.

The thermal stability of the two CBAs used in PART II was also investigated under the same conditions as above but in an air atmosphere. The evaluation of the thermal stability of the system in the presence of oxygen in a reactive atmosphere (air) is fundamental in understanding the influence of reactive gas, the temperatures at which the CBAs initial decompose, the kinetics of the reactions and the temperature range over which there is a yield of gas.

Pellets of the neat polymer were also analysed by TGA in air.

3.3.6 Density Measurements

The density of the various samples, un-foamed (PART I) and foamed (PARTs II and III), was measured using an analytical balance, Mettler Toledo NewClassic Balance (Model ME204), equipped with a density kit. This straightforward measurement allowed for the determination of mass and volume of each sample by weighing the sample firstly in air to determine its mass (the balance adjusted automatically this apparent density for the buoyant effect of the air on the sample to obtain the true sample density), and then while submerged in a liquid of known density to determine its volume. By measuring the weight in two media of different density (e.g. air and water), a procedure known as hydrostatic weighing based on Archimedes' Principle was followed, calculating the volume of the sample by its loss of weight in the liquid divided by the density of the liquid [11]. Ethanol, with a density of 0.789 g cm^{-3} [12] at 20˚C (temperature of the measurement), was used as the displacement fluid. As the value of density of water (0.988 g cm^{-3} at 20˚C) is close to that of HDPE (0.964 g cm^{-3}), a fluid with lesser density and higher buoyancy than water was preferred to ensure a high measurement accuracy.

3.3.7 Porosity, Expansion Ratio and Void Fraction

The first and most often used microstructural parameter required to describe a foam is the amount of material it contains defined as the void fraction of the foam [13]. In particular, the void fraction (defined also as *cell volume fraction*) refers to the ratio of the volume of the gas phase contained in a foamed sample to the total volume of the foam [14] and it is a measure of the foaming grade. The total volume is the sum of the volume fraction of cells/pores which the gas occupies, polymer and moisture, since the foam always sucks up some moisture from the environment [15].

In order to characterise the multitude of foamed polymer and composite samples prepared in this study (PARTs II and III) and, at the same time, verify whether the conditions adopted for the foaming process were adequate for attaining a relevant internal porosity in these structures, void fraction and volume expansion ratio of the foamed moulded parts were calculated according to equations 3.4 and 3.5, respectively [13]:

$$Void\ Fraction = 1 - \left(\frac{\rho_f}{\rho_u}\right) \tag{3.4}$$

$$Expansion\ Ratio\ = \frac{\rho_u}{\rho_f} = \frac{1}{1-Void\ fraction} \tag{3.5}$$

where, ρ_f is the bulk density of the foamed sample and ρ_u is bulk density of the analogous un-foamed sample, with ρ_u corresponding to the bulk density of the un-foamed polymer (i.e. 0.964 g cm^{-3}) for samples of neat polymer.

When expressed as a percentage, it corresponds to the percentage reduction in density achieved for the same foamed sample, calculated as:

$$Density\ Reduction = \frac{(\rho_u-\rho_f)}{\rho_u} \cdot 100 \tag{3.6}$$

It should be noted that both values of density measured and theoretical predictions (calculated using the linear rule of mixtures expressed in Equation 3.7) were considered in the term ρ_u of equations 3.4-3.6. The comparison between measured and predicted values of density would allow for the evaluation of the divergence of data fitting between the two methods, empirical (derived from experimental data) and semi-empirical (involving assumptions [d]), directly related to the pre- and post- processing of the un-foamed material.

According to the formula, the density of a composite of known composition ($\rho_{composite}$) can be calculated as [16]:

$$\rho_{composite} = \frac{\rho_{filler} \cdot \rho_{polymer}}{\rho_{polymer} \cdot m_{filler} + \rho_{filler}(1-m_{filler})} \tag{3.7}$$

where, $\rho_{composite}$ is the density of the composite, ρ_{filler} is the density of the filler (i.e. 1.75 g cm^{-3} for MWCNTs), $\rho_{polymer}$ the density of the matrix (i.e. 0.964 g cm^{-3} for HDPE), and m_{filler} the mass fraction of filler.

In particular, the ρ_u values obtained from Equation 3.7 for the compact HDPE-MWCNT composites, later employed in equations 3.4-3.6 are listed in Table 3.10.

---

[d] There are indeed some limits to the validity of the Equation 3.7, such as no air inclusions in the composites and no filler influence on density of the polymer phase (e.g. by nucleation of crystal growth).

Table 3.10. Theoretical density values calculated from the linear rule of mixtures applied for HDPE-MWCNT composites.

MWCNT loading /wt%	ρ_u /g cm-3
0	0.964
0.01	0.964
0.1	0.964
0.3	0.965
0.5	0.966
1	0.968
3	0.977
5	0.986

3.3.8 Acoustic properties: Ultrasonic measurements through transmission

Ultrasonic air-coupled measurements through transmission were performed using the experimental setup showed in Figure 3.5 to determine both the velocity and attenuation coefficient of ultrasound in the samples by frequency-domain analysis.
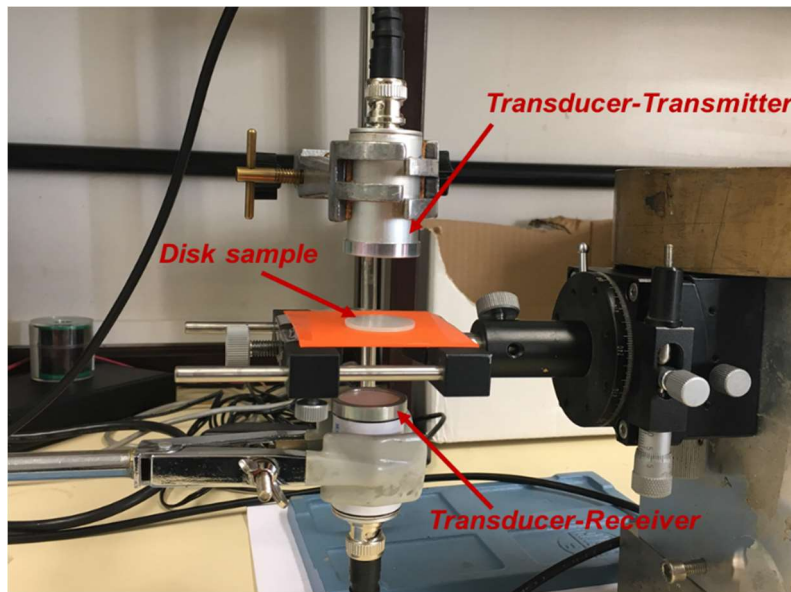
Figure 3.5. Experimental setup employed for the ultrasonic air-coupled measurements (located in the "Instituto de Tecnologías Físicas y de la Información CSIC", Madrid, Spain).

A pair of specifically designed air-coupled piezoelectric transducers (centre frequency of 673 KHz) was employed in the set-up for efficient transmission and/or reception from air to the disk sample and vice versa. An airborne ultrasonic pulse was set to impinge normally on the sample surface and the through-transmitted signal is received and analysed. The normal incidence ensured the maximum amplitude of the signal, while allowing for plane wave in order to neglect the diffraction effects of the sound beam. An optimal distance (ca. 2 cm) was fixed between transducers and sample for a

clear signal and a good signal-to-noise ratio (SNR). The frequency domain investigated in the measurements [0.4MHz - 1.1MHz] enabled the observation of the resonance peak, as the air-coupled ultrasonic technique (described in detail in [17-19]) relies on the first thickness resonance peak of the sample plate.

Figure 3.6 shows the amplitude spectrum of the transmitted signal in time domain ((A)), amplitude spectrum (insertion loss) of the transmitted signal in frequency domain ((B)) and phase spectrum of the transmitted signal in frequency domain ((C)), displayed on a PC screen connected to the digital oscilloscope (Tektronix DPO 7054). After acquisition of the signal, the digital oscilloscope stored, analysed and converted the input analogue signal into a digital record of the signal amplitude at each sample time, providing numerical values as well as visual displays.
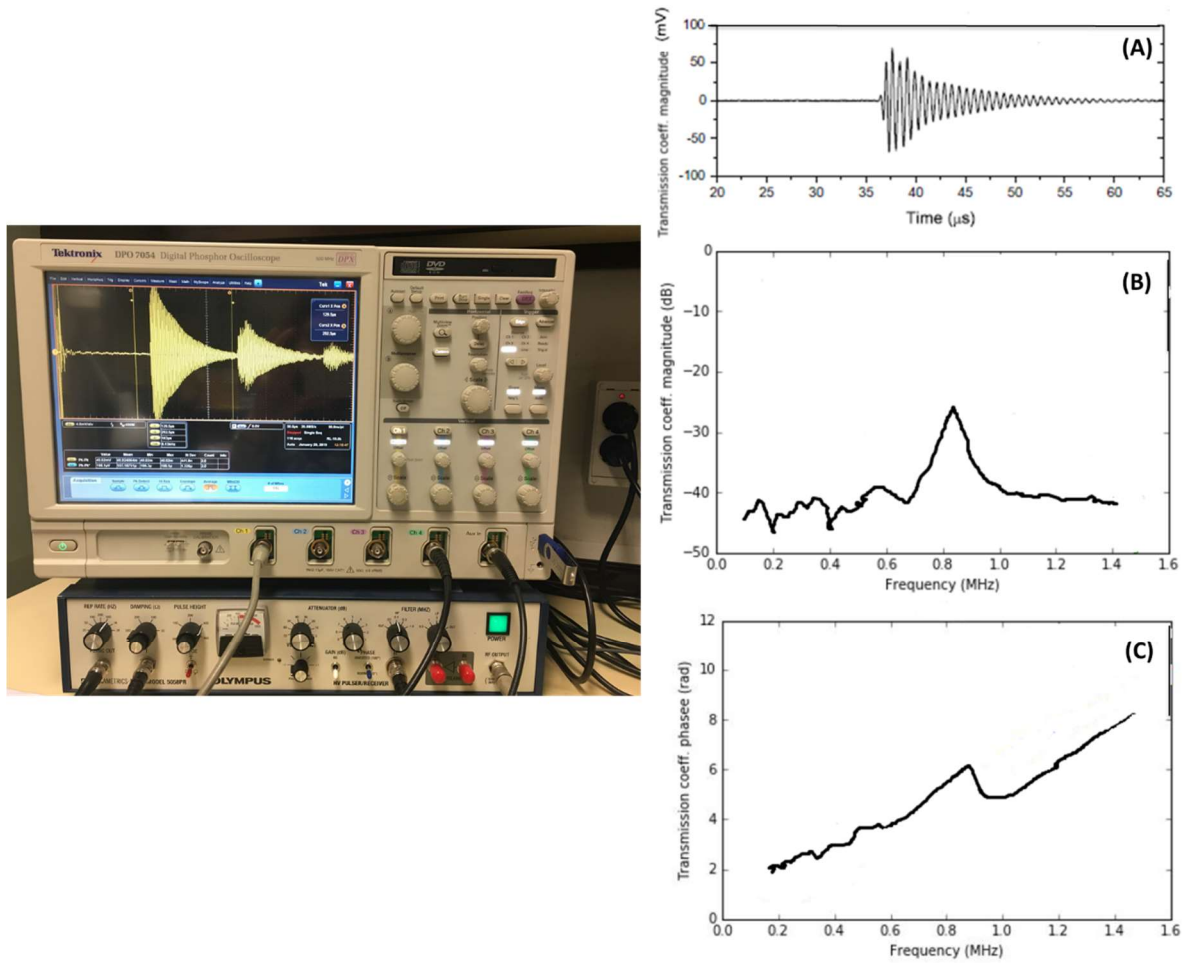
Figure 3.6. Digital oscilloscope employed for the ultrasonic air-coupled measurements and analysis of: (A) amplitude spectrum of the transmitted signal in time domain, (B) amplitude spectrum (insertion loss) of the transmitted signal in frequency domain and (C) phase spectrum of the transmitted signal in frequency domain.

The analysis of the amplitude and phase of the ultrasonic transmission coefficient in the vicinity of the first thickness resonance allowed for the determination, simultaneously, of velocity and the attenuation coefficient of the ultrasound in the material and thickness of the solid plate. Ultimately, a theoretical model (one-dimensional model) of the transmission of ultrasonic waves was applied for a best fitting of the experimental measurements with theoretical calculations, which required

specific characteristics of the samples for the outcome of the measurement (i.e. isotropic and homogeneous materials with plane and parallel surfaces and uniform thickness).

Not all the samples produced in this study however were of uniform thickness and did not have the ideal flat surfaces required due to the varied conditions applied during the injection molding processing. The fitting between experimental measurements with theoretical calculations must be as perfect as possible in the measured spectra with the resonance peak visibly identifiable, whereas reverberations within these samples made it impossible to use this method.

Alternatively, *ultrasonic measurements through transmission in water immersion* were performed when the model did not work for certain samples (PARTs II and III). Acoustic properties of the samples were estimated via the time of flight (ToF) technique, using an appropriate frequency band based on the type of material sample. Consequently, the pair of piezoelectric transducers employed in the set-up for efficient transmission and/or reception from water to the disk sample and vice versa were selected accordingly. Specifically, higher frequencies [2.3 MHz - 4.5 MHz] than in air were used for samples prepared in PART II, while adopting a pair of transducers with center frequency of 3.5 MHz. The high frequency domain investigated in the measurements allowed for identification of resonances higher than the first order in the measured acoustic spectra. A different frequency band [0 MHz – 1.6 MHz] was finally investigated when measuring ultrasonic pulse transmission (in time domain) in samples prepared in PART III while employing transducers with center frequency of 1 MHz. A clear signal and a good signal-to-noise ratio (SNR) were obtained during the experiments in the experimental setup shown in Figure 3.7.
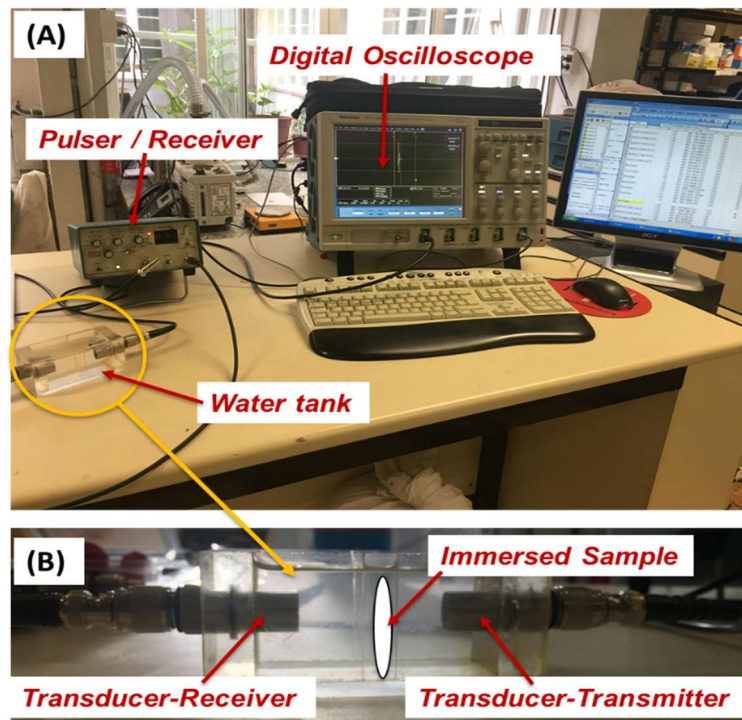
Figure 3.7. (A) Experimental setup employed for the ultrasonic measurements through transmission in water immersion. (B) Water tank in which a pair of ultrasonic transducers facing each other are inserted with the sample immersed in between.

The ultrasonic experimental set-up used (Figure 3.7(A)) consisted of a pair of bespoke designed transducers for immersion in water for efficient transmission and/or reception from water to the disk sample and vice versa, a pulser-receiver instrument, and a digital oscilloscope (Tektronix DPO 7054) connected to a PC. Distilled water was used as the coupling medium between the transducers and sample. The ultrasonic measurements were taken through transmission mode in water immersion, by using a probing acoustic pulse delay or time of flight (ToF) estimation. This method compares two ultrasonic signals (i.e. with and without the sample, with the latter used as the initial or reference ultrasonic signal) and calculates the ToF variation between them. Taking the reference signal without the test sample inserted and the measurement signal propagated through the sample [e], the difference in propagation delay (i.e. ToF) between reference and the first pulse of the measurement signal can be established [20].

When calculating the velocity of ultrasound in the sample, the sample thickness (1.65mm< thickness <1.9mm for PART II sample disks, 1.9mm< thickness <10mm for PART III sample blocks) must be taken into account as it affects the time of flight calculation, therefore the relationship to apply is the following:

$$v_{ultrasound\ in\ the\ sample} = \left(\frac{ToF}{sample\ thickness} + \frac{1}{v_{ultrasound\ in\ water}} \right)^{-1} \qquad (3.8)$$

The ultrasonic velocity in the sample was calculated from the ultrasonic signal by using the ToF and the sample thickness according to Equation 3.8, where the velocity of ultrasound in water is equal to 1450 m/s [21].

By moving from ultrasonic air-coupled measurements to measurements by water immersion, the ultrasonic velocity in the sample is no longer a straightforward accessible value but has to be estimated through calculations, using the time shift measured between the reference and the measurement signal in the sample.

In both cases of measurements, air-coupled and water coupled, it is possible to obtain both the values of attenuation and speed of sound. In the case of air-coupled and analysis of thickness resonances, the method implemented in the laboratory automatically calculates both the ultrasonic longitudinal velocity and the attenuation. Conversely, for immersion in water the method is not automated, therefore a further analysis is necessary to obtain information on the attenuation of the ultrasonic longitudinal waves inside the samples, carried out where deemed appropriate (i.e. in cases where there is an adequate acoustic impedance). This is the case of the PART III samples, for which the attenuation was estimated based on the value of velocity calculated by the phase spectrum at 1 MHz. Despite the acoustic impedance, Z, is the determining factor in deciding whether the material fits

---

[e] If the signal is travelling faster in the sample, in the screen the signal appears before the reference signal calculated in water and vice versa.

the intended application, the attenuation is also important and must be taken into consideration, as there would be no advantage in using a matching layer with the corrected impedance value which would fully absorb the acoustic energy. The value of Z was obtained by calculating the product of the ultrasonic velocity in the sample, regardless of whether this was calculated in air or water, and its density derived from analytical balance measurements.

3.3.9 Static Mechanical Testing: Tensile and Compression

Tensile testing at room temperature of neat HDPE and the HDPE-MWCNT composites (PART I) was performed on a Shimadzu Autograph AGS-X fitted with a 10 kN load cell, equipped with a twin TRViewX non-contact digital video extensometer (500 and 120 mm field of view), using a Trapezium X Version 1.4 software package. The standard dumbbell-shaped test samples (ASTM D638 V) with a gauge length of 7.62 mm were deformed using a constant crosshead speed of 10 mm min^{-1}, to determine the modulus, with an extensometer fitted using a 25.4 mm gauge length (i.e. distance between the grips). The tensile modulus was reported as the secant of the initial linear part of the stress-strain curve. A linear regression technique was utilized to define the slope of the stress-stain curve in the initial region before yield, taken to be a strain range of 0.05% and 0.25%, determined using the standard BS EN ISO 527-1:2012. A minimum of seven replicates of each sample were tested and the average values are reported with error bars (i.e. standard deviation) where appropriate.

Compression testing at room temperature of un-foamed and foamed HPDE and HDPE-MWCNT composites were performed for the evaluation of the materials behaviour under uniaxial compression load. For the compression tests, 25mm×1.65mm disks samples (PARTs I and II) and 27mm×27mm square cut sample blocks (PART III) were tested under quasi-static compression tests using a Shimadzu Autograph AGS-X fitted with a 10 kN load cell testing machine. The machine, which makes use of a Trapezium X Version 1.4 software package, is the same as that used for tensile testing in which grips were replaced by metal discs when switching test modes. The compression test was carried out at the compression speed of 1 mm/min. A maximum force of 9000 N was the limit imposed by the machine. Both the modulus and strength in uniaxial compression were obtained for each sample. A minimum of five replicates of each sample were tested and the average values are reported with error bars (i.e. standard deviation).

3.3.10 DMTA: Dynamic mechanical thermal analysis

The dynamic mechanical properties of neat HDPE and the HDPE-MWCNT composites (PART I) were determined using a Triton Tritec 2000 DMA machine equipped with a standard air oven and fitted with a dual cantilever bending test assembly and data acquisition software. The testing was performed using rectangular bars measuring approximately 80 mm × 10 mm × 4 mm prepared by

injection moulding and cut to the required length (50 mm). The dual cantilever bending geometry was set with a free length of 17.5 mm, width of 10 mm and thickness of 4 mm. A clamp mass of 5.66, geometry constant of 2.043 x 10^{-4} and strain factor of 3.918 were used. The specimens were clamped in the grips inside a heating chamber and then cooled to -180 °C by addition of liquid nitrogen to the chamber. The temperature was allowed to stabilise, and then the chamber was heated at a rate of 2 °C/min to 100 °C. A sinusoidal (dynamic) force was applied at a constant frequency of 1 Hz to produce a dynamic strain with a constant maximum and a resultant displacement of the sample of 0.01 mm. The resulting dynamical mechanical properties of the composites, such as elastic modulus E', loss modulus E' and damping (tan δ) were determined as a function of temperature.

References

[1] M.S.P. Shaffer, A.H. Windle Fabrication and Characterization of Carbon Nanotube/Poly(vinyl alcohol) Composites, Advanced Materials, 11(11), 1999, pp. 937-941.

[2] R. Cardinaud, T. McNally, Localization of MWCNTs in PET/LDPE blends, European Polymer Journal, 49(6), 2013, pp. 1287-1297.

[3] M. Rohleder, F. Jakob, Foam Injection Molding, in: Specialized Injection Molding Techniques, William Andrew Publishing, Chapter 2, 2016, pp. 53-106.

[4] J.S. Colton, The Nucleation of Microcellular Foams in Semi-Crystalline Thermoplastics, Materials and Manufacturing Processes, 4(2), 1989, pp. 253-262.

[5] S.L. Kodjie, L. Li, B. Li, W. Cai, C.Y. Li, M. Keating, Morphology and Crystallization Behavior of HDPE/CNT Nanocomposite, Journal of Macromolecular Science Part B, 45(2), 2006, pp. 231-245.

[6] A.J. Ryan, SAXS Correlation Function: New Software at Daresbury Fibre Diffraction Review 3, 1994, pp. 25-29.

[7] SasView for Small Angle Scattering Analysis, 2018. http://www.sasview.org/ (Accessed 02/04/2020).

[8] G. Porod, The small-angle X-ray scattering from densely packed colloidal systems, Kolloid-Zeitschrift, 124(2), 1951, pp. 83-114.

[9] F.J. Baltá-Calleja, C.G. Vonk, X-ray scattering of synthetic polymers, Elsevier, (1989), pp.1-317.

[10] G.R. Strobl, M. Schneider, Direct evaluation of the electron density correlation function of partially crystalline polymers, Journal of Polymer Science: Polymer Physics Edition, 18(6), 1980, pp. 1343-1359.

[11] J.E. Mark, Physical Properties of Polymers Handbook, Springer, second edition, 2007, pp. 1-1063.

[12] A.T. Bakalinsky, M.H. Penner, ALCOHOL | Properties and Determination, in: Encyclopedia of Food Sciences and Nutrition, Academic Press, Oxford, 2003, pp. 107-111.

[13] S.T. Lee, Thermoplastic Foam Processing Principles and Development, CRC Press, 2005, pp. 1-299.

[14] D.F. Baldwin, C.B Park, N.P. Suh, A microcellular processing study of poly(ethylene terephthalate) in the amorphous and semicrystalline states. Part I: Microcell nucleation, Polymer Engineering & Science, 36(11), 1996, pp. 1437-1445.

[15] K.L. Sivertsen, Polymer Foams 3.063 Polymer Physics Spring 2007, 2007, pp. 1-17.

[16] M.H. C. DeArmitt, Filled Thermoplastics, in: Particulate-Filled Polymer Composites, Rapra Technology Limited2003, pp. 357-424.

[17] T.E.G. Alvarez-Arenas, A Nondestructive Integrity Test for Membrane Filters Based on Air-Coupled Ultrasonic Spectroscopy, IEEE Transactions on Utrasonics, Ferroelectrics, and Frequency Control, 50, 2003, pp. 676-685.

[18] T.E.G. Alvarez-Arenas, Air-coupled ultrasonic spectroscopy for the study of membrane filters, Journal of Membrane Science, 213, 2003, pp. 195-2017.

[19] T.E.G. Alvarez-Arenas, Simultaneous determination of the ultrasound velocity and the thickness of solid plates from the analysis of thickness resonances using air-coupled ultrasound, Ultrasonics, 50, 2010, pp. 104-109.

[20] L. Svilainis, T.E.G. Alvarez-Arenas, K. Lukoseviciute, A. Chaziachmetovas, Comparison between Time and Frequency Domain ToF Estimators for Signals in Close Proximity, Physics Procedia, 70, 2015, pp. 574-577.

[21] V.T. Rathod, A Review of Acoustic Impedance Matching Techniques for Piezoelectric Sensors and Transducers, Sensors, 20(14), 2020, pp. 4051_1-64.

CHAPTER 4: RESULTS AND DISCUSSION- PART I

Characterisation of Un-foamed HDPE-MWCNT Composites

As discussed in the Introduction to this thesis, the crystallisation behaviour of semi-crystalline polymers is of considerable importance with regard foaming such polymers. This behaviour if further complicated by the inclusion of MWCNTs which are known to have a significant nucleation effect and alter crystallisation kinetics of semi-crystalline polymers. Therefore, it is critical to have an understanding of the effect of MWCNT inclusion on the morphology and structure of HDPE and the subsequent changes on the thermal, viscoelastic, acoustic, and mechanical properties of such composite materials before foaming.

Firstly, the state of dispersion of un-functionalised MWCNTs in the HDPE matrix was investigated by measuring the rheological properties (using a parallel plate oscillatory rheometer) supported by SEM imaging. Second, a detailed study using X-ray scattering techniques was performed to determine the crystalline structure development of un-foamed composites of HDPE and MWCNTs.

4.1 Rheological measurements

The linear viscoelastic behaviour of the un-foamed composites was investigated and melt state oscillatory rheology measurements performed to assess, indirectly, the extent of MWCNT dispersion in the HDPE matrix and to determine if rheological percolation was obtained. The formation of a percolated system can be detected by examining the changes in complex viscosity ($|\eta^*|$), storage modulus (G') and loss modulus (G'') as a function of frequency [1-4]. The change in rheological behaviour of the MWCNT filled HDPE and formation of a percolated filler-filler network results in the composites displaying 'pseudo-solid'-like behaviour, manifested by an increase of several orders of magnitude in $|\eta^*|$ and G' as a function of angular frequency. Figures 4.1(A) and 4.1(B) clearly show a dramatic increase in both $|\eta^*|$ and G' with increasing MWCNT loading at low frequencies. A very low rheological percolation threshold was observed at some MWCNT loading between 0.3 wt% and 0.5 wt%.
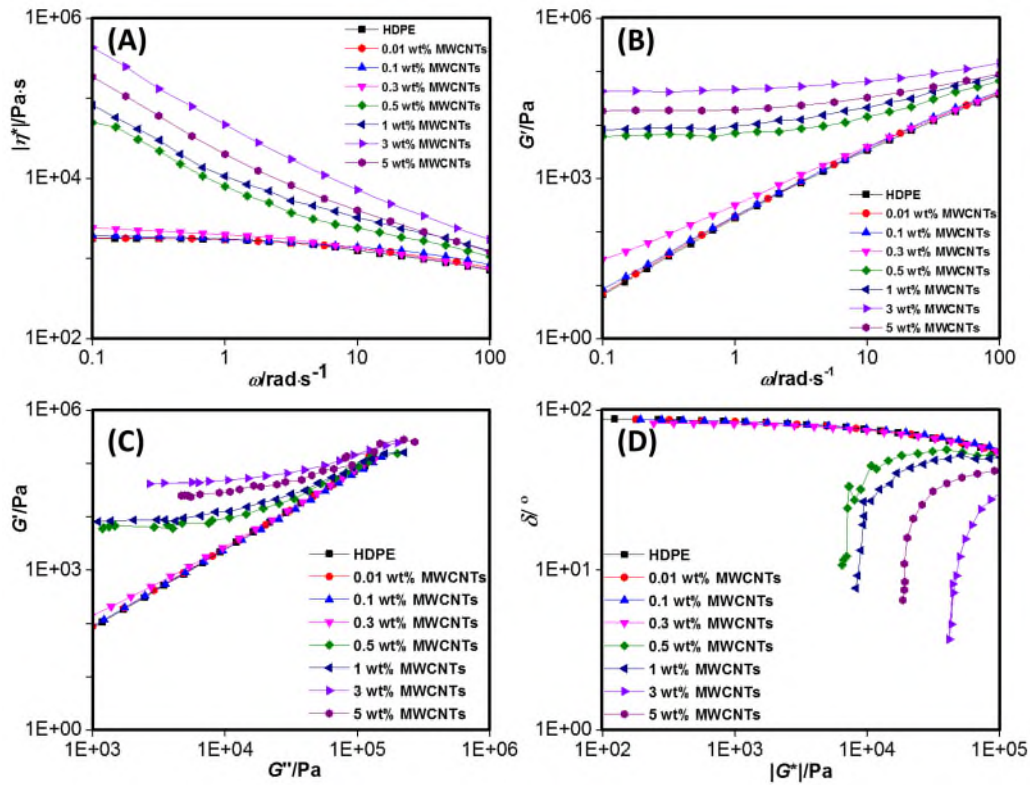
Figure 4.1. Variation in: (A) complex viscosity |η*| and (B) storage modulus (G') as a function of frequency for unfilled HDPE and MWCNT filled HDPE and, (C) Cole-Cole plot (G' versus G") and (D) Van-Gurp Palmen plot (phase angle (δ) versus complex modulus).

From the complex viscosity (|η*|) versus frequency (ω) plot (Figure 4.1(A)), the complex viscosity increases slightly as the concentration of MWCNT increases up to 0.3wt%, over the frequency range investigated. However, in the low-frequency range (i.e. <10 rads^{-1}), at some MWCNT concentration between 0.3 wt% (~0.17 vol%) and 0.5 wt% (~0.28 vol%), |η*| increases by over two orders of magnitude and by almost 3 orders for 5 wt% (~2.82 vol%) MWCNT. As expected for MWCNT loadings above 0.3 wt% there was also a concomitant monotonic increase of the storage moduli at low frequencies, Figure 4.1(B). At 0.1 rad/s the change in G' was over four orders of magnitude indicating the formation of a MWCNT percolated network which impedes the mobility of polymer chains [5].

At low frequencies (~0.1 rad/s), the size of the increase in |η*| and G' is more pronounced than that at higher frequencies (> 10 rad/s). At high frequencies indeed, the curves tended to plateau, again indicative that the MWCNT had formed a percolated network in the HDPE matrix restricting polymer chain mobility, the composite now displaying 'pseudo-solid-like' behaviour, typical of conventionally filled polymers with strong polymer-filler interactions and attributable to yield phenomena in the composites [1, 4, 6-8]. G' becomes almost independent of angular frequency (non-terminal low frequency behaviour) as MWCNT loading increases at low frequencies, indicative of the transition from 'liquid-like' to 'solid-like' viscoelastic behaviour in composites and attributable to the interconnected MWCNT network restraining the long-range motion of the polymer chains [5,

9]. In contrast, at high frequencies (>10 rad/s), the effect of the MWCNT on the rheological behaviour is relatively weak, suggesting they do not significantly influence the short-range dynamics of the HDPE chains, especially on length scales comparable to the entanglement length.

It is more correct to assess if a rheological percolation has been attained by constructing Cole-Cole and Van-Gurp Palmen plots, see Figure 4.1(C) and 4.1(D). From the Cole-Cole plot (Fig.4.1(C)), the effect of MWCNT addition on the viscoelastic behaviour is shown from a divergence from the linear relationship between log G" and log G'. It can be clearly seen there is a significant divergence, which first occurs for some MWCNT loading between 0.3 wt% and 0.5 wt%. If there were no such effect, the curves for each loading of MWCNT would superimpose on that for unfilled HDPE. This observation is confirmed from the Van-Gurp Palmen plot (δ versus $|G^*|$), Figure 4.1(D), where a significant decrease in phase angle (δ) is obtained for MWCNT loadings $\geq$0.5 wt% (~0.28 vol%) and is a consequence of the network structure relaxing differently and with varying relaxation times. Interestingly, despite numerous replicate measurements and from different batches, δ increased again on going from 3 wt% to 5wt% MWCNT loading, presumably due to the greater difficulty uniformly dispersing MWCNTs in the polymer melt at higher loadings.

4.2 SEM imaging of MWCNT dispersion in un-foamed HDPE

Qualitatively, the extent of MWCNT dispersion in composites was examined using scanning electron microscopy at different magnifications on cryo-fractured surfaces of specimens. Representative SEM images of the composites at different filler content are shown in Figure 4.2. SEM images of all the other HDPE-MWCNT composites can be found in section 3.2 of Submission Portfolio No.3. The images reflect the internal structure and morphology of the polymer/MWCNT composite formed during the processing steps.
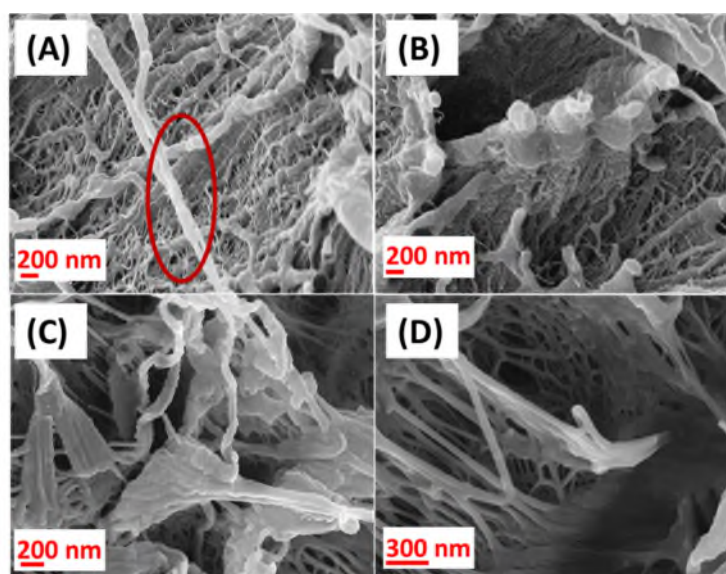
Figure 4.2. Representative high magnification SEM images of the fractured surfaces of composites of HDPE with (A-B) 3 wt% and (C-D) 5 wt% MWCNTs.

When the MWCNTs are added to the polymer, primarily the level of homogeneous dispersion and distribution that is achieved is investigated [10]. A good dispersion is necessary for achieving improved mechanical properties of the composites and insures maximum effective area for CNT/polymer interaction [11]. If any MWCNT agglomeration is present in the polymer, it results in decreases in the strength and modulus of the polymer [12]. From the SEM micrographs collected, homogeneous dispersion of the MWCNTs in HDPE was obvious and no large MWCNT agglomerations (above 8 µm) were observed. The mixing regime used resulted in uniformly dispersed and distributed MWCNTs throughout the HDPE matrix, in agreement with the behaviour obtained from rheology measurements. A thin layer of polymer appears to coat or wrap around many of the MWCNTs protruding from the fractured surface and creates a polymer sheath surrounding the MWCNTs (as highlighted by the red circle in Figure 4.2(A)). Such morphology with MWCNTs uniformly dispersed and distributed throughout the HDPE matrix provides a route for effective load transfer to the MWCNT network and result in a more uniform stress distribution [12]. The CNTs pull-out from the matrix reflects the fracture energy stored in the composites and affects the strain capacity (i.e. ductility) and toughness of the composite [13]. Critically, the inclusion of MWCNTs in HDPE and the formation of a trans-crystalline polymer layer on the surface of the MWCNTs will alter the crystallisation behaviour of the HDPE and consequently mechanical properties of the composite.

4.3 DSC: Thermal Analysis of un-foamed HDPE-MWCNT Composites

Thermal analysis was carried out by DSC to determine the melting temperature T_m, crystallisation temperature T_c, melting enthalpy ΔH_m, crystallisation enthalpy ΔH_c, and bulk crystallinity $X_{c(DSC)}$ of neat HDPE and HDPE-MWCNT composites. The full thermal analysis data collated from second cooling and second heating cycles are presented in Table 4.1. Additionally, thermograms of the first cooling (A) and second heating (B) cycles are reported in Figure 4.3.

Table 4.1. Thermal parameters determined from DSC measurements for neat HDPE and HDPE-MWCNT composites.

MWCNT loading /wt%	T_m /°C	T_c /°C	ΔH_m /J g^{-1}	ΔH_c /J g^{-1}	$X_{c\,(DSC)}$ /%
0	134.8	120.0	221.6	214.6	75.5
0.01	135.4	121.1	216.4	204.7	73.7
0.1	135.3	121.0	222.5	210.3	75.9
0.3	135.9	122.0	218.6	206.8	74.7
0.5	136.3	123.3	218.8	206.8	74.9
1	136.7	121.5	216.4	205.5	74.4
3	139.1	118.7	215.2	206.6	75.6
5	140.2	117.8	210.4	208.5	75.4
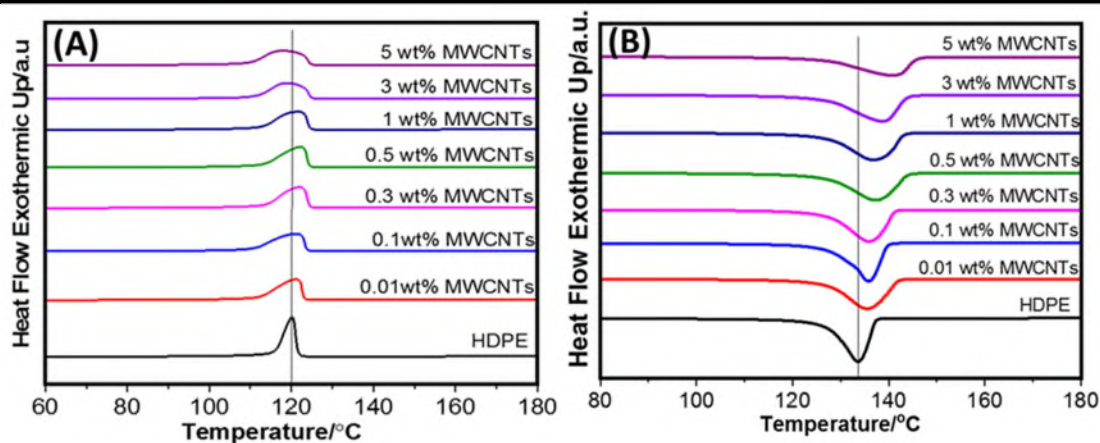
Figure 4.3. DSC thermograms for neat HDPE and HDPE-MWCNT composites; (A) cooling cycle, (B) heating cycle.

In Figure 4.3(A), for neat HDPE, T_c = 120 ℃, indicated by the vertical line in the figure. With the addition of MWCNTs, T_c tends to shift to a slightly higher temperature with up to ~0.5 wt% loading but, for higher loadings, T_c begins to decrease (allowing for instrument error) compared to that of neat HDPE. The increase in T_c is indicative of the heterogeneous nucleating effect of the MWCNT [14-18] at low loading in the HDPE matrix. However, as the MWCNT loading increases T_c tends to decrease, which is due to the confinement effect of the formation of a MWCNT network [16, 17], which inhibits crystallisation of the polymer further. This confirms the formation of a percolated MWCNT network in the HDPE matrix at loadings approaching 0.5 wt%, in agreement with observations made from oscillatory rheology measurements.

Similarly, in Figure 4.3(B), T_m is seen to increase slightly on the addition of MWCNTs, again up to ~0.5 wt% loading, and then begins to decrease, to lower than that of neat HDPE (120 ℃). The initial increase in T_m is indicative of the increased nucleation of HDPE at low MWCNT loadings that can also be attributed to the well dispersed MWCNTs in the HDPE matrix resisting the conduction of heat to the crystallites until the heat flow is enough to melt the crystallites at higher temperatures [19, 20]. As the MWCNT loading is increased, filler network formation will allow the conduction of heat to melt the crystallites at lower temperature. The significant broadening of the T_c and T_m peaks in Figure 4.3 with increasing MWCNT content, can be related to the size distribution of the crystallites. Semi-crystalline polymers commonly give rise to very broad melting peaks because of the size distribution of the crystallites. The broader peaks indicate a wider distribution of crystallite sizes, which melt over a wider temperature range compared to the narrower peak for neat HDPE, indicating a narrower range of crystallite sizes [15, 16]. Finally, from Table 4.1, the bulk crystallinity $X_{c(DSC)}$, determined from the second heating cycle, generally decreased very slightly on addition of MWCNTs accompanied by a reduction in the heat released during crystallisation. Since the narrower the peaks the more perfect are the crystals, the fact that $X_{c(DSC)}$ decreased very slightly on addition of MWCNTs (whereas an increase of polymer crystallinity is typically claimed in literature with

addition of CNTs [21]), can be attributed to the MWCNT network hindering crystal growth. Here, the MWCNTs act as heterogeneous nucleating agents for HDPE crystallization, but the reduction in crystallinity observed may be related to the formation of smaller and less perfect crystallites [22], as the MWCNT network breaks the continuity of the polymer matrix while preventing formation of large and uniform crystallites.

4.4 SAXS/WAXS Analysis of un-foamed HDPE-MWCNT Composites

The crystallization behaviour of the composites was the subject of an in-depth discussion in Submission Portfolio No. 4. To investigate the effect of adding MWCNTs on the crystallite size and crystalline content of HDPE, X-ray scattering methods, i.e. small (SAXS) and wide (WAXS) angle and, XRD were employed with, the specific aim of obtaining further insight in to the morphology and crystalline structure of the HDPE matrix and the nucleating effects of MWCNTs on HDPE.

Figure 4.4 shows the 2D SAXS/WAXS patterns of the undrawn HDPE and composites of HDPE and MWCNTs (columns two and three) and column four gives a physical interpretation of the lamellar macro-morphology structure from the SAXS/WAXS patterns. The SAXS pattern for neat HDPE shows an isotropic ring of intensity which is indicative of a randomly oriented crystalline lamellar structure [23]. Similarly, the WAXS pattern shows several rings, the two strongest are the (110) and (200) reflections of the orthorhombic unit cell of HDPE [24]. The WAXS pattern indexing also shows other strong reflections attributed to the (210) and (020) basal planes. The SAXS patterns of the un-foamed HDPE-MWCNT composites are quite different from the unfilled HDPE homopolymer. At MWCNT loadings between 0.01 wt% and 0.5 wt% the SAXS patterns show two features; an isotropic ring of scattering and concentrated spots and arcs of intensity as well, superimposed on the ring. The isotropic ring again indicates the randomly oriented crystalline lamellar structure of the HDPE, but the concentrated spots and arcing suggest some orientation of the lamellar structure, leading to a fibril or 'shish-kebab' type of structure [23], which is usually seen in polymers having undergone deformation [25, 26]. Here, the CNTs can act as the shish offering heterogeneous nucleation sites for the HDPE polymer chains to wrap around, and crystallites (kebabs), grow epitaxially outwards. This structure is often termed a nanohybrid shish-kebab (NHSK) morphology and is often seen during solution crystallization of the polymer on to the surface of the CNTs [27].
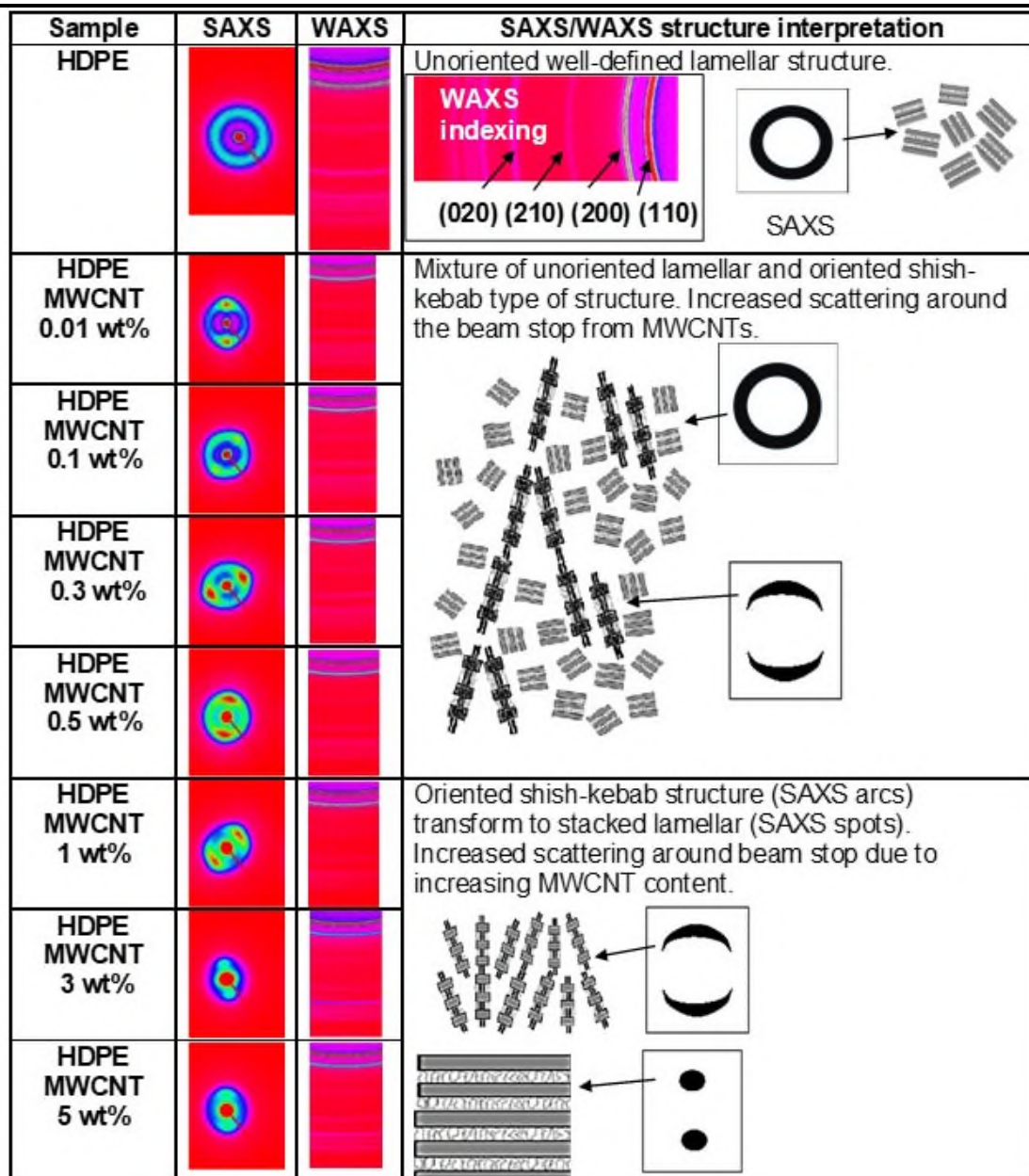
Figure 4.4. 2D SAXS/WAXS patterns for undrawn HDPE and composites of HDPE and MWCNTs, including crystalline lamellar structure interpretation.

This NHSK structure was also observed in melt-processed composites of PET and MWCNTs [26, 28, 29] where the MWCNTs have been aligned in the polymer during extrusion, and act as oriented nucleation sites for the crystallization of the polymer [30]. Here, for the composites of HDPE and MWCNTs the MWCNTs have some residual orientation from the initial injection moulding of the samples, where they act as stiff rod-like structures in the polymer melt and do not relax in the mould once aligned in the polymer matrix, even on cooling. The HDPE chains in close proximity of the oriented MWCNTs can then crystallize epitaxially out from the CNT surface. The HDPE matrix not in near contact with a MWCNT will crystallize as an un-oriented lamellar structure.

To investigate the orientation of the shish-kebab/lamellar stack structure in the composites of HDPE and MWCNTs, 1D azimuthal profiles were obtained from the 2D SAXS patterns and the FWHM obtained from the averaged fits of the peaks in the 1D azimuthal profiles.
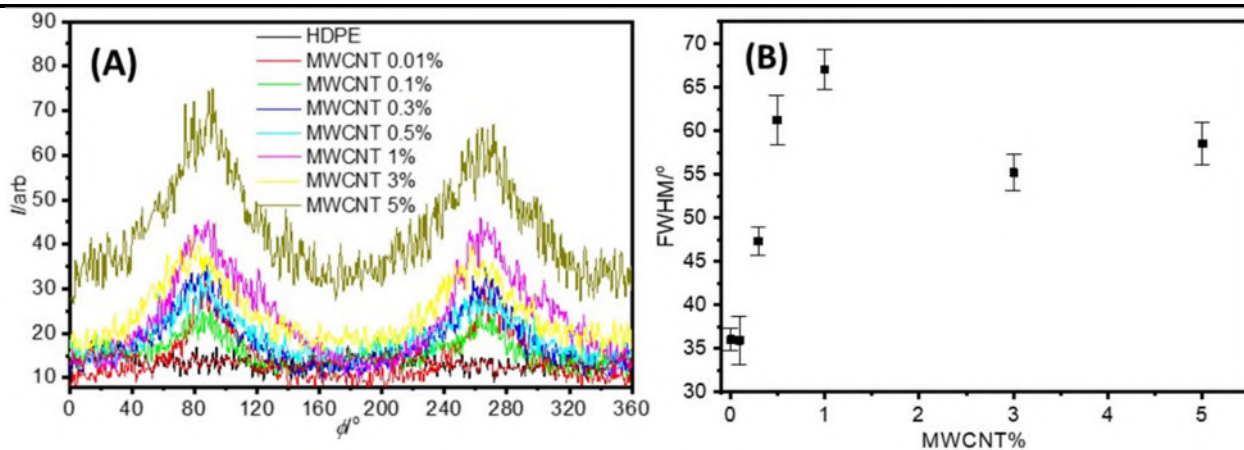
Figure 4.5. (A) 1D Azimuthal profiles from SAXS of undrawn HDPE and composites of HDPE and MWCNTs and, (B) change in FWHM from 1D azimuthal scans of the HDPE-MWCNTs composites.

Figure 4.5(A), shows the 1D azimuthal profiles of the samples and the averaged widths of the two peaks for each sample are, shown in Figure 4.5(B). Lower values of FWHM indicates a higher relative orientation of the lamellar stacks.

The unfilled HDPE did not show any preferred orientation so the azimuthal 1D profile is flat. However, for the composites of HDPE and MWCNTs there is preferred orientation as shown by the development of the peaks in the 1D azimuthal profiles.

The orientation of lamellar/shish-kebab stacks are greatest for the lowest MWCNTs loading, up to 0.1 wt%. Stack orientation decreases as the content of MWCNTs increase up to 1 wt%. As the morphology changes to a lamellar structure at MWCNTs > 1 wt%, the orientation starts to increase slightly again and then plateaus. At low MWCNTs loadings of between 0.01-0.1 wt% the MWCNTs being more isolated from each other [16], can easily be oriented in the polymer matrix during melt processing (moulding) and do not relax on cooling, so an oriented nanohybrid shish-kebab (NHSK) structure is formed; confirmed by the 2D SAXS patterns (Figure 4.4). As the MWCNT loading increases the CNTs entangle more and agglomerate and, are more difficult to orient during the moulding process, so the shish-kebab morphology is less oriented. This structure then develops into an interconnected lamellar structure [14, 16] with increasing MWCNTs loading > 1 wt%.

To investigate the crystallite lattice structure of the composites, 1D WAXS profiles were obtained from the 2D WAXS patterns (in Figure 4.4), along with the XRD profiles. Figure 4.6(A), shows the 1D WAXS profiles of the moulded HDPE and composites of HDPE and MWCNTs. The 1D WAXS profiles of all samples show two intense peaks which correspond to the (110) and (200) orthorhombic unit cell peaks of polyethylene [31] (as indexed in Figure 4.6(A)). There is no significant difference in the position of these peaks with increasing MWCNTs loading thus it can be, concluded that the MWCNTs do not influence or modify the orthorhombic unit cell of HDPE. Furthermore, there is no real evidence of the (002) peak at 26°, which corresponds to the d-spacing between graphene sheets of 3.42 Å [32, 33]. Other MWCNTs peaks are in similar positions to the

HDPE peaks so cannot be confirmed as extinct or not, i.e. (100) at 43° and (101) at 44° corresponding to the in-plane graphitic structure and lateral spacing of graphite layers [33]).
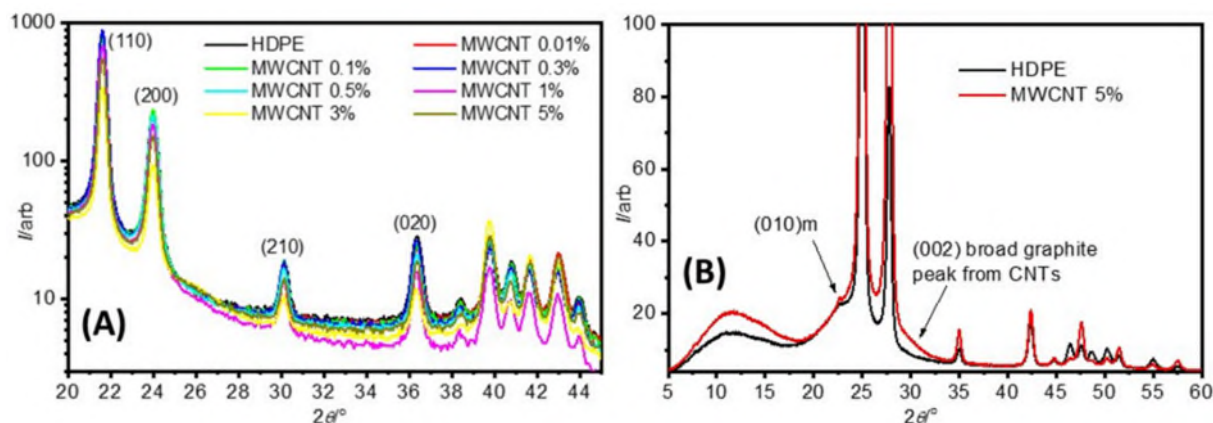
Figure 4.6. (A) 1D WAXS profiles of moulded HDPE and composites of HDPE and MWCNTs and (B) XRD profiles of neat HDPE and a composite of HDPE and 5 wt% MWCNTs.

In Figure 4.6(B), the XRD profiles of neat HDPE and the 5 wt% composite are shown. From the XRD profiles there is some evidence of the (010) monoclinic polyethylene peak (labelled as (010)m) therefore, there is some mixture of unit cells in the samples, but other monoclinic peaks are absent, so this phase is only a very minor component [34] and is not influenced by the addition of MWCNTs to the polymer matrix. There is a very broad shoulder at ~30°, which can possibly be assigned to the (002) graphitic sheet spacing [33, 35], but again this is very weak. The lack of distinct strong MWCNTs peaks in both the WAXS and XRD data for the composites is attributed to the good dispersion of the MWCNTs in the polymer matrix [35, 36].

To investigate the shish-kebab and lamellar macrostructure of the moulded HDPE and composites, 1D SAXS profiles were obtained from the 2D SAXS patterns and are shown in Figure 4.7. All samples show a main SAXS peak at q ~0.027 Å^{-1} which represents the average length of the crystalline and amorphous regions of the lamellar stacks in the polymer, or long period (L_{p}). As the weight fraction of MWCNTs is increased in the composites, the low angle scattering intensity ($q <$ 0.02 Å^{-1}) increases which is attributed to scattering from the MWCNTs [14, 37].
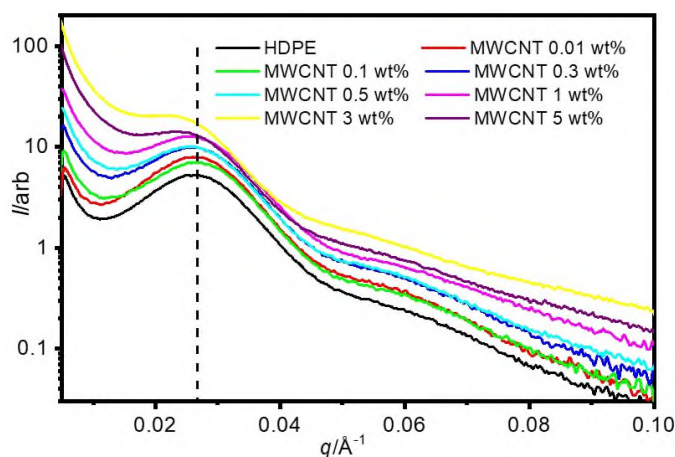
Figure 4.7. 1D SAXS profiles of neat HDPE and composites of HDPE and MWCNTs with up to 5 wt% MWCNTs. Vertical dashed line indicates the peak maximum at 0.027 Å^{-1}.

From the 1D SAXS profiles, correlation functions were obtained to investigate the crystalline morphology development in the samples. Several parameters were extracted from the correlation functions, such as long period (L_p), crystalline layer thickness (H_b) and local crystallinity (X_c) and the data is collated in Table 4.2.

Table 4.2: Correlation function parameters extracted from the 1D SAXS profiles of neat HDPE and composites of HDPE and MWCNTs.

Sample	L_p/Å	H_b/ Å	X_c/%
HDPE	203	53	26
HDPE+0.01wt%MWCNT$_S$	204	54	27
HDPE+0.1wt%MWCNT$_S$	201	54	27
HDPE+0.3wt%MWCNT$_S$	205	51	25
HDPE+0.5wt%MWCNT$_S$	207	49	24
HDPE+1wt%MWCNT$_S$	204	41	20
HDPE+3wt%MWCNT$_S$	224	38	17
HDPE+5wt%MWCNT$_S$	215	35	16

The L_p, tends to increase from a MWCNT loading of > 0.5 wt%, which is confirmed by the shift to low q in the 1D scattering profile (Figure 4.7). Similarly, H_b, tends to increase slightly and then decreases with MWCNT loadings of > 0.3 wt%. As the L_p is the average length scale of the crystalline layer plus amorphous layer, the increase (and as such decrease in H_b), indicates that the amorphous layer increases with increasing MWCNT loading. This is mirrored with the decrease in X_c, where a reduction in the local crystallite size follows a decrease in crystallinity. Hence, from these results the MWCNTs at low loadings (up to 0.1 wt%) can have a nucleating effect on HDPE increasing the crystallite size and crystallinity slightly. However, at MWCNT loadings >0.3 wt% and above, there tends to be a reduction in the crystallite size and local crystallinity, indicating that the MWCNTs when more concentrated in the matrix, hinder nucleation and growth of crystallites [26]. This is also seen in the DSC data, where the bulk crystallinity ($X_{c(DSC)}$), is reduced at higher MWCNTs loadings due to the confinement effect of the MWCNTs.

4.5 Static Tensile Mechanical Properties of un-foamed HDPE-MWCNT Composites

As the change in crystallization behaviour of HDPE on inclusion of MWCNTs is expected to alter the mechanical properties of the HDPE matrix, the variation in the tensile mechanical properties of HDPE as a function of MWCNT loading was studied under static mechanical tensile loading and representative stress-strain curves are shown in Figure 4.8. Additionally, the average (from 7 replicates) values for the elastic modulus (Young's modulus), tensile strength (yield stress, σ), strain at tensile strength (elongation at yield) and tensile strain at break (elongation at break, ε) for the composites are listed in Table 4.3.
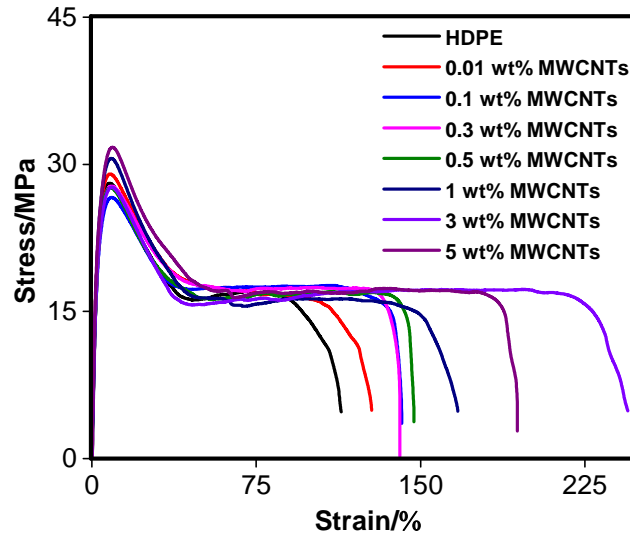
Figure 4.8. Variation of stress as function of strain for unfilled HDPE and HDPE-MWCNT composites.

The stress versus strain curves in Figure 4.8 show that each composite sample tends to reach the upper yield point (yield stress), drawing through its neck (where the sample extends elastically), and reaches the lower yield point, after which it draws until break. Necking of the composite samples is followed by a plateau region that extends until the breaking point due to strain induced crystallisation of the polymer resulting in the material hardening.

Table 4.3. Changes in tensile mechanical properties of HDPE and HDPE-MWCNT composites.

Sample	Young`s Modulus /GPa	Tensile Strength /MPa	Strain at Tensile Strength /%	Tensile strain at break /%
HDPE	1.69± 0.16	30.78± 5.63	9.83± 1.02	109.35± 48.66
HDPE+0.01wt%MWCNT$_S$	1.15± 0.39	28.70± 0.99	10.12± 2.60	133.25± 35.15
HDPE+0.1wt%MWCNT$_S$	1.49± 0.22	28.11± 2.63	10.98± 0.62	190.76± 59.66
HDPE+0.3wt%MWCNT$_S$	1.64± 0.14	29.55± 4.02	11.73± 0.71	157.73± 82.02
HDPE+0.5wt%MWCNT$_S$	1.53± 0.13	28.10± 0.96	11.13± 0.46	107.85± 22.60
HDPE+1wt%MWCNT$_S$	1.75± 0.10	30.87± 1.05	10.23± 0.48	78.66± 53.85
HDPE+3wt%MWCNT$_S$	1.96± 0.13	34.97± 0.63	9.62± 0.34	50.12± 5.72
HDPE+5wt%MWCNT$_S$	1.81± 0.09	33.32± 0.81	10.33± 0.38	72.78± 19.03

Overall, a modest improvement in the stiffness of HDPE was obtained on inclusion of MWCNT. Effective reinforcement in composites requires individual nanotubes to be coated with polymer in order to ensure load transfer from matrix to nanotube [38]. Commonly, enhancements in polymers stiffness are reported to be prominent mostly in low CNT weight fractions up to 5 wt% [39].

Here, the elastic modulus (Young's modulus) and tensile strength (yield stress, σ) of HDPE overall increased on addition of MWCNTs. The greatest increases in the elastic modulus (↑16%) and tensile

strength (↑14%) were observed for composites containing 3 wt% MWCNT. The presence of MWCNT stiffens the polymer matrix, resulting in increased values for elastic modulus relative to the unfilled HDPE [20]. The aspect ratio of CNTs plays an important role in the reinforcement of polymers, especially in the value for Young`s Modulus [13]. Elastic modulus and tensile strength trends are also reported graphically in Figure 4.9(A) and 4.9(B), respectively, as a function of MWCNT contents.
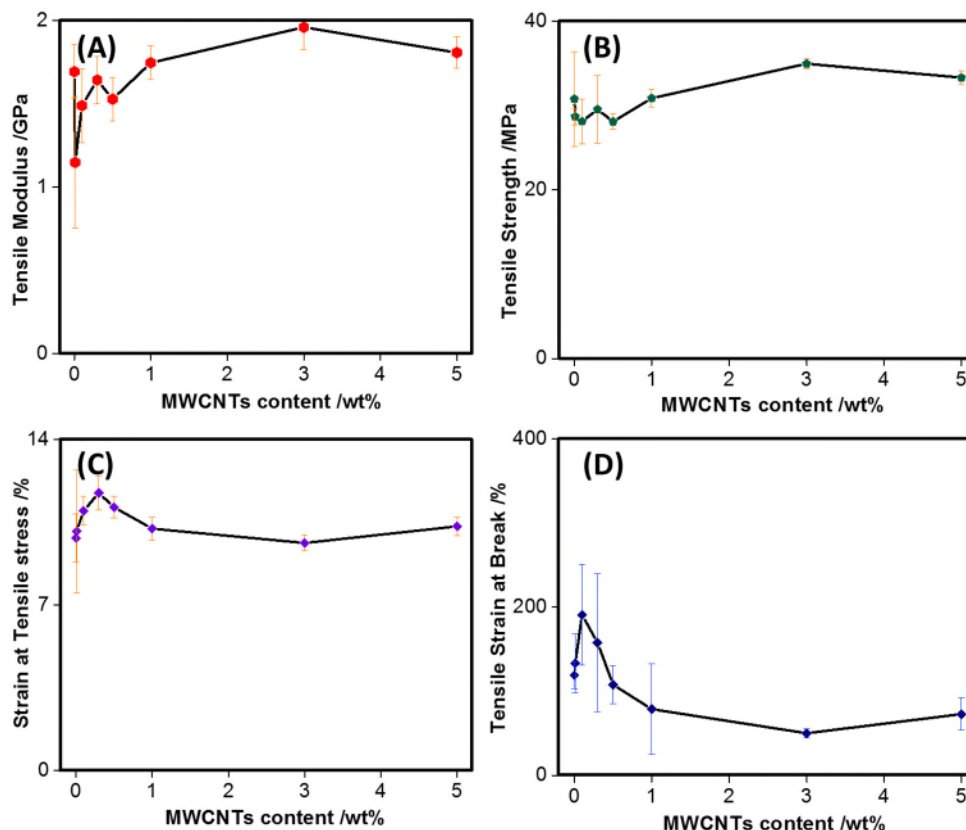
Figure 4.9. Variation in (A) Young`s modulus, (B) tensile strength (yield stress), (C) strain at tensile strength (elongation at yield), and (D) tensile strain at break (elongation at break) as function of MWCNT loading.

The tensile strength (i.e. maximum stress a material can sustain under uniaxial tensile loading) of MWCNT filled HDPE composites slightly improved for MWCNT contents increases higher than 1 wt%, whereas decreased for MWCNT reinforcement ratios below (<1 wt%). Inclusion of MWCNTs at ≤ 3wt% provided a slight improvement in tensile strength associated with the homogeneous distribution of the filler in the polymer matrix, increased polymer-filler entanglements and stress transfer from the tubes to the matrix.

Slight changes of increased stiffness and reduced strength have been commonly reported for plastics when adding reasonably low concentrations of fillers [40]. Here, the polymer ductility increased sharply below percolation before decreasing again above percolation. Although less crystalline content in composites support higher elongations [41], the trends in elongation at yield (tensile strength) and even more so elongation at break (tensile strain at break, ε) versus weight percent of

MWCNTs, reported in Figures 4.9(C) and 4.9(D), respectively, showed a rather interesting behaviour.

The results revealed a steep increase in elongation at break (i.e. tensile strain at break) moving from neat polymer to composites with filler loadings up to 0.5 wt%, while further increases of MWCNTs negatively affected the ductility of the composites. Generally, addition of rigid particles to a polyolefin matrix reduces the elongation at break [42]. As reductions in elongation at break are reported to be dependent on the segmental flexibility of the polymer chains [43], the presence of MWCNTs restricted the conformational change in the polymer chains. Surprisingly, inclusion of MWCNTs between 0.01 and 0.3 wt% increased the amount of deformation achieved by the composites before failure instead of inducing a decline in elongation at break. Stabilisation and growth of a neck occurred in the composites at low MWCNT content up to 0.3 wt%, indicating that polymer chains in the amorphous regions were still able to orientate and stretch in the direction of the applied tensile stress despite the presence of the MWCNTs. Thus, overcoming the increase in stress due to the reduced cross-sectional area. Addition of MWCNTs, above the percolation threshold, hindered orientation of the polymer chains such that failure occurred before necking during tensile testing, the inclusion of MWCNTs altered the uniaxial deformation behaviour of HDPE. On the other hand, the presence of a MWCNT-polymer network formed provides a high resistance to polymer chain orientation as, fundamentally, the rheological percolation threshold is determined by polymer chain immobility [4].

The strain at break (ε) of HDPE steadily increases by 22%, 74% and 44% for the composites with MWCNT content of 0.01, 0.1, and 0.3 wt%, respectively. The highest increase in ε was achieved for the composite with 0.1 wt% MWCNTs. In contrast, on inclusion of 3 wt% MWCNTs, ε is reduced by 54% compared to the neat polymer. Addition of MWCNT to HDPE increased the ductility of the matrix. This was quantified by integrating the area under the stress-strain curves and, determining the ratio of plastic to elastic energy (i.e. ratio between tensile toughness and resilience), see Table 4.4 [a].

This ratio increases with increasing MWCNT loading. Several different processes can come into play (e.g. spherulite and/or lamella breakup in crystalline polymers in addition to amorphous chain

---

[a] Table 4.4 provides an estimation of the values of tensile toughness, resilience and their ratio (i.e. ratio of plastic to elastic energy) for neat HDPE and composites of HDPE and MWCNTs, calculated from the stress-strain plots as integrated area under the entire stress-strain curve to the break point (i.e. ultimate toughness), the integrated area up to yield (i.e. resilience) and their ratios. Tensile toughness, expresses in units of $J/m^3 = N/m^2 = Pa$ is commonly used as a useful means of comparing materials and is a measure of the ability of the material to absorb energy without fracture. Tensile toughness, as just defined, should not be confused with fracture toughness, which is the resistance to failure in the presence of a crack, considered to be the primary measure of toughness for engineering purposes. The units of J/m or J/m^2 commonly found in literature for the toughness are determined from impact strength tests rather than from the integration of the tensile curves. Although the impact test is more accurate to determine the toughness, an initial screening from the calculation of the area under the stress-strain curve might give a reliable estimation.

segment reorientation) [44]. It is clear from the necking behaviour observed during tensile testing that the, inclusion of MWCNT alters the uniaxial deformation behaviour of HDPE.

Table 4.4: Estimated values of tensile toughness, resilience and the ratio between tensile toughness and resilience (i.e. ratio of plastic to elastic energy) for neat HDPE and composites of HDPE and MWCNTs.

MWCNT loading /wt%	Tensile Toughness/ GPa	Resilience/ GPa	Ratio of Plastic:Elastic Energy
0	2.01	0.16	12.6
0.01	2.31	0.19	12.2
0.1	2.58	0.20	12.9
0.3	2.61	0.19	13.7
0.5	2.63	0.17	15.5
1	2.89	0.20	14.5
3	4.18	0.19	22.0
5	3.59	0.23	15.6

4.6 SAXS/WAXS Analysis of Uni-axially Drawn HDPE and HDPE-MWCNT composites

To investigate the effect of the MWCNTs on the crystalline morphology development in HDPE during uniaxial deformation, 2D SAXS/WAXS data was taken at the neck section of a drawn sample. Figure 4.10 shows selected 2D WAXS/WAXS patterns of the drawn samples, where the draw direction is vertical in all cases.
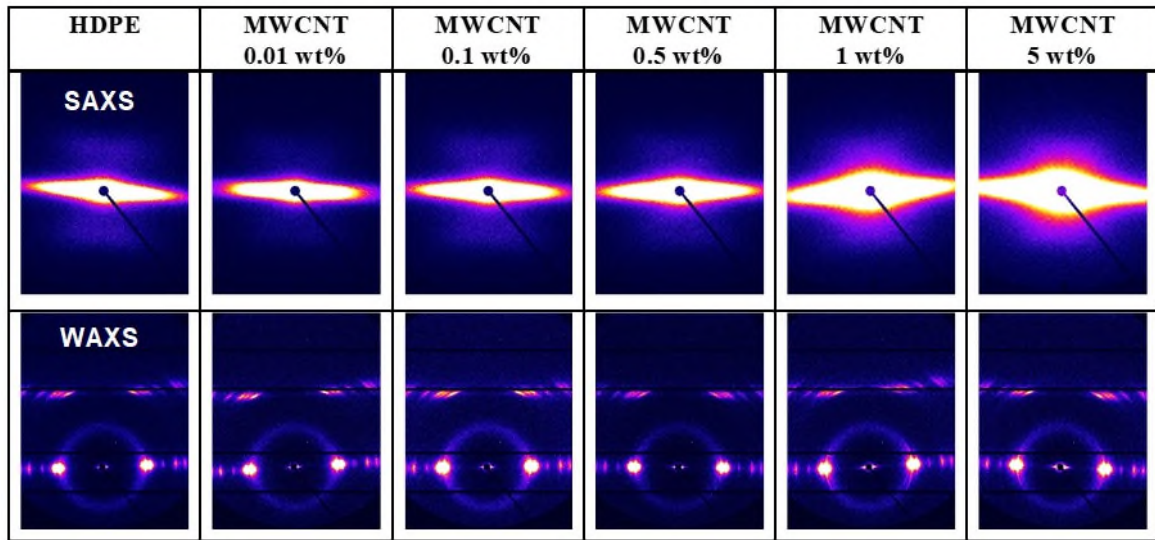
Figure 4.10. 2D SAXS/WAXS patterns of HDPE and composites of HDPE and MWCNTs post-drawing. (The draw direction is vertical in all patterns).

All 2D SAXS patterns showed intense lozenge shaped scattering in the equatorial direction for all samples. This equatorial scattering is due to cavitation occurring when the samples were deformed, (SEM images in Figure 4.12). Furthermore, diffuse scattering around the central beam stop is seen due to, the increasing MWCNTs content. In the vertical direction the, SAXS patterns for the neat

HDPE and the composites show evidence of a 4-point pattern, which indicates an oriented sheared herringbone lamellar structure [23, 26]. Hence, on cold drawing the un-oriented crystalline lamellar structure of the HDPE matrix becomes oriented in the draw direction. This is also confirmed in the 2D WAXS patterns in Figure 4.10, where in all samples the rings from the orthorhombic crystal structure of HDPE, are now concentrated as spots, indicating highly oriented crystallites are now present.
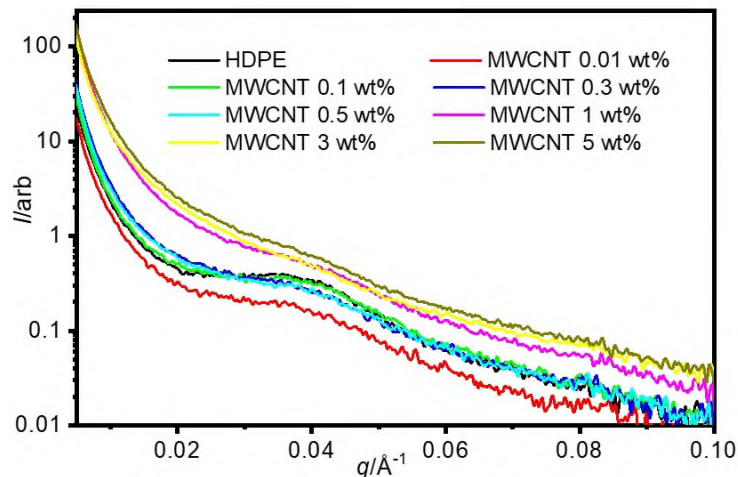
Figure 4.11. 1D SAXS profiles of drawn HDPE and composites of HDPE and MWCNTs.

Figure 4.11 shows the 1D SAXS profiles obtained from the vertical sector integration of the 2D SAXS patters in Figure 9. The main peak position has shifted to lower q (~0.037 Å^{-1}) compared to the undrawn samples. However, this peak is masked at higher MWCNTs loadings (> 0.5 wt%) from the low angle scattering intensity due to the MWCNTs themselves. 1D correlation functions obtained from the 1D SAXS profiles (where a fit was possible), were obtained and the data collated in Table 4.5.

Table 4.5. Correlation function parameters extracted from the 1D SAXS profiles of drawn HDPE and composites of HDPE and MWCNTs.

Sample	L_p/Å	H_b/ Å	X_c/%
HDPE	152	44	29
HDPE+0.01wt%MWCNTs	145	44	30
HDPE+0.1wt%MWCNTs	145	40	28
HDPE+0.3wt%MWCNTs	146	30	21
HDPE+0.5wt%MWCNTs	144	30	21

From this data, the shift in L_p of the peak is confirmed, being reduced compared with the undrawn samples. There is also a reduction in crystallite thickness, which is likely due to the insertion of thinner lamellae in the amorphous regions due to some strain-induced crystallization. The local

crystallinity X_c, is seen to increase very slightly, again this can be attributed to the insertion of thin lamellae in the amorphous regions during strain (elongation) induced crystallization. The same trend in crystallinity is seen in the drawn samples compared with the undrawn samples, that is, a nucleating effect occurs on addition of MWCNTs at lower loadings (up to 0.1 wt%) in the HDPE. At MWCNTs loadings of >0.3 wt%, there is a reduction in local crystallinity, indicating that the MWCNTs, hinder nucleation and growth of crystallites of the HDPE matrix, irrespective of the rate of HDPE crystallization kinetics.

During tensile testing of both the HDPE and the composites of HDPE and MWCNTs, a stress-whitening zone developed perpendicular to the draw direction. The surface of the samples in this region were imaged with a SEM and the, micrographs obtained are shown in Figure 4.12.
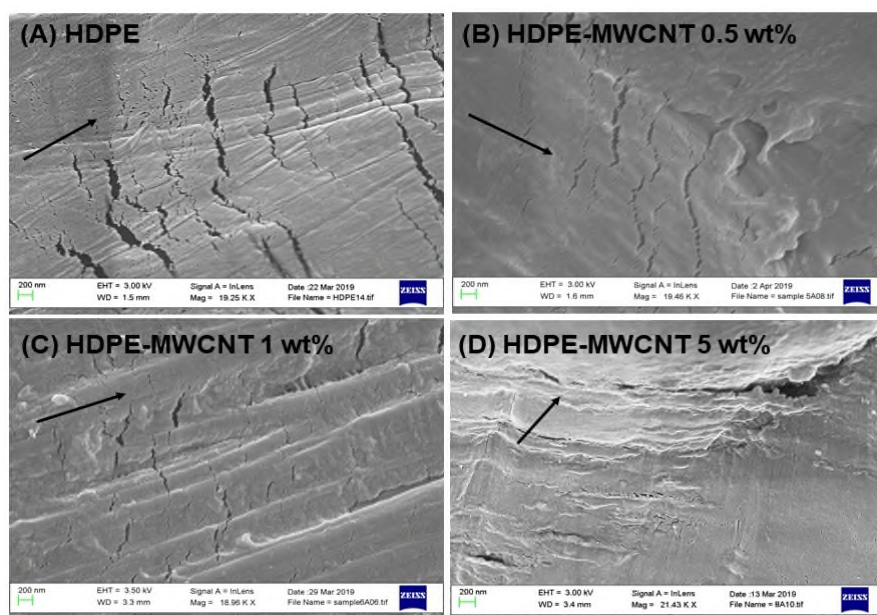
Figure 4.12. SEM images of crazed regions in drawn (A) HDPE and composites of HDPE and MWCNTs at loadings of (B) 0.5 wt%, (C) 1 wt% and (D) 5 wt%. Arrows in each image indicates the draw direction (scale bar 200nm).

The SEM images in Figure 4.12, all show evidence of crazing and voiding occurring perpendicular to the draw direction (indicated by the arrow in the images). This explains the stress whitening occurring in the drawn samples and the intense equatorial scattering observed in the 2D SAXS patterns in Figure 4.10.

4.7 DMTA: Dynamic mechanical properties of un-foamed HDPE-MWCNT composites

The dynamic mechanical thermal properties of the composites were measured using Dynamic Mechanical Thermal Analysis (DMTA), an important tool to study the effects of temperature/frequency on the viscoelastic properties of polymeric composites [45], hence here it was used to determine the dynamic stiffness, glass transition temperature and damping

characteristics of the composites. It should be recalled that the acoustic properties of polymers depend on frequency and temperature since their viscoelastic properties depend on these. The speed of sound and absorption in fact depend on the free volume in the polymer. The largest change in acoustic properties of polymers occur across the *glass transition temperature*, T_g. As was discussed in chapter 2 (literature review, section 2.5), the material microstructure highly influences the propagation of ultrasonic waves, affecting acoustic attenuation and vibration damping of the material. The vibrational energy can be dissipated by shearing motion (deformation) of the viscoelastic material, and the inherent capacity of a damping material for dissipating vibrational energy can be assessed. For a given polymer, acoustic damping is reported to depend on the temperature and frequency of the measurements and is dominated by the glass transition occurring in the amorphous phase of the polymer.

In this work, a dual cantilever bending geometry, a cooling/heating rate of 2 °C/min and a constant frequency of 1 Hz were applied during the tests. During the test, the sample response to a dynamic load was monitored and the temperature dependence of loss tangent (tan δ), storage modulus (E'), and loss modulus (E'') for each sample is reported in Figure 4.13 ((A), (B), (C), respectively). It is noteworthy to state that E' is a measure of a material ability to store energy (i.e. elastic energy) and therefore it is a measure of material stiffness [46]. The mechanical damping was assessed through the loss tangent (tan δ= E''/E'), while E'' reflects the energy loss in the form of heat during deformation in a loading cycle [47]. The maxima in the tan δ curve is associated with the main relaxation processes of the material of interest. Semi-crystalline polymers exhibit a complex combination of thermal transitions that occur in the crystalline phase as well as in the amorphous phase [48]. Three main relaxation processes characterise linear PEs and thus HDPE and all are visible in the temperature dependence plots of DMTA.

The temperature corresponding to the maximum in the tan δ curve is defined as the glass transition temperature (T_g) [49].
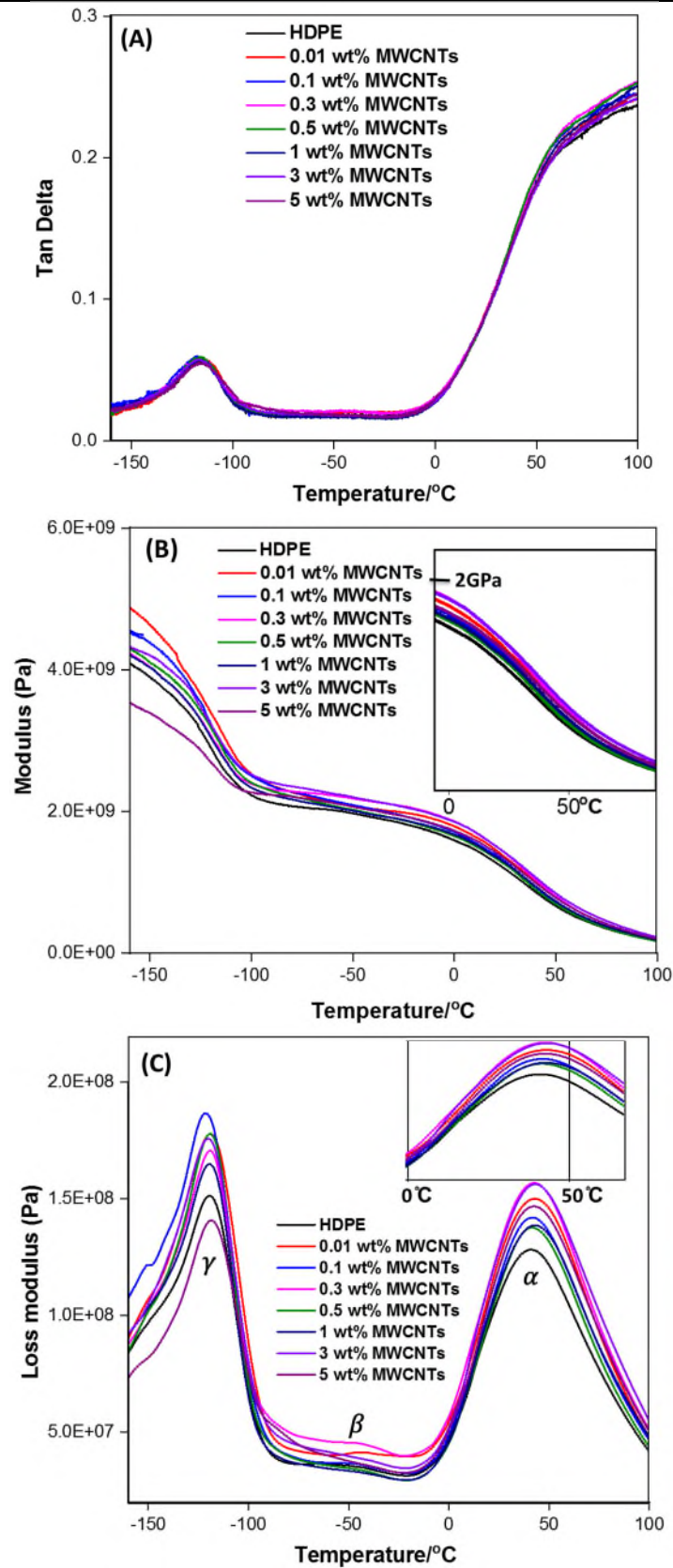
Figure 4.13. Temperature dependence of; (A) loss tangent, also called damping factor (tan δ), (B) storage modulus (E'), (C) loss modulus (E'') obtained for neat HDPE and HDPE-MWCNT composites.

From the comparison of the variation of E', E'', and tan δ as a function of temperature reported in Figure 4.13, it can be seen that samples displayed two well-resolved relaxations, *α* and *γ*, and a very weak *β* relaxation peak. In order of increasing temperature; the γ-relaxation process is related to the

glass transition of the PE, the β-relaxation (usually present only in branched PEs) is attributed to the relaxation mechanisms in the amorphous regions and, the α-relaxation is derived from the relaxation mechanisms in the polymer crystalline regions (i.e. processes related to molecular motions within crystallites) [50]. The γ relaxation, seen here as a maximum in the loss modulus curve (Figure 4.13(C)), positioned at $-119\,°C$ for the HDPE and between $-118\,°C$ and $-122\,°C$ for the composites, but also as a maximum in the tan δ plot (Figure 4.13(A)) at slightly higher temperatures and an associated drop in the storage modulus (Figure 4.13(B)). The γ relaxation has been associated with a single relaxation process, predominantly occurring in the amorphous region of semi-crystalline polymers, due to the joint movements of chains containing three or more methylene groups (units) in the main chain [51, 52]. A decrease in the intensity of the γ relaxation can be attributable to a decrease in the quantity of the amorphous phase, whereas the position of the γ peak in the loss modulus plot changes depending on the type of PE (e.g. LDPE, LLDPE, or HDPE) and crystalline content (between 20% and 70%) between $-125\,°C$ and $-105\,°C$ [51, 53]. The β relaxation can be observed as a weak maximum in the loss modulus plot (Figure 4.13(C)), appearing here at ca. $-40\,°C$ for the neat HDPE and at higher temperatures for the composites. In particular, the composite with 0.3 wt% MWCNT loading showed the most intense β transition peak amongst all the samples, presumably due to increased interfacial interactions between HDPE matrix and MWCNT prior the formation of the percolated network. Depending upon the type of polyethylene, the β relaxation process was found to occur between $-5\,°C$ and $-50\,°C$ [52, 54]. Some authors attributed the β relaxation to the motion of chain units in the interfacial region [54], others to the glass transition [53]. However, the absence of the β relaxation in typical linear polyethylene suggests a different molecular origin of the process in linear PEs with high molecular weights compared to those aforementioned for branched polyethylene. Nitta and Tanaka [52] defined the β relaxation as a consequence of the motion of the loose tie molecules in polyethylene with high molecular weights, as loose tie and loop molecules typically form in the amorphous layers of this PE type, whereas linear PEs with a thinner amorphous layer promote taut tie molecules and lack loose tie molecules. The α relaxation process is attributed to the reorientation of molecules within the crystal [55]. The position of the α relaxation maximum is connected with crystallite thickness, whereas the intensity of the peak is related to the crystalline content [52]. The α relaxation process is hence affected by polymer chain mobility in the crystallites, occurring at higher temperatures as crystallite thickness increases [51]. In Figure 4.13(C), the α relaxation is well resolved as a maximum in loss modulus centred at $41\,°C$ for HDPE, and its value strongly depends on filler type and content. The α relaxation can be detected also from the small hump before the melting process in the tan δ plot (Figure 4.13(A)). The addition of MWCNT increased the α relaxation to about $43\,°C$ for a MWCNT content

of 3 wt%. As a result of the increased stiffness in the material, the composites displayed a more intense α peak compared to neat HDPE.

The effect of MWCNT content on the storage modulus of HDPE-MWCNT composites is shown in Figure 4.13(B). The storage modulus of the composites was higher than corresponding HDPE in the β and α relaxations regions, due to the stiffening effect of the MWCNTs. The inclusion of MWCNTs can hinder polymer chain mobility in the amorphous phase of HDPE thus improving the modulus, with a storage modulus at the interface higher than that of the bulk polymer [51].

Surprisingly, no significant changes were observed in E' of the composites upon addition of the MWCNT above the percolation threshold due to the formation of a matrix-filler network. Likewise, no significant differences in storage modulus were observed at high temperatures.

Polymers damp significantly near their glass transition temperature; the moduli and speed of sound drop above T_g while absorption increases until reaching a maximum. At the glass transition temperature, polymers experience a substantial change in properties and change from being hard and brittle to soft and pliable and the polymeric structure turns into rubbery upon heating and glassy upon cooling [45]. It should be pointed out that the glass temperature of a composite is the temperature at which the matrix changes its properties, so it could be used as a measure of the change in matrix properties due to the addition of an inorganic filler (i.e. second phase). E' is considerably high below T_g (see Figure 4.13(B)), since the polymer is in its glassy state. The stiffness (higher modulus) of the polymer in this state is related to the change in the elastic energy stored on deformation, which is associated with small displacements of the molecules from their equilibrium position. At around -115°C, where the polymer passes from the glassy state to the rubbery state, the macromolecular chains are more flexible and this favours conformations that are maximizing the entropy with a consecutive decrease in stiffness. A shift in T_g upon filler addition is related to the degree of interaction between the phases (i.e. micro-particles/matrix interaction) regardless of any mechanical reinforcement effects of the filler [56]. Here, changes in the T_g as a function of the MWCNT loading are reported in Table 4.6.

Table 4.6. Glass transition temperature of neat HDPE and HDPE-MWCNT composites obtained from tan δ peaks.

Sample	Tg /°C
HDPE	-115.5
HDPE+0.01wt%MWCNTS	-114.5
HDPE+0.1wt%MWCNTS	-117.5
HDPE+0.3wt%MWCNTS	-115.7
HDPE+0.5wt%MWCNTS	-115.9
HDPE+1wt%MWCNTS	-115.7
HDPE+3wt%MWCNTS	-116.0
HDPE+5wt%MWCNTS	-114.9

The data in Table 4.6 shows a modest decrease in T_g in the composites but overall, it did not change to a marked extent. Many researchers have reported a common increase in the T_g as a function of filler content, yet decreases in the T_g have also been attained mostly in amorphous polymers [49, 57]. Shifts in the T_g could be related to the degree of adhesion (e.g. molecular contact at the interface) between the polymer and the filler, as well as to the interfacial area available [56]. The interaction occurring between the surface of the filler particles and the polymer chains can lead to drastic alterations of the chain dynamics in the region immediately surrounding the particle [57]. Even low filler fractions, for a well-dispersed system, could provide a huge interfacial area through which, over a finite distance, the bulk properties of the polymer can ultimately be altered. The eventual presence of mobile polymer regions around the particles would explain the decrease in T_g, allowing more degrees of freedom for chain relaxation [57]. Nonetheless, changes in T_g upon addition of fillers are classified as significant if they show differences of more than $\pm 5\,°C$ compared to the T_g of the pure matrix [49], while the trend reported in the data in Table 4.6 did not show such significant changes in T_g. However, the composites with 0.01 wt% and 5 wt% MWCNT loadings manifested a small increase in T_g of $1\,°C$ and $0.6\,°C$ respectively, when compared to the neat polymer, which indicates a plausible decrease of free volume in the material amorphous region.

The shifting of T_g towards higher temperatures for the composites can be attributed to the enhancement of a polymer region with reduced molecular mobility compared to that of the neat polymer [11]. As the T_g is related to the amount of free volume in the amorphous part of the polymer, an increase in T_g means a decrease in the free volume and, therefore, in the mobility of the chains which are constrained due to the presence of the filler in this phase. The polymer matrix can be seen as formed by two parts; despite the part of polymer characterised by a reduced molecular mobility adjacent to the filler particles, there is the remaining of unaffected polymer with the same flexibility as in bulk [56]. Moreover, the presence of the crystalline phase can also impose restrictions on the mobility of the amorphous phase [58].

All composites exhibited enhanced stiffness compared to the neat polymer. The presence of the MWCNTs resulted in increased damping due to the development of an interphase where a new shear mechanism takes place because of the stress transfer at the filler/matrix interface [59]. In addition to the viscoelastic behaviour of both filler and matrix, the role of the interphase region in governing damping in polymer composites is notable where high shear strain energy is stored. The filler/matrix interphase region is in fact characterized by a complex state of stress, caused by geometric and material discontinuities existing between the filler and the matrix and the mismatch in their properties [59].

DMTA analysis revealed that MWCNT filled HDPE composites produced high loss materials with inherent damping capacity even at room temperature, especially for MWCNT contents of 3 and 5

wt% (with E'~1.5 GPa and E''~132 MPa at 25℃). As a result, these materials have the potential of being applied in passive damping control systems, where the noise generated by sound, vibration, and shock needs to be reduced, providing a means of enhancing the acoustic attenuation and vibration damping without a great loss of stiffness and strength. Nonetheless, passive damping typically requires thermal control in addition to high loss materials and both temperature and frequency range requirements are distinctive in selecting the polymers for damping applications.

A more in-depth study at different temperature and frequency ranges (and possibly different MWCNT loading > 5 wt%) would be useful in tailoring such composite materials as acoustic absorbers and/or acoustic dampers for a specific task (e.g. backing layer in acoustic transducers). The backing layer is an acoustically absorbing (highly lossy) material placed on the back of the transducer that couples the backward travelling waves with a consecutive damping. The requirements for the backing material in ultrasonic sensors are a high toughness for backings to withstand high pressures, dimensional stability, low coefficient of thermal expansion and characteristics of high attenuation and appropriate acoustic impedance (2–25 MRayl, depending on the transducer design) [60]. Tungsten is one of the most used fillers in backing materials. A heavily loaded backing generally is made by high volume fractions of tungsten (about 60 to 70%) in filled epoxy. However, the disadvantages are a relatively high coefficient of thermal expansion and high curing times as well as the fact that tungsten is expensive. Conversely, the use of HDPE-MWCNT composites for backing transducers would be very advantageous as they could offer damping properties and high stiffness, while ensuring strength and temperature characteristics at low cost. Furthermore, during manufacturing, storage, transportation and operation, an ultrasound transducer may be exposed to a large thermal interval (e.g. common range between -30℃ and +60℃), whereas a maximum allowed operational temperature exists for transducers operating at room temperature [60]. Therefore, when designing ultrasound transducers it is important to use backing materials having improved dimensional stability and low glass transition temperature outside this thermal range. A low coefficient of thermal expansion is also important to minimise thermal stresses that occur during both manufacturing and use of sensors, as these can damage the piezoelectric core (i.e. the active layer) and welded joints. Composites of HDPE and MWCNTs with a T_g below -115℃ could be considered as novel alternatives for the purpose.

4.8 TGA: Thermogravimetric Analysis of un-foamed HDPE-MWCNT Composites

The comparison of the thermogravimetric (TG) and derivative thermogravimetric (DTG) curves for HDPE, MWCNTs, and HDPE-MWCNT composites obtained from TGA are reported in Figure 4.14. As it is hard to distinguish between curves in the DTG graph of Figure 4.14(B) (as the curves overlap), each curve was shifted vertically and reported in a different plot, see Figure 4.14(C). In

addition, the relevant thermal parameters and the traces recorded at 10 K/min for HDPE and HDPE-MWCNT composites are listed in Table 4.7.
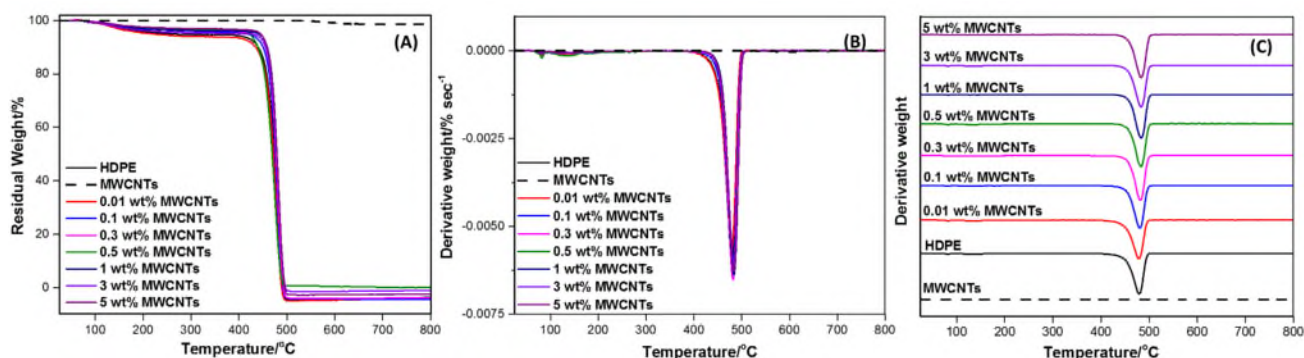
Figure 4.14. TGA curves (A) and corresponding DTG curves ((B), (C)) obtained for HDPE, MWCNT and HDPE-MWCNT composites.

As TGA is an effective method to understand the thermal stability of materials, the plots of TG-DTG in Figure 4.14 proved there was not a notable quantity of mass loss for the MWCNTs in the temperature range investigated (i.e. from T_{ROOM} to 800 °C) at a constant heating rate of 10 K min^{-1}. This result confirms the thermal stability of the MWCNTs, attributable, in part, to their high surface area and aspect ratio [61]. No degradation occurred at the temperatures used during melt processing as none of the samples tested degraded at temperature below 420 ℃, whereas the maximum temperature employed during processing was set at 160 ℃ during injection moulding. The weight losses recorded showed that degradation of the HDPE-MWCNT composites samples occur totally in a one-step process due to the presence of only one peak in the DTG (Figure 4.14(B)-(C)), between 479 ℃ and 483 ℃, which can be correlated with the temperature for maximum weight loss from HDPE (479 ℃). The thermal degradation reaction of HDPE, due to random molecular chain scission, occurs in a one-step process and forms alkyl and alkyl peroxyl radicals that are susceptible to inhibition reagents capable of trapping the radicals [21]. Products of the reaction are generally the formation of solid hydrocarbon residues (i.e. alkanes and alkenes) and numerous gaseous hydrocarbons [62]. The relevant thermal parameters such as onset temperature of decomposition (T_{dec_onset}), temperature of maximum weight loss (T_{dec_peak}), the temperatures at which 20% and 80% weight losses occurred, referred to as T_{20} and T_{80}, respectively, are all listed in Table 4.7.

TGA data confirmed mass loss degradation temperatures of the composites increased with MWCNT loadings increased. Inorganic substances possess higher thermal stability and can operate over a wide range of temperature, acting as heat barriers and retard volatilisation [51, 63]. CNTs enhanced the thermal stability of the polymer as they have high electron affinities and as such can act as scavengers for free radicals [21, 64], hindering the diffusion of heat mass transfer (outmigration of

degraded volatiles) to the surface, thus inhibiting thermal oxidation and retarding decomposition rates.

Table 4.7. Thermogravimetric data for un-foamed HDPE-MWCNT composite samples tested.

Sample	T_{dec_onset} /^{o}C	T_{dec_peak} /^{o}C	T_{20} /^{o}C	T_{80} /^{o}C
HDPE	418	479	458	482
HDPE+0.01wt%MWCNT$_S$	421	479	455	480
HDPE+0.1wt%MWCNT$_S$	425	481	463	484
HDPE+0.3wt%MWCNT$_S$	430	482	466	485
HDPE+0.5wt%MWCNT$_S$	433	483	453	480
HDPE+1wt%MWCNT$_S$	433	483	468	488
HDPE+3wt%MWCNT$_S$	437	483	467	487
HDPE+5wt%MWCNT$_S$	438	483	468	488

The TGA data in Table 4.7 show that the incorporation of MWCNTs improved the thermal stability of HDPE, proportionally to MWCNT content up to 5 wt%. HDPE is the first component that starts to decompose at 418 ℃, reaching its maximum value of decomposition rate at 479 ℃. With additions of MWCNT, the onset of decomposition is shifted to higher temperatures, by a further 3 ℃ at loadings of 0.01 wt% but by up to a further 25 ˚C at loadings of 5 wt%, indicating a more thermally stable system. The trend obtained for the temperature at which there was a maximum weight loss (T_{dec_peak}) showed that further increase in MWCNT loading above the threshold content of 0.3 wt% (at which percolation was achieved) did not alter the degradation behaviour of the composites. Furthermore, for both MWCNT loadings of 1 and 5 wt%, T_{20} and T_{80} of HDPE increased by 10 ℃ and 6 ℃, respectively. Moreover, the fact that no small weight losses were detected for temperatures below 400 ℃ suggests that the MWCNT had a low amorphous carbon content [4].

4.9 Density Measurements of un-foamed HDPE-MWCNT Composites

The density of HDPE and the HDPE-MWCNT composites was determined as density is a key factor in understanding the properties of polymers and/or composite foams. Density is related to mechanical (e.g. tensile strength and brittleness) and physical properties [40], and critically, it influences the acoustic properties of foams. The density of a polymer is a measure of how tightly the polymer chains can pack together (high density means close packing), and often used as an arbitrary indication of the degree of crystallinity of a polymer. Moreover, as an important characteristic of polymers is lightweight [65], density is one of the first material properties measured for lightweight materials since it expresses a measure of mass per unit volume of the material. A

reduction in density is equivalent to a reduction in weight and thus in cost, where the cost covers materials, manufacturing and transportation.

Density values for HDPE and HDPE-MWCNT composites were determined both theoretically (from Equation 3.7, reported in section 3.3.7) and experimentally (via analytical balance measurements) and results are presented in Table 4.8. Disks samples were tested by weighing each sample in air prior to immersion in the liquid (i.e. ethanol) and the arithmetic average values (from 3 replicates) of each sample are listened as following.

Table 4.8. Density values for neat HDPE and HDPE-MWCNT composites, obtained theoretically from predictions of the linear rule of mixtures (Equation 3.7) and experimentally from analytical balance measurements.

Sample	Predicted density /g cm^{-3}	Measured density /g cm^{-3}
HDPE	0.964	0.951
HDPE+0.01wt%MWCNTS	0.964	0.950
HDPE+0.1wt%MWCNTS	0.964	0.949
HDPE+0.3wt%MWCNTS	0.965	0.952
HDPE+0.5wt%MWCNTS	0.966	0.954
HDPE+1wt%MWCNTS	0.968	0.955
HDPE+3wt%MWCNTS	0.977	0.974
HDPE+5wt%MWCNTS	0.986	0.967

From the densities reported in Table 4.8, it should not be surprising if theoretical numerical values do not match exactly with the experimental ones. Sample disks underwent different steps of processing (i.e. grounding of the polymer to a fine powder in freezer mill, melt mixing step in the extruder and injection moulding step for the realisation of a disk sample). Differences in the thermal, mechanical, and chemical history of a polymer can lead to appreciable variations in density measurements [66].

Numerical values of sample densities obtained experimentally were smaller than those predicted. Nevertheless, it should be noted that all density measurements of solids are subject to error due to the presence of in-homogeneities, including surface imperfections, trapped air bubbles, etc. [66]. The possible presence of voids needs to be taken into account besides the samples thermal history. Nonetheless, density trends agreed quite well with each other. As expected, addition of MWCNTs resulted in a composite of higher density than that of the unfilled polymer. In general, the density of filled polymers (i.e. composites) increases with increasing filler content because of the high density of the latter compared to the polymer [67]. Furthermore, an increase in crystallinity is usually accompanied by an increase in the density of the composite, as crystals are of much higher density than amorphous regions in polymers [67]. However, here the correlation between density and

percent crystallinity ($X_{c(DSC)}$) did not show a strong linear relationship, may be related to the reduction in crystallinity observed from DSC due to the formation of smaller and less perfect crystallites.

4.10 Acoustic Properties of un-foamed HDPE-MWCNT Composites

The acoustic properties of the HDPE-MWCNT composites were evaluated via transmission of acoustic energy in air and across the sample disks produced via IM. In particular, the ultrasonic velocity (longitudinal) and attenuation coefficient of ultrasound in the samples (which determine the main acoustic characteristics of a material [68]), were acquired by frequency-domain analysis through ultrasonic air-coupled measurements in transmission. In the case of polymers, ultrasonic waves propagate through the material in response to forces acting along chain segments and between molecular chains that create displacements into neighbouring zones [68]. Measurements encompass comparing the ultrasonic transmissions through each sample to the transmission in air without a sample present. A minimum of two specimens for composite type of a given thickness (i.e. 1.65 mm) were tested and results are summarised in Table 4.9. No measurement percentage error (standard deviation) values are reported in the following tables 4.9 and 4.10 as using only two measurements resulted in errors of up to 0.05% which can be discarded.

The attenuation coefficients reported in Table 4.9 were determined from the change in the amplitude of the acoustic signal and can be seen as a measure of dissipative energy since they refer to the loss of acoustical energy as the wave travels through the material [68].

Table 4.9. Acoustic properties of neat HDPE and HDPE-MWCNT composites samples.

Sample	Velocity of sound /m s^{-1}	Attenuation at Resonance Frequency /Np m^{-1}
HDPE	2339.19	12.41
HDPE+0.01wt%MWCNTS	2367.32	14.69
HDPE+0.1wt%MWCNTS	2428.64	17.25
HDPE+0.3wt%MWCNTS	2434.95	17.55
HDPE+0.5wt%MWCNTS	2427.89	14.03
HDPE+1wt%MWCNTS	2481.88	16.80
HDPE+3wt%MWCNTS	2498.57	15.35
HDPE+5wt%MWCNTS	2516.17	16.86

Acoustic properties are affected by density [67] and even more so by the elastic properties of the material in which the sound waves travel through [69]. As the speed of sound in a homogenous medium is directly related to both elastic modulus and density, changes in either elasticity or density will alter the ultrasonic velocity in the composite samples.

In section 4.9, the addition of MWCNT was confirmed to increase the density of the host HDPE polymer, although negligibly. Albeit sound generally travels at a slower speed in a more dense material, the stiffness has a greater effect than density on the propagation speed of a sound wave. Specifically, the velocity of sound increases with stiffness [69] and this explains why the sound velocities reported in Table 4.9 are higher with increasing MWCNT content. Increased longitudinal ultrasonic velocities were indeed obtained for the composites when compared to neat HDPE, with the highest increases registered for composites at MWCNT content above 1 wt%.

Typical values of the velocity of sound in dense crystalline solids reported in literature are of the order of 3 to 6×10^3 m/s [70]. Specifically, the longitudinal sound velocity for a common PE polymer at 25°C and 1 MHz was found to be 2.43 m/s [66]. Therefore, the values of the speed of sound obtained in this study (Table 4.9) are in good agreement, i.e. a similar order of magnitude.

In general, a more dense substance has more mass per volume and thus transmits the sound slower as it can retain the vibrational energy less than lighter materials can do. On the other hand, an increase in material density results in an increase in sound absorption at medium and high frequencies, with the acoustic energy being absorbed instead of passing straight through the sample [71]. Therefore, unless materials with high density possess great elastic modulus, they would be expected to have poor acoustic properties [72]. In addition, crystallinity undoubtedly plays a key role in determining the speed of sound in polymer composites through its linear relationship with density and modulus [73]. Normally, an increase in crystallinity also drives a decrease in attenuation [74], as the acoustic loss in polymers is dependent on their degree of crystallinity.

Here, attenuation was higher for the composites compared to the pure polymer sample (see Table 4.9) due to the attenuation contribution from the filler. The attenuation in composites is related to different factors such as the polymer matrix, the filler and its properties (e.g. particle size, shape, and the filler acoustic impedance relative to the polymer matrix), and the interaction between the two [74]. Poor adhesion between the filler and matrix causes loss mechanisms such as antiphase vibrations, and interfacial friction, as the particle may vibrate causing friction and absorption of energy into the polymer matrix that would increase attenuation. Conversely, strong adhesion between the polymer and the particle hinders the particle to vibrate freely when the ultrasonic wave is incident on the particle, lowering the attenuation.

From the values reported in Table 4.9, it is not surprising that the most attenuating composite sample was that at 0.3 wt% MWCNT loading, while the least attenuating was that at 0.5 wt% MWCNT loading. The largest change in attenuation occurred at the attainment of the percolated filler network threshold, confirming that the adhesion between HDPE and MWCNT played a role in determining multiscattering effects and thus the attenuation coefficients in the composites. At percolation, where a continuous path from particle to particle is created and particle-particle interactions exist, the

acoustic energy can pass through the inter-particle contacts, largely avoiding interaction with the matrix [75]. Yet the other composite systems displayed average amounts of attenuation.

Furthermore, the experimental values of the acoustic impedance obtained by multiplying the samples densities (from measurements) with the velocities of ultrasound in the samples are reported in Table 4.10. Additionally, the trend in the variation of acoustic impedance as a function of the MWCNT content is shown graphically in Figure 4.15.

Table 4.10. Acoustic impedances of neat HDPE and HDPE-MWCNT composites samples.

Sample	Acoustic Impedence /MRayl
HDPE	2.22
HDPE+0.01wt%MWCNTS	2.25
HDPE+0.1wt%MWCNTS	2.30
HDPE+0.3wt%MWCNTS	2.32
HDPE+0.5wt%MWCNTS	2.32
HDPE+1wt%MWCNTS	2.37
HDPE+3wt%MWCNTS	2.43
HDPE+5wt%MWCNTS	2.43
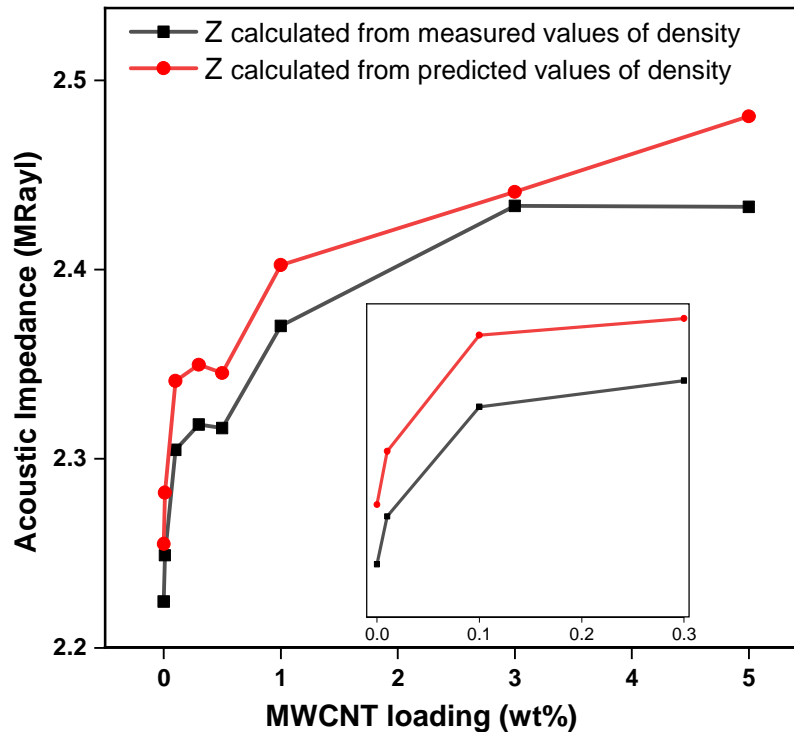
Figure 4.15. Acoustic impedance trends obtained for the HDPE-MWCNT composites.

As the acoustic impedance defines the characteristic resistance of the material to the propagation of ultrasound waves, a lower specific acoustic impedance of the medium ensures less resistance. Here, composites with loadings of 3 and 5 wt% MWCNT provided the highest impedances as a result of the incorporation of high impedance particles in the polymer matrix which increased the impedance. The comparison between the acoustic impedance values obtained from both the measured and predicted density values confirmed the same trend (Figure 4.15) and therefore the adaptation of the data between pre and post-processing of the non-foamed composite materials.

As discussed in Submission Portfolio No.2, when there is a large impedance mismatch at an interface (in this case the air-composite interface), only a small amount of energy is transmitted across the interface while most of the energy is reflected back. The fraction of incident energy transmitted through the interface is dependent on the acoustic impedances of the two media, air (Z_1) [b] and composite sample (Z_2). The efficiency of sound transmission into a solid material from air is unlikely to be high, since the density of the solid is much higher than a gas, unless the speed of sound in the solid can be decreased dramatically [76]. Therefore, it is clear that foamed composites of MWCNT filled HDPE may provide a route to achieving a material with the low impedance values required for matching layers used in transducers.

4.11 Concluding Remarks

The combination of techniques used in the work described in this chapter provided detailed understanding of the extent of MWCNT dispersion in HDPE, some resulting properties and the crystalline structure development for HDPE on inclusion of MWCNTs at loadings up to 5 wt%.

In summary, the major finding from this work are:

- Oscillatory rheology measurements and SEM imaging confirmed the MWCNTs were highly dispersed and distributed in the HDPE matrix, and a rheological percolation threshold was attained at some MWCNT loading between 0.3 and 0.5 wt%.
- Thermal analysis and SAXS data revealed the MWCNTs act as nucleating agents for HDPE and induce an oriented NHSK crystalline structure (where the MWCNTs act as shish for the epitaxial growth of HDPE crystallites), in part an artefact of the injection moulding process but which governs the uniaxial deformation behaviour of these composites. The NHSK structure was confirmed by SEM micrographs, where the polymer was seen to coat/wrap around the MWCNTs.
- The amorphous layer (related to the amorphous content in the composites) increased with increasing MWCNTs loading, seen by the decrease in X_c, where a reduction in the local crystallite

---

[b] The typical speed of sound in dry air at ambient temperature and pressure is c= 344 m/s, a value that when multiplied by the density of air of 1.213 Kg/m^3 provides an acoustic impedance for air of about 417.3 Rayl.

size followed a decrease in crystallinity. Hence, from these results the MWCNTs at low loadings (up to 0.1 wt%) can have a nucleating effect on HDPE increasing the crystallite size and crystallinity slightly. However, at MWCNT loadings >0.3 wt% and above, there tends to be a reduction in crystallite size and local crystallinity, indicating that the MWCNTs when more concentrated in the matrix, hinder nucleation and growth of crystallites. This behaviour was also suggest from the DSC data, where the bulk crystallinity ($X_{c(DSC)}$), was reduced at higher MWCNT loadings due to the confinement effect of the MWCNT.

- TGA confirmed the thermal stability of the MWCNTs attributable to its large surface area and aspect ratio, and no degradation occurred at the temperatures the MWCNTs and HDPE were melt processed.

- DMTA analysis revealed that MWCNT filled HDPE composites produced high loss materials with inherent damping capacity (especially at higher MWCNT loadings > 3 wt%), potentially applicable in passive damping control systems, where the noise generated by sound, vibration, and shock needs to be reduced but stiffness, strength and low cost need to be preserved.

- Furthermore, MWCNT loadings of 3 and 5 wt% provided the highest acoustic impedance value (2.43 MRayl) among the composites.

References

[1] P. Pötschke, M. Abdel-Goad, I. Aligb, S. Dudkinb, D. Lellinger, Rheological and dielectrical characterization of melt mixed polycarbonate-multiwalled carbon nanotube composites, Polymer, 45(26), 2004, pp. 8863-8870.

[2] A.R. Bhattacharyya, P. Pötschke, M. Abdel-Goad, D. Fischer, Effect of encapsulated SWNT on the mechanical properties of melt mixed PA12/SWNT composites, Chemical Physics Letters, 392(1), 2004, pp. 28-33.

[3] C.A. Mitchell, J.L. Bahr, S. Arepalli, J.M. Tour, R. Krishnamoorti, Dispersion of Functionalized Carbon Nanotubes in Polystyrene, Macromolecules, 35(23), 2002, pp. 8825-8830.

[4] T. McNally, P. Pötschke, P. Halley, M. Murphy, D. Martin, S.E.J. Bell, G.P. Brennan, D. Bein, P. Lemoine, J.P. Quinn, Polyethylene multiwalled carbon nanotube composites, Polymer, 46(19), 2005, pp. 8222-8232.

[5] F. Du, R.C. Scogna, W. Zhou, S.B. John, E. Fischer, K.I. Winey, Nanotube Networks in Polymer Nanocomposites: Rheology and Electrical Conductivity, Macromolecules, 37(24), 2004, pp. 9048-9055.

[6] R. Krishnamoorti, E. P. Giannelis, Rheology of End-Tethered Polymer Layered Silicate Nanocomposites, Macromolecules, 30(14), 1997, pp. 4097-4102.

[7] S. Agarwal, R. Salovey, Model filled polymers. XV: The effects of chemical interactions and matrix molecular weight on rheology, Polymer Engineering & Science, 35(15), 1995, pp. 1241-1251.

[8] L.A. Utracki, Flow and flow orientation of composites containing anisometric particles, Polymer Composites, 7(5), 1986, pp. 274-282.

[9] A.J. Paleo, J. Silva, F.W.J. van Hattum, S. Lanceros-Mendez, A.I. Ares, Rheological and Electrical Analysis in Carbon Nanofiber Reinforced Polypropylene Composites, Journal of Polymer Science Part B: Polymer Physics, 51(3), 2013, pp. 207-213.

[10] M. Tasyurek, S. Ekinci, M. Mirik, Investigation of Mechanical Properties of Carbon Nanotubes/High Density Polythylene Composites Produced by Extrusion Method, Athens Journal of Technology and Engineering, 2(3), 2015, pp. 181-192.

[11] A. Eitan, F.T. Fisher, R. Andrews, L.C. Brinson, L.S. Schadler, Reinforcement mechanisms in MWCNT-filled polycarbonate, Composites Science and Technology, 66(9), 2006, pp. 1162-1173.

[12] S. Kanagaraj, F. R. Varanda, T.V. Zhil'tsova, M.S.A. Oliveira, J.A.O. Simões, Mechanical properties of high density polyethylene/carbon nanotube composites, Composites Science and Technology, 67(15), 2007, pp. 3071-3077.

[13] R.K. Abu Al-Rub, A.I. Ashour, B.M. Tyson, On the aspect ratio effect of multi-walled carbon nanotube reinforcements on the mechanical properties of cementitious nanocomposites, Construction and Building Materials, 35, 2012, pp. 647-655.

[14] D. Liu, X. Li, H. Song, P. Wang, J. Chen, Q. Tian, L. Sun, L. Chen, B. Chen, J. Gong, G. Sun, Hierarchical structure of MWCNT reinforced semicrystalline HDPE composites: A contrast matching study by neutron and X-ray scattering, European Polymer Journal, 99, 2018, pp. 18-26.

[15] D. Xiang, E. Harkin-Jones, D. Linton, P. Martin, Structure, mechanical, and electrical properties of high-density polyethylene/multi-walled carbon nanotube composites processed by compression molding and blown film extrusion, Journal of Applied Polymer Science, 132(42), 2015, pp.1-30.

[16] D. Xiang, E. Harkin-Jones, D. Linton, Processability, structural evolution and properties of melt processed biaxially stretched HDPE/MWCNT nanocomposites, RSC Advances, 4(83), 2014, pp. 44130-44140.

[17] S.L. Kodjie, L. Li, B. Li, W. Cai, C.Y. Li, M. Keating, Morphology and Crystallization Behavior of HDPE/CNT Nanocomposite, Journal of Macromolecular Science, Part B, 45(2), 2006, pp. 231-245.

[18] J. Kim, S. Kwak, S.M. Hong, J.R. Lee, A. Takahara, Y. Seo, Nonisothermal Crystallization Behaviors of Nanocomposites Prepared by In Situ Polymerization of High-Density Polyethylene on Multiwalled Carbon Nanotubes, Macromolecules, 43(24), 2010, pp. 10545-10553.

[19] S.K.H. Gulrez, M.E.A. Mohsin, S.M. Al-Zahrani, Studies on crystallization kinetics, microstructure and mechanical properties of different short carbon fiber reinforced polypropylene (SCF/PP) composites, Journal of Polymer Research, 20(10), 2013, pp. 265-274.

[20] M.E.A. Mohsin, A. Arsad, O.Y. Alothman, Enhanced Thermal, Mechanical and Morphological Properties of CNT/HDPE Nanocomposite Using MMT as Secondary Filler, International Journal of Chemical and Molecular Engineering, 8(2), 2014, pp. 117-120.

[21] S.L. Kodjie, L. Li, B. LI, W. Cai, C.Y. Li, M. Keating, Morphology and Crystallization Behavior of HDPE/CNT Nanocomposite, Journal of Macromolecular Science, Part B, 45(2), 2006, pp. 231-245.

[22] A.L. Simal, A.R. Martin, Structure of heat-treated Nylon 6 and 6.6 fibers. II. Recrystallization mechanism, Journal of Applied Polymer Science, 68(3), 1998, pp. 453-474.

[23] S. Röber, P. Bösecke, H.G. Zachmann, Small angle X-ray scattering pole figures of semicrystalline polymers obtained by synchrotron radiation, Makromolekulare Chemie. Macromolecular Symposia, 15(1), 1988, pp. 295-310.

[24] C.W. Bunn, The crystal structure of long-chain normal paraffin hydrocarbons. The "shape" of the <CH2 group, Transactions of the Faraday Society, 35(0), 1939, pp. 482-491.

[25] I.M. Ward, Structure and properties of oriented polymers, Springer Science & Business Media, 2012, pp. 1-535.

[26] E.L. Heeley, D.J. Hughes, E. Crabb, M. Kershaw, O. Shebanova, S. Leung, B. Mayoral, T. McNally, Structure evolution in poly(ethylene terephthalate) (PET) – Multi-walled carbon nanotube (MWCNT) composite films during in-situ uniaxial deformation, Polymer, 92, 2016, pp. 239-249.

[27] E.D. Laird, C.Y. Li, Structure and morphology control in crystalline polymer–carbon nanotube nanocomposites, Macromolecules, 46(8), 2013, pp. 2877-2891.

[28] E.L. Heeley, D.J. Hughes, E.M. Crabb, J. Bowen, O. Bikondoa, B. Mayoral, T. McNally, Confirmation of a nanohybrid shish-kebab (NHSK) structure in composites of PET and MWCNTs, Journal of Polymer Science Part B: Polymer Physics, 55(2), 2017, pp. 132-137.

[29] E.L. Heeley, D.J. Hughes, E.M. Crabb, J. Bowen, O. Bikondoa, B. Mayoral, S. Leung, T. McNally, The formation of a nanohybrid shish-kebab (NHSK) structure in melt-processed composites of poly (ethylene terephthalate)(PET) and multi-walled carbon nanotubes (MWCNTs), Polymer, 117, 2017, pp. 208-219.

[30] J. Yang, K. Wang, H. Deng, F. Chen, Q. Fu, Hierarchical structure of injection-molded bars of HDPE/MWCNTs composites with novel nanohybrid shish–kebab, Polymer, 51(3), 2010, pp. 774-782.

[31] D. Li, H. Garmestani, S.R. Kalidindi, R. Alamo, Crystallographic texture evolution in high-density polyethylene during uniaxial tension, Polymer, 42(11), 2001, pp. 4903-4913.

[32] H-B. Zhang, G-D. Lin, Z-H. Zhou, X. Dong, T. Chen, Raman spectra of MWCNTs and MWCNT-based H2-adsorbing system, Carbon, 40(13), 2002, pp. 2429-2436.

[33] B.D. Che, B.Q. Nguyen, L.T. Nguyen, H.T. Nguyen, V.Q. Nguyen, T. Van Le, N.H. Nguyen, The impact of different multi-walled carbon nanotubes on the X-band microwave absorption of their epoxy nanocomposites, Chemistry Central Journal, 9(10), 2015, pp. 1-13.

[34] R. Caminiti, L. Pandolfi, P. Ballirano, Structure of Polyethylene from X-Ray Powder Diffraction: Influence of the Amorphous Fraction on Data Analysis, Journal of Macromolecular Science, Part B, 39(4), 2000, pp. 481-492.

[35] T. Lu, H. Ye, A. Zheng, X. Xu, C. Xu, H. Wang, L. Sun, L. Xu, Hybrid modification of high-density polyethylene with hyperbranched polyethylene-functionalized multiwalled carbon nanotubes and few-layered graphene, Journal of Applied Polymer Science, 134(27), 2017, pp. 44848.

[36] F. Chouit, O. Guellati, S. Boukhezar, A. Harat, M. Guerioune, N. Badi, Synthesis and characterization of HDPE/N-MWNT nanocomposite films, Nanoscale Research Letters, 9(1), 2014, pp. 288-294.

[37] A. Linares, J.C. Canalda, M.E. Cagiao, M.C. García-Gutiérrez, A. Nogales, I. Martín-Gullón, J. Vera, T.A. Ezquerra, Broad-Band Electrical Conductivity of High Density Polyethylene Nanocomposites with Carbon Nanoadditives: Multiwall Carbon Nanotubes and Carbon Nanofibers, Macromolecules, 41(19), 2008, pp. 7090-7097.

[38] M. Morcom, K. Atkinson, G. P. Simon, The effect of carbon nanotube properties on the degree of dispersion and reinforcement of high density polyethylene, Polymer, 51(15), 2010, pp. 3540-3550.

[39] J.M. Wernik, S.A. Meguid, Recent Developments in Multifunctional Nanocomposites Using Carbon Nanotubes, Applied Mechanics Reviews, 63(5), 2010, pp. 050801-40.

[40] A.B. Strong, Plastics: Materials and Processing, Pearson Prentice Hall, 2006, pp. 1-917.

[41] F.Y. Castillo, B.P. Grady, Filler Reaggregation and Network Formation Time Scale in Extruded High-Density Polyethylene/Multiwalled Carbon Nanotube Composites, Polymer Engineering and Science, 52(8), 2012, pp. 1761-1774.

[42] S.H. Yetgin, Effect of multi walled carbon nanotube on mechanical, thermal and rheological properties of polypropylene, Journal of Materials Research and Technology, 8(5), 2019, pp. 4725-4735.

[43] L. Juan, Multiwalled carbon nanotubes reinforced polypropylene composite material, Journal of Nanomaterials, 2, 2017, pp. 1-5.

[44] L.E. Nielsen, R.F. Landel, Mechanical Properties of Polymers and Composites, Marcel Dekker, 1994, pp. 1-130.

[45] K.K. Kar, Composite Materials: Processing, Applications, Characterizations, Springer, 2017, pp. 1-686.

[46] A. Vasiljevic-Shikaleska, F. Popovska-Pavlovska, S. Cimmino, D. Duraccio, C. Silvestre, Viscoelastic properties and morphological characteristics of polymer-modified bitumen blends, Journal of Applied Polymer Science, 118(3), 2010, pp. 1320-1330.

[47] D. Wang, B. Yang, Q-T. Chen, J. Chen, L-F. Su, P. Chen, Z-Z Zheng, J-B. Miao, J-S Qian, R. Xia, Y. Shi, A facile evaluation on melt crystallization kinetics and thermal properties of low-density polyethylene (LDPE)/Recycled polyethylene terephthalate (RPET) blends, Advanced Industrial and Engineering Polymer Research, 2(3), 2019, pp. 126-135.

[48] B. Alcock, N.O. Cabrera, N.-M. Barkoula, C.T. Reynolds, L.E. Govaert, T. Peijs, The effect of temperature and strain rate on the mechanical properties of highly oriented polypropylene tapes and all-polypropylene composites, Composites Science and Technology, 67(10), 2007, pp. 2061-2070.

[49] C. Becker, H. Krug, H. Schmidt, Tailoring of Thermomechanical Properties of Thermoplastic Nanocomposites by Surface Modification of Nanoscale Silica Particles, Materials Research Society Symposium Proceedings, 435, 1996, pp.237-242.

[50] M. Pluta, Z. Bartczak, A. Pawlak, A. Galeski, M. Pracella, Phase structure and viscoelastic properties of compatibilized blends of PET and HDPE recyclates, Journal of Applied Polymer Science, 82(6), 2001, pp. 1423-1436.

[51] R. Jeziorska, M. Zielecka, B. Gutarowska, Z. Zakowska, High-density polyethylene composites filled with nanosilica containing immobilized nanosilver or nanocopper: thermal, mechanical, and bactericidal properties and morphology and interphase characterization, International Journal of Polymer Science, 2014, 2014, pp. 1-13.

[52] K-H. Nitta, A. Tanaka, Dynamic mechanical properties of metallocene catalyzed linear polyethylenes, Polymer, 42(3), 2001, pp. 1219–1226.

[53] M.L. Cerrada, R. Benavente, E. Perez, Effect of short glass fiber on structure and mechanical behavior of an ethylene-1-octene copolymer, Macromolecular Chemistry and Physics, 202(13), 2001, pp. 2686–2695.

[54] R. Popli, M. Glotin, L. Mandelkern, Dynamic mechanical studies of α and β relaxations of polyethylenes, Journal of Polymer Science B: Polymer Physics, 22(3), 1984, pp. 407–448.

[55] K. Jordens, G.L. Wilkes, J. Janzen, D.C. Rohlfing, M.B. Welch, The influence of molecular weight and thermal history on the thermal, rheological, and mechanical properties of metallocene-catalyzed linear polyethylenes, Polymer, 41(19), 2000, pp. 7175–7192.

[56] H.D. Droste, A.T. DiBenedetto, The glass transition temperature of filled polymers and its effect on their physical properties, Monsanto Research Corporation, 1968, pp. 1-20.

[57] B.J. Ash, L.S. Schadler, R.W. Siegel, Glass transition behavior of alumina/polymethylmethacrylate nanocomposites, Materials Letters, 55(1), 2002, pp. 83-87.

[58] S.J. Chin, S. Vempati, P. Dawson, M. Knite, A. Linarts, K. Ozols, T. McNally, Electrical conduction and rheological behaviour of composites of poly(ε-caprolactone) and MWCNTs, Polymer, 58, 2015, pp. 209-221.

[59] I.C. Finegan, R.F. Gibson, Recent research on enhancement of damping in polymer composites, Composite Structures, 44(2-3), 1999, pp. 89-98.

[60] M. State, P.J. Brands, F.N. van de Vosse, Improving the thermal dimensional stability of flexible polymer composite backing materials for ultrasound transducers, Ultrasonics, 50(4), 2010, pp. 458-466.

[61] F. Xu, L.X. Sun, J. Zhang, Y.N. Qi, L.N. Yang, H.Y. Ru, C.Y. Wang, X. Meng, X.F. Lan, Q.Z. Jiao, F.L. Huang, Thermal stability of carbon nanotubes, Journal of Thermal Analysis and Calorimetry, 102(2), 2010, pp. 785-791.

[62] E. Piiroja, H. Lippmaa, Thermal degradation of polyethylene, Makromolekulare Chemie. Macromolecular Symposia, 27(1), 1989, pp. 305-309.

[63] O.O. Daramola, I.O. Oladele, B.O. Adewuyi, R. Sadiku, S.C. Agwuncha, Thermal, structural and morphological properties of High Density Polyethylene matrix composites reinforced with submicron agro silica particles and Titania particles, Journal of Taibah University for Science, 11(4), 2017, pp. 645-653.

[64] P.C.P. Watts, P.K. Fearon, W.K. Hsu, N.C. Billingham, H.W. Kroto, D.R.M. Walton, Carbon nanotubes as polymer antioxidants, Journal of Materials Chemistry, 13(3), 2003, pp. 491-495.

[65] N.E. Dowling, Mechanical Behavior of Materials: Engineering Methods for Deformation, Fracture, and Fatigue, Pearson Education Limited, Fourth edition, 2013, pp. 1-933.

[66] J.E. Mark, Physical Properties of Polymers Handbook, Springer, Second edition, 2007.

[67] C. DeArmitt, M. Hancock, Filled Thermoplastics, in: Particulate-Filled Polymer Composites, Rapra Technology Limited, chapter 8, 2003, pp. 357-424.

[68] F. Lionetto, A. Maffezzoli, Polymer characterization by ultrasonic wave propagation, Advances in Polymer Technology, 27(2), 2008, pp. 63-73.

[69] G.H.P. Laugier, Introduction to the Physics of Ultrasound, in: Bone Quantitative Ultrasound, Springer, Chapter 2, 2011, pp. 29-45.

[70] M. Sinha, D.J. Buckley, Acoustic Properties of Polymers, in: Physical Properties of Polymers Handbook, Springer, Chapter 60, 2007, pp. 1021-1031.

[71] A.E. Tiuc, O. Vasile, A-D. Usca, T. Gabor, H. Vermecan, The Analysis of Factors That Influence the Sound Absorption Coefficient of Porous Materials, RJAV, 11(2), 2014, pp. 105-108.

[72] M.M. Jalili, S.Y. Mousavi, A.S. Pirayeshfar, Investigating the Acoustical Properties of Carbon Fiber-, Glass Fiber-, and Hemp Fiber-Reinforced Polyester Composites, Polymer Composites, 35(11), 2014, pp. 2103-2111.

[73] D.W. Van Krevelan, Acoustic Properties, in: Properties of Polymers, Elsevier Science, (Chapter 14), 2009, pp. 505–522.

[74] M.G. Grewe, T.R. Gururaja, T.R. Shrout, R.E. Newnham, Acoustic properties of particle/polymer composites for ultrasonic transducer backing applications, IEEE Transactions on Ultrasonics, Ferroelectrics, and Frequency Control, 37(6), 1990, pp. 506 - 514.

[75] M. Alonso, A. Gonzalez, A. Requejo, M. Arribas, J.A. de Saja, Air-borne sound absorption and sound speed in talc-filled polypropylene, Polymer Testing, 11(1), 1992, pp. 71-78.

[76] W.R. Hendee, E.R. Ritenour, Ultrasound Waves, in: Medical Imaging Physics, Wiley-Liss Inc, Chapter 19, 2002, pp. 303-316.

CHAPTER 5: RESULTS AND DISCUSSION- PART II

Characterisation of Foams of HDPE and HDPE-MWCNT Composites prepared by Chemical Foaming Methods

A systematic and comprehensive study was carried out to investigate the effect of processing conditions and CBA concentration on the morphology of foamed HDPE and HDPE-MWCNT composite parts prepared via chemical foaming and is discussed here. Two types of endothermic CBAs, herein referred to as CBA_1 and CBA_2, were used to foam unfilled HDPE and MWCNT filled HDPE, using industrially relevant polymer processing methods such as extrusion and injection moulding (IM). The key objective is to assess whether such moulded expanded parts have the required properties to function as passive layers within acoustic sensors. It is not only the polymer itself that contributes to the properties of the foam, but the gas-filled space between them [1]. In comparison to other non-polymeric foams where the voids or gas-filled spaces do not interact with the surrounding matrix, in polymer foams the intercellular gas interacts with the matrix, affecting its properties and behaviour even over time. How varying the processing parameters affects selected physical and acoustic properties of these materials was also evaluated. Following this study, a preliminary screening of the materials was completed, assessing density reduction, acoustic characteristics and morphological features of the moulded unfilled and filled HDPE foams obtained by varying processing conditions.

Firstly, a preliminary analysis of the morphology and thermal characteristics of the two CBAs was carried out in order to establish the most suitable conditions for foaming the polymer. Second, a detailed study was conducted focusing on the production and characterization of various unfilled HDPE foams derived from varying processing conditions as described in section 5.2. Next, addition of MWCNT to create expanded HDPE-MWCNT composite foams is discussed in section 5.3. Experimental detailing the processing conditions adopted during foaming are provided in this chapter.

5.1 Preliminary Work: Selection and Characterisation of CBAs

5.1.1 The choice of the Hydrocerol blowing agents

When selecting the correct CBA for a specific polymer, there are some key aspects to take into consideration, such as the type of gas generated, the particle size of the foaming agent, the decomposition rate of the CBA and the melt viscosity of the polymer to process. It is fundamentally important to choose the decomposition temperature range to match the processing temperature of the polymer while equally ensuring the compatibility between the gas released and the polymer [2]. For semi-crystalline polymers, the requirement for the decomposition temperature is to be higher

than the melting point of the polymer by at least $10°C$ [3]. Since the melting point of HDPE is ~$135℃$, a temperature higher than $145℃$ must to be ensured. Hydrocerols, which have decomposition temperatures between 160 and $210°C$ [4], can therefore be used as CBAs to foam HDPE. This is critical, to ensure the CBA does not decompose completely when being melt mixed with the HDPE in the extruder, such that there is efficient amounts of the CBA available during IM to foam the polymer. To achieve an efficient foaming process, besides ensuring a sufficiently high processing temperature for a complete decomposition of the CBA, it is paramount to ensure an adequately high pressure so the gas remains dissolved in the polymer melt. Once the correct processing conditions are known, the choice of blowing agent, the amount of gas evolved, the decomposition rate, and the influence of the exothermic or endothermic decomposition on the process must be considered [2].

In this work, endothermic CBAs were preferred to exothermic agents for several reasons. Unlike exothermic decomposition processes that generate heat during the course of the reaction and produce gas, e.g. N_2, an endothermic process absorbs heat, produces CO_2 and foaming stops when the energy flow is cut-off. The application of endothermic CBAs considerably shortens the cooling time and thereby the entire production cycle, as opposed to exothermic reactions [a] [5]. Moreover, as endothermic CBAs need heat to continue decomposing, the process of foaming can be simply controlled by changing temperature [6].

The two types of Hydrocerol used are endothermic foaming agent mixtures, composing of mixtures of citric acid ($C_6H_8O_7$) and sodium bicarbonate ($NaHCO_3$), blended in stoichiometric proportions, which give rise to an endothermic reaction:

$$CBA_{endothermi} \xrightarrow{+\Delta E} CO_2 + H_2O + inorganic\ byproducts \qquad (5.1)$$
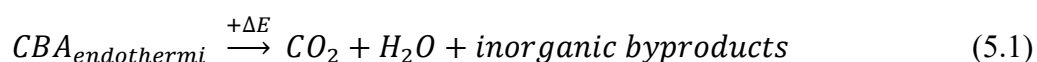
Equation (5.1) describes the decomposition process, with the releases of CO_2 as the main component while liberating other various gases, liquids and solid products including H_2O, sodium carbonate (Na_2CO_3), acetic oxalic anhydride ($C_6H_6O_6$), furandicarboxylic acid ($C_6H_4O_5$), and furoic acid ($C_5H_4O_3$). As shown in Equation (5.1), Hydrocerol typically yields water among its decomposition products, which is not problematic for HDPE as it is not a hydroscopic polymer sensitive to moisture (i.e. no risk of hydrolysis of the polymer by reaction with water) [2, 7]. The solid residues react as nucleation centres, leading to a finer cell structure and better solubility of the gas in the polymer melt [8].

---

[a] Exothermic reactions may cause local overheating during extrusion processing, resulting in foamed products with an irregular cellular structure which need to be intensely cooled for a long time to prevent distortions and keep the specific cellular structure obtained [5] L.D. T. Garbacz, Porophors used in the extrusion process, Chemistry & Chemical Technology 7(1) (2013) 113-118..

Highly soluble and dense gases usually lead to satisfactory polymer swelling as the quantity of dissolved gas is appreciable [9]. Solubility of CO_2 in several polymers is higher than that of N_2 and therefore potentially able to generate more cell nuclei, essential to foam a polymer. However, the solubility of CO_2 is dependent on the total amount of crystallinity in HDPE [10]. As the gas does not dissolve in the crystallites, the high crystallinity of HDPE explains the low solubility of CO_2 for this polymer. On the other hand, the size of the gas particle is also important in foaming technology; CO_2 molecules are small, and can diffuse fast through a polymer, that is the cell growth rate could be high but, at the same time, CO_2 may escape more easily to atmosphere causing a collapse of the foamed material [6].

Hydrocerol foaming agents have been extensively used in thermoplastic foams in the last few years, as their use makes it possible to achieve a highly uniform structure of very small cells, providing uniform and smooth surface finishing. In general, the cell-population (density) increases as the pressure during processing increases, however the nucleation of foams using Hydrocerol (e.g. polypropylene foams) was confirmed to be governed by a heterogeneous nucleation mechanism [11]. When incorporated during plastics processing, such CBAs forms microscopic air pockets in the plastic resin, reducing the amount of plastic needed. Beyond the weight reduction and the material savings, there are other sustainability benefits such as those related to reduced fuel consumption as it is easier to transport foams due to their lighter weight [12]. Furthermore, its use is not problematic from a health and safety point, as it does not contain hazardous materials since the base substances (i.e. bicarbonates and citric acid) are also approved as food additives so they are environmentally friendly and safe to process [5].

5.1.2 Characterisation of CBAs

Understanding the structure of the powder particles and their thermal behaviour is important to evaluate and optimise foam production since it affects the properties of the final products.
A comparative discussion of the two Hydrocerols is presented below.

5.1.2.1 Morphological characterisation of materials by SEM

The morphology of the two CBA powders was examined using scanning electron microscopy at different magnifications. The SEM images obtained were further analysed using ImageJ software to estimate the average particle size of the powders, based on an average of 30 particles per image. Representative high magnification SEM micrographs for each CBA are shown in figures 5.1 and 5.2, relative to CBA_1 and CBA_2, respectively.

Figure 5.1. Representative high magnification SEM images of CBA₁ surface (*Hydrocerol Compound*) at different length scales.
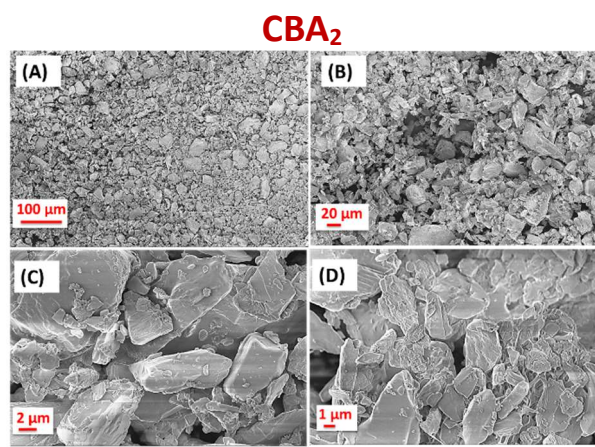
Figure 5.2. Representative high magnification SEM micrographs of the CBA₂ surface (*Hydrocerol CF*) at different length scales.

From the analysis of the SEM images obtained at different magnification, it is clear the particles are non-spherical and irregular shaped, characterised by a variable size and rough surfaces for both CBAs. Both CBAs have a multi-layered structure with irregular shaped particles agglomerated in clusters having dimensions on the micrometre scale. An obvious coexistence of layers of agglomerates and thick clusters is evident from the micrographs of both CBAs, and even more markedly in Figure 5.2 for CBA₂. Although the irregular flake-like structure did not allow for a precise estimation of the dimensions of the particles, a distribution of flake sizes ranging from ca. 0.1 to 4 µm can be seen in Figure 5.1 for CBA₁. In contrast, thicker clusters with sizes up to 30 µm are visible in Figure 5.2 for CBA₂. The minimal observable size of flakes in Figure 5.2 is ca. 0.3 µm, despite powder specifications from the manufacturer (Clariant) stating that CBA₂ was ground to a finer particle size compared to CBA₁. This suggests that the agglomerations are composed of smaller particles [13]. The small particles are attracted to each other by strong van der Waals forces, resulting in the formation of agglomerates. Consequently, the SEM images of CBA₂ showed an apparent bigger flake size distribution than CBA₁.

5.1.2.2 Thermal characterisation of HDPE and CBAs by DSC

The thermal characterisation of the polymer and two CBA powders, as received, was performed so as to determine the HDPE melting and decomposition temperatures of each reaction of the reactive elements of the CBAs, respectively. For the characterisation of foams, DSC provides valuable data on the melting properties of the polymer as well as the assessment of the decomposition temperature of the CBAs. The DSC thermograms obtained from the first heating cycle are shown in Figure 5.3.
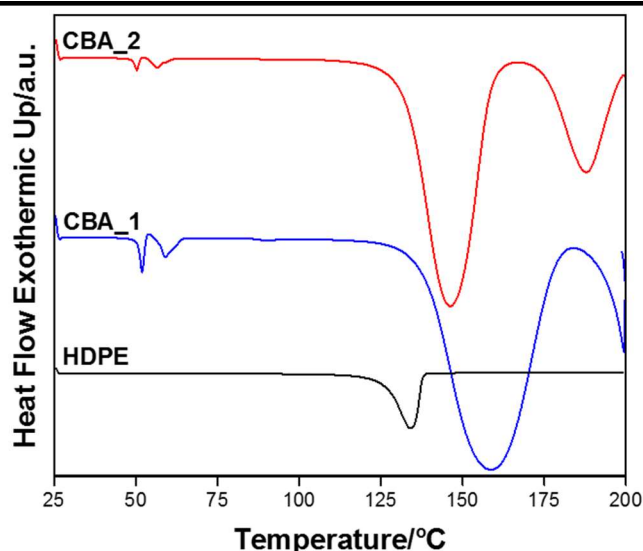
Figure 5.3. DSC first heating curves obtained for HDPE, CBA₁ and CBA₂ at a constant heating rate of 10K/min, from ambient temperature to 200˚C.

The visible peaks displayed in the blue and red curves in Figure 5.3 correspond to the decomposition reactions of the reactive elements of each Hydrocerol CBA, specifically sodium bicarbonate and 2-hydroxypropanoic-tricarboxylic acid (citric acid). In particular, the peak located between 150˚C and 175˚C are related to the sodium bicarbonate decomposition reaction, whereas the peak between 190˚C and 200˚C are associated with the decomposition of citric acid [14]. The DSC measurements revealed that the maximum rate of decomposition occurs when the first reactive element (i.e. sodium bicarbonate) decomposes, that is at 158.6˚C for CBA₁ and 146.3˚C for CBA₂ (allowing for instrument error), to which the following enthalpies of decomposition of 910.7 J/g and 296.1 J/g are associated, respectively.

From the trend of the curves, it is evident that all the decomposition reactions of the CBAs start after fusion of the HDPE (detected from the peak in the melting point (black curve) at 134.8˚C), which assures that the gas obtained from each CBA can be diluted into the molten matrix.

5.1.2.3 Thermal characterisation of materials by TGA

Temperature control is critical in the production of foams and the production of gases. The foaming reaction of the CBAs can be complicated due to the complex thermal conditions of the various processes involved. Despite the broad temperature range in which the CBA decomposes, it needs to be close to that of the melting temperature of the polymer resin to avoid premature or incomplete decomposition, strong temperature gradients could be generated during melting [15] which would compromise the thermal stability of the system.

The thermal stability of the two CBAs was verified from thermo-gravimetric analysis (TGA) in an air atmosphere. The curve of the residual weight loss (percentage) versus temperature was recorded during the heating process and the thermogravimetric (TG) and derivative thermogravimetric (DTG) curves for HDPE, CBA₁, and CBA₂ are reported in Figure 5.4.
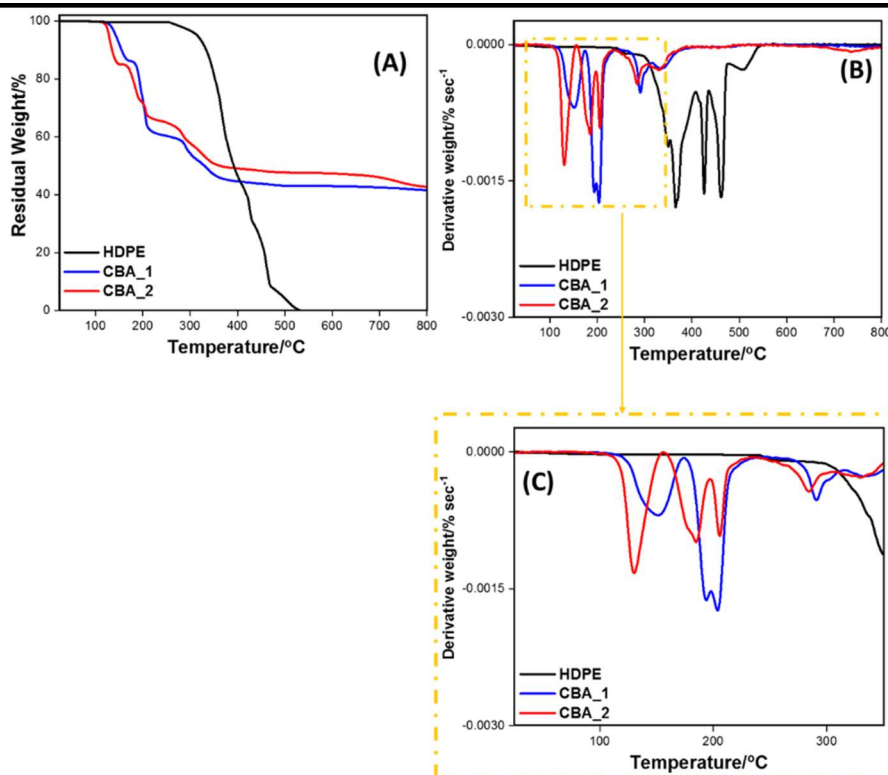
Figure 5.4. TGA curves (A) and corresponding DTG curves (B), (C) of the first derivative of the loss of mass signal for HDPE, CBA_1, and CBA_2.

The weight loss in Figure 5.4(A) shows that most of the blowing agents decompose between 120 and 200 °C, in agreement with the work of Heda et al. [16] and, that a multiple stage reaction characterises the decomposition of the CBAs occurring at temperature well below the degradation of HDPE which begins to take place over 300 °C. These observations are also reflected in the DTG curves (Figure 5.4(B-C)) from the presence of multiple peaks.

In particular, the DTG curves (Figure 5.4 (B)) showed multiple peaks for the polymer (black curve), all over 300 °C, which are derived from with multiple degradation steps of HDPE in presence of oxygen in an air atmosphere. The thermal degradation of HDPE is due to random molecular chain scission, forming alkyl and alkyl peroxyl radicals that are susceptible to inhibition reagents capable of trapping the radicals [17]. The mechanisms of thermal degradation correspond to the polymer cracking reactions yielding smaller olefinic chains and gases [18]. Scission of the polymer chains occurs leading to a high number of short primary radicals, which undergo successive scission reactions and eliminate small molecules. Products of the reaction are generally the formation of solid hydrocarbon residues (i.e. alkanes and alkenes) and numerous gaseous hydrocarbons generated by the HDPE partial combustion and reduction reactions occurring in presence of oxygen in an air atmosphere [18, 19]. Among the products typically observed from the combustion reaction (predominant in Fig.4(B) at temperatures between 350 °C and 530 °C), are relatively low yields of carbon monoxide (CO) and high yields of carbon dioxide (CO_2), ethylene and heavy hydrocarbons with fractions of C_3 (mainly propylene) and C_4 (mainly butadiene). Methane is also a stable product

of the propagation reactions of the thermal decomposition of polyethylene. An intense cracking of heavy hydrocarbons (i.e. secondary reactions) also occurs to produce gases and light fractions that in turn react to generate aromatic and heavy polyaromatic compounds, resulting in a combined effect of cracking and aromatic production reactions [18].

On the other hand, as shown in Figure 5.4 (B-C), the DTG curves of the CBAs showed asymmetric peaks, indicating the whole decomposition of the reactive elements present. In particular, sodium bicarbonate and citric acid, main components of CBA_1 and CBA_2 decompose according to equations 5.2 and 5.3, respectively [15]:

- **Decomposition of sodium bicarbonate**

$$2\ NaHCO_3 \rightarrow Na_2CO_3 + H_2O + CO_2 \qquad\qquad (5.2)$$
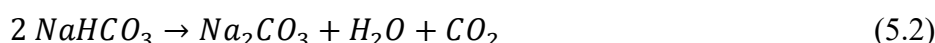
- **Decomposition of citric acid**
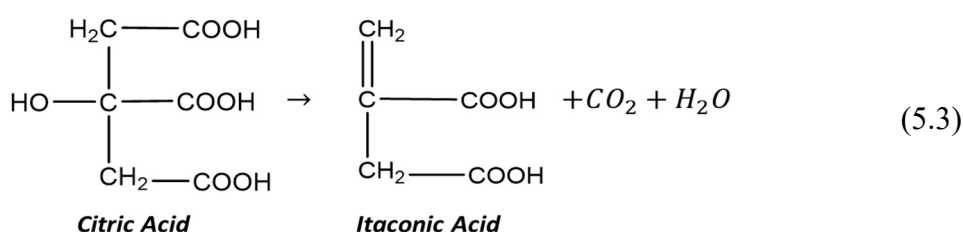
The kinetics can be modelled by first-order equations for sodium bicarbonate compounds and two or more decomposition steps for citric acid compounds due to reaction intermediates [15]. More specifically, the decomposition of citric acid involves a cascade of reactions, which can be described by the following formula:

$$C_6H_8O_7 \rightarrow C_6H_6O_6 + H_2O \qquad\qquad (5.4)$$

$$C_6H_6O_6 \rightarrow C_6H_4O_5 + H_2O \qquad\qquad (5.5)$$

$$C_6H_4O_5 \rightarrow C_5H_4O_3 + CO_2 \qquad\qquad (5.6)$$

The peak temperatures (T_{max}) and corresponding weight losses (mass loss) of each main peak detected in Figure 5.4 (C) are listed in Figure 5.5.

Sodium bicarbonate decomposes at low temperature over a broad temperature range (100–180 °C) in a first-order reaction according to Equation 5.2 or a 2/3 order reaction [b] [15, 20-22].

---

[b] Some authors reported a reaction order of 2/3, corresponding to shrinking-core model kinetics for a spherical particle in which the intra-particle diffusional resistance becomes so important that the chemical reaction is the rate-controlling step. The decomposition reaction of a large particle may be also influenced by other external factors such as heat and mass transfer or internal effects such as conduction and diffusion, which will affect somehow the kinetic parameters (although these are not intrinsic values) and eventually lower the value of the activation energy for large particles.

Peaks	$T\_max/^\circ C$	Mass Loss/%
1	130.5	6.7
1	151.5	8.1
2	184.8	23.4
2	193.5	21.2
3	205.5	30.6
3	203.5	30.8
4	284.2	39.4
4	290.5	43.4
5	329.3	46.5
5	334.8	50.8
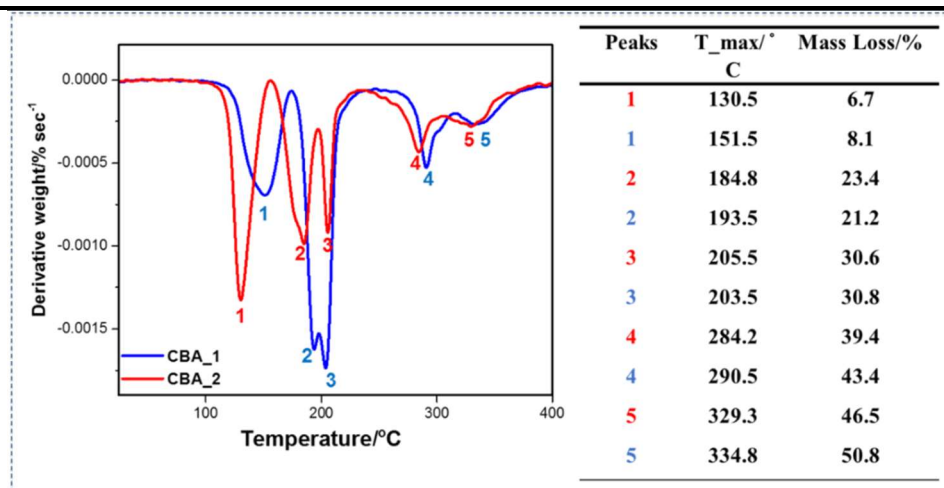
Figure 5.5. DTG peak values detected for CBA_1 and CBA_2 from the first derivative of the loss of mass signal reported in Figure 5.4(C). Each peak corresponds to a maximum weight loss caused by the multi-step reaction of decomposition of the blowing agents. Temperatures (T_max) and weight loss (mass loss) for each peak are listed at the top right of the figure.

The differences in the reaction order reported between authors may essentially be due to different CBA powder particle size [23]. This explains why CBAs with smaller particle size undergo faster decomposition than those of larger particle with the same composition [24]. The finer the grade, the faster the decomposition rate. Accordingly, TGA data confirmed CBA_2 decomposes first at 103.2 ℃, whereas the onset of decomposition for CBA_1 was higher at 115.8 ˚C. The thermal decomposition reactions of the acid (equations 5.4-5.6) were also found to be influenced by particle size and the different heating rates used [25]. Citric acid decomposes over a broad temperature range, 160–270 °C [15]. Barbooti et al. [25] showed that citric acid first melts at 153 °C and then decomposes at higher temperatures by dehydration to give aconitic acid after a conversion of one third of the blowing agent, and finally methyl maleic anhydride (citraconic acid anhydride) by decarboxylation. The overall reaction order was found to be close to 2, as it decomposes in two steps with overlapping peaks between 170 and 260 °C (figures 5.4 and 5.5), which correspond to citric acid and intermediate products [26, 27]. Thermal studies conducted by Wyrzykowski et al. [28] confirmed the reaction intermediates as, cis-aconitic acid and trans-aconitic acid ($C_6H_6O_6$) (Equation 5.4), and the dehydration and decarboxylation reactions that further yield transaconitic anhydride ($C_6H_4O_5$) (Equation 5.5), or itaconic anhydride ($C_5H_4O_3$) (Equation 5.6).

As Hydrocerol (Clariant) CBAs are typical mixtures of citric acid and sodium bicarbonate generally blended in stoichiometric proportions, the general decomposition reaction of this mixture can now be defined by Equation 5.7, by combining the Equations 5.2 and 5.3 as:

- **Decomposition for a mix of sodium bicarbonate/citric acid**

$$C_6H_8O_7 + 3NaHCO_3 \rightarrow C_6H_5Na_3O_7,\ 2H_2O + 3CO_2 + H_2O \qquad (5.7)$$
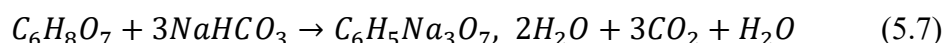
The decomposition reaction shown in Equation 5.7 starts at ~160 °C and is completed at about 210°C, and generates various gases, liquids and solid products among which the main ones are

water vapour (H_2O), carbon dioxide (CO_2) and a solid residue (the sodium citrate dehydrate, $C_6H_5Na_3O_7$) [15].

Behravesh et al. [11] demonstrated that the decomposition behaviour of these CBAs made of mixes of citric acid and sodium bicarbonate is sensitive to the heating rate. At the heating rate of 10 K/min used in this study, the decomposition mainly occurs in three distinct steps. The first step between 120 and 167 °C corresponds to the decomposition of sodium bicarbonate, the second step between 167 and 200 °C corresponds to the reaction of sodium bicarbonate and citric acid, the third step between 200 and 240 °C may correspond to the decomposition of traces of citric acid [15]. From the peaks identified in the DTG plot in Figure 5.5, all the values of temperature associated with such peaks (T_{max}) in both CBAs were included in these temperature ranges, confirming the same kinetics of the decomposition reaction.

Results from this preliminary work conducted on the two Hydrocerol types show that the range of decomposition of the mix of citric acid and sodium bicarbonate fits well with that of the processing of HDPE, i.e. between 160 and 180 °C. In particular, the values of mass loss obtained at 155, 160, 165, 175 and 180 °C (i.e. main peak temperatures reached during extrusion with the five profiles defined in Chapter 3, section 3.2.2) for both CBAs were extrapolated from TGA data to ascertain that a sufficient amount of gas is released during decomposition of the blowing agents during foaming. This (from TGA) data is listed in Table 5.1.

Table 5.1. Thermogravimetric data of mass loss obtained at the peak temperatures related to the extrusion temperature profiles used to prepare blends of HDPE and CBAs.

Sample	Mass Loss/% @T=155°C	MassLoss/% @T=160°C	Mass Loss/% @T=165°C	Mass Loss/% @T=175°C	Mass Loss/% @T=180°C
CBA$_1$	9.9	11.8	13.1	13.9	14.2
CBA$_2$	15.0	15.1	15.4	18.6	20.7

The mass loss reported in Table 5.1 refers to the gas released during the reaction of decomposition of the CBA escaping the sample, composed of both CO_2 and H_2O, with the H_2O expected to remain in the sample as condensed water vapour even after foaming and cooling of foams [14]. Clearly, in the case of a decomposition reaction not completed in the plasticization unit (twin screw extruder), some of the gas remains unreacted in the CBA particles, and the foaming process begins even when all the gas has not been totally created, yielding a relatively complicated physical system to analyse [14].

From the values shown in Table 5.1 only, it is thought that the use of CBA$_2$ to foam the polymer may release a higher amount of gas, eventually leading to a larger number of pores, compared to CBA$_1$. However, this is only a hypothesis as the specific percentage of gas released during further

processing steps will be unknown. The conditions applied during polymer processing will be undoubtedly different from conditions applied in the TGA experiments as a number of different factors will come into play when considering the high viscosity of the polymer melt.

5.2 PART II-A: Characterisation of unfilled HDPE foam parts

The different setting conditions selected in this work for processing the mixture of HDPE and CBAs in the plasticizing system first, and then in the micro-IM machine where eventually foaming occurred and/or was completed, enabled the production of a variety of foamed samples.

Polymer melting and mixing of the polymer with the CBAs took place in the extruder with a further homogenisation of the gas distribution within the polymer melt. The quality of the mixing in the extruder barrel strongly influenced the resulting cell density [11]. Properties such as the final cell density are directly limited by the size of the cell walls [29]. A shear field generates competing mechanisms, which determine cell density by either increasing the number of cells (i.e. the case of a dispersive mixing) or decreasing the number of cells (i.e. the case of cell coalescence which leads to a reduction in cell density). The use of IM ensured completion of nucleation of any amount of gas that remained unreacted from the CBA particles, followed by expansion of the gas and shaping of the final product (i.e. a disk test specimen) in the mould cavity. Details on the selection of the processing conditions employed can be found in Submission Portfolio No. 5. The multitude of HDPE foamed samples realised at different conditions during the processing were subsequently characterised by a range of techniques which enabled a first screening of the materials based on their degree of porosity, expansion ratio, density reduction and acoustic impedance.

5.2.1 SEM: Morphology of foamed HDPE by addition of CBAs

The cell size and morphology of the cellular HDPE structures obtained at different foaming conditions were determined using scanning electron microscopy. The shape and distribution of the cells in the foamed samples were influenced by the methods and parameters used during processing, which in turn determines the final properties of the foam materials including acoustic. Foaming settings, processing parameters and composition of the foamed material are crucial factors in determining the final morphology of a foam [6]. In particular, the bubble growth has been claimed to increase with the melt temperature, mould temperature and blowing agent concentration in foam injection processes, leading to non-uniform cell size and distribution [30]. The use of a powerful imaging technique allows for an understanding of the variety of physical phenomena including foaming under dynamic conditions, providing a direct and effective way to investigate the effect of the filling stage, jetting, bubble nucleation, cell growth, and collapse of foam morphology [30]. A series of micrographs of the fractured surface of cellular HDPE foams produced with different CBA_1 and CBA_2 content prepared using different processing conditions are shown in figures 5.6-

5.16. The images reflect the internal microstructure and morphology of the moulded disks formed during the two-step processing (extrusion followed by IM and thus the pressurized, two-stage expansion process).

Effect of small additions (< 1 wt%) of CBA content on the structure of HDPE
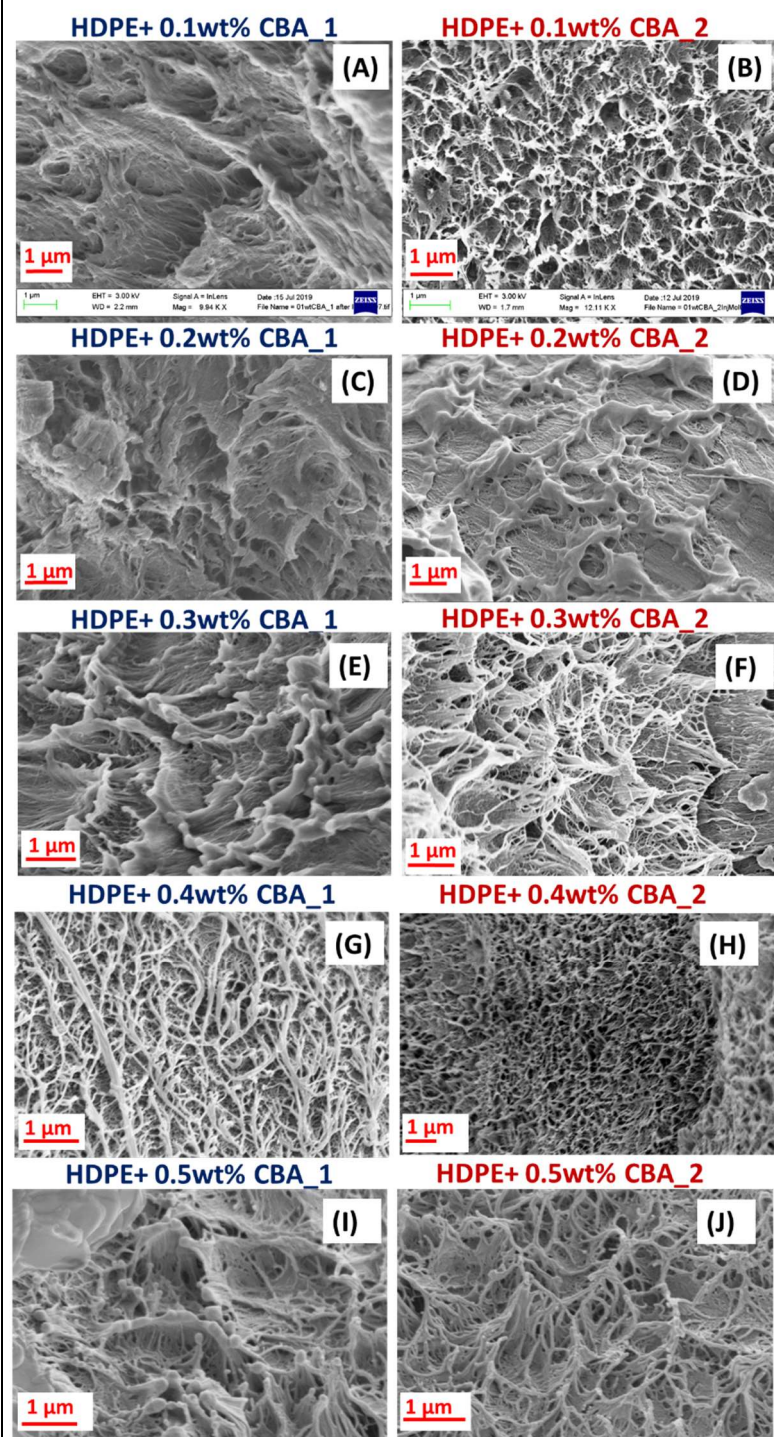
Figure 5.6. Representative SEM images of foamed HDPE moulded microstructure obtained using *Profile 3* and *Method 4* prepared with (A) 0.1 wt% CBA₁, (B) 0.1 wt% CBA₂, (C) 0.2 wt% CBA₁, (D) 0.2 wt% CBA₂, (E) 0.3 wt% CBA₁, (F) 0.3 wt% CBA₂, (G) 0.4 wt% CBA₁, (H) 0.4 wt% CBA₂, (I) 0.5 wt% CBA₁, (J) 0.5 wt% CBA₂.

Comments

The polymer morphology changed even after addition of low loadings of the foaming agents.
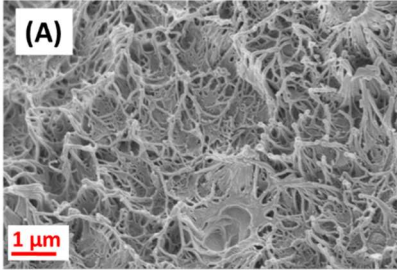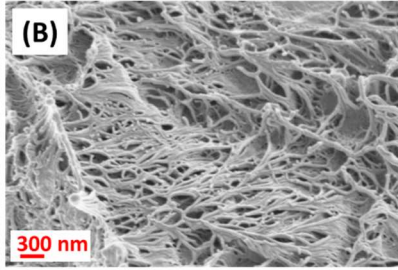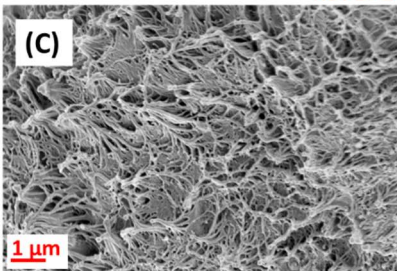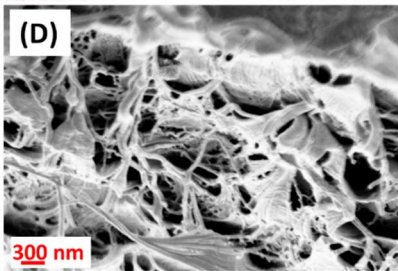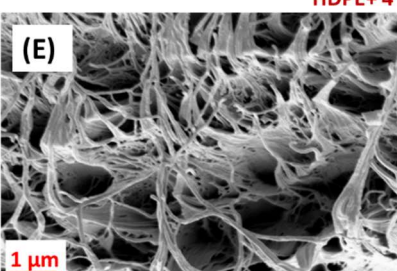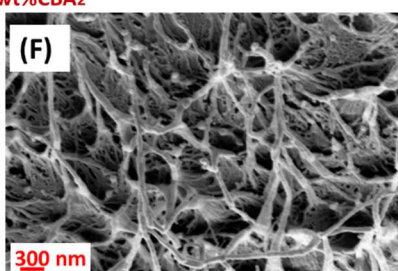
Different microstructures resulted by increasing the content of both CBAs, although samples were all manufactured at the same process parameters, clearly confirming that the size and density of the cells produced during the processing steps depends on the CBA content as well as the processing parameters employed and the properties of the polymer.

Based on the analysis of the images obtained, the pores visible are few and varied, the cell distribution is non-uniform, which did not allow for the assessment of an average cell diameter to estimate the total cell density.

The difficulty of foaming crystalline resins[c] with low CBAs content, i..e below 1 wt% most likely resulted in not enough gas being liberated during the decomposition reaction, yielding a non-uniform and irregular foam morphology. Therefore, further morphology investigations were carried out on cells produced at higher CBA content (i.e., 1 wt% and 4 wt%) within the polymer matrix.

[c]As discussed in the former sections, crystalline resins are difficult to foam due to their chain entanglement and crystallite formation during cooling, which disturbs the cell growth process as the gas dissolves exclusively in the amorphous phase [6].

The effect of increasing CBA content on the structure of HDPE is more clear in Figure 5.7. The cell structure in the foamed polymer is shown from cross-sectional images of the specimens obtained with identical processing regimes (i.e. *Profile 3* and *Method 4*) after incremental additions of 0.5 wt%, 1 wt% and 4 wt% of CBA_2.

Effect of increasing CBA content on the structure of HDPE	*Comments*
	The size of the voids varies through the cross section of the specimens, with the largest micro-voids (up to 4 μm) found for loadings of 4 wt% CBA_2 (see Figure 5.7 (E-F)). The content of open cells increased with increasing amounts of CBA_2, all other parameters were constant. Relatively large pressures such in this case, a pressure drop of 400 bar, resulted in relatively small cells in the nucleated polymer/gas solution. For a nucleated solution, smaller cell sizes imply larger interfacial distances between adjacent cells which reduces the probability that adjacent cells will come in contact leading to coalescence and cell density reduction. A gradient size distribution can be observed in all the images.
Figure 5.7. Representative high magnification SEM images of foamed HDPE moulded microstructure obtained from *Profile 3* and *Method 4* with addition of: (A-B) 0.5 wt% CBA_2, (C-D) 1 wt% CBA_2 and (E-F) 4 wt% CBA_2.	

From the literature it has been reported that an increase in injection pressure (and hence injection speed) in foam injection moulding processes causes a decrease in bubble growth with a uniform cell size and distribution [30]. In this case however, a gradient size distribution was observed in all the images reported in Figure 5.7, most probably associated with the two-step processing adopted.

The progress of the cell structure when foaming HDPE as a result of the effects of CBA_1 content (1 wt% and 4 wt%) employing various process parameters (extrusion and IM) on the degree of foaming can be observed in Figure 5.8.

Evolution of the cell structure in foamed HDPE on addition of 1 wt% (A-D) and 4 wt% (E-H) CBA₁, prepared using different extruder and injection moulding settings.	*Comments*

Evolution of the cell structure in foamed HDPE on addition of 1 wt% (A-D) and 4 wt% (E-H) CBA$_1$, prepared using different extruder and injection moulding settings.
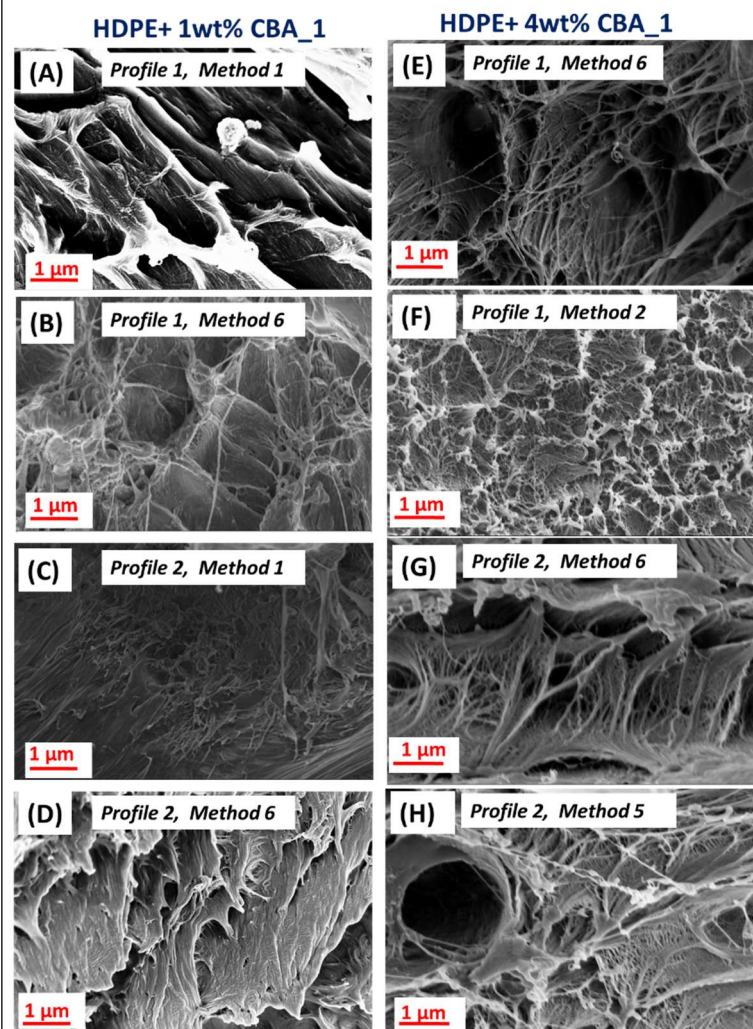
Figure 5.8. Representative SEM images of foamed HDPE moulded microstructure after addition of: (A-D) 1 wt% CBA$_1$ and (E-H) 4 wt% CBA$_1$, obtained at different temperature profiles in the extruder (i.e. profile 1 and 2) and parameter settings during injection moulding (methods 1, 2, 5, or 6), as specified in the figure.

Comments

Addition of 1 wt% CBA$_1$ to the polymer matrix did not yield a regular cellular morphology for the processing regimes adopted.

Despite the use of profile 1 some porous microstructure was obtained (Figure 5.8(A-B)) but the use of profile 2 resulted in no foaming (Figure 5.8(C-D)), the size and distribution of the cells obtained were highly irregular and non-uniform. Nucleation may have occurred in the samples, but the growth of stable nuclei is not sufficient for them to be identified.

Figure 5.8(A) shows the largest void size (up to 5 μm) when compared to the other structures obtained for the same 1 wt% CBA$_1$, likely being the case in which cell coalescence occurred.

Addition of 4 wt% CBA$_1$ to the polymer visibly resulted in unstable morphologies with elongated cells and thin cell wall thickness (Figure 5.8 (E, G, H)), leading to a poor foam quality (i.e. low cell density and excessive cell collapse) of ruptured heterogeneous cell structure.

The use of *Method 6* (Figure 5.8 (E,G)) resulted in big voids (up to 10 μm) with no uniformity and/or integrity of the cells detectable through the whole cross section imaged, regardless of the type of profile (i.e. 1 or 2) adopted for extrusion.

The large size pores identified in these samples with thin cell walls form relatively weak zones from a foam stability point of view.

The cell size distribution was found to be more uniform in Figure 5.8(F) when *Method 2* with a higher post pressure (i.e. 250 bar) was applied for a shorter time (i.e. 5 sec) during the IM step, after being processed with profile 1 in the extruder. The same pressure drop of 350 bar applied during the IM of the same composition material but after using profile *2* in the extruder (see Figure 5.8(H)) affected differently the polymer microstructure, conferring a different cell geometry, more elliptical-like in shape and irregularly distributed. The presence of holes such as the relatively big one shown in Figure 5.8(H) may be a consequence of the cryo-fracture technique that requires the destruction of the sample through the use of a hammer.

A comparison of SEM images taken at two diverse magnification for specimens obtained on addition of 1 wt% and 4 wt% of both CBA$_1$ and CBA$_2$ is reported in Figure 5.9. The images reflect the sample morphology obtained after processing the various CBA-polymer systems at a constant temperature profile of 155°C in the extruder (i.e. *Profile 4*) prior to applying a pressure drop of 400 bar (i.e. *Method 6*) in the IM machine.

Evolution of the cell structure in foam HDPE on addition of 1 wt% and 4 wt% CBAs, when the generation of the gas takes place directly in the mini-IM moulding machine.	*Comments*
Figure 5.9. Representative SEM images of foamed HDPE moulded microstructure obtained from *Profile 4* and *Method 6* in injection moulding after addition of: (A-B) 1 wt% CBA$_1$, (C-D) 4 wt% CBA$_1$, (E-F) 1 wt% CBA$_2$ and (G-H) 4 wt% CBA$_2$.	The cell morphology of the microcellular polymer was influenced by the CBA content and type. However, a low void content was found in all the samples for the processing conditions applied. Predominantly, the images exhibit a combined compact crystalline structure of the polymer in which CBAs could not dissolve (and so microcells could not nucleate and grow) with micron and submicron cell sizes in the ''bulk-phase'' of the matrix. Possibly, the temperature of extrusion, lower than the actual decomposition temperature of the CBAs (i.e. 160°C), would account for the small cell densities observed in the figures. The polymer may not have flowed easily in the mould cavity to allow cells to nucleate and grow at the same time, and the driving force of the gas may not have been high enough to overcome the crystalline attractive forces and polymer chain entanglements [31]. Nonetheless, some foams appeared to have a cellular structure with finer microcells observed for a CBA content of 1 wt%. The presence of some holes in Figure 5.9(E, F) could be simply derived from the rupture of the sample during sample preparation prior to SEM imaging.

A compact crystalline structure of the polymer can be also seen in Figure 5.10, in which images, taken at high magnifications for specimens obtained with addition of 1 wt% and 4 wt% of both CBAs in the polymer, reflect the sample morphology obtained at a constant temperature profile of 160°C in the extruder (i.e. *Profile 5*). These images can be compared with the previous ones shown

in Figure 5.9 as, after the extrusion step, the specimens were prepared with exactly the same settings during IM (i.e. *Method 6*). The only difference between the two cases studied was a rise of only 5°C in the temperature of the extrusion step.

Evolution of the cell structure in foaming HDPE on addition of 1 wt% and 4 wt% CBAs, after a rise of only 5°C in the extrusion step from previous case (Figure 5.11) **Figure 5.10**. Representative SEM images of foamed HDPE moulded microstructure obtained using *Profile 5* and *Method 6* on addition of: (A) 1 wt% CBA_1, (B) 4 wt% CBA_1, (C) 1 wt% CBA_2 and (D) 4 wt% CBA_2.	***Comments*** Here again, the images suggest a low void fraction and an even more compact crystalline structure than of the polymer shown in Figure 5.9, especially at CBA loadings of 4 wt%. A 'pseudo-porous' pattern was observed in the sample showed in Figure 5.10(C), despite a cellular structure was only developed locally, probably due to a higher concentration of CO_2 in certain zones in the polymer melt compared to other regions where the gas was distributed. However, on the whole, the matrix stiffness of the samples prepared under these conditions was sufficiently large so as to prevent nucleated cells from growing to detectable sizes.
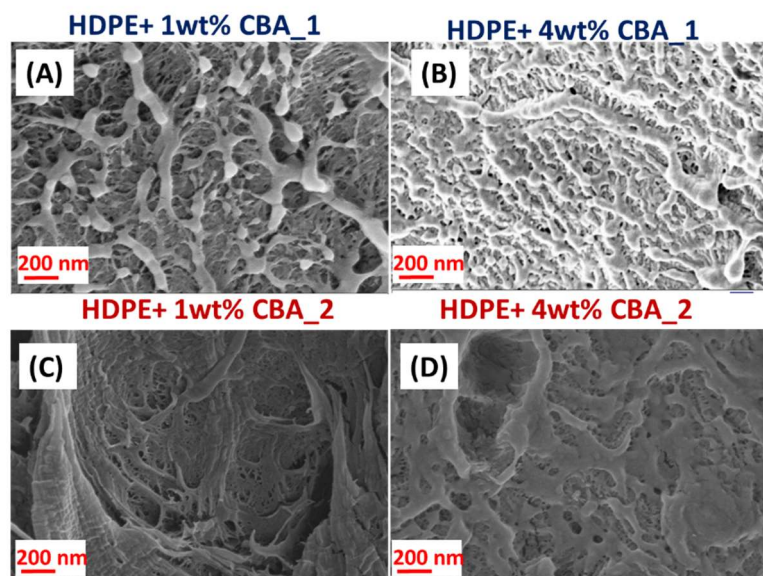
Although the foaming temperature of HDPE was above its melting point and the foaming time was long enough (first in the extruder and then in the IM) to allow the gas molecules to diffuse within the polymer melt into the cells, the void fraction did not significantly increase.
This very low generation of foam is undoubtedly related to the high crystallinity of HDPE.

The crystallization and the resulting change in viscoelastic behaviour in these polymer/gas systems tend to play a major role in microcellular processing. Crystallization is an important factor in improving melt strength and foaming ability of thermoplastics as it influences microcellular processing through its effects on both the mechanisms of cell nucleation, which starts around crystallites, and cell growth [32]. Too high crystallinity has a negative effect on cell generation by suppressing foam expansion [4]. Decreasing the amount of crystallinity would be effective for increasing the void fraction in the samples, overcoming the problem of the high melt viscosity and stiffness of the HDPE matrix which will in turn also decrease with crystallinity [10]. Moreover, the gas solubility would also benefit from this as in semi-crystalline polymers it decreases with increasing degree of crystallinity. In order to address the issue of high polymer crystallinity, a new set of experiments was completed, adopting an isothermal process during IM where the temperatures

in the injection piston and in the mould were both set at 180°C (*Method 8*) and 185°C (*Method 9*) and, the (hot) mould was subjected to a rapid quenching in a cold water tank. The reason for the tank was to hasten the cooling rate affecting the resulting crystallinity in an attempt to optimize the processing conditions and achieve a larger void fraction. The existing cooling rate dependence of crystallinity is in fact expressed by a decrease of crystallinity at faster cooling rates [33].

Furthermore, a larger circular disk-shaped mould of 35 mm diameter $\times$ 5 mm thickness was employed for trials when using these latter methods, as well as the smaller disk 25 mm diameter $\times$ 1.65 mm thickness used in Methods 1-6. The need to investigate a new disk geometry arose from the fact that foam morphology, i.e. cell shape, growth, distribution and size have been reported to be strongly influenced by sample/mould geometries in addition to IM conditions [34]. A fixed quantity of compound, (0.8 g and 4.2 g) was used to partially fill the harvesting cylinder and decrease the shot volume before injection it into the small and big disk moulds, respectively.

The morphologies obtained for the two type of sample geometries (i.e. big and small disks) adopting *Profile 4* and *Method 8* were compared and shown in Figure 5.11 and Figure 5.12 on addition of CBA_1 and CBA_2, respectively. The morphologies obtained using these moulding conditions are completely diverse to those derived from the main parameters settings, where the higher system pressure tended to suppress cell growth and even caused cell collapse. Under the revised processing conditions, also the holding pressure, which has a dominant effect on the dynamics of bubble growth [30], was considerably lowered.

It should be noted that despite SEM being the most utilized method for characterizing the cell structure of foamed samples, there are several disadvantages associated with it. The fact that it requires the destruction of the sample to capture a single cross-sectional image of the micro-structure is one major drawback. Besides the sample destruction, there is the problem that the SEM only provides a 2D image, which is unrepresentative of the true pore structure [35], i.e. in 3D. This should be considered when analysing the images reported below. Another important consideration that should also be taken into consideration is the possible presence of contaminants and/or air holes which can cause obvious cell non-uniformity [36]. The heterogeneous nucleation mechanism is certainly involved in the cell formation process here. It is likely that some pre-existing voids or moisture retained in the neat resin acted as one type of nucleation agent, while the dissolved CO_2 acted as another type. The nucleated cells resulting from moisture form big bubbles due to their larger free volume.

Evolution of the cell structure in foamed HDPE on addition of 1 wt% and 4 wt% CBAs, when adopting an isothermal process (i.e. *Method 8)* during IM
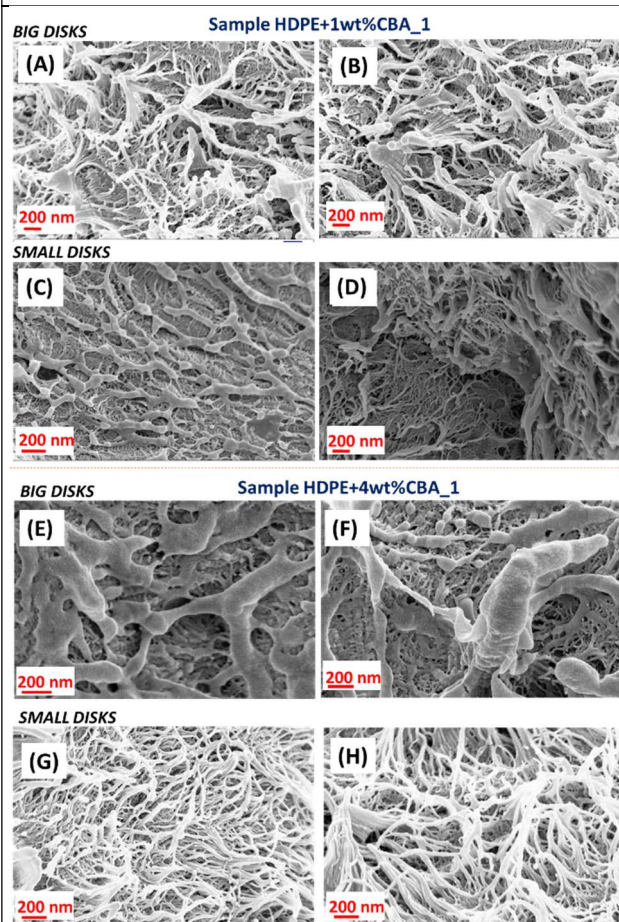
Figure 5.11. Representative SEM images of foamed HDPE moulded microstructure obtained using *Profile 4* and *Method 8* on addition of: (A-D) 1 wt% CBA$_1$; (E-H) 4 wt% CBA$_1$. The moulding was carried out using two different mould geometries of: (A-B, E-F) big circular mould shape; and (C-D, G-H) small circular mould shape.
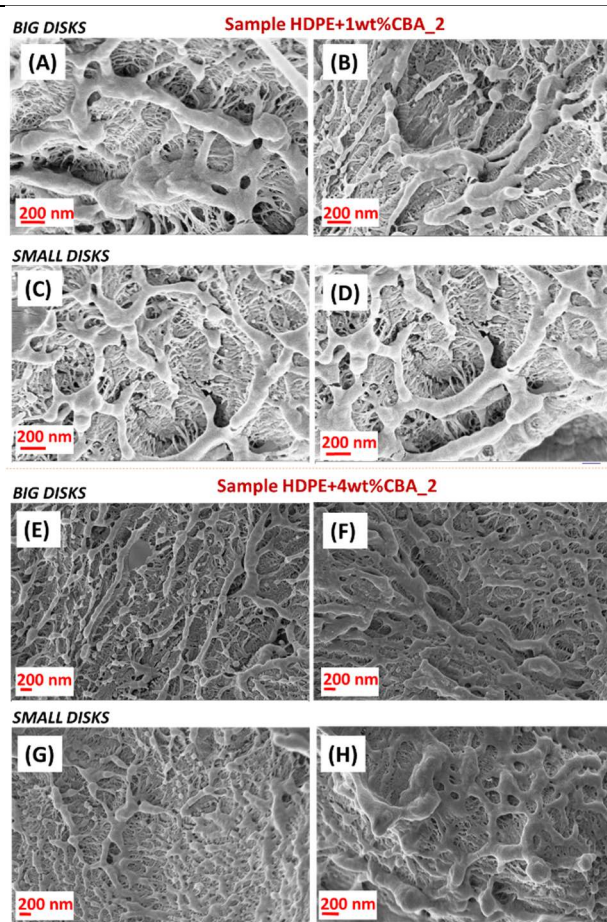
Figure 5.12. Representative SEM images of foamed HDPE moulded microstructure obtained using *Profile 4* and *Method 8* after addition of: (A-D) 1 wt% CBA$_2$; (E-H) 4 wt% CBA$_2$. The moulding was carried out using two different mould geometries of: (A-B, E-F) big circular mould shape; and (C-D, G-H) small circular mould shape.

Comments

The expansion ratio and cell morphology of the samples reported here were most probably influenced by part thickness and even more by the newly adopted moulding conditions. By comparing all the images, the finest cell structure with the highest void fraction was formed on addition of 4 wt% CBA$_1$ using the small disk geometry (see Figure 5.11(G-H)). When using a CBA$_1$ content of 1 wt% in combination with the big circular mould geometry, the new conditions allowed for the formation of a multitude of small pores characterised by a heterogeneous distribution in the polymer matrix (Figure 5.11(A-B)). However, the same geometry seems to have favoured the coalescence phenomenon leading to thick cell walls for concentrations of 4 wt% CBA$_1$ and 1 wt% CBA$_2$. The formation and growth of cells strongly depends on shot size [37]. Possibly, the larger room for expansion provided by the bigger disk mould caused many bubbles to be nucleated, grow, and merge so that cell coalescence is evident in Figure 5.13(E-F) and Figure 5.12(A-B).

Addition of CBA$_1$ resulted in a higher number of pores compared to CBA$_2$, especially at the 4 wt% content.

The fact that addition of CBA$_1$ resulted in a higher number of pores compared to CBA$_2$, especially at the 4 wt% content, perhaps is due to the high levels of gas escape inside the melt, in the latter case

when the melt entered the tool cavity which caused the melt to be depleted of blowing agent eventually creating a poor foam structure and a low expansion. Indeed, the gas escape phenomenon further reduces the amount of dissolved gas in the polymer melt as the gas inside the injected melt tends to escape due to the over-saturated state of the solution [30]. This could explain why, despite the evidence from TGA results (see section 5.1.2.3), that the use of CBA_2 to foam the polymer released a higher amount of gas during the reaction of decomposition than CBA_1 at the temperatures investigated, a larger number of pores was found in the structures foamed with CBA_1 instead, especially at CBA contents of 4 wt%.

Further investigations were carried out on the morphology of foamed samples obtained from processing at different temperature profiles in the extruder while maintaining unchanged the hitherto optimal conditions of *Method 8*, geometry of the small disc mould, and CBA content of 4% by weight. Figure 5.13 shows the cellular structure of the polymer on addition of 4 wt% CBA_1 prepared with *Profile 2*.
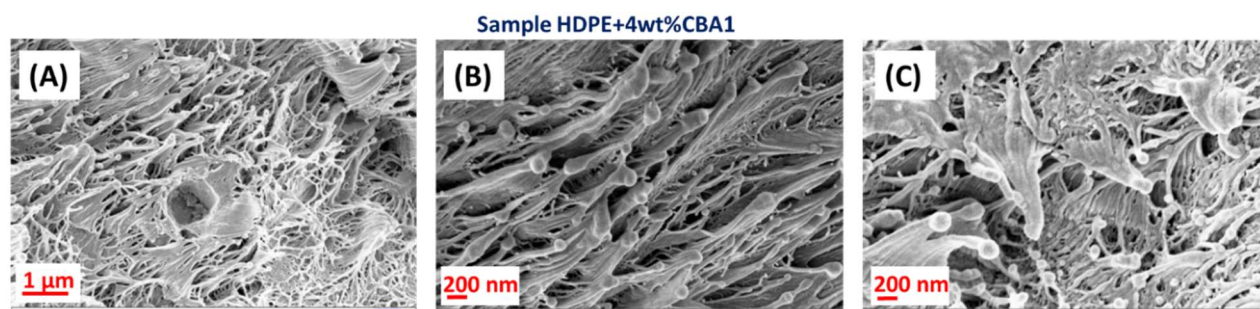
Figure 5.13. Representative SEM images of foamed HDPE moulded microstructure obtained using *Profile 2* and *Method 8* for a 4 wt% CBA_1 content.
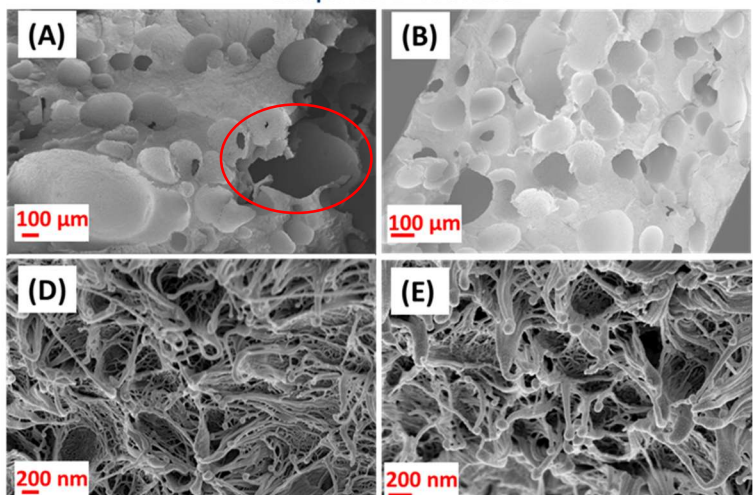
The three images at high magnifications in Figure 5.13 were taken from different areas of the same sample demonstrating the inhomogeneous morphology obtained. The processing conditions employed did not allow for a high cell volume fraction nor a homogeneous distribution of cell sizes. Even the images shown in Figure 5.14, of the HDPE moulded microstructure obtained using extrusion *Profile 3* with addition of 4 % by weight of CBA_2, did not lead to satisfactory foams, showing different pore shape and size distributed in stratified layers of the sample.
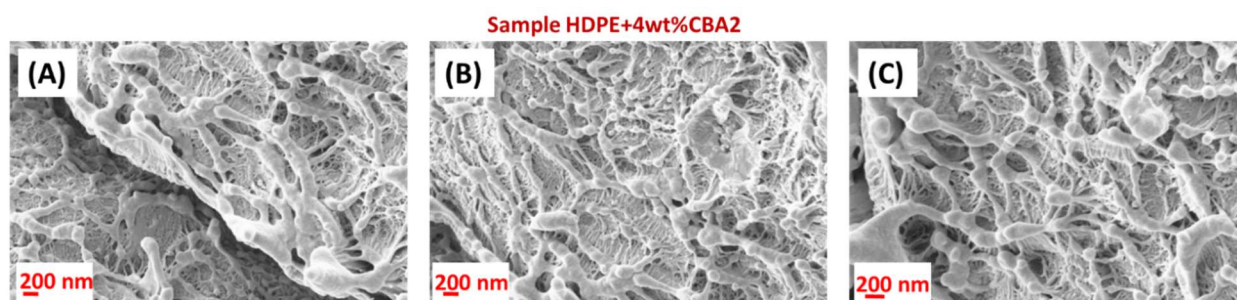
Figure 5.14. Representative SEM images of foamed HDPE moulded microstructure obtained from processing with *Profile 3* and *Method 8* with 4 wt% CBA_2 content.

Additional morphological analysis were conducted on a foamed HDPE specimens moulded using *Method 8* after being compounded with a 4 wt% CBA_1 inside the extruder set to *Profile 1*.

Evolution of the cell structure in foam HDPE obtained from processing using *Profile 1* and *Method 8* with 4 wt% CBA₁ content	*Comments*
Figure 5.15. Representative SEM images of foamed HDPE moulded microstructure obtained from processing with *Profile 1* and *Method 8* with 4 wt% CBA$_2$ content.	As seen from the four images taken at different magnifications, a highly porous microstructure, although not uniform, was obtained with these processing conditions. The increased cells diameter up to [150 μm - 300 μm] visible in Figure 5.15(A-B) indicated that a large number of bubbles were formed and most importantly grown to an extent not seen in this study to this point. The reduced cavity pressure and the high temperature of the mould allowed for further cell growth and foam expansion. Clearly, the images reflect also the presence of big voids caused by the cryo-fracture of the sample at the time of preparation for SEM imaging, as highlighted in the red circle in Figure 5.15(A).

The small bubble sizes obtained from higher injection pressures discussed up to this point could be, related to increases in the elasticity of the polymer through melt compressibility so that the bubbles may have needed more energy to grow. Conversely, the energy content required by the cells to grow may have been reduced by lower injection pressures. The images in Figure 5.15 suggest the possibility of obtaining higher void fractions and therefore density reductions compared to the previous processing conditions. The density measurements and the calculation of the void fraction in next section 5.2.2 highlight whether a significant reduction in density was achieved for the samples obtained with the processing adopted. Moreover, cells with larger diameters have to support smaller internal pressures compared to cells with small diameters since the pressure supported by a void inside a polymer depends on the size of such voids, eventually affecting the mechanical stability of the cells [29].

Lastly, a further increase of 5 ℃ was investigated for the isothermal injection moulding process while keeping all other processing conditions exactly the same as in the previous case, see Figure 5.15. Therefore, the images reported in Figure 5.16 refer to the foamed HDPE microstructure obtained from processing using *Profile 1* and *Method 9* in injection moulding after addition of 4 wt% CBA₁.

Evolution of the cell structure in foamed HDPE obtained from processing using *Profile 1* and *Method 9* with 4 wt% CBA$_1$ content, after a rise of only 5˚C in the IM step from previous case (Figure 5.15)	*Comments*
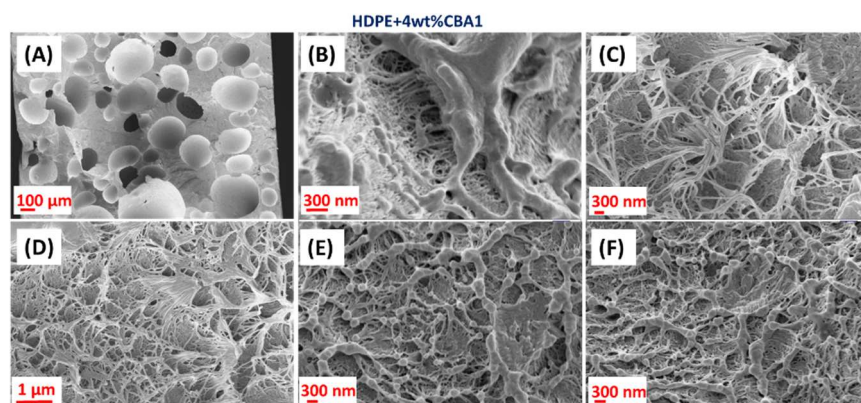
HDPE+4wt%CBA1

Figure 5.16. Representative SEM images of foamed HDPE moulded microstructure obtained from processing using *Profile 1* and *Method 9* with addition of 4 wt% CBA$_1$.

The images at different magnifications in Figure 5.16 show a highly porous structure, although characterized again by a lack of uniformity in the distribution of cell sizes.

The figure confirmed the high efficiency of the new processing conditions in creating numerous cells, although the calculation of pore population (density) in this group of samples was neglected because it was considered unreliable due to the irregular morphology.

Nonetheless, the cell geometry showed in Figure 5.18(A) indicates a predominant circular pore shape, in contrast to the elliptical shaped features of the previous sample moulded at 5˚C lower Figure 5.15(A-B).

Cell size and cell size distribution are normally a function of processing conditions and melt viscosity of the polymer. In this last set of experiments, in this section, using different moulding conditions (*Methods* 8 and 9), the addition of CBA$_1$ to the polymer melt seems to have reduced significantly the melt viscosity. Typically, cells grow fast and have larger sizes in low viscous melts than in a more viscous system [6]. The melt viscosity and the melt strength of the polymer in combination with the degree of crystallinity related to the dynamics of cooling have a high impact on the final cell morphology as a consequence of the cell growth process dependency on them [4]. Moreover, the mechanism of cell growth in a semi-crystalline matrix is controlled by the stiffness of the gas/polymer system, the rate of gas diffusion and the amount of gas loss at each foaming time and temperature adopted [38]. In general, melt viscosity and melt strength strongly affect the foam quality, mainly the solid-state density and the open cell fraction, thus influencing the porosity and the morphology of foamed poly(olefin)s. The reduction in melt viscosity obtained in the system was the outcome from selecting the appropriate CBA parameters, temperatures and pressures for processing, combined with the molecular structure of the polymer.

5.2.2 Density Measurements and Characterisation of foamed HDPE: Calculation of Expansion Ratio, Void fraction and Density Reduction

Density is an important property to take into account when evaluating the performance and economics of a foam [36]. In the specific case of a polymeric foam, the density is a measure of how much air there is inside the polymer. The emerging microcells are filled with both air and gases which increase the volume of the polymer, resulting in reduced density of the cellular product produced. Whether a microcellular foaming process occurred at the conditions employed has to be checked in relation to the bulk density of HDPE, enhanced by the presence of the gaseous phase in the samples. In the final plastic parts, the molecular chains of the polymer are tightly packed together and the air, that was originally present in the bulk density, is removed when the polymer contracts at the time of cooling [39].

Density is related to mechanical (e.g. tensile strength and brittleness) and physical properties [40], and critically, it influences the acoustic properties of foams. The final foam density depends principally on the original content of gas released by the decomposition reaction of the CBA, the fraction of gas remains dissolved in the polymer matrix after this solidifies, the gas that is lost to the environment and the depressurisation rate [14].

Since under normal circumstances gases possess a large volume to weight ratio, the more gas dissolved in, the lower the density of the polymer-gas mixture, whereas a rise in density generally is caused by a low gas content and/or an increase of attraction among the molecules in a bulk gas which causes a decrease in volume due to the reduced average distance between the gas molecules.

Three foamed sample disks for each formulation, randomly selected from the many samples produced at each condition employed in this study, were tested by weighing each sample in air prior to immersion in the liquid (i.e. ethanol) and the arithmetic average values (from 3 replicates) of each sample are listed as measured density ρ_{foam} in tables 5.2-5.5. In addition, the effect of the processing parameters on the relative density of each specimen (i.e. ratio between the bulk density of the foamed polymer,ρ_f, and the bulk density of the un-foamed polymer, ρ_p (i.e. 0.964 g cm^{-3})) was investigated by defining the void fraction, expansion ratio and density reduction obtained for each disk sample analysed. No measurement percentage error (standard deviation) values are reported in the following tables 5.2-5.5 as measurements resulted in errors of up to 0.05% which can be discarded.

Table 5.2. Values for density, expansion ratio, void fraction and density reduction obtained for foamed HDPE disks sample prepared with different processing methods at different loadings (≤ 0.5 wt%) of CBA_1 and CBA_2.

CBA loading	Method of Preparation		Measured Density ρ_{foam} /g cm^{-3}	Expansion Ratio $\frac{\rho_{polymer}}{\rho_{foam}}$	Void Fraction $1 - (\frac{\rho_{foam}}{\rho_{polymer}})$ /%	Density Reduction /%
	Extrusion Profile	*IM Method*				
0.1wt% CBA₁	*Profile 3*	*Method 3*	0.952	1.013	1.24	1.24
	Profile 3	*Method 7*	0.961	1.003	0.31	0.31
	Profile 3	*Method 8*	0.958	1.006	0.62	0.62
0.1wt% CBA₂	*Profile 3*	*Method 3*	0.941	1.024	2.39	2.39
	Profile 3	*Method 7*	0.956	1.008	0.83	0.83
	Profile 3	*Method 8*	0.939	1.027	2.59	2.59
0.2wt% CBA₁	*Profile 3*	*Method 3*	0.952	1.013	1.24	1.24
	Profile 3	*Method 7*	0.962	1.002	0.21	0.21
	Profile 3	*Method 8*	0.959	1.005	0.52	0.52
0.2wt% CBA₂	*Profile 3*	*Method 3*	0.952	1.013	1.24	1.24
	Profile 3	*Method 7*	0.959	1.005	0.52	0.52
	Profile 3	*Method 8*	0.950	1.015	1.45	1.45
0.3wt% CBA₁	*Profile 3*	*Method 3*	0.952	1.013	1.24	1.24
	Profile 3	*Method 7*	0.952	1.013	1.24	1.24
	Profile 3	*Method 8*	0.940	1.026	2.49	2.49
0.3wt% CBA₂	*Profile 3*	*Method 3*	0.953	1.012	1.14	1.14
	Profile 3	*Method 7*	0.955	1.009	0.93	0.93
	Profile 3	*Method 8*	0.951	1.014	1.35	1.35
0.4wt% CBA₁	*Profile 3*	*Method 3*	0.954	1.010	1.04	1.04
	Profile 3	*Method 7*	0.963	1.001	0.10	0.10
	Profile 3	*Method 8*	0.930	1.037	3.53	3.53
0.4wt% CBA₂	*Profile 3*	*Method 3*	0.953	1.012	1.14	1.14
	Profile 3	*Method 7*	0.962	1.002	0.21	0.21
	Profile 3	*Method 8*	0.950	1.015	1.45	1.45
0.5wt% CBA₁	*Profile 3*	*Method 3*	0.954	1.010	1.04	1.04
	Profile 3	*Method 7*	0.961	1.003	0.31	0.31
	Profile 3	*Method 8*	0.938	1.028	2.70	2.70
0.5wt% CBA₂	*Profile 3*	*Method 3*	0.952	1.013	1.24	1.24
	Profile 3	*Method 7*	0.960	1.004	0.41	0.41
	Profile 3	*Method 8*	0.949	1.016	1.56	1.56

The density measurements performed on the first set of foamed HDPE samples produced with a low blowing agent content (≤ 0.5 wt%) using the processing conditions specified in Table 5.2 revealed on average a low void fraction (< 3.6 %) was achieved. This clearly translated to a small reduction in density (< 3.6 %) due to the negligible gaseous phase developed within these structures, as

previously anticipated from the few and varied pores seen in the SEM images in Figure 5.6. The reasons behind this can be correlated with the difficulty of foaming a semi-crystalline resin in combination with the low CBA loading used in this experimental trial. The foamed sample produced by adding 0.4 wt% CBA$_1$ and processed using *Profile 3* and *Method 8* showed the highest void content and density reduction of 3.53 %, which is still quite far away from the material requirements for the final application.

Results from density measurements performed on foamed HDPE samples produced at different processing conditions with higher CBA loadings, 1 and 4 wt%, are listed in tables 5.3 and 5.4 with reference to CBA$_2$ and CBA$_1$, respectively.

Table 5.3. Values of density, expansion ratio, void fraction and density reduction obtained for foamed HDPE disks sample prepared with different processing methods at different loadings (1 and 4wt%) of CBA$_2$.

CBA$_2$ loading	Method of Preparation		Measured Density	Expansion Ratio	Void Fraction	Density Reduction
	Extrusion Profile	*IM Method*	$\boldsymbol{\rho_{foam}}$ /g cm^{-3}	$\dfrac{\boldsymbol{\rho_{polymer}}}{\boldsymbol{\rho_{foam}}}$	$1-(\dfrac{\rho_{foam}}{\rho_{polymer}})$ /%	/%
1wt% CBA$_2$	*Profile 1*	*Method 6*	0.960	1.004	0.41	0.41
	Profile 1	*Method 8*	0.879	1.097	8.82	8.82
	Profile 3	*Method 6*	0.961	1.003	0.31	0.31
	Profile 3	*Method 8*	0.899	1.072	6.74	6.74
	Profile 4	*Method 6*	0.956	1.008	0.83	0.83
	Profile 4	*Method 8*	0.933	1.033	3.22	3.22
4wt% CBA$_2$	*Profile 1*	*Method 6*	0.956	1.008	0.83	0.83
	Profile 1	*Method 8*	0.855	1.127	11.31	11.31
	Profile 3	*Method 6*	0.964	1.000	0.00	0.00
	Profile 3	*Method 8*	0.810	1.190	15.98	15.98
	Profile 4	*Method 6*	0.963	1.001	0.10	0.10
	Profile 4	*Method 8*	0.911	1.058	5.50	5.50

The results shown in Table 5.3 confirmed that addition of 4 wt% CBA resulted in higher void content in the samples than when 1 wt% was added, since more gas is released during decomposition of the foaming agent. Moreover, for an isothermal process during IM in which the pressure of injection drops from 150 bar to 0 bar seems the appropriate route to foam HDPE. In this set of experiments, a maximum density reduction of 15.98% was achieved by foaming the polymer with 4 wt% CBA$_2$ using *Profile 3* and *Method 8*. This type of CBA, as opposed to CBA$_1$, required a temperature of 180℃ inside the extruder and IM tool to ensure the release of the highest amount of gas possible. While the use of *Profile 1* (i.e. constant temperature of 165℃) and *Method 8* when processing the unfilled polymer resulted in a void content of 11.31% when using CBA$_2$ (see Table 5.3), the same conditions ensured a much higher void fraction (25.31%) on addition of 4 wt% CBA$_1$ (see Table 5.4).

Table 5.4. Values of density, expansion ratio, void fraction and density reduction obtained for foamed HDPE disks sample prepared using different processing methods at different loadings (1, 4 and 5 wt%) of CBA$_1$.

CBA$_1$ loading	Method of Preparation		Measured Density ρ_{foam} /g cm^{-3}	Expansion Ratio $\frac{\rho_{polymer}}{\rho_{foam}}$	Void Fraction $1-(\frac{\rho_{foam}}{\rho_{polymer}})$ /%	Density Reduction /%
	Extrusion Profile	IM Method				
1wt% CBA$_1$	Profile 1	Method 1	0.953	1.012	1.14	1.14
	Profile 1	Method 2	0.956	1.008	0.83	0.83
	Profile 1	Method 3	0.951	1.014	1.35	1.35
	Profile 1	Method 4	0.952	1.013	1.24	1.24
	Profile 1	Method 5	0.956	1.008	0.83	0.83
	Profile 1	Method 6	0.954	1.010	1.04	1.04
	Profile 1	Method 7	0.958	1.006	0.62	0.62
	Profile 1	Method 8	0.942	1.023	2.28	2.28
	Profile 1	Method 9	0.940	1.026	2.49	2.49
	Profile 2	Method 1	0.953	1.012	1.14	1.14
	Profile 2	Method 2	0.953	1.012	1.14	1.14
	Profile 2	Method 3	0.952	1.013	1.24	1.24
	Profile 2	Method 4	0.954	1.010	1.04	1.04
	Profile 2	Method 5	0.957	1.007	0.73	0.73
	Profile 2	Method 6	0.959	1.005	0.52	0.52
	Profile 2	Method 7	0.960	1.004	0.41	0.41
	Profile 2	Method 8	0.910	1.059	5.60	5.60
	Profile 2	Method 9	0.899	1.072	6.74	6.74
	Profile 3	Method 8	0.899	1.072	6.74	6.74
	Profile 4	Method 6	0.955	1.009	0.93	0.93
	Profile 4	Method 8	0.907	1.063	5.91	5.91
	Profile 4	Method 9	0.879	1.097	8.82	8.82
4wt% CBA$_1$	Profile 1	Method 1	0.960	1.004	0.41	0.41
	Profile 1	Method 2	0.962	1.002	0.21	0.21
	Profile 1	Method 3	0.959	1.005	0.52	0.52
	Profile 1	Method 4	0.963	1.001	0.10	0.10
	Profile 1	Method 5	0.959	1.005	0.52	0.52
	Profile 1	Method 6	0.961	1.003	0.31	0.31
	Profile 1	Method 7	0.963	1.001	0.10	0.10
	Profile 1	Method 8	**0.720**	**1.339**	**25.31**	**25.31**
	Profile 1	Method 9	**0.620**	**1.555**	**35.68**	**35.68**
	Profile 2	Method 1	0.956	1.008	0.83	0.83
	Profile 2	Method 2	0.957	1.007	0.73	0.73
	Profile 2	Method 3	0.960	1.004	0.41	0.41
	Profile 2	Method 4	0.959	1.005	0.52	0.52
	Profile 2	Method 5	0.962	1.002	0.21	0.21
	Profile 2	Method 6	0.960	1.004	0.41	0.41
	Profile 2	Method 7	0.963	1.001	0.10	0.10
	Profile 2	Method 8	0.800	1.205	17.01	17.01
	Profile 2	Method 9	0.767	1.257	20.44	20.44
	Profile 3	Method 8	0.911	1.058	5.50	5.50
	Profile 4	Method 6	0.959	1.005	0.52	0.52
	Profile 4	Method 8	0.860	1.121	10.79	10.79
	Profile 4	Method 9	0.854	1.129	11.41	11.41
	Profile 5	Method 6	0.963	1.001	0.10	0.10
	Profile 5	Method 8	0.880	1.095	8.71	8.71

Profile 5	*Method 9*	0.860	1.121	10.79	10.79

The different temperature profiles applied in the extruder and mini-IM employed revealed interesting findings with increasing CBA_1 loading in the polymer. It should be noted that regardless of the temperature profile applied during the extrusion step and the initial CBA_1 content the isothermal *Methods 8* and *9*, among all the nine methods investigated, always gave the foams with the highest fraction of voids. Evidently, the high pressures during injection applied for *Methods 1-7*, in combination with the relatively long holding time (> 5 sec) and the low mould temperatures (< 180 ℃) did not produce a highly porous structure within these materials, providing void fractions below 1.4%. The 'collapse' phenomenon in fact depends strongly on both the exerted holding pressure and growth time [30]. The agglomeration of adjacent cells which can lead to cells merging into a single cell and therefore a reduction in the nucleated cell density (i.e. coalescence) can be promoted by the compression, extension, and shear flow associated with shaping operations and couples the three steps of cell nucleation, cell growth, and shaping during foaming [32]. As had already been suggested by Mahmoodi et al. [41] in their study conducted on foams produced by an IM process, cell collapse is generally evident when the holding pressure is high and the growth time is shortened. Accordingly, the high system pressure in this work most likely suppressed cell growth and could also have resulted in cell collapse.

While adding 1 wt% CBA_1 to HDPE a maximum density reduction of 8.82 % was obtained when the foam was produced with *Profile 4* (i.e. constant temperature of 155 ℃) and *Method 9*, the increase in CBA_1 content to 4 wt% significantly enhanced the volume fraction of cells within the polymer matrix. In particular, the highest reduction in density of ca. 36 % was obtained by foaming the polymer at a constant temperature of 165 ℃ in the extruder (i.e. *Profile 1*) prior a to a further foaming step using *Method 9*. In this case, the density of the polymer dropped from 0.964 g cm^{-3} to 0.620 g cm^{-3} indicating the presence of ca. 36% of voids in the sample generated by the addition of 4 wt% CBA_1.

Syntactic foams, currently employed as conventional matching layers inside the *Elster New Generation Ultrasonic Transducers* construct (i.e. the final product application of this study) are the benchmark materials for reference when selecting the most promising foamed HDPE samples produced in this work in terms of density reduction and acoustic properties for use in ta transducer. Syntactic foams have densities of ca. 0.71 g cm^{-3}, accounting for a 26.35% void fraction and expansion ratio of 1.37. The data shown in Table 5.3 noticeably confirmed that the foamed HDPE samples with 4 wt% CBA_1 produced under the relevant conditions could be potential substitutes for syntactic foams in gas sensors as they are characterised by a further 26% increase in density reduction. It interesting to note that an increase in the injection temperature of only 5 ℃ (when

moving from *Method 8* at 180 °C to *Method 9* at 185 °C) enhanced the void fraction from 25.31% to 35.68%, accounting for a total gain in density reduction of 29%.

It is worth mentioning that also a higher content than 4 wt% of CBA_1 was investigated in this study. The attempt of adding an extra 1 wt% initial content of CBA_1 (i.e. 5 wt% CBA_1), which could have allowed the release of more gas in the polymer melt, did not bring further void content when employing a *Profile 1* in the extruder and a *Method 8* in IM, rather the void fraction dropped to 3.53% instead and a density of 0.930 g cm^{-3} and expansion ration of 1.037 were recorded.

The change of the mould disk geometry in the production of foam samples also affected the bulk density of the foamed polymer, as confirmed from density measurement results reported in Table 5.5.

Table 5.5. Values of density, expansion ratio, void fraction and density reduction obtained for foamed HDPE (Big Disk) samples prepared with a *Profile 4* for different loadings (1 and 4wt%) of CBA_1 and CBA_2 and *Methods 6* and *8*.

CBA loading	Method of Preparation		Measured Density ρ_{foam} /g cm^{-3}	Expansion Ratio $\frac{\rho_{polymer}}{\rho_{foam}}$	Void Fraction $1 - (\frac{\rho_{foam}}{\rho_{polymer}})$ /%	Density Reduction /%
	Extrusion Profile	*IM Method*				
1wt% CBA₁	*Profile 4*	*Method 6*	0.940	1.026	2.49	2.49
	Profile 4	*Method 8*	0.945	1.020	1.97	1.97
1wt% CBA₂	*Profile 4*	*Method 6*	0.890	1.083	7.68	7.68
	Profile 4	*Method 8*	0.888	1.086	7.88	7.88
4wt% CBA₁	*Profile 4*	*Method 6*	0.885	1.089	8.20	8.20
	Profile 4	*Method 8*	0.875	1.102	9.23	9.23
4wt% CBA₂	*Profile 4*	*Method 6*	0.900	1.071	6.64	6.64
	Profile 4	*Method 8*	0.889	1.084	7.78	7.78

The data reported in Table 5.5 refer to the samples foamed with the big disk geometry. *Profile 4* (i.e. constant temperature of 155 °C) ensured that the polymer was mixed with the CBA without reaching the temperature for decomposition of the blowing agents when inside the extruder. Unlike what occurred using the smaller disk mould, the different mould dimensions influenced the degree of foaming allowing the formation of a cellular structure even at the high injection pressures of 600 bar and large pressure drops of 400 bar applied in *Method 6*. It could be the case where the larger sample thickness provided extra space for foam expansion, while the high pressure inside the cavity entrapped the gas preventing further escape of gas [30].

The comparison between the two types of CBA shows that an initial CBA content of 4 wt% was necessary to achieve a void fraction above 8% when using CBA_1, whereas a content of 1 wt% was sufficient and even slightly better than using 4 wt% of CBA_2. Clearly, the difference in the particle

size between the two CBA types contributes to this behaviour. Nonetheless, the use of 4 % by weight of CBA_1 in this instance resulted in the highest void fraction (i.e. 9.23%) of the samples listed in Table 5.5, although this value is still far away from the void fractions reported in Table 5.4 (> 25%) achieved when using the mould of the smaller disk geometry.

It should be pointed out that a further case study was employed in order to verify whether the potential issue of gas escape from the polymer melt within the harvesting cylinder to atmosphere during micro-IM could be prevented by employing a conventional all-electric IM machine (i.e. an *Engel E Victory 60T*, see section 3.1.4 of Submission Portfolio No. 5). The control of cell growth and expansion stages becomes problematic in a system such as the micro-IM used in this work which fails to prevent the gas escape problem, on the contrary, the gas continuously diffuses out of the cylinder as it moves from the nucleation step to the cell growth step. Pressurized gas pockets within the small cylinder of the micro-IM are likely to diffuse out of the cylinder (escape) due to the floating piston which lifts up and down as uncontrollable expansion starts. The high temperature gas tends to fuse the polymer pellets causing further pressure fluctuations and resulting in a cascading instability of the solution system when moving from the nucleation to the cell growth step. Therefore, it was the aim of this case study to try and achieve a higher porosity foam samples by using a machine that is widely used in industry for large lightweight components and is characterised by a clamping pressure lock in a closed system. In this case, a loading of 1 wt% CBA_2 was selected and incorporated into the HDPE matrix using *Profile 4,* 155°C along the barrel in the extruder prior IM [c]. However, the results from this case study confirmed that there was almost no foaming (i.e. density reductions below 2%) for the conditions employed in the Engel E Victory 60T IM machine. Possibly, adding more CBA_2 to HDPE, or using CBA_1 instead, would have led to higher reduction in density, likewise modifying other parameters and machine settings. Nevertheless, these initial unsatisfactory results in combination with the fact that a machine of such size requires kilos of material to be first compounded could not justify further trials at this stage of the project, especially given the target was to produce specimens for preliminary testing protocols only.

5.2.3 Acoustic Properties of foamed HDPE by addition of CBAs

The acoustic properties of the foamed HDPE samples produced (small disk geometry) were evaluated via transmission of acoustic energy in air (or water). Measurements were made by comparing the ultrasonic transmission through each sample to the transmission in air (or water)

---

[c] A standard screw geometry with a screw diameter of 30 mm was used in this case. Moulding was carried out using an injection pressure drop of 50 bar (from 60 to 10 bar) and a fixed constant temperature along the barrel ranging from 160 °C to 200 °C, filling a shot volume of 0.01 cm^3 per time. The temperature in the mould was set at 50 °C, while the time of injection was set at 3 sec, with a holding pressure time in the mould cavity (i.e. time of packing) of 10 sec. The total cycle time was 74.6 sec.

without a sample present. A minimum of two specimens for each foam type were tested and results are summarised in tables 5.6 and 5.7. In particular, Table 5.6 summarises the ultrasonic velocities (longitudinal) and attenuation coefficients of ultrasound (which determine the acoustic characteristics of a material [42]), acquired by frequency-domain spectra analysis through ultrasonic air-coupled measurements in transmission in the foam samples. The acoustic properties derived by the characterisation of the materials by ultrasonic waves through transmission in water immersion are summarised in Table 5.7 and, include the velocity of sound in the foamed polymer samples estimated via the time of flight (ToF) technique. In this case, the ultrasonic velocity (i.e. the velocity of the propagation of elastic waves) is calculated from the measured time of flight (ToF) i.e. the time taken by the sound wave to travel through the sample.

It should be pointed out that the ToF refers to the difference in time of flight of the ultrasound signals received with and without the sample between two transducers kept at the same position (i.e. ToF = t_{sample} - t_{ref}). Although the values displayed in the ToF column in Table 5.7 are all reported as positive numbers (i.e. the absolute values of the ToF numbers), the measurements of each sample characterized produced negative values of the ToF. When the signal with the sample located in between the transducers at normal incidence arrives before that of the reference signal (i.e. the signal that travels through pure water), then this time ToF is negative, meaning that the ultrasound velocity in the sample is then larger than in water (1450 m/s), as expected. Conversely, when the signal with the sample arrives after the reference signal ($t_{sample} > t_{ref}$), then t_{sample}-t_{ref} is positive and the ultrasound velocity in the sample is smaller than in water.

The experimental values of the acoustic impedance, obtained by multiplying the densities of the foams by the velocities of ultrasound in the samples are reported in both tables. The speed of sound in a homogenous medium is directly related to both the elastic modulus and density. Changes in either elasticity or density will affect the pulse transit time through a sample of given thickness [42]. As a consequence of the fact that the velocity of a sound wave, *c*, propagating in a medium varies with the physical properties of the medium [43], sound velocities in air transmission slightly differed from the velocities obtained in water. This was proven by the slightly higher values of *c*, although of the same order of magnitude, obtained for the same type of samples measured with both methods (i.e. 0.1-0.4 wt% CBA_1 and 0.1-0.4 wt% CBA_2, produced with *Profile 3* and *Method 3*) when the medium of propagation was water instead of air.

The attenuation coefficients reported in the last column of Table 5.6 were determined from the change in the amplitude of the acoustic signal and can be seen as a measure of dissipative energy since they refer to the loss of acoustic energy as the wave travels through the material [42].

Table 5.6. Acoustic properties obtained in air transmission for foamed HDPE samples produced by different methods with varying CBA_1 and CBA_2 loading.

CBA loading	Method of Preparation		Velocity of sound c /m s^{-1}	Measured Density ρ_{foam} /g cm^{-3}	Acoustic Impedence $Z = c \cdot \rho_{foam}$ /MRayl	Attenuation @Resonance Frequency /Np m^{-1}
	Extrusion Profile	IM Method				
0.1wt% CBA$_1$	Profile 3	Method 3	2309.50	0.952	2.20	22.42
0.1wt% CBA$_2$	Profile 3	Method 3	2330.67	0.941	2.19	18.21
0.2wt% CBA$_1$	Profile 3	Method 3	2423.75	0.952	2.31	23.39
0.2wt% CBA$_2$	Profile 3	Method 3	2297.15	0.952	2.19	23.02
0.3wt% CBA$_1$	Profile 3	Method 3	2388.03	0.952	2.27	10.73
0.3wt% CBA$_2$	Profile 3	Method 3	2379.24	0.953	2.27	19.96
0.4wt% CBA$_1$	Profile 3	Method 3	2381.00	0.954	2.27	13.12
0.4wt% CBA$_2$	Profile 3	Method 3	2443.15	0.953	2.33	18.49
0.5wt% CBA$_1$	Profile 3	Method 3	2441.73	0.954	2.33	15.15
0.5wt% CBA$_2$	Profile 3	Method 3	2400.18	0.952	2.28	14.62
1wt% CBA$_1$	Profile 1	Method 1	2391.46	0.953	2.28	11.18
	Profile 1	Method 2	2417.07	0.956	2.31	11.12
	Profile 1	Method 3	2329.22	0.951	2.22	10.24
	Profile 1	Method 4	2385.41	0.952	2.27	12.01
	Profile 1	Method 5	2389.93	0.956	2.28	10.71
	Profile 1	Method 6	2395.00	0.954	2.28	11.30
	Profile 2	Method 1	2354.31	0.953	2.24	12.83
	Profile 1	Method 2	2427.33	0.953	2.31	11.76
	Profile 2	Method 3	2415.12	0.952	2.30	11.42
	Profile 2	Method 4	2412.94	0.954	2.30	10.91
	Profile 2	Method 5	2417.07	0.957	2.31	11.12
	Profile 2	Method 6	2391.70	0.959	2.29	9.26
4wt% CBA$_1$	Profile 1	Method 1	2404.26	0.960	2.31	14.56
	Profile 1	Method 3	2391.13	0.959	2.29	10.54
	Profile 1	Method 4	2403.17	0.963	2.31	11.10
	Profile 1	Method 5	2417.21	0.961	2.32	11.13
	Profile 1	Method 6	2380.11	0.959	2.28	13.15
	Profile 2	Method 1	2360.82	0.956	2.26	12.41
	Profile 2	Method 3	2349.90	0.957	2.25	10.17
	Profile 2	Method 6	2421.97	0.959	2.32	12.21
4wt% CBA$_2$	Profile 4	Method 6	2443.15	0.956	2.33	22.36

From this analysis, it emerged that all the samples listed in Table 5.6 had acoustic impedance values in the order of 2 MRayl. The different methods of preparation as well as varying CBA type and content did not result in significantly lower acoustic impedance (Table 5.6), associated with the negligible porosity obtained for the foamed moulded parts when prepared with the processing conditions employed. This result is not surprising given the morphologies observed from SEM imaging, reported in section 5.2.1 and the subsequent density measurements (section 5.2.2) for these same samples.

Acoustic absorption occurs when acoustic energy is transmitted indirectly through the air, interacting with a solid structure. The way it interacts with the air critically depends on the morphology of the material. The introduction of porosity can greatly expand the range of acoustic properties of polymer materials [44]. Sound absorption occurs when sound enters a porous material. Its surface allows sound waves to enter the material through a multitude of small holes or openings [45]. In porous sound absorbers, sound propagation takes place in a network of interconnected pores throughout the material. The velocity of sound depends mainly on the elastic modulus and density of the material, which are in the main governed by the different phases present and eventually any damages to the material. Porous materials are characterized by lower speeds of sound than non-porous materials [44]. The high compressibility of porous materials, due to the presence of a large proportion of gas, normally results in low speed of sound, whereas sound velocities displayed in Table 5.6 showed values greater than or equal to 2300 m/s.

When searching for the best sound absorption properties of a material, there is an optimum density value, which does not have to be necessarily the smallest density value, but a density value combined with an appropriate number and size of pores such that the material absorbs most of the sound waves [46]. Too low or too high densities affect the sound absorption properties of the samples. Specifically, high densities imply low absorption coefficients, which can be explained by a low porosity developed in such samples and the diminution of pore size, both key parameters with regard sound absorption [19]. Indeed, the foam densities (i.e. ρ_{foam}) reported in Table 5.6 are high values, greater than or equal to 0.950 g cm^{-3}. Despite the small reduction in density of these samples (Table 5.6), a consequence of the poor level of porosity obtained for the foaming conditions employed, the use of 1 and 4 wt% of CBA$_1$ resulted in very low attenuation coefficients ($\leq$ 15 Np/m).

The attenuation is a measure of dissipative acoustic energy due to the two main mechanisms of scattering and absorption losses generated from viscous boundary layer losses, thermo-elastic effects, inelastic hysteresis or dislocation damping. Besides the reflection losses occurring at these macroscopic defects or other material discontinuities, most of the energy loss results from absorption and scattering of the ultrasonic waves [42].

Further measurements were conducted in water transmission to evaluate the acoustic properties of the other foamed HDPE samples, see Table 5.7. No measurement percentage error (standard deviation) values are reported in the following table as using only two measurements resulted in errors of up to 0.05% which can be discarded.

Table 5.7. Acoustic properties obtained in water transmission for foamed HDPE samples produced by different processing methods with varying CBA_1 and CBA_2 content.

| *CBA loading* | ***Method of Preparation*** | | **ToF** | **Velocity of sound** | **Measured Density** | **Acoustic Impedence** |
	Extrusion Profile	*IM Method*	/ns	c /m s^{-1}	ρ_{foam} /g cm^{-3}	$Z = c \cdot \rho_{foam}$ /MRayl
0.1wt% **CBA₁**	*Profile 3*	*Method 3*	505	2632.69	0.952	2.51
	Profile 3	*Method 7*	455	2512.64	0.961	2.41
0.1wt% **CBA₂**	*Profile 3*	*Method 3*	490	2546.57	0.941	2.40
	Profile 3	*Method 7*	455	2500.96	0.956	2.39
0.2wt% **CBA₁**	*Profile 3*	*Method 3*	480	2542.21	0.952	2.42
	Profile 3	*Method 7*	455	2478.37	0.962	2.38
0.2wt% **CBA₂**	*Profile 3*	*Method 3*	500	2598.91	0.952	2.47
	Profile 3	*Method 7*	460	2497.83	0.959	2.39
0.3wt% **CBA₁**	*Profile 3*	*Method 3*	470	2491.83	0.952	2.37
	Profile 3	*Method 7*	450	2470.08	0.952	2.35
0.3wt% **CBA₂**	*Profile 3*	*Method 3*	485	2562.31	0.953	2.44
	Profile 3	*Method 7*	455	2512.64	0.955	2.40
0.4wt% **CBA₁**	*Profile 3*	*Method 3*	480	2530.51	0.954	2.41
	Profile 3	*Method 7*	450	2481.20	0.963	2.39
0.4wt% **CBA₂**	*Profile 3*	*Method 3*	415	2298.57	0.953	2.19
	Profile 3	*Method 7*	455	2500.96	0.962	2.40
0.5wt% **CBA₁**	*Profile 3*	*Method 7*	458	2347.82	0.961	2.26
0.5wt% **CBA₂**	*Profile 3*	*Method 7*	440	2453.36	0.960	2.35
1wt% **CBA₂**	*Profile 4*	*Method 6*	405	2299.18	0.956	2.20
4wt% **CBA₁**	*Profile 1*	*Method 8*	340	**2084.29**	0.720	**1.50**
	Profile 1	*Method 9*	180	**1692.75**	0.620	**1.05**
4wt% **CBA₂**	*Profile 4*	*Method 6*	420	2359.42	0.963	2.27

Of the foamed HDPE samples listed in Table 5.7, the lowest speed of sound (highlighted by the red rectangle in the table) were registered for the samples foamed on inclusion of 4 wt% CBA_1 and

processed using *profile 1* and *methods 8* and *9*. The low values of *c* can be associated to the presence of a large proportion of gas developed inside the disk sample under the processing conditions employed. Considering that the propagation of ultrasonic waves in polymers is determined by the density and viscoelastic properties of the polymer [42] and that velocity of sound increases with stiffness [47], the stiffness of this matrix material surely had a great effect on the propagation speed of the sound waves.

Table 5.7 also lists the acoustic impedances calculated for each foamed HDPE sample, which is a measure of the relationship between density and velocity of sound obtained in each case. The high degree of porosity developed in these samples (with 4wt% CBA_1) manifested in a low speed of sound as well as a low value of bulk density, whose product inevitably gives low values of acoustic impedance. Under these conditions, the acoustic impedance values are in the order of 1 MRayl, values comparable with the benchmarking sample, i.e. syntactic foams which have impedance values ranging from 1.75 to 2.22 MRayl derived from a value of *c* of 2486.65 m/s.

The foamed HDPE with 4 % by weight of CBA_1 using a two-step processing route is clearly a potential candidate for use as a passive layer within acoustic sensors to measure the velocity of gas in a pipeline. Furthermore, based on the void fraction and the acoustic characteristics obtained from this preliminary study, these moulded plastic samples seem to represent a possible substitute for the syntactic foams already in use.

5.3. PART II-B: Foams of HDPE-MWCNT Composites via Chemical Foaming

Nano-sized particles (i.e. order of 10^{-9} m) such as MWCNTs can be added as fillers to modify and improve the properties of a matrix polymer, due to their high aspect ratio and large effective surface area which can offer the potential for a high reinforcing efficiency, good barrier properties, and improved dimensional and thermal stability [48]. The inclusion of nanoparticles in foams has great potential for improving foam properties and create novel foamed composite materials with advantageous characteristics, including lightweight and high specific strength [48] as well as lower cost [49]. Nanoparticles can act as heterogeneous nucleation agents for bubble generation, reducing the nucleation free energy allowing for the formation of foam cells with a controlled structure and uniform distribution [48]. The foam morphology, provided by the number, size and spacing of the cells, accounts for the final bulk density and thus foam properties [50] in combination with the bulk properties of the matrix, and physical and chemical properties of the nanofiller(s) dispersed and distributed in the matrix [51]. As the state of nanoparticle dispersion affects the microcellular morphology, whether a well dispersed system is achieved or not can result in a more nucleated system during the microcellular foaming process [52]. The effects of filler dispersion on the cell

morphology of HDPE-MWCNT composite foams prepared in this work were investigated. Determining how the polymer modification affected selected physical and acoustic properties and the structure of the foamed composite parts (first extruded and then injection moulded) is described in this section. The morphological features, degree of porosity, expansion ratio, density reduction and acoustic impedances are presented and discussed below.

It should be emphasized that, based on the main results obtained in the previous section 5.2 (PART II-A) from preliminary testing protocols on unfilled HDPE foam parts, *Profile 1* in the extruder proved to be the most promising among the five profiles investigated along the barrel for obtaining parts suitable for the final application, therefore, profile 1 was used to produce all foams from this point.

5.3.1 SEM: Morphology of foamed HDPE-MWCNT Composites by addition of CBAs

A series of micrographs of the fractured surface of cellular HDPE-MWCNT composite foams produced with addition of 1 and 4 wt% CBA_1 and CBA_2 at different foaming conditions (i.e. pressure and temperature) are shown in Figures 5.17-5.22. The images reflect the internal microstructure and morphology of the moulded disks formed during the two-step processing and thus the pressurized two-stage expansion process. The morphologies obtained illustrate the effects of the conditions applied during foaming on the volume expansion ratio of HDPE-MWCNT composite foams.

Representative SEM images of microcellular HDPE-MWCNT composite structures obtained using *Profile 1* in the extruder and *Method 6* in IM, at various MWCNT content and 1 wt% CBA_1 loading, are presented in Figure 5.17.

The use of the second blowing agent, CBA_2, at the same 1wt%, while not changing the processing parameters during foaming, resulted in even lower volume expansions and a lower number of cells compared to that for CBA_1, as shown in Figure 5.18.

Evolution of the cell structure in foam HDPE-MWCNT composites obtained from processing using *Profile 1* and *Method 6* with 1 wt% CBA$_1$ content and different MWCNT loadings.
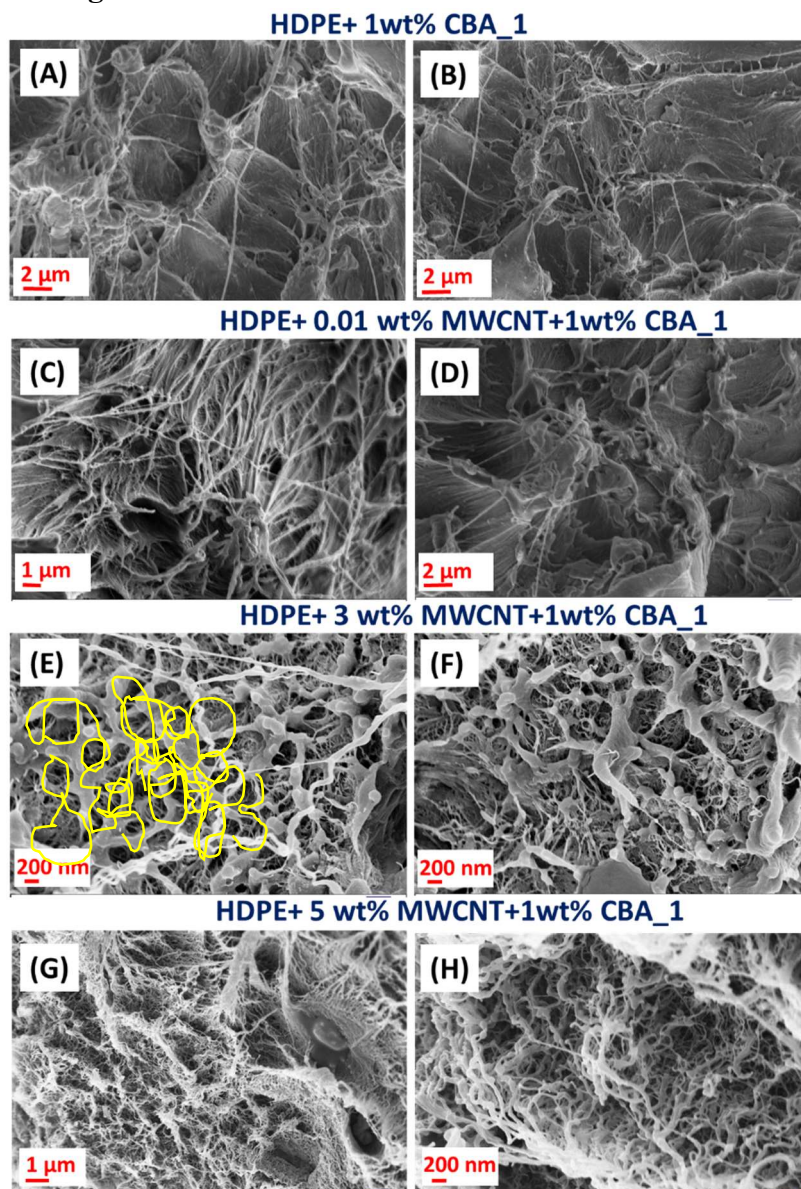
Figure 5.17. Representative high magnification SEM images of foamed moulded microstructure of (A-B) unfilled HDPE and (C-H) HDPE-MWCNT composites produced using *Profile 1* (extruder) and *Method 6* (injection moulding) with 1 wt% CBA$_1$. The images refer to the MWCNT loadings of (C-D) 0.01 wt%, (E-F) 3 wt% and (G-H) 5 wt% at three different magnifications.

Comments

From a comparison of the SEM images reported in Figure 5.17, and although these samples were manufactured using the same processing conditions and CBA$_1$ content (1wt%), the insertion of CNTs into the polymer altered the polymer morphology and thus the size and density of the cells produced.

Comparing unfilled HDPE foams (figures (A-B)) to filled ones (figures (C-H)), the microstructure was altered after adding even a small percentage of (0.01 wt%) of MWCNTs, albeit a poor cell structure was attained in the latter case.

As reported in the literature, the size, the number of cells and the uniformity of cell distribution in filled materials should differ from unfilled ones [51]. A much better nuclei structure than the unfilled material is expected and, actually, structures of the composites show an increased cell wall rigidity due to the nanofiller inclusion. While leading to an increase in energy dissipation, the presence of MWCNTs may have assisted cells withstand the stretching force that otherwise might have broken a thin walled cell, conferring strength to the foam providing protection for the cells from being destroyed by external forces [53]. The addition of MWCNTs to polymers is known to increase melt viscosity.

Increasing MWCNT loadings promoted the interconnectivity of MWCNTs in the HDPE matrix as can be observed from the formation of a continuous network of MWCNTs at 3 and 5 wt% MWCNT loadings (as highlighted in yellow in Figure 5.17(E)). However, if cell nucleation was really enhanced by the heterogeneous nucleating agent` action of the nanoparticles is questionable. Cell size and distribution of cell size resulted was irregular and non-uniform at all filler content, suggesting the HDPE matrix, reinforced by MWCNTs, was too stiff to achieve any observable foam expansion. Consequently, a very low void content was obtained in such foams.

Evolution of the cell structure in foamed HDPE-MWCNT composites obtained using *Profile 1* and *Method 6* with 1 wt% CBA₂ content and different MWCNT loadings.
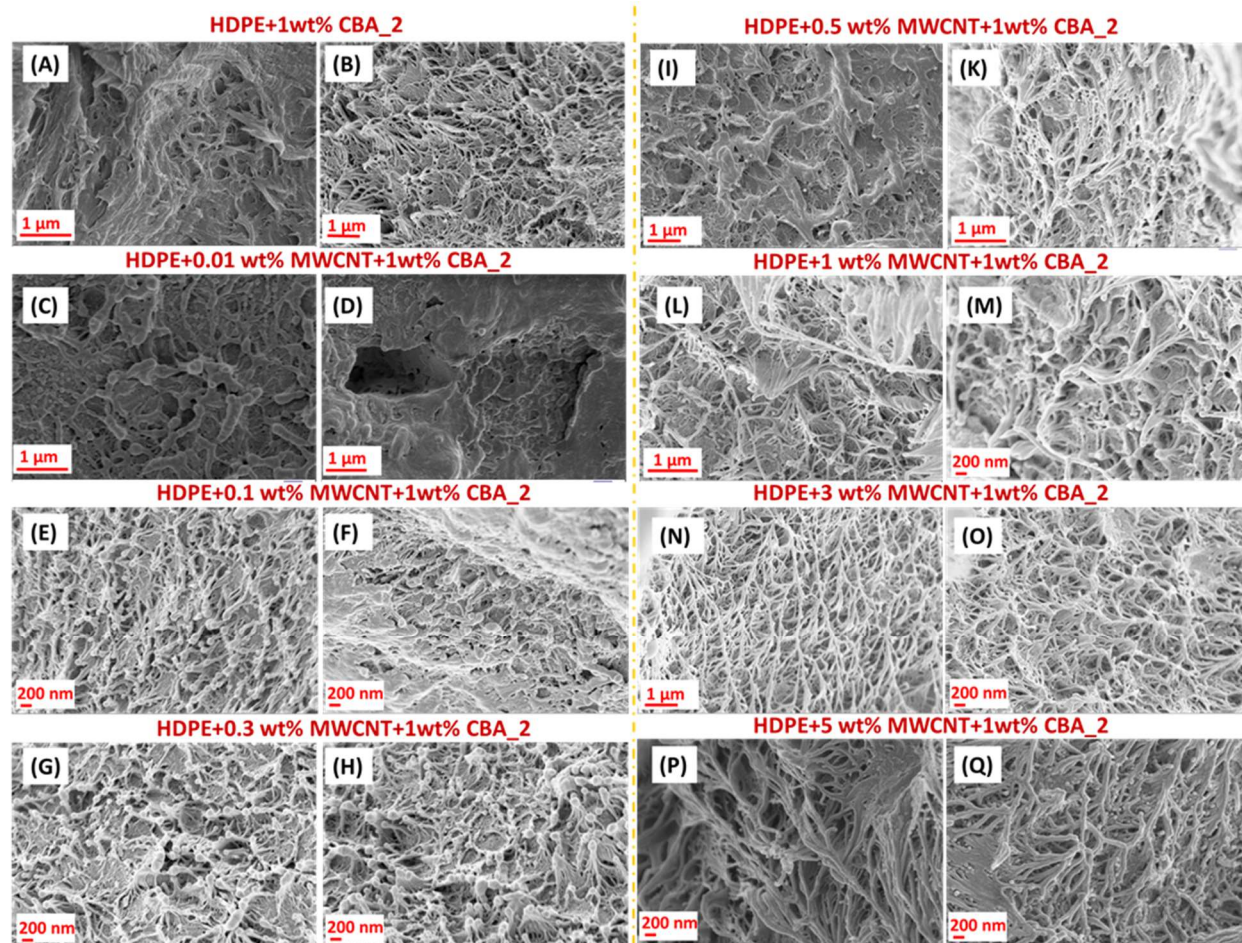
Figure 5.18. Representative high magnification SEM images of foamed moulded microstructure of (A-B) unfilled HDPE and (C-Q) HDPE-MWCNT composites produced using *Profile 1* (extruder) and *Method 4* (injection moulding) with 1 wt% CBA₂. The images refer to the MWCNT loadings of (C-D) 0.01 wt%, (E-F) 0.1 wt%, (G-H) 0.3 wt%, (I-K) 0.5 wt%, (L-M) 1 wt%, (N-O) 3 wt%, (P-Q) 5 wt% at three different magnifications.

Comments

The use of CBA₂ with the conditions employed during foaming did not produce appreciable foam expansion for the formulations shown in Figure 5.18. As the holding injection pressure has a dominant effect on the dynamics of bubble growth [30], the high pressure in the moulding system (i.e. 600 bar was applied for 6 sec before being dropped to a post pressure of 200 bar applied for 10 sec) possibly tended to suppress cell growth. High pressures usually promote both high gas solubility and gas diffusivity in plastics. However, a high gas diffusivity is not beneficial in controlling cell growth as it promotes instead the escape of gas, causing the melt to be depleted with blowing agent, eventually creating a poor foam structure and a low expansion. A low diffusivity would offer the advantage of controlling cell growth allowing for high expansion ratios, since the growth rate is slow and thus, gas escape can be easily prevented [54].

The composites had an overall more uniform morphology than that of the unfilled polymer (figures (A-B)) but the micrographs in the figure barely show any appreciable cell size has formed in the samples and only sub-micron sized cells can be observed. Nonetheless, homogeneous dispersion of the MWCNT in HDPE was obvious at all loadings and no MWCNT agglomerations were observed from the SEM micrographs collected. Therefore, the mixing regime used resulted in uniformly distributed and dispersed MWCNTs and CBA throughout the HDPE matrix.

Figures 5.19 and 5.20 are analogous to figures 5.17 and 5.18, except for the samples contain the higher CBA$_1$ loading, 4 wt% (up from 1 wt%).

As the concentration of the foaming agent determines the final foam cell density [48], foam morphologies evolve from having a high cell density with fine cells at 1 wt% CBA to a reduced cell density with larger cells for a CBA content of 4 wt%. On the other hand, the filler content also contributed to determining cell densities of each composite foam [6].

Evolution of cell structure in foamed HDPE-MWCNT composites with 4 wt% CBA content and different MWCNT loadings.
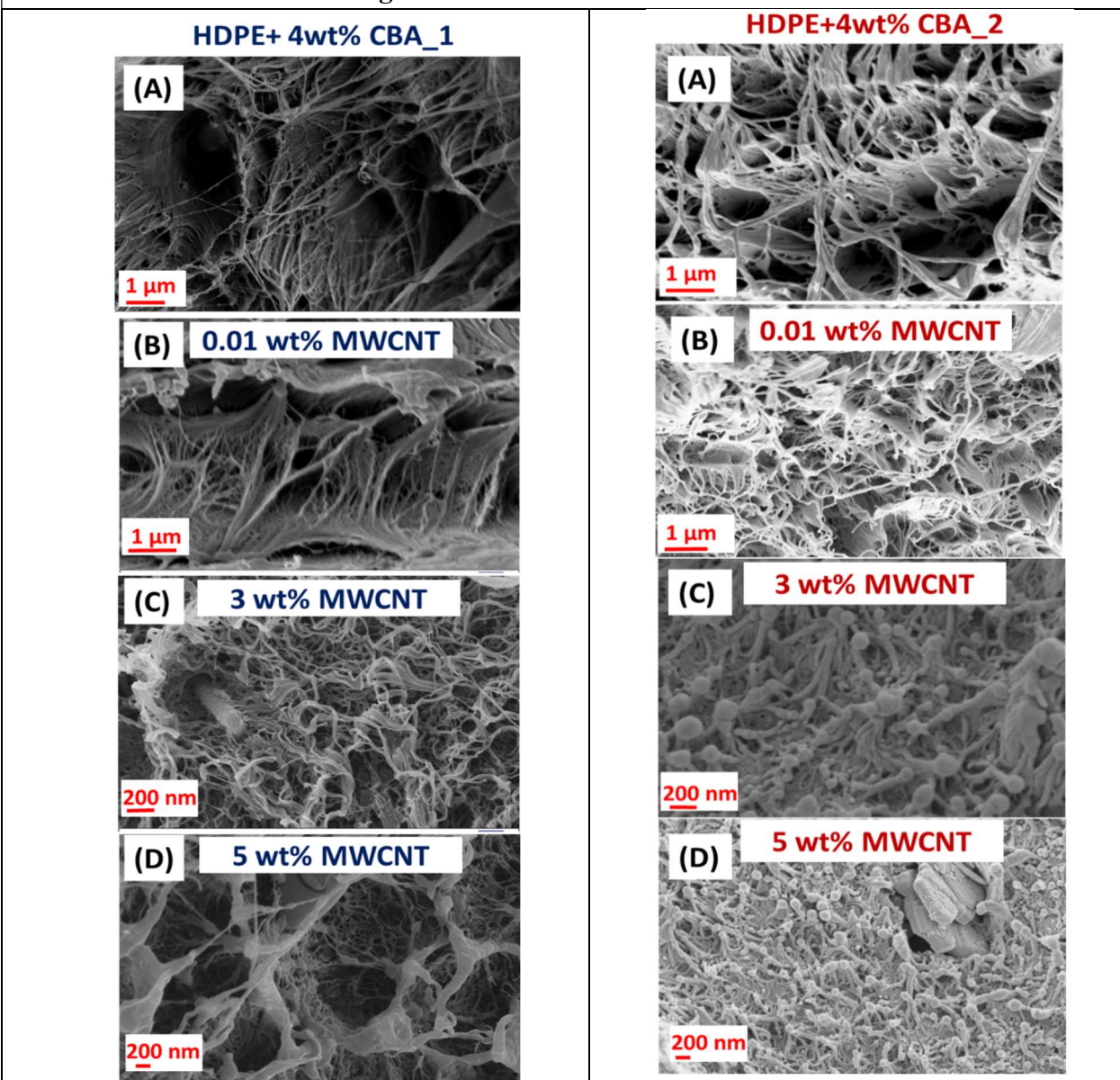
Figure 5.19. Representative high magnification SEM images of the microstructure of foamed moulded (A) unfilled HDPE and (B-D) HDPE-MWCNT composites produced using *Profile 1* (extruder) and *Method 6* (IM) with 4 wt% CBA$_1$. The images refer to the MWCNT loadings of (B) 0.01 wt%, (C) 3 wt% and (D) 5 wt% at two different magnifications.

Figure 5.20. Representative high magnification SEM images of foamed moulded microstructure of (A) unfilled HDPE and (B-D) HDPE-MWCNT composites produced using *Profile 1* (extruder) and *Method 4* (IM) with 4 wt% CBA$_2$. The images refer to the MWCNT loadings of (B) 0.01 wt%, (C) 3 wt% and (D) 5 wt% at two different magnifications.

Comments

The representative SEM images (see Figure 5.19) revealed a non-uniform cell structure at all the filler loadings investigated. Coalescence appears to have occurred during the expansion phase, leading to a reduction of the nucleated cell density. Since it is inevitable that compression, extension and shear flows are associated with shaping operations in a foaming process [32], the presence of flow around solid filler (MWCNT) particles may have promoted agglomeration of adjacent cells, resulting in variable gas pressure between cells of different sizes and therefore rupture of the cell membrane which induced further cell growth [55]. It should be noted that although the combined effects of high pressure during the injection process (i.e. 600 bar) and increasing concentration of the blowing agent resulted in non-uniform morphologies with excessive cell collapse. The largest cell size (~4 μm) found for a MWCNT content of 5 wt% (see Figure 5.19(D)), was significantly reduced from the largest initial void size (~10 μm) found for the unfilled polymer under the same conditions (see Figure 5.19(A)). This suggests cell size was reduced in the presence of MWCNTs.

On the other hand, as shown in Figure 5.20, addition of 4 wt% CBA_2 to the polymer resulted in an even lower void content than that obtained using CBA_1. Probably, the increase in the CBA_2 content to 4% by weight made the escape of gas worse than before with 1% by weight. Additionally, the addition of MWCNTs to the polymer matrix resulted in a more uneven cell distribution with regard both cell sizes and distance between cells than in the unfilled HDPE foam. This could be attributed to the increased melt strength of the cell wall and reduced CO_2 diffusivity as MWCNT loading increased in the composites from 0.01 to 5 wt%. Although in the composites there are heterogeneous interfaces that facilitate bubble nucleation, the void fraction was still low. Even though the cells were able to nucleate, the polymer melt was too viscous and hindered cell growth.

From the analysis of the whole cross sections of the SEM microstructures reported hitherto, irregular morphologies were obtained from a combination of the foaming and processing parameters and material composition. The use of *Method 6* (IM) resulted in no uniformity and/or damage of the cells also in presence of MWCNTs in the composites. The experimental observations for unfilled HDPE foams discussed in section 5.2.1 proved the use of *Methods 8* and *9* [d] achieved the best foam quality in terms of density reduction, void fraction and acoustic properties when using 4 wt% CBA_1. Therefore, the same conditions were also applied for moulding the filled HDPE foams, with the target of achieving cell size and uniformity which can contribute to enhancing acoustic properties, thus improve the sound absorbing properties, of such foam discs.

---

[d] It is worth recalling that *Methods 8* and *9* are the isothermal processes in the IM where both the temperatures in the injection piston and mould were both set at 180℃ and 185℃, respectively, and a rapid quenching of the (hot) mould in a cold water tank followed injection.

Evolution of the cell structure for foamed HDPE-MWCNT composites obtained after addition of a fixed 4 wt% CBA$_1$ content and different MWCNT loadings in a two-stage foaming process based on *Profile 1* (extrusion) and *Method 8* (see Figure 5.21) and *Method 9* (see Figure 5.22) in IM.

HDPE+4wt%CBA$_1$	HDPE+4wt%CBA$_1$ +0.01wt%MWCNT	HDPE+4wt%CBA$_1$ + 0.1wt%MWCNT	HDPE+4wt%CBA$_1$ + 0.3wt%MWCNT	HDPE+4wt%CBA$_1$ + 0.5wt%MWCNT	HDPE+4wt%CBA$_1$ + 1wt%MWCNT	HDPE+4wt%CBA$_1$ + 3wt%MWCNT	HDPE+4wt%CBA$_1$ + 5wt%MWCNT
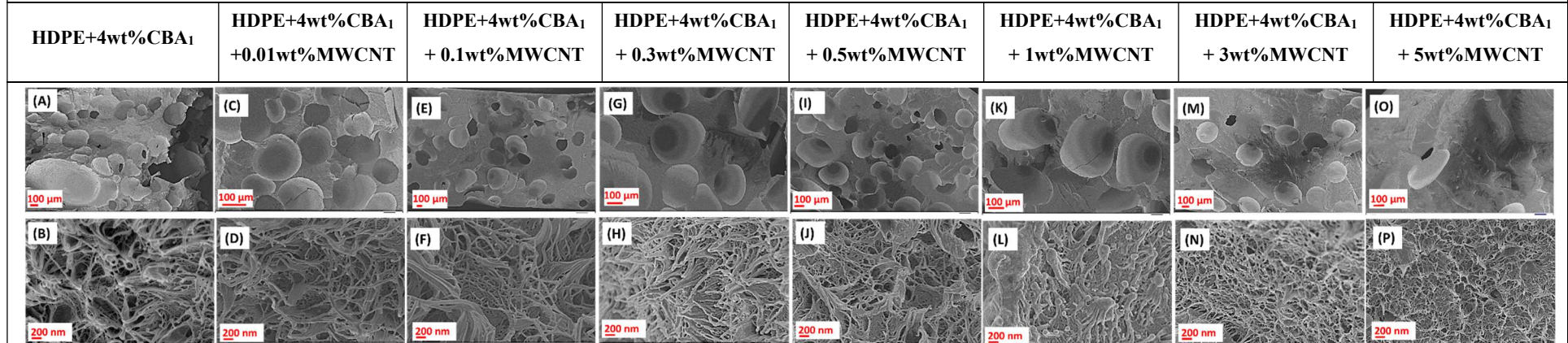
Figure 5.21. Representative high magnification SEM images of foamed moulded microstructure of (A-B) unfilled HDPE and (C-P) HDPE-MWCNT composites produced using *Profile 1* (extruder) and *Method 8* (IM) with 4 wt% CBA$_1$. The images refer to the MWCNT loadings of (C-D) 0.01 wt%, (E-F) 0.1 wt%, (G-H) 0.3 wt%, (I-J) 0.5 wt%, (K-L) 1 wt%, (M-N) 3 wt%, (O-P) 5 wt% at two different magnifications.

HDPE+4wt%CBA$_1$	HDPE+4wt%CBA$_1$ +0.01wt%MWCNT	HDPE+4wt%CBA$_1$ + 0.1wt%MWCNT	HDPE+4wt%CBA$_1$ + 0.3wt%MWCNT	HDPE+4wt%CBA$_1$ + 0.5wt%MWCNT	HDPE+4wt%CBA$_1$ + 1wt%MWCNT	HDPE+4wt%CBA$_1$ + 3wt%MWCNT	HDPE+4wt%CBA$_1$ + 5wt%MWCNT
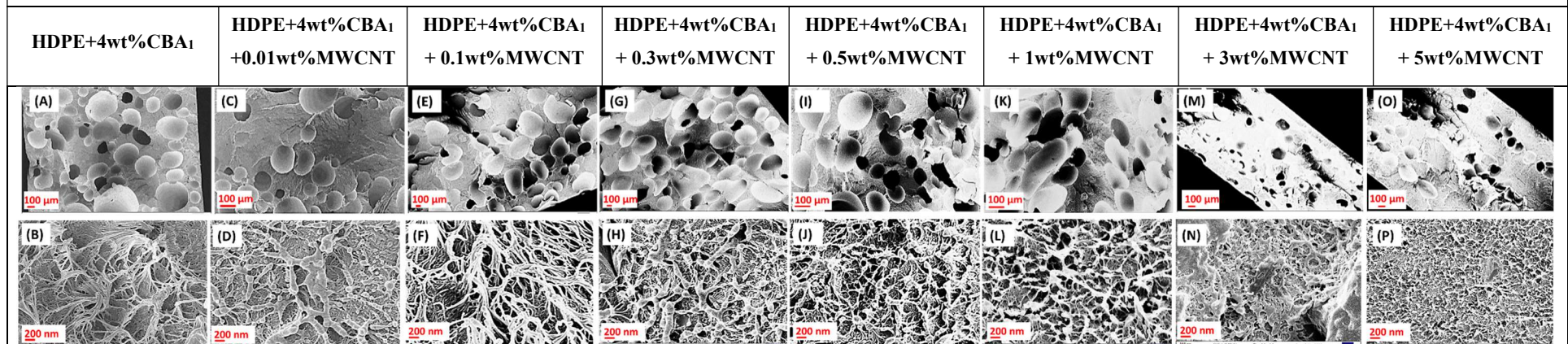
Figure 5.22. Representative high magnification SEM images of foamed moulded microstructure of (A-B) unfilled HDPE and (C-P) HDPE-MWCNT composites produced using *Profile 1* (extruder) and *Method 9* (IM) with 4 wt% CBA$_1$. The images refer to the MWCNT loadings of (C-D) 0.01 wt%, (E-F) 0.1 wt%, (G-H) 0.3 wt%, (I-J) 0.5 wt%, (K-L) 1 wt%, (M-N) 3 wt%, (O-P) 5 wt% at two different magnifications.

Comments

The micrographs shown in the figures 5.21 and 5.22 are from the fractured surfaces of cellular HDPE-MWCNT composite foams produced with 4 wt% CBA_1 and different MWCNT loadings in a two-stage foaming process based on Profile 1 (extrusion) and Method 8 (see Figure 5.21) and Method 9 (see Figure 5.22) in IM.

The morphologies obtained differ from those produced initially, where the higher pressure system tended to suppress cell growth and even caused cell collapse. Other than raising temperature during injection, the holding pressure, which has also a dominant effect on the dynamics of bubble growth [30], was considerably lowered in methods 8 and 9 to 150 bar (from the initial 600 bar of Method 6), which is an effective approach to tuning cell morphology, narrowing cell size distribution. SEM imaging was used to characterize the morphology of the foamed samples and the micrographs of the foams obtained were further analysed to estimate the cell population density and cell size of the foamed composites. In particular, the cell size of foamed samples was determined from the micrographs showing 20 or more bubbles in the micrographs, whereas the cell population density per unit volume of the original un-foamed polymer (N_0) was determined by using the following equation 5.8 [56]:

$$N_0 = \left[\frac{n}{A}\right]^{\frac{3}{2}}$$
(5.8)

where, n is the number of cells in the micrograph, A is the area of the micrograph (cm^2).

Figure 5.21: The representative SEM images related to the use of CBA_1 revealed a non-uniform cell structure at all filler loadings investigated. Coalescence appears to have occurred during expansion, leading to a reduction in cell density. The images shown in the first row (i.e. images A, C, E, G, I, K, M and O) were taken from the outermost surfaces from the cross section of each sample, (100 μm scale bar), where the images in the second row are taken from the innermost structure of each foam, nanometre scale (~200 nm). Increasing the MWCNT loading resulted in composite foams characterised by more isotropic cells of almost regular shape (about spherical) with an average cell diameter of ca.150 μm and a more uniform cell size distribution than the unfilled polymer foam (figure (A)). These changes in foam morphology will be reflected in the corresponding properties, including acoustic.

From Figure 5.21 however it is evident that a filler content between 0.01 and 0.5 wt% led to the development of the highest number of pores within the foam structures. A rough calculation of the cell density for these foams gave approximate values of~$5x10^5$ cells/cm^3 (fig.(C)), $4x10^4$ cells/cm^3 (fig.(E)), $2x10^5$ cells/cm^3 (fig.(G)), $10x10^4$ cells/cm^3 (fig.(I)), $2x10^4$ cells/cm^3 (fig.(K)). Allowing for errors due to the assumption of perfect spherical cell shape and dimensional uniformity, the values of cell density obtained are in the range of 10^4-10^5 cells/cm^3, typical of macrocellular foams [48].

It is known that the foamability of polymers is affected by the sorption of gas in the polymer [52]. The presence of MWCNTs was shown to promote accumulation of gas at the polymer–particle interface. On the other hand, additions of higher MWCNT loadings (3 and 5 wt%) did not achieve a visibly high

porous structure, especially at 5 wt%, most likely because at these loadings the already high melt viscosity of the HDPE matrix was even higher, preventing bubble growth.

Foam morphologies evolved as the mould temperature was increased by an additional 5˚C (i.e. *Method 9*) as shown in Figure 5.22.

Figure 5.22: The cell geometries of HDPE-MWCNT composite foams shown in the figure indicate an increased number of pores and larger volume expansions compared to the foams shown in Figure 5.21, while a predominantly circular pore shape (average cell diameter~160 μm) was retained with the new production conditions applied. The narrower cell size distribution resulted was roughly uniform at MWCNT loadings up to 0.3 wt%, whereas at higher loadings (>0.5 wt%), it became more heterogeneous. The dispersed CNTs act as nucleating sites for cell formation and cell growth occurring on their surfaces. Using equations 5.8, the cell densities for these foams were approximately of ~$2x10^5$ cells/cm^3 (fig.(C)), $8x10^4$ cells/cm^3 (fig.(E)), $9x10^4$ cells/cm^3 (fig.(G)), $2x10^5$ cells/cm^3 (fig.(I)), $1x10^5$ cells/cm^3 (fig.(K)). These values are again within that expected for a typical cell density range for macrocellular foams, although the cell density was reduced for both MWCNT loadings of 0.01 and 0.3 wt% and increased for MWCNT content ≥ 0.5 wt%.

From a modelling study conducted by Park and co- workers [57], the optimal performance of cellular morphologies on sound absorption behaviour is expected from samples with higher porosity, lower cell density, and larger cell size (e.g. samples such as HDPE+0.1wt%MWCNT+4wt%CBA$_1$ and HDPE+0.3wt%MWCNT+4wt%CBA$_1$).

Again, the inclusion of MWCNTs at 3 and 5 wt% prevented the development of very highly porous structures, resulting in a non-uniform cell size distribution with the foams having more cells in certain areas (e.g. areas rich in nucleating agents) rather than others (less cells in nucleating agent deficient areas). Possible reasons for the non-uniform cell morphology with higher MWCNT concentrations could be due to agglomerations that retard the formation of the cells, and/or the increase in viscosity of the polymer melt because of the high particle loadings that makes cell generation difficult [4]. The presence of MWCNTs indeed can significantly increase melt viscosity [58].

Because the number and size of the bubbles are determined by the concentration of the foaming agent, the uniformity of the cell structure and the cell density are limited by the method used to mix the foaming agents and the polymer [48]. Nevertheless, the mixing employed in this study (a 16 mm co-rotating parallel twin-screw extruder) resulted in overall effective mixing and ensured a homogeneous dispersion and distribution of the MWCNTs and CBAs in the polymer matrix. The greatest enhancement in properties can only be realized when the nanoparticles are dispersed uniformly in the polymer matrix [36].

The SEM images reported in figures 5.21 and 5.22, in fact, also show the dispersion of MWCNT in the polymer matrix in the foamed composites.
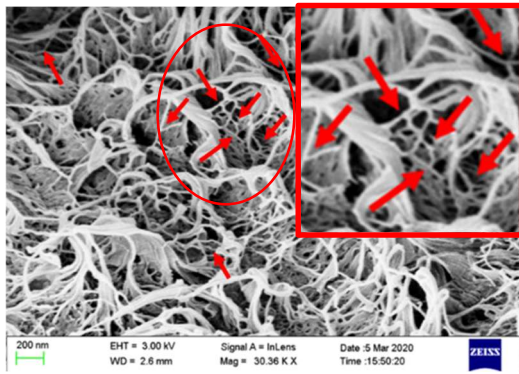
MWCNTs are mostly localised around the bubbles and aligned along the cell walls as indicated by the red arrows in the SEM image at high magnification reported on the left, taken from the innermost structure of the foam sample HDPE+0.1wt%MWCNT+4wt%CBA$_1$, (scale 200 nm).

5.3.2 Density Measurements and Characterisation of foamed HDPE-MWCNT Composites: Calculation of Expansion Ratio, Void fraction and Density Reduction

Although the cell structure is an important factor in determining the final properties of a microcellular foam, density reduction or weight reduction is still the dominant feature that primarily affects properties [51], and critically, the acoustic properties of foams. When evaluating the performance and economics of such composite foams, density becomes a crucial factor [36]. Clearly, the addition of particles to a PE matrix will alter the bulk density of the resulting composite structures [59]. Nonetheless, microcellular foaming processes reduce the bulk density of microcellular composites by enhancing the presence of the gaseous phase in the samples.

Each foamed composite was tested by weighing each sample in air prior to immersion in a liquid (i.e. ethanol) and the average arithmetic values (from 3 replicates) of each specimen are listed as the measured density ρ_{foam} in tables 5.8-5.10. No measurement percentage error (standard deviation) values are reported in the following tables 5.8-5.10 as measurements resulted in errors of up to 0.05% which can be discarded. In addition, the effect of the processing parameters on the relative density of each specimen (i.e. ratio between the bulk density of the foamed composite, ρ_{foam}, and the measured bulk density of the un-foamed composite from Table 4.8 in chapter 4, $\rho_{unfoamed}$) was investigated by defining the void fraction, expansion ratio and density reduction obtained for each disk sample measured.

Density measurements were first performed on HDPE-MWCNT composite samples foamed using IM methods 1, 2 and 6 of samples with 1 wt% and 4 wt% CBA$_1$.

Table 5.8. Values of density, expansion ratio, void fraction and density reduction obtained for foamed HDPE-MWCNT disks sample prepared at certain processing conditions and loadings of CBA$_1$.

CBA$_1$ loading	MWCNT loading /%	Measured Density ρ_{foam} /g cm^{-3}	Expansion Ratio $\frac{\rho_{polymer}}{\rho_{foam}}$	Void Fraction $1-(\frac{\rho_{foam}}{\rho_{polymer}})$ /%	Density Reduction /%
1wt% CBA$_1$	0	0.953	1.012	1.14	1.14
Profile 1	0.01	0.952	1.013	1.24	1.24
Method 1	0.1	0.954	1.010	1.04	1.04
	0.3	0.959	1.006	0.62	0.62
	0.5	0.961	1.005	0.52	0.52
	1	0.966	1.002	0.21	0.21
	3	0.977	1.000	0.00	0.00
	5	0.985	1.001	0.10	0.10
1wt% CBA$_1$	0	0.952	1.013	1.24	1.24
Profile 1	0.01	0.953	1.012	1.14	1.14
Method 2	0.1	0.952	1.013	1.24	1.24
	0.3	0.959	1.006	0.62	0.62
	0.5	0.961	1.005	0.52	0.52
	1	0.966	1.002	0.21	0.21
	3	0.980	0.997	0.00	0.00
	5	0.986	1.000	0.00	0.00
1wt% CBA$_1$	0	0.954	1.010	1.04	1.04
Profile 1	0.01	0.954	1.010	1.04	1.04
Method 6	0.1	0.953	1.012	1.14	1.14
	0.3	0.960	1.005	0.52	0.52
	0.5	0.959	1.007	0.72	0.72
	1	0.967	1.001	0.10	0.10
	3	0.978	0.999	0.00	0.00
	5	0.991	0.995	0.00	0.00
4wt% CBA$_1$	0	0.960	1.004	0.41	0.41
Profile 1	0.01	0.961	1.003	0.31	0.31
Method 1	0.1	0.959	1.005	0.52	0.52
	0.3	0.960	1.005	0.52	0.52
	0.5	0.962	1.004	0.41	0.41
	1	0.967	1.001	0.10	0.10
	3	0.983	0.994	0.00	0.00
	5	0.994	0.992	0.00	0.00
4wt% CBA$_1$	0	0.962	1.002	0.21	0.21
Profile 1	0.01	0.962	1.002	0.21	0.21
Method 2	0.1	0.956	1.008	0.83	0.83
	0.3	0.962	1.003	0.31	0.31
	0.5	0.964	1.002	0.21	0.21
	1	0.969	0.999	0.00	0.00
	3	0.973	1.004	0.41	0.41
	5	0.990	0.996	0.00	0.00
4wt% CBA$_1$	0	0.959	1.005	0.52	0.52
Profile 1	0.01	0.960	1.004	0.41	0.41
Method 6	0.1	0.961	1.003	0.31	0.31
	0.3	0.962	1.003	0.31	0.31
	0.5	0.965	1.001	0.10	0.10
	1	0.968	1.000	0.00	0.00
	3	0.984	0.993	0.00	0.00
	5	0.993	0.993	0.00	0.00

Analysis of the data reported in Table 5.8, showed that by varying the injection process in the range 165-170 ℃ (temperature in the cylinder), 60-75 ℃ (temperature in the mould), 450-600 bar (injection pressure), 6-10 sec (holding pressure time) and 200-250 bar (post-holding pressure of injection) were found to be ineffective for producing foams with uniform cell size and distribution. On average, an expansion ratio of 1 (i.e. a high-density foam) and a very low void fraction (< 1.3 %) was achieved in such samples, regardless of the CBA_1 content and MWCNT loading. This clearly is a consequence of a negligible gaseous phase developed within these structures as previously anticipated by the study conducted on the unfilled polymer (section 5.2, PART II-A), see also SEM micrographs in figures 5.17 and 5.19. The use of 4wt% CBA_1 resulted in a reduction in the density of the samples (< 1%). Among all the MWCNT loadings investigated, 0.01 and 0.1 wt% proved to have the most beneficial effect on the volume expansion ratio of the composites.

Density measurements were also performed on HDPE-MWCNT composite foams formed with CBA_2, see Table 5.9.

Table 5.9. Values of density, expansion ratio, void fraction and density reduction obtained for HDPE-MWCNT foams prepared using different processing conditions and CBA_2 content.

CBA_1 loading	*MWCNT loading* /%	Measured Density ρ_{foam} /g cm^{-3}	Expansion Ratio $\dfrac{\rho_{polymer}}{\rho_{foam}}$	Void Fraction $1-(\dfrac{\rho_{foam}}{\rho_{polymer}})$ /%	Density Reduction /%
1wt% CBA₂	0	0.960	1.004	0.41	0.41
Profile 1	0.01	0.963	1.001	0.10	0.10
Method 4	0.1	0.950	1.015	1.45	1.45
	0.3	0.955	1.010	1.04	1.04
	0.5	0.959	1.007	0.72	0.72
	1	0.967	1.001	0.10	0.10
	3	0.974	1.003	0.31	0.31
	5	0.978	1.008	0.81	0.81
4wt% CBA₂	0	0.963	1.001	0.10	0.10
Profile 1	0.01	0.965	0.999	0.00	0.00
Method 4	0.1	0.960	1.004	0.41	0.41
	0.3	0.971	0.994	0.00	0.00
	0.5	0.964	1.002	0.21	0.21
	1	0.970	0.998	0.00	0.00
	3	0.976	1.001	0.10	0.10
	5	0.982	1.004	0.41	0.41

As is evident from values listed in Table 5.9, the use of CBA_2 also produced high density composite foams (expansion ratio of ~1) with low void fractions (< 1.5 %). The addition of MWCNTs resulted in a very small increase in the density of the composites relative to the unfilled polymer. In general, the density of polymer composites increases with increasing filler content because of the higher density of the latter compared to the polymer [60]. However, in microcellular foams the trend should be different. Microcellular foaming processes lead to reduced bulk density of microcellular

composites by enhancing the presence of the gaseous phase in the samples [59]. A slight decrease in the density of microcellular composites is generally claimed with increasing nanofiller content in the matrix as the presence of nanofillers promotes the accumulation of gas at the polymer–particle interface [52, 61].

These results for MWCNT filled HDPE foams are similar to that found for the unfilled HDPE foams (section 5.2, PART II-A). The very low generation of void fraction obtained previously for the foamed HDPE samples is undoubtedly related to the relatively high crystalline HDPE (above 70%). Decreasing the amount of crystallinity would be effective for increasing the void fraction in the samples, overcoming the problem of the high melt viscosity and HDPE stiffness which would result in a decrease in crystallinity [10]. Moreover, the gas solubility would also benefit as in semi-crystalline polymers solubility increases with decreasing degree of crystallinity. When an adequate energy is provided to the system (e.g. through a temperature rise) sufficient crystallinity in the polymer can be disrupted in order to allow the gas to overcome the attractive forces and entanglements and diffuse through the melt [10]. Accordingly, the isothermal *Methods 8* and *9* enabled a significant reduction in melt viscosity when using a CBA_1 (4 wt%), which realised an appreciable void fraction for unfilled HDPE foams. Density measurements performed on HDPE-MWCNT composites foamed via methods 8 and 9 confirmed that an equal if not greater void fraction forms for the MWCNT filled HDPE foams (see Table 5.10).

Table 5.10. Values of density, expansion ratio, void fraction and density reduction obtained for HDPE-MWCNT foams prepared at 4wt% CBA_1 content prepared using IM methods 8 and 9.

CBA$_1$ loading	*MWCNT loading* /%	Measured Density ρ_{foam} /g cm^{-3}	Expansion Ratio $\dfrac{\rho_{polymer}}{\rho_{foam}}$	Void Fraction $1-(\dfrac{\rho_{foam}}{\rho_{polymer}})$ /%	Density Reduction /%
4wt% CBA$_1$	0	0.72	1.339	25.31	25.31
Profile 1	0.01	0.70	1.377	27.39	27.39
Method 8	**0.1**	**0.65**	**1.483**	**32.57**	**32.57**
	0.3	0.72	1.340	25.39	25.39
	0.5	0.76	1.271	21.33	21.33
	1	0.71	1.363	26.65	26.65
	3	0.85	1.149	13.00	13.00
	5	0.93	1.060	5.68	5.68
4wt% CBA$_1$	0	0.62	1.555	35.68	35.68
Profile 1	0.01	0.69	1.397	28.42	28.42
Method 9	**0.1**	**0.62**	**1.555**	**35.68**	**35.68**
	0.3	0.72	1.340	25.39	25.39
	0.5	0.70	1.380	27.54	27.54
	1	0.67	1.445	30.79	30.79
	3	0.80	1.221	18.12	18.12
	5	0.92	1.072	6.69	6.69

As can be seen from Table 5.10, higher values of foam expansion ratio and void fraction were obtained for the moulding conditions employed in methods 8 and 9, with increasing MWCNT

loading, confirming that the temperature and pressure applied during moulding had pronounced effects on the volume expansion ratios of HDPE-MWCNT foams.

The role of MWCNTs in polymer foaming is not merely limited to the nucleation of cells, they also promote foam morphologies and play a major role in determining the foamability of polymers [52]. The higher foam expansion ratio in the composites resulted from some uptake in gas absorption and hence provided more heterogeneous nucleating sites for higher filler loading. In equal measure, the MWCNT content and extent of MWCNT dispersion resulted in an increase in volume expansion ratio. In particular, the use of 0.1 wt% MWCNTs proved to provide the highest expansion ratio in this study to this point with values of ca. 32.6% and 35.7% obtained via methods 8 and 9, respectively. Furthermore, small increases in foam density of the HDPE-MWCNT composites followed MWCNT loadings when larger than 1 wt%.

5.3.3 Acoustic Properties of foamed HDPE-MWCNT Composite

The acoustic properties of all the HDPE-MWCNT composite foams produced were evaluated via transmission of acoustic energy in air (or water) and across the sample, i.e. disks produced via IM. Measurements were performed by comparing ultrasonic transmissions through each sample to the transmission in air (or water) without a sample present. A minimum of two specimens for each foam type were tested and results are summarised in tables 5.11, 5.12, and 5.13.

In particular, Table 5.11 summarises the ultrasonic velocities (longitudinal) and attenuation coefficients of ultrasound (which determine the acoustic characteristics of a material), acquired by frequency-domain analysis through ultrasonic air-coupled measurements in transmission in the composite foam samples. The acoustic properties derived by the characterisation of the materials by ultrasonic waves through transmission in water immersion are summarised in tables 5.12 and 5.13, where the velocity of sound in the foamed composite samples was estimated via the time of flight (ToF) technique (see section 5.2.3 PART II-A). The experimental values of the acoustic impedance obtained by multiplying the densities of the foams with the velocities of ultrasound in the samples are reported in both tables. No measurement percentage error (standard deviation) values are reported in the following tables 5.11-5.13 as using only two measurements resulted in errors of up to 0.05% which can be discarded.

The attenuation coefficients reported in the last column of Table 5.11 were determined from the change in the amplitude of the acoustic signal.

Table 5.11. Acoustic properties obtained in air transmission for foamed HDPE-MWCNT composites prepared at certain processing conditions and loadings of CBA_1.

CBA_1 loading	*MWCNT loading* /%	**Velocity of sound** c /m s^{-1}	**Measured Density** ρ_{foam} /g cm^{-3}	**Acoustic Impedence** $Z = c \cdot \rho_{foam}$ /MRayl	**Attenuation @Resonance Frequency** /Np m^{-1}
1wt% CBA_1	0	2391.46	0.953	2.28	11.18
Profile 1	0.01	2400.18	0.952	2.28	13.51
Method 1	0.1	2402.56	0.954	2.29	11.54
	0.3	2418.15	0.959	2.32	10.47
	0.5	2522.60	0.961	2.42	9.58
	1	2434.56	0.966	2.35	10.30
	3	2520.33	0.977	2.46	11.91
	5	2527.17	0.985	2.49	13.86
1wt% CBA_1	0	2389.93	0.952	2.28	10.71
Profile 1	0.01	2451.07	0.953	2.34	10.75
Method 2	0.1	2406.21	0.952	2.29	10.33
	0.3	2412.94	0.959	2.31	10.91
	0.5	2370.69	0.961	2.28	9.50
	1	2402.92	0.966	2.32	12.19
	3	2515.81	0.980	2.47	11.62
	5	2508.92	0.986	2.47	15.65
1wt% CBA_1	0	2395.00	0.954	2.28	11.30
Profile 1	0.01	2441.73	0.954	2.33	15.15
Method 6	0.1	2393.48	0.953	2.28	10.56
	0.3	2436.81	0.960	2.34	9.81
	0.5	2430.95	0.959	2.33	12.31
	1	2437.68	0.967	2.36	14.03
	3	2506.38	0.978	2.45	13.70
	5	2508.92	0.991	2.49	13.81
4wt% CBA_1	0	2404.26	0.960	2.31	11.30
Profile 1	0.01	2417.13	0.961	2.32	13.20
Method 1	0.1	2409.88	0.959	2.31	11.18
	0.3	2453.38	0.960	2.36	10.43
	0.5	2430.95	0.962	2.34	10.98
	1	2377.30	0.967	2.30	14.11
	3	2473.97	0.983	2.43	14.10
	5	2472.82	0.994	2.46	14.26
4wt% CBA_1	0	2403.17	0.962	2.31	11.10
Profile 1	0.01	2416.94	0.962	2.33	12.38
Method 2	0.1	2415.08	0.956	2.31	10.61
	0.3	2449.98	0.962	2.36	10.26
	0.5	2430.75	0.964	2.34	9.45
	1	2509.69	0.969	2.43	12.51
	3	2497.42	0.973	2.43	13.41
	5	2471.42	0.990	2.45	16.93
4wt% CBA_1	0	2380.11	0.959	2.28	13.15
Profile 1	0.01	2374.80	0.960	2.28	11.97
Method 6	0.1	2432.69	0.961	2.34	14.41
	0.3	2441.43	0.962	2.35	12.44
	0.5	2517.86	0.965	2.43	9.48
	1	2515.16	0.968	2.43	12.51
	3	2500.89	0.984	2.46	11.51
	5	2512.75	0.993	2.50	15.96

From the analysis of the acoustic properties, all the samples listed in Table 5.11 had an acoustic impedance ranging from 2.3 to 2.5 MRayl. The different methods of injection as well as CBA$_1$ content used did not significantly lower the acoustic impedance, confirming that a negligible porosity was achieved in such moulded parts in agreement with that expected, considering the foam morphologies observed by SEM imaging and subsequent density measurements, see sections 5.3.1 and 5.3.2, respectively. Porous materials are characterized by low speeds of sound, whereas sound velocities listed in Table 5.11 showed values greater or equal to ca. 2,400 m/s, confirming the non-porous structure.

The attenuation coefficients reported in the last column of Table 5.11 refer to the loss of acoustic energy as the wave travels through the material [42]. Generally, a sound wave is reflected at the solid-gas interface and dissipated in the cellular structure on the propagation route [62]. Despite the negligible reductions in density displayed in Table 5.11 for the composite samples reported, addition of 1 and 4 wt% CBA$_1$ did result in very low attenuation coefficients ($\leq$ 15 Np/m). Nonetheless, a polymer with low attenuation and an impedance mismatch can still result in multiple reflections within the sensor and consequent reduction of signal-to-noise [63].

Further analysis were conducted in water transmission to evaluate the acoustic properties of other composite samples foamed with CBA$_2$ instead of CBA$_1$, see Table 5.12. The ultrasonic velocity (i.e. velocity of propagation of elastic waves), this time was calculated from the measured ToF.

Table 5.12. Acoustic properties obtained in air transmission for foamed HDPE-MWCNT composites prepared at certain processing conditions and loadings of CBA$_1$.

CBA$_2$ loading	MWCNT loading /%	ToF /ns	Velocity of sound c /m s^{-1}	Measured Density ρ_{foam} /g cm^{-3}	Acoustic Impedence $Z = c \cdot \rho_{foam}$ /MRayl
1wt% CBA$_2$	0	405	2299.18	0.960	2.21
Profile 1	0.01	435	2403.44	0.963	2.31
Method 4	0.1	445	2409.85	0.950	2.29
	0.3	560	2925.44	0.955	2.79
	0.5	455	2467.43	0.959	2.37
	1	445	2461.75	0.967	2.38
	3	430	2395.19	0.974	2.33
	5	465	2529.40	0.978	2.47
4wt% CBA$_2$	0	420	2359.42	0.963	2.27
Profile 1	0.01	432	2392.59	0.965	2.31
Method 4	0.1	460	2497.83	0.960	2.40
	0.3	470	2525.86	0.971	2.45
	0.5	485	2587.12	0.964	2.49
	1	435	2413.48	0.970	2.34
	3	475	2583.26	0.976	2.52
	5	465	2541.45	0.982	2.50

As anticipated in previous sections (5.3.1 and 5.3.2), the insufficient void fraction developed in the composite samples prepared using CBA_2 and high injection pressure (see *Method 4*) resulted again in poor acoustic properties (Table 5.11). Samples exhibited high values of both acoustic impedance and sound velocity in the order of 2.4 MRayl and 2,400 m/s, respectively.

Finally, the acoustic properties of the most promising composite samples in this study are shown in Table 5.13.

Table 5.13. Acoustic properties obtained in water transmission for foamed HDPE-MWCNT composites prepared with 4wt% CBA_1 using IM methods 8 and 9.

CBA₂ loading	*MWCNT loading* /%	ToF /ns	Velocity of sound c /m s⁻¹	Measured Density ρ_{foam} /g cm⁻³	Acoustic Impedence $Z = c \cdot \rho_{foam}$ /MRayl
4wt% CBA₁	0	340	2084.30	0.72	1.50
Profile 1	0.01	120	1589.90	0.70	1.11
Method 8	0.1	300	1842.99	0.65	1.20
	0.3	300	1833.51	0.72	1.32
	0.5	320	1973.17	0.76	1.50
	1	300	1860.91	0.71	1.32
	3	357	1985.44	0.85	1.69
	5	516	2375.19	0.93	2.21
4wt% CBA₁	0	180	1692.75	0.62	1.05
Profile 1	0.01	230	1773.14	0.69	1.22
Method 9	0.1	330	1931.32	0.62	1.20
	0.3	210	1723.78	0.72	1.24
	0.5	260	1866.34	0.70	1.31
	1	340	1947.46	0.67	1.30
	3	361	1993.28	0.80	1.59
	5	434	2156.92	0.92	1.98

As the introduction of porosity can greatly expand the range of acoustic properties of polymer materials [44], the low values of c displayed in Table 5.13 can be associated with the presence of a large proportion of gas developed inside the disk samples during manufacture.

It should be pointed out that the ToF numbers reported in Table 5.13 are the absolute values of the negative ToF values obtained for all the samples tested and listed (i.e. the signal with the sample located in between the transducers at normal incidence arrived before the reference signal through pure water, meaning that the ultrasound velocity obtained for this sample is larger than in water (1450 m/s)).

A low sound velocity is preferred in matching layers since it has a direct influence on the acoustic impedance of the material [64]. The satisfactory degree of porosity developed in these last samples (with 4wt% CBA_1) indeed manifested in a low speed of sound as well as a low value of bulk density, when combined gives a low value of acoustic impedance. Materials comprises bubble through the introduction of gas having low density and low velocity are needed for use as a matching layer.

Since the speed of sound in polymeric materials varies with the properties of density and elastic modulus (c =(elastic modulus/ density)$^{1/2}$), which are also affected by crystallinity, it follows that crystallinity of polymers affects c [65]. Therefore, the reduced speed of sound manifested by these latter composite samples in Table 5.13 may be derived from the lowered crystallinity from the use of methods 8 and 9 in the IM machine. Under these IM conditions, the acoustic impedance was lowered to the order of 1 MRayl, enabling these foamed samples to be comparable with the benchmarking samples of syntactic foams, which has an impedance ranging from 1.75 to 2.22 MRayl with a value of c of 2486.65 m/s.

The presence of MWCNTs have influenced the acoustic properties of the foams by improving sound absorbing properties and lowering the speed of sound in most of the composite samples moulded via a *Method 8* when compared to the neat polymer foam. The acoustic impedance (the most important parameter for the application of this work)) varied accordingly with the density, the reason why overall, lower values of Z were obtained for samples moulded via a *Method 9*.

From this preliminary study, novel acoustic nanostructured materials have been developed that possess better acoustic impedance matching and acoustic absorbing properties than the syntactic foams currently available. The combination of the resulting void fraction and acoustic characteristics for these moulded plastic samples appears to offer a possible replacement for the syntactic foams already in use. Characterization of the acoustic properties of these materials revealed a low value of acoustic impedance of 1.05 MRayl. A quarter-wavelength matching layer made of a material having an appropriate acoustic impedance and attenuation coefficient as low as possible can significantly improve the sensitivity and thus the performance of these sensors.

However, the acoustic energy transmission through the matching layer in air-coupled ultrasonic sensors is at its maximum if the matching layer has an acoustic impedance which is the geometric mean of the acoustic impedances of piezoelectric materials and air ($Z_{ML}=(Z_{AIR} \cdot Z_{PIEZO})^{0.5} \sim 0.1$ MRayl). Clearly this means that the acoustic impedance still needs to be lowered by a further order of magnitude to ensure a significant improvement in sensor performance.

Although the design of acoustic matching layers with optimum properties for ultrasonic transducers has been studied extensively, such materials can be difficult to obtain and achieving high sensitivity with broad bandwidth remains a challenge. The availability of consistent conventional materials for acoustic impedance matching with very low acoustic impedance, very low attenuation, and the desired thickness for the designed geometry (i.e. 2.5 mm in the specific application of *Elster New Generation Ultrasonic Transducers*) and frequency (i.e. nominal frequency of 200 KHz) is limited. Furthermore, as the fabrication accuracy is undoubtedly very important, the requirements of very thin layers at high frequencies equivalent to quarter wavelength increases the manufacturing cost

considerably or makes the design process difficult. While at low frequencies the accuracy is manageable because the wavelength is large, at high frequencies, the quarter-wavelength requirement of the matching layer becomes almost impractical to achieve. The cost-effective production of these composite HDPE foams using a two-step processing route with 4 wt% CBA_1 to foam is another point in their favour for air-coupled ultrasonic applications as acoustic matching layers. In addition to the low cost, there are other benefits of using IM, such as the production at high output rates of highly repeatable parts and the fact that it is primarily an automated process that requires little post-mould finishing/polishing of final parts, whose size can be adapted by designing suitable moulds.

The choice of available polymers for ultrasonic uses is limited by the requirement of reasonable mechanical properties (e.g. strength and toughness) in addition to impedance match and low attenuation. The mechanical response of a foam is dictated by its structure [1]. One of the common problems in polymer foams is the loss of toughness and ductility of the material due to the generation of the cells [66]. Ductile polymers such as HDPE generally have high absorption coefficients, in the range 20–40 dB/cm as the same molecular structures and mobility, which contribute to ductility, also contribute to absorption of ultrasonic energy [63]. An attempt was made to measure the mechanical properties (in compression) of foamed HDPE and the HDPE-MWCNT composites, when applying a maximum force of 9000 N (<10,000 N which is the max value allowed by the instrument used). The limited measurement performance under static mechanical compression loading did not allow for significant variations in the compression mechanical properties of the foamed samples tested. None of the samples tested reached a yield point or the breaking point in which the pore structure was destroyed. Possibly, the conditions applied during testing did not enable the compression process to be completed and the test stopped before this stage was reached. Overall, a modest improvement in the stiffness and compressive strength of HDPE was obtained on addition of MWCNTs regardless of whether the structure was porous or not, overall showing that values of Young`s Modulus in compression and compression strength remained in the order of ~30 MPa and ~18 MPa, respectively. The details of the results of the calculation of compression modulus, yield stress (compression strength) and compression at yield (strain at compression strength) derived from stress-strain curves are provided in Submission Portfolio No.6 (section 3.4).

5.4 Concluding Remarks

A systematic and comprehensive study was carried out to investigate the effect of processing conditions and CBA content on the morphology of unfilled and MWCNT filled HDPE foams. It is known that solid-state microcellular foaming of pure HDPE is very difficult to achieve due to its high crystallinity [59]. Controlling the cellular structure and thus, the resulting properties of the parts

is challenging, especially when foaming a semi-crystalline polymer, such as HDPE which also has a very high melt viscosity and rapid crystallisation kinetics. Endothermic CBAs should produce fine cell sizes and yield a smaller reduction in density [15]. The high degree of HDPE crystallinity (> 70%) interferes with the process of foaming, as it decreases the solubility and diffusivity of the CO_2 gas released by the CBA, while CO_2 can dissolve only in the amorphous phase of the polymer [10, 31, 38, 67, 68]. For this reason, an initial CBA content below 4 wt% was not effective for producing foams.

In order to reduce weight and promote cell morphology by providing small cells in diameter and high cell density, favourable processing conditions for foaming (e.g. gas dosage, injection velocity, melt temperature and mould temperature, and pressure) were determined from systematic experiments during extrusion and conventional IM. The CBA concentration was varied in order to address gas dosage. As in semi-crystalline polymers the foaming temperature is used to control the rate of cell growth and cell size [32], five different temperature profiles were set to investigate the foaming process. By injecting the molten material into the disk mould, further cell nucleation occurred activated by a rapid depressurization in the inter-lamellar amorphous regions of the HDPE matrix in which CO_2 was dissolved. Setting of the IM parameters correctly and dosing with CBA had a critical effect in improving the properties of the foams. Depending on the polymer viscosity and melt strength, cell morphology changed. However, the issue of the gas escape in a system such as the micro-IM used in this work was inevitable. In terms of costs of the final parts, the use of a mini-lab IM machine can be considered a cost-efficient form of manufacturing desired MLs for initial low volume manufacturing. For small parts, the cost of the material has a small effect on the unit price and the production rate has a large effect, whereas on large parts the cost of the material has a major effect on the unit price along with the production rate. The low initial investments involved with a small IM machine, as well as the possibility of fast design changes and the short product life cycles are the main economical benefits behind this machining approach. The costs involved for manufacturing injection molded parts can be broken down into two categories: a one-time cost for IM tooling and the cost for producing the parts. The main factors that decide for the ultimate cost of the moulded disks are the size and intricacy of the parts, besides the material used and the number of parts being produced. Clearly, in addition to the expected quantities of manufacture, a determining element is the cost of the mould tool, which is due to the combination of factors such as the part size, complexity, and material. The use of a small and less complex mold tool such the mould type (disk shape) used herein with a single cavity would allow to fabricate cheap disk samples (few £ per unit), whose price will be further lowered as the production increases to create more and more units with the same mold and the initial start-up costs are recovered. Increased production rates of the parts can reduce the overall costs.

Overall, utilization of a 4wt% CBA_1 content, extrusion *Profile 1* (i.e. constant temperature of 165˚ C in the extruder) and IM *Method 9* (i.e. isothermal injection at 185˚C, holding pressure of 150 bar ˣ 1 sec, post-holding pressure of 0 bar ˣ 7 sec, total pressure drop of 150 bar) were found to be the most favorable conditions for yielding the highest degree of porosity when producing both unfilled and filled HDPE foams via this two-steps process.

From SEM imaging of foam morphology, none of the foams produced showed a regular structure with uniform distribution of the pores size, in agreement with other studies found in literature focused on foaming polyolefin-filler mixtures. This may have resulted from the heterogeneous nature of the semi-crystalline polymer [67] as well as from the fact that the gas did not distribute uniformly in the polymer since it does not dissolve in the crystallites. As a decrease in polymer crystallinity would make foaming production easier [31], an isothermal processes, i.e. methods *8* and *9* adopted during IM altered the cooling rate of the polymer which in turn affecting the resulting crystallinity (crystallinity decreases at faster cooling rates).

The use of MWCNTs as nucleation agents during the foaming process increased the cell nucleation rate while narrowing the cell size distribution, hence benefiting from the effectiveness of the particles on hetero-nucleation. Furthermore, the addition of MWCNTs was shown to reinforce the micro-scaled cell walls, thus achieving macroscopic enhancement of sound absorbing properties in the foam by increasing tortuosity (at MWCNT loadings ≤ 1wt%) confirming the homogenous dispersion of the nanoparticles in the polymer matrix when melt mixed with a CBA_1 content of 4 wt%.

The highest degree of porosity obtained using 4wt% CBA_1 for the unfilled polymer resulted in a void content of ~36%, a density reduction of ~36%, and an expansion ratio of ~1.6. This translated in to a lowering of the speed of sound and thus acoustic impedance from the initial values of 2339.2 m/s and 2.22 MRayl for the un-foamed counterpart reported in chapter 4 to 1692.75 m/s an of 1.05 MRayl, respectively.

A MWCNT content of 0.1 wt% and a CBA_1 loading of 4wt% s was found to be the optimum loadings for achieving microcellular HDPE-MWCNT composite foams. The sample HDPE+0.1wt%MWCNT$_s$+4wt%CBA_1 had the highest void fraction (~36%) and expansion ratio (~1.6%) achieved in this study when moulded using IM *Method 9*, and a void fraction of 33% and expansion ratio of ~1.6% when using IM *Method 8*. The moderate degree of porosity developed in these last samples translated to a low speed of sound as well as a low value of bulk density, that combined to give a low value of acoustic impedance. The presence of MWCNTs seems to have altered the acoustic properties of the foams by improving sound absorbing properties and lowering the speed of sound in most of the composite samples moulded via *Method 8* when compared to the

neat polymer foam. However, lower values of Z were obtained for samples moulded via *Method 9*, since the acoustic impedance varied accordingly with the density, whose reduction may be derived from the lowered crystallinity when using such method in the IM machine. Under such IM conditions, the acoustic impedance was reduced to 1 MRayl, enabling these foamed samples to be comparable with the benchmarking sample, syntactic foams (ρ_{foam}=0.71 g cm^{-3}, void fraction =26.35%, expansion ratio= 1.37%, c =2486.65 m/s and Z values ranging between 1.75 and 2.22 MRayl).

In conclusion, the composite foams produced in this work, not only had comparable properties to that of the benchmarking syntactic foams already in commercial use for the application of interest, but they also could substitute them to achieve higher frequencies in the sensors.

Nevertheless, Z still needs to be lowered by a further order of magnitude to ensure a significant improvement in the *Elster New Generation Ultrasonic Transducers* performance in measuring gas flow rate in large gas pipelines.

References

[1] K.L. Sivertsen, Polymer Foams, conference paper, 3.063 Polymer Physics, Spring 2007, pp. 1-17.

[2] Á. Kmetty, K. Litauszki, D. Réti, Characterization of Different Chemical Blowing Agents and Their Applicability to Produce Poly(Lactic Acid) Foams by Extrusion, Applied Sciences, 8, 2018, pp. 1960-1977.

[3] P.S. Liu, G.F. Chen, Producing Polymer Foams, in: Porous Materials Processing and Applications, Elsevier, Chapter 7, 2014, pp. 345-381.

[4] M. Altan, Thermoplastic Foams: Processing, Manufacturing, and Characterization, in: Recent Research in Polymerization, Intech Open, Chapter 6, 2018, pp. 117-137.

[5] T. Garbacz, L. Dulebova, Porophors used in the extrusion process, Chemistry & Chemical Technology, 7(1), 2013, pp. 113-118.

[6] M. Kozlowski, Lightweight Plastic Materials, in: Thermoplastic Elastomers, InTech, Chapter 14, 2012, pp. 291-318.

[7] S-T. Lee, C.B. Park, Foam Extrusion, Taylor & Francis, CRC Press: Boca Raton, second edition, 2014, pp. 1-587.

[8] A.K. Bledzki, O. Faruk, Effects of the chemical foaming agents, injection parameters, and melt-flow index on the microstructure and mechanical properties of microcellular injection-molded wood-fiber/polypropylene composites, Journal of Applied Polymer Science, 97(3), 2005, pp. 1090-1096.

[9] Y. Sato, K. Fujiwara, T. Takikawa, Sumarno, S. Takishima, H. Masuoka, Solubilities and diffusion coefficients of carbon dioxide and nitrogen in polypropylene, high-density polyethylene, and polystyrene under high pressures and temperatures, Fluid Phase Equilibria, 162(1), 1999, pp. 261-276.

[10] P. Rachtanapun, S.M. Selke, Strategy to Produce High-Void Fraction in Microcellular Foamed Polyolefins, CMU Journal, 5(1), 2006, pp. 15-31.

[11] A.H Behravesh, C.B. Park, L.K. Cheung, R.D. Venter, Extrusion of polypropylene foams with hydrocerol and isopentane, Journal of Vinyl and Additive Technology, 2(4), 1996, pp. 349-357.

[12] Hydrocerol Chemical foaming agents, 2013. www.MASTERBATCHES.CLARIANT.COM. (Accessed 20/04/2020).

[13] G. Dercz, K. Prusik, L. Pająk, X-ray and SEM studies on zirconia powders, Journal of Achievements in Materials and Manufacturing Engineering, 31(2), 2008, pp. 408-414.

[14] J.A.R. Ruiz, M. Vincent, J-F. Agassant, T. Sadik, C. Pillon, C. Carrot, Polymer foaming with Chemical Blowing Agents: Experiment and modeling, Polymer Engineering and Science, 55(9), 2015, pp. 2018-2029.

[15] T. Sadik, C. Pillon, C. Carrot, J. Reglero Ruiz, DSC studies on non-isothermal and isothermal decomposition of chemical blowing agents based on citric acid and sodium bicarbonate, Thermochimica Acta, 659, 2017, pp. 74-81.

[16] P.K. Heda, D. Dollimore, K.S. Alexander, D. Chen, E. Law, P. Bicknell, A method of assessing solid state reactivity illustrated by thermal decomposition experiments on sodium bicarbonate, Thermochimica Acta, 255, 1995, pp. 255-272.

[17] S.L. Kodjie, L. Li, B. LI, W. Cai, C.Y. Li, M. Keating, Morphology and Crystallization Behavior of HDPE/CNT Nanocomposite, Journal of Macromolecular Science Part B, 45(2), 2006, pp. 231-245.

[18] F.J. Mastral, E. Esperanza, C. Berrueco, M. Juste, J. Ceamanos, Fluidized bed thermal degradation products of HDPE in an inert atmosphere and in air–nitrogen mixtures, Journal of Analytical and Applied Pyrolysis, 70(1), 2003, pp. 1-17.

[19] E. Piiroja, H. Lippmaa, Thermal degradation of polyethylene, Macromolecular Symposia, 27(1), 1989, pp. 305-309.

[20] E. Shefter, A. Lo, S. Ramalingam, A Kinetic Study of the Solid State Transformation of Sodium Bicarbonate to Sodium Carbonate, Drug Development Communications, 1(1), 1974, pp. 29-38.

[21] K.S. Subramanian, T.P. Radhakrishnan, A.K. Sundaram, Thermal decomposition kinetics of sodium bicarbonate by differential thermal analysis, Journal of thermal analysis, 4(1), 1972, pp. 89-93.

[22] T.C. Keener, G.C. Frazier, W.T. Davis, Thermal Decomposition of Sodium Bicarbonate, Chemical Engineering Communications, 33(1-4), 1985, pp. 93-105.

[23] Y-L. Wu, S-M. Shih, Intrinsic kinetics of the thermal decomposition of sodium bicarbonate, Thermochimica Acta, 223, 1993, pp. 177-186.

[24] J.R. Wagner, E.M. Mount, H.F. Giles, Foam Extrusion, in: Extrusion, William Andrew Publishing, Chapter 53, 2014, pp. 603-607.

[25] M.M. Barbooti, D.A. Al-Sammerrai, Thermal decomposition of citric acid, Thermochimica Acta, 98, 1986, pp. 119-126.

[26] M.C. Ball, C.M. Snelling, A.N. Strachan, R.M. Strachan, Thermal decomposition of solid sodium bicarbonate, Journal of the Chemical Society, Faraday Transactions 1: Physical Chemistry in Condensed Phases, 82(12), 1986, pp. 3709-3715.

[27] E.M. Barall, L.B. Rogers, Differential thermal analysis of the decomposition of sodium bicarbonate and its simple double salts, Journal of Inorganic and Nuclear Chemistry, 28(1), 1966, pp. 41-51.

[28] D. Wyrzykowski, E. Hebanowska, G. Nowak-Wiczk, M. Makowski, L. Chmurzyński, Thermal behaviour of citric acid and isomeric aconitic acids, Journal of Thermal Analysis and Calorimetry, 104(2), 2011, pp. 731-735.

[29] S. Estravis, A.H. Windle, M. van Es, J.A. Elliott, Thermodynamic limits on cell size in the production of stable polymeric nanocellular materials, Polymer, 186, 2020, pp. 122036.

[30] A. Ahmadzai, A.H. Behravesh, M.T. Sarabi, P. Shahi, Visualization of foaming phenomena in thermoplastic injection molding process, Journal of Cellular Plastics, 50(3), 2014, pp. 279-300.

[31] J.S. Colton, The Nucleation of Microcellular Foams in Semi-Crystalline Thermoplastics, Materials and Manufacturing Processes 4(2) (1989) 253-262.

[32] D.F. Baldwin, Microcellular polymer processing and the design of a continuous sheet processing system, Doctoral Thesis, Department of Mechanical Engineering, Massachusetts Institute of Technology, 1994, pp. 1-267.

[33] J.E.K. Schawe, Cooling rate dependence of the crystallinity at nonisothermal crystallization of polymers: A phenomenological model, Journal of Applied Polymer Science, 133(6), 2016, pp. 42977_1-17.

[34] R. Nobe, J. Qiu, M. Kudo, G. Zhang, Morphology and mechanical investigation of microcellular injection molded carbon fiber reinforced polypropylene composite foams, Polymer Engineering & Science, 2020, pp. 1-13.

[35] C. Timpano, H. Abdoli, S.N. Leung, G.W. Melenka, Characterization of open-cellular polymeric foams using micro-computed tomography, Polymer, 202, 2020, pp. 122628_1-12.

[36] D. Eaves, Handbook of Polymer Foams, Rapra Technology Limited, 2004, pp. 1-277.

[37] A. Osorio, L-S. Turng, Mathematical modeling and numerical simulation of cell growth in injection molding of microcellular plastics, Polymer Engineering & Science, 44(12), 2004, pp. 2274-2287.

[38] L.M. Matuana, C.B. Park, J.J. Balatinecz, Processing and cell morphology relationships for microcellular foamed PVC/wood-fiber composites, Polymer Engineering & Science, 37(7), 1997, pp. 1137-1147.

[39] T. Garbacz, L. Dulebova, Processing Characteristics and Properties of the Cellular Products Made by Using Special Foaming Agents, Scientific Proceedings 2012, 20(1), 2012, pp. 74-80.

[40] A.B. Strong, Plastics: Materials and Processing, Pearson Prentice Hall, third edition, 2006, pp. 1-917.

[41] M. Mahmoodi, A.H. Behravesh, S.A.M. Rezavand, A. Pashaei, Visualization of bubble dynamics in foam injection molding, Journal of Applied Polymer Science, 116(6), 2010, pp. 3346-3355.

[42] F. Lionetto, A. Maffezzoli, Polymer characterization by ultrasonic wave propagation, Advances in Polymer Technology, 27(2), 2008, pp. 63-73.

[43] P. Laugier, G. Haïat, Introduction to the Physics of Ultrasound, in: Bone Quantitative Ultrasound, Springer, Chapter 2, 2011, pp. 29-45.

[44] A. Kovalenko, M. Fauquignon, T. Brunetb, O. Mondain-Monval, Tuning the sound speed in macroporous polymers with a hard or soft matrix, Soft Matter, 13(25), 2017, pp. 4526-4532.

[45] M. J. Crocker, J. P. Arenas, Use of Sound-Absorbing Materials, in: Handbook of Noise and Vibration Control, John Wiley & Sons Inc., Chapter 57, 2007, pp. 696-713.

[46] L. Lyu, Y. Liu, J. Bi, J. Guo, Sound Absorption Properties of DFs/EVA Composites, Polymers, 11(5), 2019, pp. 811-828.

[47] M.A. Kuczmarski, J.C. Johnston, Acoustic Absorption in Porous Materials, NASA/TM, Conference Paper, NASA Glenn Research Center, Cleveland, US, March 2011, pp. 1-20.

[48] C. C. Ibeh, M. Bubacz, Current Trends in Nanocomposite Foams, Journal of Cellular Plastics, 44(6), 2008, pp. 493-515.

[49] A.K. Bledzki, O. Faruk, Influence of Processing Temperature on Microcellular Injection-Moulded Wood–Polypropylene Composites, Macromolecular Materials and Engineering, 291(10), 2006, pp. 1226-1232.

[50] L.M. Chen, D. Rende, L.S. Schadler, R. Ozisik, Polymer nanocomposite foams, Journal of Materials Chemistry A, 1(12), 2013, pp. 3837-3850.

[51] J. Xu, Microcellular injection molding, John Wiley & Sons, Inc., 2010, pp. 1-618.

[52] M.M. Khorasani, S.R. Ghaffarian, A. Babaie, N. Mohammadi, Foaming Behavior and Cellular Structure of Microcellular HDPE Nanocomposites Prepared by a High Temperature Process, Journal of Cellular Plastics, 46(2), 2010, pp. 173-190.

[53] S.S. Ray, M. Okamoto, Polymer/layered silicate nanocomposites: a review from preparation to processing, Progress in Polymer Science, 28, 2003, pp. 1539–1641.

[54] T. Azdast, E.K. Lee, K-M. Lee, C.B. Park, H.E. Naguib, A.H. Behravesh, E. Pachner, A. Praller, Extrusion Foaming of High-Melt-Strength PP with Supercritical Carbon Dioxide I: Cell Nucleation Behaviors, ANTEC 2008 Plastics: Annual Technical Conference Proceedings, 2008, pp. 997-1002.

[55] M. Nofar, C.B. Park, Introduction to Plastic Foams and Their Foaming, in: Polylactide Foams, William Andrew Publishing, Chapter 1, 2018, pp. 1-16.

[56] D. Aydemir, A. Kiziltas, D. Gardner, Y. Han, G. Gündüz, Morphological characterization of foamed natural filler-reinforced styrene maleic anhydride (SMA) composites, Journal of Porous Materials, 21, 2014, pp. 1059-1067.

[57] M.Y. Serry Ahmed, N. Atalla, C.B. Park, Assessment of the Potentiality of Microcellular Plastic Foams for Passive Noise Control in Automotive Structures, ANTEC 2008 Plastics: Annual Technical Conference Proceedings, 2008, pp. 1109-1112.

[58] L. Chen, H. Sheth, R. Kim, Gas absorption with filled polymer systems, Polymer Engineering & Science, 41(6), 2001, pp. 990-997.

[59] M.M. Khorasani, S.R. Ghaffarian, S.H. Goldansaz, N. Mohammadi, A. Babaie, Solid-state microcellular foaming of PE/PE composite systems, investigation on cellular structure and crystalline morphology, Composites Science and Technology, 70(13), 2010, pp. 1942-1949.

[60] C. DeArmitt, M. Hancock, Filled Thermoplastics, in: Particulate-Filled Polymer Composites, Rapra Technology Limited, Chapter 8, 2003, pp. 357-424.

[61] L. J. Lee, C. C. Zeng, X. Cao, X. Han, J. Shen, G. Xu, Polymer nanocomposite foams, Composites Science and Technology, 65(15-16), 2005, pp. 2344-2363.

[62] Y. Fei, W. Fang, M. Zhong, J. Jin, P. Fan, J. Yang, Z. Fei, L. Xu, F. Chen, Extrusion Foaming of Lightweight Polystyrene Composite Foams with Controllable Cellular Structure for Sound Absorption Application, Polymers, 11(1), 2019, pp. 106-116.

[63] M. Sinha, D.J. Buckley, Acoustic Properties of Polymers, in: Physical Properties of Polymers Handbook, Springer, Chapter 60, 2007, pp. 1021-1031.

[64] H. I. Schlaberg, J. S. Duffy, Piezoelectric polymer composite arrays for ultrasonic imaging applications, Sensors and Actuators A, 44, 1994, pp. 111-117.

[65] D.W.Van Krevelan, Acoustic Properties, in: Properties of Polymers, Elsevier Science, chapter 14, fourth edition, 2009, pp. 505–522.

[66] F. Ramsteiner, N. Fell, S. Forster, Testing the deformation behaviour of polymer foams, Polymer Testing, 20(6), 2001, pp. 661–670.

[67] S. Doroudiani, C.B. Park, M.T. Kortschot, Effect of the crystallinity and morphology on the microcellular foam structure of semicrystalline polymers, Polymer Engineering & Science, 36(21), 1996, pp. 2645-2662.

[68] L. Matuana, F. Mengeloglu, Microcellular foaming of impact-modified rigid PVC/wood-flour composites, Journal of Vinyl and Additive Technology, 7(2), 2001, pp. 67-75.

CHAPTER 6: RESULTS AND DISCUSSION- PART III

Characterisation of Foams of HDPE and HDPE-MWCNT Composites via Physical Foaming

In chapter 5, the feasibility of using a mini IM system to complete the process of chemical foaming initiated in the extruder by addition of CBAs to un-filled and MWCNT filled HDPE was demonstrated. This chapter discusses further processing strategies pursued with the aim of controlling cell nucleation and growth within the mould cavity in an advanced foam moulding process. This in order to obtain more uniform cell structures with higher void fractions than those previously obtained. Increasing the porosity of foamed samples can lead to improved acoustic properties. The object of this research is to study the evolution of the foaming characteristics of HDPE and the effects of MWCNT loading up to (0.1%, 0.5% and 1%, by weight) when moving from a chemical to a physical based foaming process.

Among the various special IM processes, microcellular injection moulding (MIM), based on a reciprocating-type IM machine which combines microcellular plastics with IM, has proven to be successful in saving on material costs and energy while improving dimensional stability and production efficiency [1]. The MIC process continues to attract attention by producing lightweight parts with a microcellular structure that can offer many advantages (e.g. enhanced thermal and acoustic properties) as well as additional degrees of freedom in product design and part thickness variation, while requiring less material, lower injection pressures and energy, and shorter cycle times than conventional IM systems. In particular, MuCell technology is today acknowledged as the most widely used techniques commonly employed for physical foaming in IM [2]. Supercritical fluids (SCFs) are used as physical blowing agents (PBAs) to produce cellular structures potentially with uniform cell sizes and an average cell size of 100 μm or less [1].

In this work, large reductions in density (>50%) were achieved by using a special mould and process design, allowing for the production of foam injection moulded parts of HDPE and HDPE-MWCNT composites having pronounced porosity, significantly exceeding those of benchmark materials. The investigation conducted focused on the effects of varying moulding methods and critical processing parameters (e.g. SCF-CO_2 content and injection flow rate) on foaming and morphology. The range of techniques used in this work to characterise the foamed parts prepared by MIM enabled a further screening of the degree of porosity, expansion ratio, density reduction and acoustic impedance, allowing eventually to assess the potential of the foams prepared for the target application. Therefore, the acoustic emission profile of a new sensor built on the best candidate foam was evaluated and is also described in this chapter.

6.1 Morphological Characterization of foamed parts

Firstly, imaging of the cellular structure of all the foams produced in this work was performed by scanning electron microscopy and compared with the morphology of benchmark materials, i.e. materials currently used commercially as MLs. In addition, a non-destructive complementary method, micro-X-ray CT scanning, was used to examine the three-dimensional cellular structure of foamed parts and estimate the level of porosity achieved. The average diameter of the pores, distribution of the cell size, pore volume fraction, cell density and the percentage of porosity in the samples were determined using both techniques.

It is important to point out that the type of structure of the foams produced by the different MIM trials is a typical three-layer structure, as shown in Figure 6.1. Clearly, the type of polymer selected is also a decisive factor in determining the type of foam structure obtained, based on its sorption behaviour. The three-layer structure, is expected to influence (e.g. from localisation of the filler in the matrix) the properties of the final parts, including acoustic and mechanical. The cell size distribution usually varies across the part thickness. Therefore, morphology and thus properties vary also across the part thickness, certainly complicating characterization of such types of foamed structures [3].
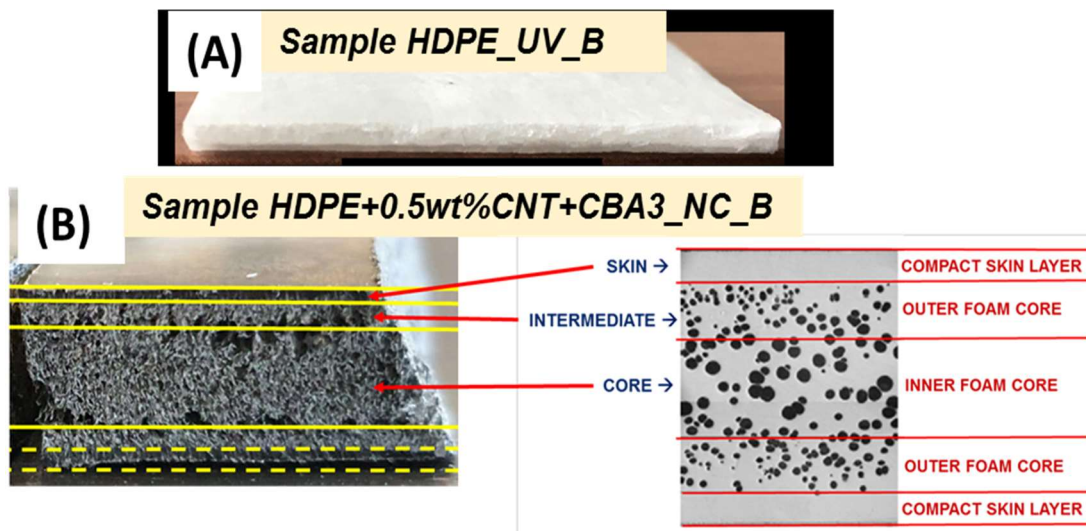
Figure 6.1. Cross sections showing representative morphology of injection moulded parts obtained from (A) *Trial 1* and (B) *Trials 2-3* in MuCell. A well-defined three-layer structure with skin, intermediate, and core layers was obtained in all trials.

In this type of three-layer morphology (more evident in Figure 6.1(B)), the skin layer is solid (compact layer without collapsed foam pores), the intermediate layer consists mainly of stretched cells, and the core layer contains spherical cells [4]. In close proximity to the compact layers, the average cell size is small but increases steadily towards the centre of the part.

6.1.1 Imaging of Foams using Scanning Electron Microscopy (SEM)

The cell size and morphology of the cellular unfilled HDPE and HDPE-MWCNT composite structures produced in this work were examined using SEM. The shape and distribution of the cells

obtained in the foamed parts were influenced by the processing methodology and parameters used during processing, and will, in turn, determine the final properties of the foams, including acoustic properties. Foam settings and composition of the foamed material are crucial factors in determining the final morphology [5].

Before analysing the images reported in this section, there are important considerations to highlight:

1) The formation of a three-layer structure (compact skin and a cellular core) involves a certain degree of material inhomogeneity in the injection moulded samples. Consequently, SEM micrographs are expected to show some inhomogeneity in the final foam morphology.

2) For a complete analysis of the morphology of the foams along the longitudinal and transverse flow directions, several predetermined cross sections from different locations from the same area of the moulded samples must be studied. Nonetheless, the fractured surfaces observed were taken from the inner foam core regions (where most of the cells are) of the thick B layer for each sample.

3) The visualization of more or less fine pores may also depend on practical difficulties such as cutting surfaces from the same region of corresponding samples.

4) The skin layer was not examined in this work as the main objective of this study was to study the size, shape, population and size distribution of foam cells predominantly located within core layers [4]. It should be emphasized however that the fractured surfaces taken from samples produced in *TRIAL 1* are also inclusive of solid skin layers as, in this case, the entire sample thickness is relatively thin (~3 mm) and distinguishing each single layer is difficult, as seen from Figure 6.1(A).

5) Despite SEM being the most utilized method for characterizing the cell structure of foams, there are several disadvantages associated with it. The fact that it requires the destruction of the sample to capture a single cross-sectional image of the micro-structure is one major drawback. Besides, there is also the issue that an SEM image is a 2D image of a surface, which is unrepresentative of the true pore structure [6], i.e. in 3D. Two-dimensional image-based techniques such as optical and SEM can provide quantitative information on microstructural features but require innumerable images and serial sectioning of the sample, which is a laborious and challenging task.

A series of micrographs of the fractured surfaces of expanded HDPE and HDPE-MWCNT composite moulded parts produced using physical blowing process during MIM from the various trials are shown in Figures 6.2-6.5. The images reflect the internal microstructure and morphology of moulded parts cut from the thick layer, B, of the sample plates. In particular, the fractured surface were taken from the core layers of the thick layers B of each sample (i.e. inner foam core region shown in Figure 6.1(B)) and multiple micrographs were taken for each sample.

Finally, a comparison with the internal microstructure of the benchmark materials can be made by comparing the morphologies of Figures 6.2-6.5 with those captured in the micrographs obtained for these samples (i.e. syntactic foam, *Commercial ML* and *ML-Trelleborg*) which are shown in Figure 6.6.

Representative SEM images of cross sections of unfilled HDPE expanded moulded microstructures obtained during foam IM trials, at different magnifications.
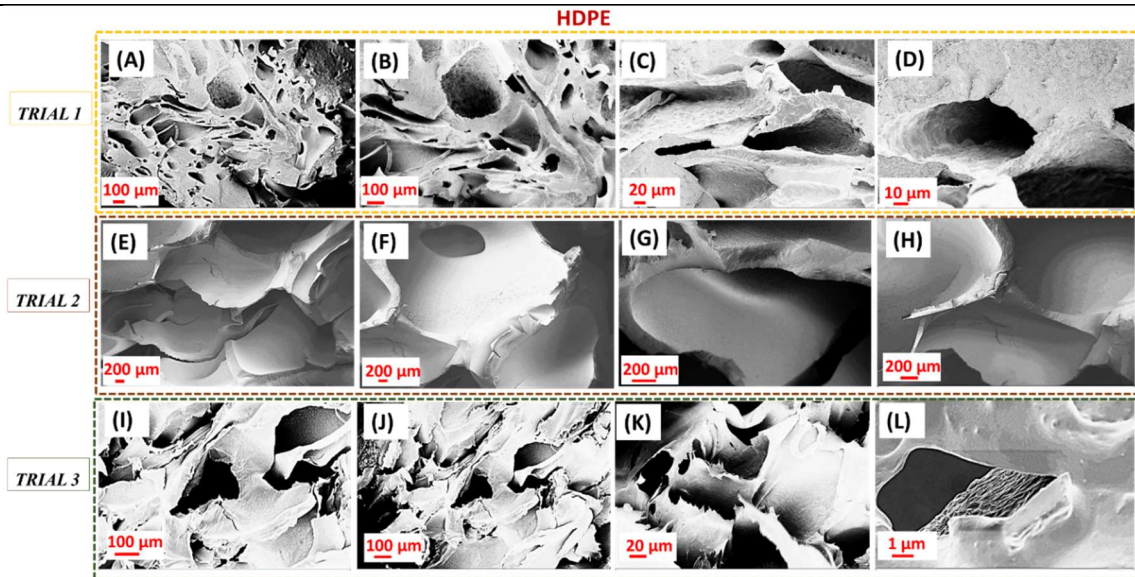
Figure 6.2. Representative SEM images of foams of (A-D) HDPE_UV_B; (E-H) HDPE _NC_B; and (I-L) HDPE+CBA$_3$_NC_B.

Comments

From a first comparison of the micrographs shown in Figure 6.2, it is evident that the processing used affected tremendously the morphology of the foams obtained. Unfilled polymers, particularly semi-crystalline polymers, have a tendency to form non-uniform cell structures with PBAs [4]. This is due to the fact that there are only two contributors to cell nucleation when using PBAs with unfilled polymers, i.e. the rate of pressure drop and the amount of SCF used.

Figures (A-D), from *TRIAL 1*, showed a very irregular and inhomogeneous cell structure containing a number of elongated pores surrounded by a dense skin was and a wide cell distribution with cell sizes ranging from 60-80 μm, but up to 300 μm.

The introduction of a breathing delay during the IM of the parts in the core-back process, *TRIAL 2*, (see figure (E-H)), led to the formation of much bigger pores, with cell size reaching the millimetre scale (average size of the cell is between 1.2 and 2 mm). As the opening of the mould occurred at a fixed point in time (2 sec) after complete filling of the cavity, more polymer containing gas was still at elevated temperatures, independent of the cavity surface temperature (60°C), suitable for cell nucleation and growth. When the mould was opened, additional space for the polymer to foam was available, accompanied by a sudden pressure reduction, hence, the molten core started foaming and thus expand. The 2 sec breathing delay and the opening distance of 3 mm employed in this trial allowed a greater amount of melt to expand. Therefore, during a core back expansion process bigger cells with a higher expansion ratio were created in comparison to when the under-volumetric moulding process was used.

A more uniform cell structure was expected where the chemical foaming agent, CBA$_3$, was added to assist physical foaming. The benefit of self-nucleation with CBAs when using unfilled polymers, especially with unfilled HDPE and PP as reported in the literature [7], is very significant when compared to PBAs, resulting in a more uniform cell structure from the gate to the end of fill.

Moreover, the use of an endothermic CBA (which develops more CO_2) tends to provide both a more uniform cell structure and a thicker skin layer as compared to PBAs, as $CO_{2,gas}$ comes out of solution slowly. A greater amount of blowing agent increases nucleation in the polymer melt, leading to a greater pore density while creating smaller pore diameters, since the average diameter of the pores is mainly determined by the amount of blowing agent [4]. In this study, the combination of a core back expansion process and the addition of an extra 1 wt% CBA_3 on top of the 1.75 wt% SCF-CO_2 allowed for a reduction in the average size of the cells, compared to the previous *TRIAL 2*, resulting in cells sizes mostly in the range between 60 µm and 80 µm. Nevertheless, smaller cells with diameters of ca. 10 µm (see Figure 6.2(L)) and bigger than 200 µm (see Figure 6.2(I)) were also observed. Allowing for errors involved in applying equation 5.8 (see chapter 5, paragraph 5.3.1), due to the assumptions of perfect spherical cell shape and dimensional uniformity, the values of cell density obtained for this foamed sample is in the range of 10^6 cells/cm^3, typical of macro-cellular plastics (conventional foams) [8], as shown in Table 6.1.

Representative SEM images of of cross-sections of filled HDPE expanded molded microstructures with 0.1 wt% MWCNT content obtained during foam IM trials, at different magnifications.
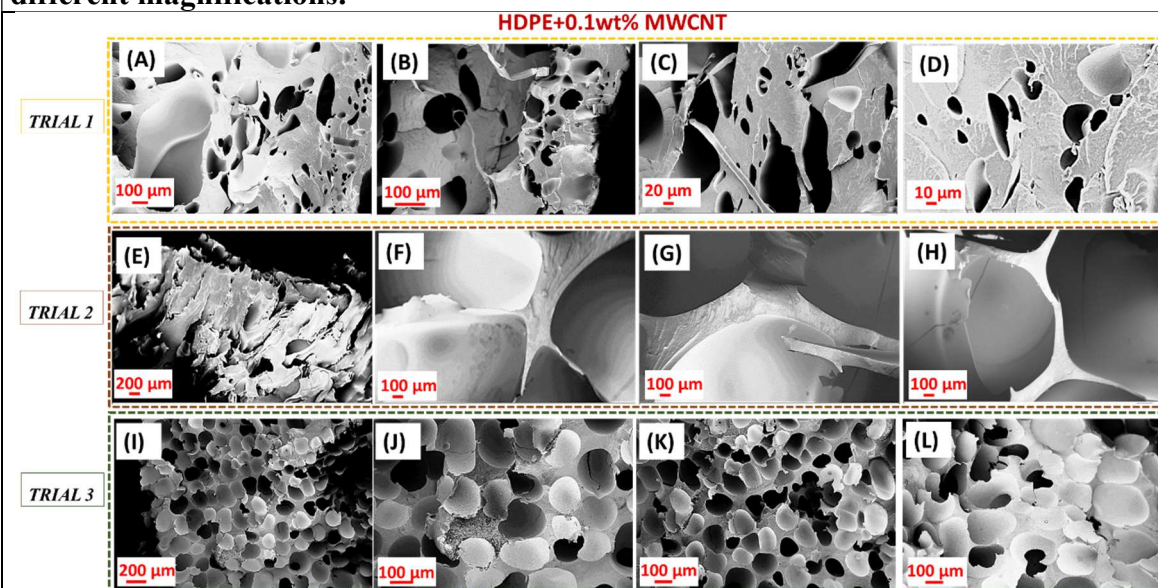
Figure 6.3. Representative SEM images of foams of (A-D) HDPE+0.1wt%CNT_UV_B; (E-H) HDPE+0.1wt%CNT_NC_B; and (I-L) HDPE+0.1wt%CNT+CBA_3_NC_B.

Comments

The inclusion of MWCNTs into the HDPE altered the polymer morphology and thus the size and density of the cells produced even after adding a small loading (0.1 wt%) of MWCNTs. As reported in the literature, the size, number of cells and the uniformity of cell distribution in filled and unfilled polymers differ and a reinforced nuclei structure is expected [9]. The number of pores seems to steadily increase after addition of 0.1 wt% MWCNT, even when filling the mould cavity under-volumetrically in *TRIAL 1* (see Figure 6.2(A-D) in comparison to Figure 6.3(A-D)). In this case, however, the cellular structure showed no uniformity of cell distribution with average pore diameters

varying from 20 μm up to 350 μm, predominantly in the range between 60 μm and 120 μm (see figures 6.2(A-D)).

The morphology of foams of the composites with the same filler content of 0.1wt% appeared much bigger (average cell diameter size between 0.8 mm and 1.5 mm) in Figures (E-H), where thicker cell walls than the previous sample (HDPE+0.1wt%CNT_UV) can be seen. The presence of MWCNTs may have assisted the cells withstand the stretching force that otherwise might have broken and formed a thin walled cell, conferring strength to the foam providing structural support for the cells from being destroyed by external forces [10].

The addition of CBA_3 significantly increased the population of pores (see Table 6.1) while the MWCNTs served to nucleate cells, leading to smaller cells (see figures (I-L)) as now most of the cells are characterised by an average diameter of 80 μm. The SEM images taken at different magnifications for this sample (HDPE+0.1wt%CNT+CBA_3_NC), confirmed a level of uniformity of cell distribution achieved for the manufacturing conditions employed. Undoubtedly, the inclusion of MWCNTs significantly contributed to improving the microcellular structure by enhancing nucleation acting as heterogeneous nucleating agents.

Representative SEM images of cross-sections of filled HDPE expanded molded microstructures with 0.5 wt% MWCNT content obtained during foam IM trials, at different magnifications.
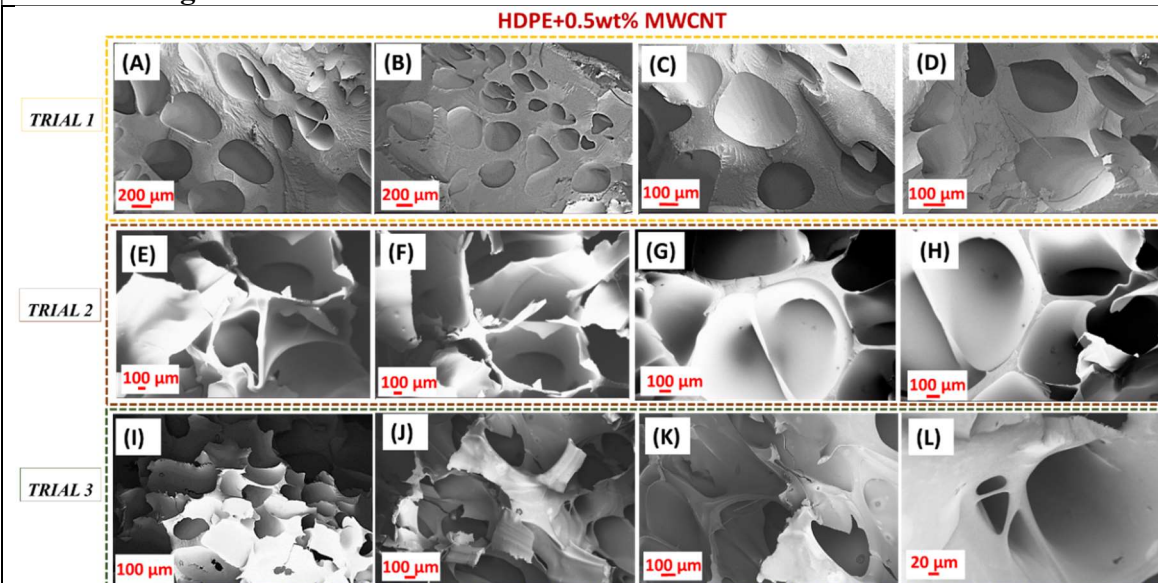
Figure 6.4. Representative SEM images of foams of (A-D) HDPE+0.5wt%CNT_UV_B; (E-H) HDPE+0.5wt%CNT_NC_B; and (I-L) HDPE+0.5wt%CNT+CBA_3_NC_B.

Comments

When the MWCNT content was increased, SEM micrographs of the fracture surfaces obtained from the foamed HDPE-MWCNT composite specimens showed a further decrease in cell size. Since the under-volumetric process so far has resulted in the production of less uniform cell structures (see figures 6.2(A-D) and 6.3(A-D)), the obvious change in the morphology of the foam shown in figures 6.4(A-D) can be solely attributed to the addition of 0.5 wt% MWCNT. The images included in figures

6.4(A-D) show a more regular morphology, where pores have a more spherical cell shape and dimensional uniformity. Additionally, this can be related to the effect of increased injection velocity (i.e. from 100 to 125 cm^3/s) when moving from neat HDPE to the composite foams, as higher injection speeds tend to produce more uniform cell distributions throughout foamed samples. The increase in the injection velocity caused the cell density as well as the amount and size of bubbles in the foamed parts to increase, suggesting a weight reduction for the composite foam parts.

The effect of 0.5wt% MWCNT content on the increase in cell number and decrease in cell size can also be seen in the images in Figure 6.4(E-H), where the mean diameter is now reduced to 150-500 µm from the millimetre size of the cells that characterized the composites with a lower filler content (0.1wt%) (see figures 6.4(E-H)). These results again indicate that the MWCNTs serve as sites for heterogeneous nucleation during the foaming process. In a heterogeneous nucleating system, including with filler particles, cells nucleate at the boundary between the polymer matrix and the dispersed filler particles.

Representative SEM images of cross-sections of filled HDPE expanded molded microstructures with 1 wt% MWCNT content obtained during foam IM trials, at different magnifications.
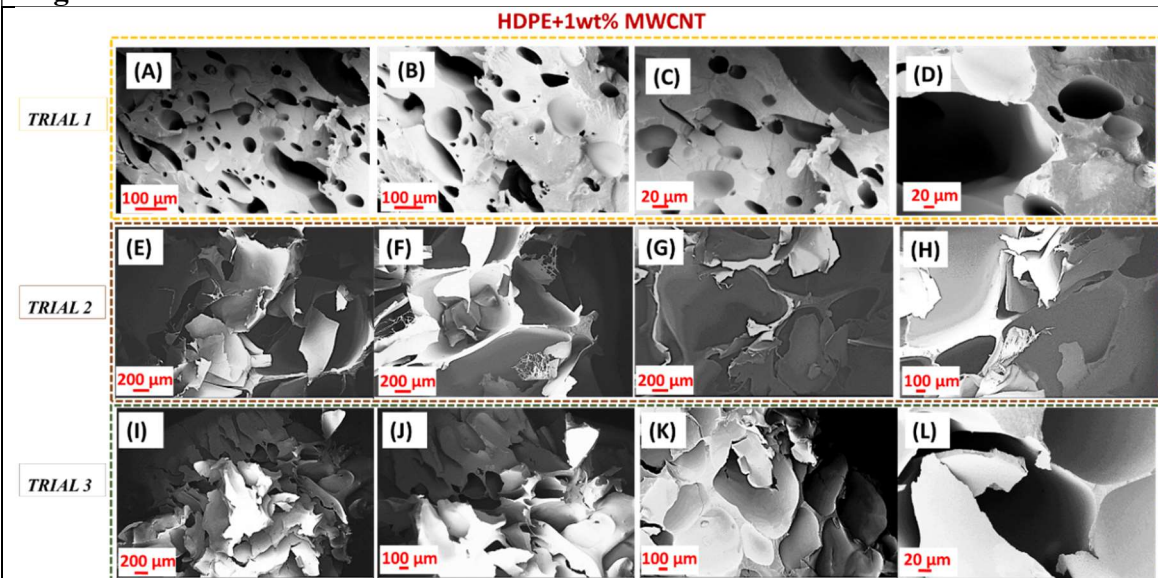
Figure 6.5. Representative SEM images of foams of (A-D) HDPE+1wt%CNT_UV_B; (E-H) HDPE+1wt%CNT_NC_B; and (I-L) HDPE+1wt%CNT+CBA$_3$_NC_B.

Comments

The cell size levelled off when the MWCNT loading was ≥ 0.5 wt%, as in *TRIAL 3* (Figures 6.4(I-L), 6.5(I-L)), where the morphology obtained was irregular and non-uniform. The difference in cellular structure for HDPE+0.5wt%CNT+CBA$_3$_NC_B and HDPE+1wt%CNT+CBA$_3$_NC_B could be a response to changes in the effect of SCF content, as it was lowered for the composites with MWCNT loadings ≥ 0.5 wt%. This was in the belief that a significant improvement in the microcellular structure would result with increased MWCNT loading due to the effects on both cell nucleation and a decrease in matrix content, the SCF gas content was reduced from 2 wt% (for

MWCNT loading of 0.1 wt%) to 1.5 wt% (for MWCNT loading > 0.1 wt%). The cell size distribution narrows and the solid structure (in the form of ligaments) greatly stiffened with increasing MWCNT content [4]. As the MWCNT content increases, the size of the interface between the matrix and the filler is also expected to increase and cell nucleation promoted. Moreover, the formation of a filler network could suppress cell growth and cell coalescence on the micro-scale. The micrographs presented in figures 6.4(I-L) and 6.5(I-L) illustrate cell structures achieved from *TRIAL 3* as a function of MWCNT content at 0.5 and 1 wt%, respectively. It can be seen that, although the cell roundness (cell cross sections are relatively circular) was preserved, larger cell size (up to 600 μm) and distribution characterised samples with the highest MWCNT content (1 wt%) investigated, most likely caused by weak interfacial interactions between HDPE and the MWCNTs rather than cell coalescence.

Different morphologies can be finally observed in Figure 6.6 for the benchmark materials of the matching layers currently in commercial use, see also Table 6.1.
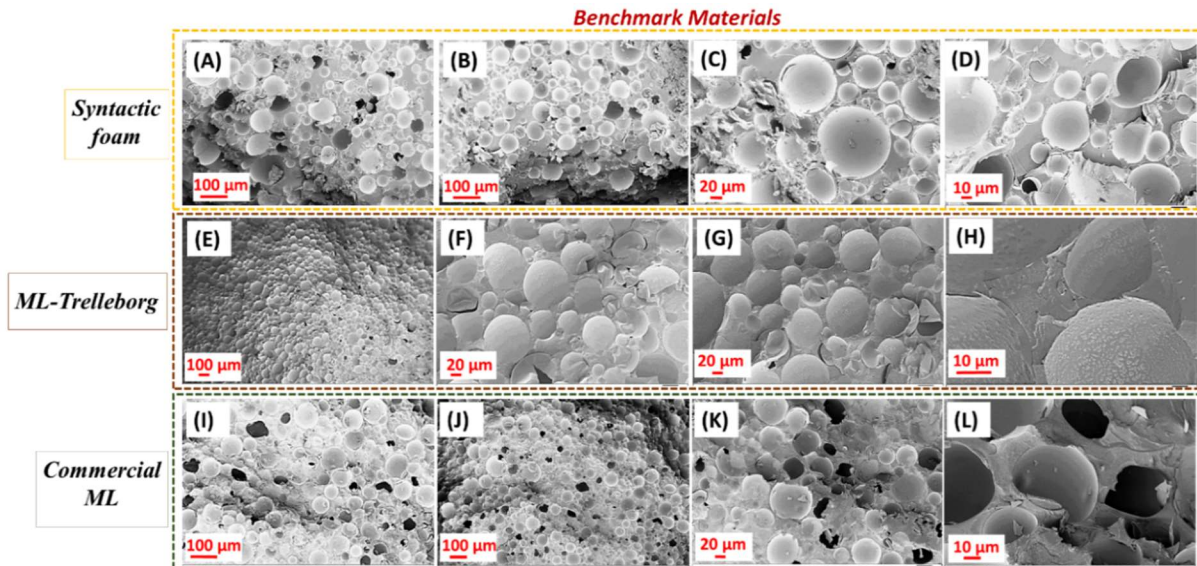
Figure 6.6. Representative SEM images of cross-sections of benchmark materials of (A-D) *syntactic foam*; (E-H) *ML-Trelleborg*; (I-L) *Commercial ML*.

Table 6.1. Microscopic cell characteristics of benchmark materials and selected foams produced in this work observed from SEM.

Sample	Minimum cell size diameter	Average cell size diameter	Maximum cell size diameter	Cell density / cells/cm^3
HDPE+CBA$_3$_NC	10 μm	60-80 μm	300 μm	$2.16 \cdot 10^6$
HDPE+0.1wt%CNT+CBA$_3$_NC	10 μm	50-70 μm	290 μm	$4.50 \cdot 10^6$
HDPE+0.5wt%CNT+CBA$_3$_NC_B	80 μm	120-350 μm	600 μm	$2.48 \cdot 10^6$
HDPE+1wt%CNT+CBA$_3$_NC_B	150 μm	180-350 μm	600 μm	$1.02 \cdot 10^6$
Syntactic foam	10 μm	40-60 μm	150 μm	$1.29 \cdot 10^7$
Commercial ML	20 μm	50-60 μm	80 μm	$1.01 \cdot 10^7$
ML-Trelleborg	25 μm	50-60 μm	80 μm	$8.43 \cdot 10^6$

The cell densities of the foamed parts produced in this work are almost comparable with that of the benchmark samples, despite the broader cell size distribution of the former. Nevertheless, the three-dimensional (3D) analysis of cellular materials using a non-destructive technique such as X-ray computed tomography (XCT) can provide meaningful information about the morphology of the second phase (i.e. cavities) in the bulk material that is not easy to capture using standard surface microscopy techniques. Understanding pore distribution and porosity formation is essential in understanding the acoustic properties of the foams produced in this work.

6.1.2 3D X-Ray Computed Tomography
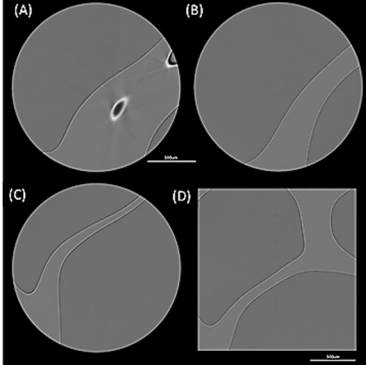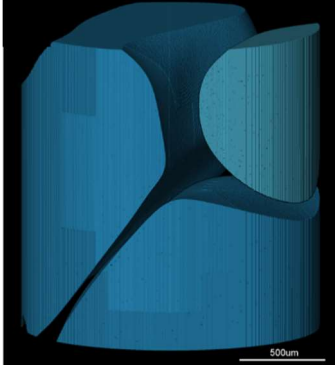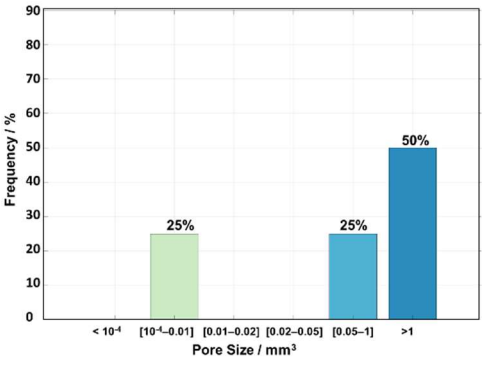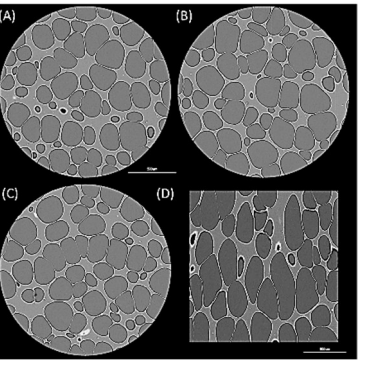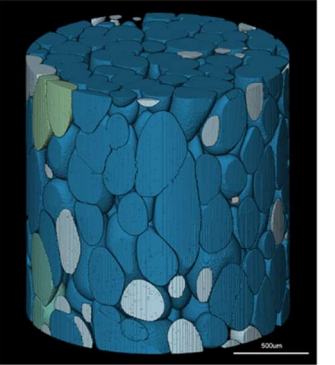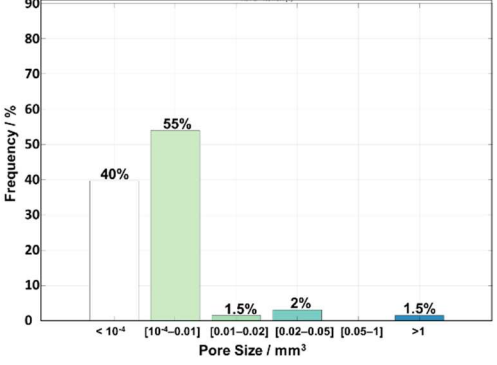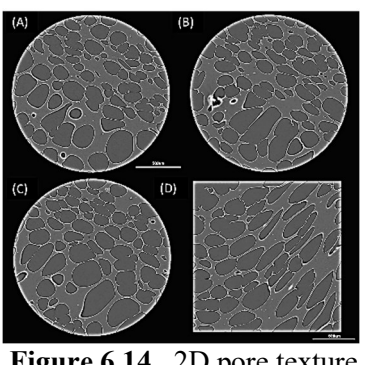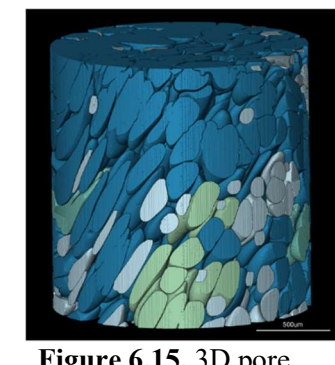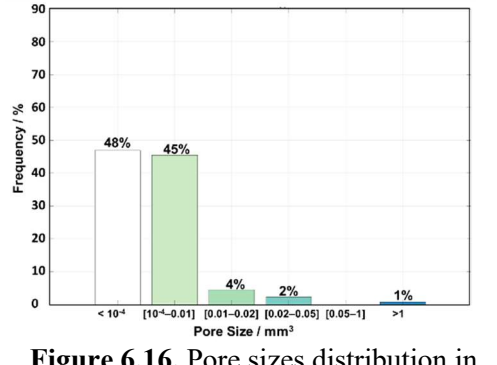
In order to quantify and compare the morphology of foamed HDPE and the HDPE-MWCNT composites produced using the physical blowing process, six samples were selected and scanned and porosity measured. XCT allowed for the extraction quantitatively of key topological parameters from 3D images (quantitative characterisation of microstructure from a single 3D volume) and quantify the pore texture according to the spatial resolution (voxel size). Different morphological parameters (volume fraction spatial distribution, pore size and porosity content) were imaged and subsequently quantified. The results from the scans with images of each foam along with porosity analysis are discussed in this section. However, most of these measurements were performed using approximations calculated using discretised (voxelised) images which can have a strong influence on the results in terms of the surface length and surface area, which can be overestimated for smooth objects (e.g. spheres). The resolution achieved from these voxel datasets in the tomography measurements provided the required statistical information of pore size, pore size distribution, volume fraction and pore position. From the 3D processed binary images, the porosity (i.e. total volume fraction of pores) was calculated for each sample. These values as well as the properties of the pores were determined by subjecting the pore label fields to label analysis followed by sieve analysis, see Table 6.2. The slice location of each of the 2D images supplied for each sample volume and the corresponding colour scheme for the sieve analysis images (kept the same during the entire analysis) are shown in Figure 6.7.
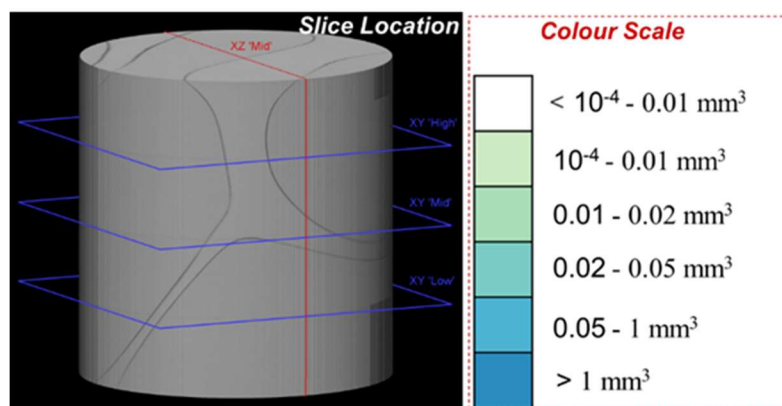
Figure 6.7. Slice location of the 2D images for each volume and corresponding colour scheme for the sieve analysis images.

It should be noted that the 2D images taken from each slice location for each sample volume are reported on the left column (see Figures 6.8, 6.11, 6.14, 6.17, 6.20 and 6.23). Specifically, these indicate the horizontal slice through the foam in the directions; (A) 'XY Mid', (B) 'XY High', and (C) 'XY Low', and the vertical slice through the foam in the (D) in 'XZ Mid' direction.

The scale bar in all the images in Figures 6.8-6.25 is 500 μm.

Radiographs of the horizontal and vertical slice through the foamed sample, showing the pore structure.	Sieve analysis showing the distribution, shape and size of each colour-coded pore throughout the entire volume in the dataset.	Statistical distribution of the pore sizes in the foamed sample in a percentage frequency plot of pores by volume.
POLYMER FOAM SAMPLE HDPE_NC_B		
Figure 6.8. 2D pore texture of the foam.	**Figure 6.9.** 3D pore texture of the foam.	**Figure 6.10.** Pore sizes distribution in the foam.
POLYMER FOAM SAMPLE HDPE+CBA₃_NC_B		
Figure 6.11. 2D pore texture of the foam.	**Figure 6.12.** 3D pore texture of the foam.	**Figure 6.13.** Pore sizes distribution in the foam.
COMPOSITE FOAM SAMPLE HDPE+0.1wt%CNT+CBA₃_NC_B		
Figure 6.14. 2D pore texture of the foam.	**Figure 6.15.** 3D pore texture of the foam.	**Figure 6.16.** Pore sizes distribution in the foam.

Radiographs of the horizontal and vertical slice through the foamed sample, showing the pore structure.	Sieve analysis showing the distribution, shape and size of each colour-coded pore throughout the entire volume in the dataset.	Statistical distribution of the pore sizes in the foamed sample in a percentage frequency plot of pores by volume.
COMPOSITE FOAM SAMPLE HDPE+0.5wt%CNT_NC_B		
Figure 6.17. 2D pore texture of the foam.	**Figure 6.18.** 3D pore texture of the foam.	**Figure 6.19.** Pore sizes distribution in the foam.
COMPOSITE FOAM SAMPLE HDPE+0.5wt%CNT+CBA$_3$_NC_B		
Figure 6.20. 2D pore texture of the foam.	**Figure 6.21.** 3D pore texture of the foam.	**Figure 6.22.** Pore sizes distribution in the foam.
COMPOSITE FOAM SAMPLE HDPE+1wt%CNT+CBA$_3$_NC_B		
Figure 6.23. 2D pore texture of the foam.	**Figure 6.24.** 3D pore texture of the foam.	**Figure 6.25.** Pore sizes distribution in the foam.
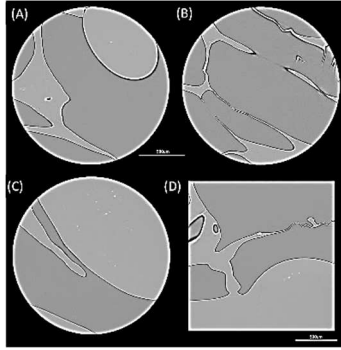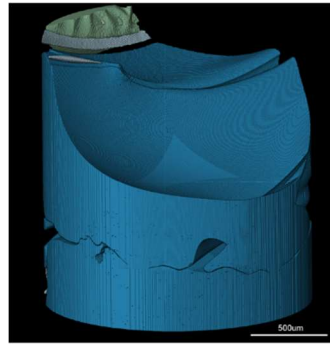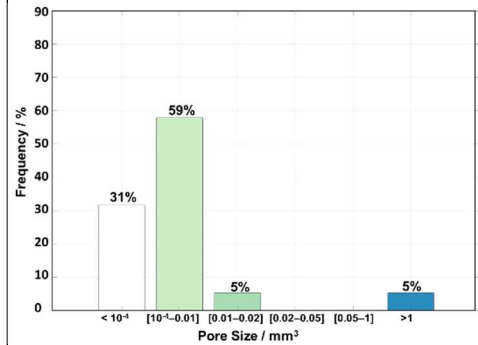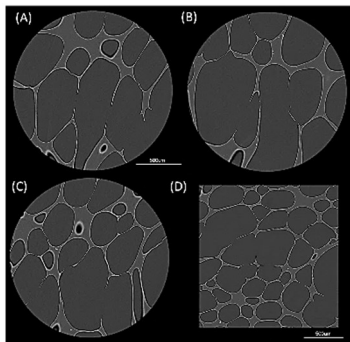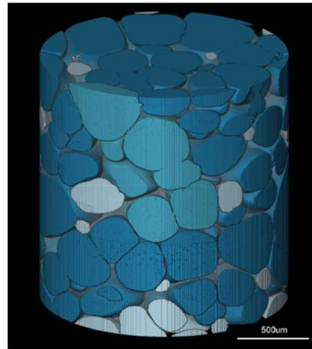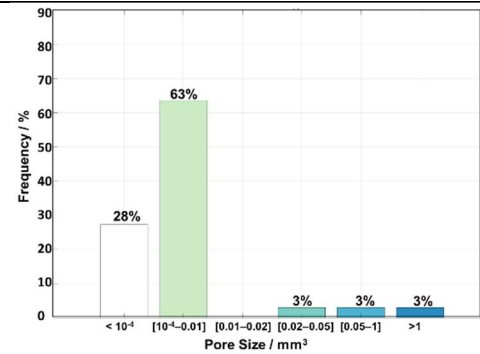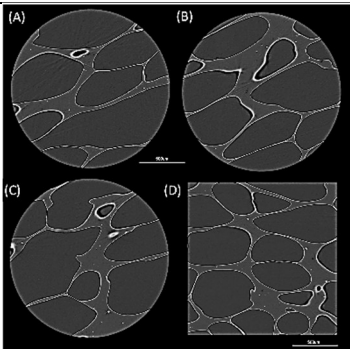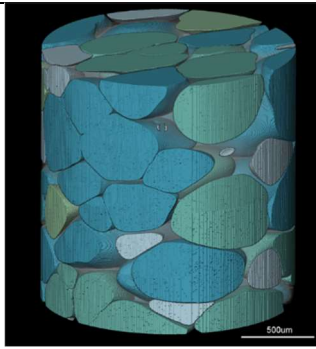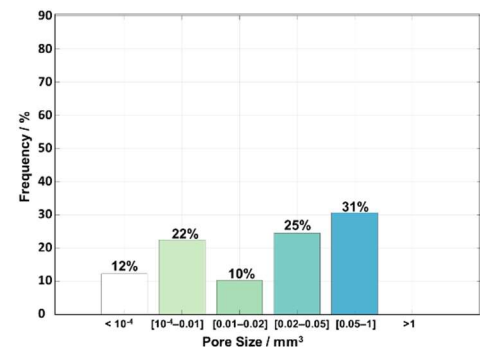
Table 6.2. Morphology parameters (volume fraction, pore size and porosity content) obtained from X-CT scans of foamed HDPE and composites of HDPE and MWCNTs.

Sample	Total Pore Volume / mm³	Total Foam Volume / mm³	Pore Volume Fraction / %	Mean Pore Size / mm³	Max Pore Size / mm³	Min Pore Size / mm³
HDPE_NC_B	3.33	0.95	77.74	0.83 (4)	1.90	0.004
HDPE+CBA$_3$_NC_B	3.20	1.09	74.68	0.05 (63)	3.09	$1.2 \cdot 10^{-6}$
HDPE+0.1wt%CNT+CBA$_3$_NC_B	2.76	1.53	64.24	0.02 (134)	2.48	$1.0 \cdot 10^{-6}$
HDPE+0.5wt%CNT_NC_B	2.43	1.85	56.76	0.13 (19)	2.41	$1.9 \cdot 10^{-6}$
HDPE+0.5wt%CNT+CBA$_3$_NC_B	3.46	0.84	80.54	0.10 (33)	3.21	$1.1 \cdot 10^{-6}$
HDPE+1wt%CNT+CBA$_3$_NC_B	3.39	0.89	79.12	0.07 (49)	0.50	$1.1 \cdot 10^{-6}$

The values summarised in Table 6.2 refer to:

- Total Pore Volume (i.e. the total volume of voids), a measure of the accessible cellular volume of each sample.

- Total Foam Volume (i.e. total volume of solid polymer), i.e. the remaining un-foamed volume of the material for each sample occupied by closed cells, cell walls and solid polymer.

- Pore Volume Fraction (i.e. percentage of porosity of the sample), given by the ratio between total pore volume and total volume of the material for each sample.

- Mean pore size which is the average pore size from the total number of pores represented in the dataset reported in brackets in the table for each sample.

- Maximum pore size which represents here a single large networked pore across the whole specimen. It should be taken into account that in the case of interconnected pore networks, the sample often effectively contains a single large interconnected pore in which measuring the typical size of the pore becomes problematic.

- Minimum pore size which represents here a pore only partially represented in the dataset.

From the 3D characterization of the foams pore texture, it emerged there was a highly interconnected pore system in all samples along with the presence of partial pores that are cropped out of the area considered. The quantification of the morphology of connected pores in highly porous materials is generally not an easy task and the difficulty is due to the fact that the phases are fully connected. Furthermore, given that an internal volume of the core foam layer was used, it is likely that the pore size information is strongly skewed towards both ends of their distributions.

The experimental variables used during the foaming process and the composition of the polymer formulation strongly affected the final network of pores and the pore size distribution observed from

the scans of each foamed sample. From a comparison of the two samples with the same composite formulation (i.e. MWCNT content of 0.5 wt%), *TRIAL 3* was again confirmed to be more effective than *TRIAL 2* in increasing the porosity of the volume of material considered. The fact that the unfilled HDPE foams had higher porosity when produced by *TRIAL 2* may simply be a consequence of the limitations of the measurement of the HDPE_NC_B sample (from *TRIAL 2*) containing only four pores in the dataset (see Figures 6.8 and 6.9). The very large pores of this sample meant that each pore was only partially represented in the volume of sample considered with the rest cut off from the area (Figure 6.8). This sample was shown to have the largest pore size (ultra-macropores of millimetre size) among all the foams produced in this work, an observation in agreement with the observations made from SEM imaging, see Figure 6.2(E-H) in section 6.1.1.

A number of larger datasets (e.g. 63 pores) allow a more accurate texture characterization of the expanded HDPE+CBA$_3$_NC_B sample (from *TRIAL 3*) for which a slightly lower porosity was found, although still as high as ca. 75%. It is evident from Figure 6.11 that the pores are mostly connected to create a single large pore network indicating a predominant open-cell structure for this foam with many cell walls that appeared to be damaged or not fully formed (see Figure 6.11(D)). The pore size distribution in the form of frequency expressed as a percentage (i.e. the number fraction of pores) against the volume size confirmed for this foam (Figure 6.13) the microscale size of the cell structure with most pores (55 % pore population) having dimensional volumes between 1×10^{-4} and 1×10^{-2} mm^3.

The addition of 0.1 wt% MWCNTs made it possible to significantly decrease the size of the cells (see cell distribution in Figure 6.16) while increasing the number of pores and therefore the cell density. This is also demonstrated by the fact that the same small total volume of material used for analysis (~ 4.28 mm^3) in this case was shown to contain 134 pores in the dataset, more than double the number for the previous case (sample HDPE+CBA$_3$_NC_B). From Figure 6.14, it can be seen that the cell walls separating the numerous small pores appeared to be reinforced by the MWCNTs acting as reinforcing elements for the microstructure.

The images obtained for HDPE+0.5wt%CNT_NC_B, Figure 6.17(A), show very large pores and walls with variable thickness across the sample slices. The fact that none of the pores is fully represented within the dataset and/ or the volume and cell walls are broken in some areas could be due in this case to damage during cutting the sample.

The highest porosity was obtained for MWCNT loadings of 0.5 wt% and 1 wt% for HDPE+0.5wt%CNT+CBA$_3$_NC_B and HDPE+1wt%CNT+CBA$_3$_NC_B produced from *TRIAL 3*, which have porosities of 80.54 % and 79.12 %, respectively. This further confirms the strong nucleating effect of the MWCNTs (also seen from the SEM image analysis), although the radiographs in Figure 6.20 revealed an irregular morphology with most of the cell walls ruptured for

the foam with 0.5 wt% MWCNTs (see Figure 6.20), a different morphology to that obtained for a MWCNT loading of 1 wt% (see Figure 6.23). In this latter case, the separation of the pores is well defined and cell walls appear reinforced. Moreover, the statistical pore size distribution obtained for the foam with the highest MWCNT content from a careful observation of Figure 6.25 showed a size distribution of the pores mostly in the size range of $[0.05 \text{ mm}^3- 1 \text{ mm}^3]$, with a large number fraction of macro-pores (frequency 31%) that contributed to the pore volume.

Overall, the use of X-Ray tomography in the observation of the cellular structures showed a continuous distribution in which small pores ($< 1 \times 10^{-4} \text{ mm}^3$) coexist with large pores ($> 1 \text{ mm}^3$). This behaviour is derived from the mechanism of foaming and in particular the competition between the rate of bubble nucleation and growth which determines the number and size of formed bubbles/cells. During foaming there is a competition between pore formation, pore annihilation and coalescence of pores. On the one hand, the presence of smaller bubbles can be explained by a higher nucleation rate, but the presence of macro-pores is associated with increased cell growth rate leading to the production of large bubbles and which, at the same time favours the coalescence of bubbles that have had much more time to grow [11].

It is clear that the average cell size (see mean pore size column in Table 6.2) decreased and the cell size distribution became narrower (indicating a more uniform cell size distribution) as the MWCNT content was increased from 0 wt% (sample HDPE+CBA$_3$_NC_B) to 0.01 wt% first (sample HDPE+0.1wt%CNT+CBA$_3$_NC_B) and then to 1 wt% (sample HDPE+1wt%CNT+CBA$_3$_NC_B). The average cell size obtained for sample HDPE+0.5wt%CNT_NC_B was somewhat bigger than those derived from addition of MWCNT content at 0.01 or 1 wt%. The increase in cell size increase may have been due to a low cell nucleation rate or a reduction in cell density. The rupturing of cell walls observed in the foam cores may be due to cells coming in contact with the mould surface and thus the skin layer tends to rupture [12]. This behaviour may also be a reflection of the reduced melt stability of the HDPE. A reduction in the elongational viscosity of HDPE can also result in significant rupture of cell walls during the expansion process which, subsequently, leads to pronounced cell coalescence. The influence of the molecular architecture of polymers on the resulting foam morphology is a well -known phenomenon [3]. Low melt viscosity polymers indeed favour fast nucleation and high rates of cell growth [13]. In case the polymer melt strength is high, the neighbouring cells may grow individually, whereas when it is low, the cell walls may disrupt due to an internal gas pressure and coalescence of cells occurs [14]. As the cells grow and the wall thickness decreases, the probability of coalescence between neighbouring cells increases. The lower the melt strength, the larger the cells generated [5]. HDPE has a high melt viscosity.

6.2 Density Measurements and Characterisation of foamed HDPE-MWCNT Composite parts: Calculation of Expansion Ratio, Void fraction and Density Reduction

In order to evaluate the performance and the potential cost-effectiveness of such novel foams, density reduction or weight reduction is still the dominant characteristic that must be controlled as density affects many properties, including acoustics, of the foams. It is well known that compared to dense polymers, cellular foams, especially when produced by means of PBAs, provide a substantial weight reduction. When aiming to produce foams with densities below 400 kg/m^3, the use of PBAs is practically the only alternative, also from an economic point of view [15]. Therefore, higher void fraction and density reductions than those achieved in samples prepared via chemical foaming in part II (chapter 5) are expected.

Three foamed (square cut) sample blocks, randomly selected from the many parts produced by each processing trial were tested by weighing each sample in air prior to immersion in the liquid (i.e. ethanol) and the arithmetic average values (from 3 replicates) of each sample are listed as measured density ρ_{foam} in Table 6.3. In addition, the effect of varying the processing parameters on the relative density of each specimen (i.e. ratio of the bulk density of the foamed composite, ρ_{foam}, and the measured bulk density of the un-foamed composite) (see Table 4.8, in chapter 4, $\rho_{unfoamed}$) was investigated by defining the void fraction, expansion ratio and density reduction obtained for each sample studied. No measurement percentage error (standard deviation) values are reported in the following table 6.3 as measurements resulted in errors of up to 0.05% which can be discarded.

Table 6.3. Values for density, expansion ratio, void fraction and density reduction obtained for foamed HDPE-MWCNT composites prepared by MIM.

	Sample	Measured Density ρ_{foam} /g cm^{-3}	Expansion Ratio $\dfrac{\rho_{polymer}}{\rho_{foam}}$	Void Fraction $1-(\dfrac{\rho_{foam}}{\rho_{polymer}})$ /%	Density Reduction /%
TRIAL 1	HDPE_UV_A	0.841	1.146	12.76	12.8
	HDPE_UV_B	0.790	1.220	18.05	18.0
TRIAL 2	HDPE_NC_A	0.543	1.775	43.67	43.7
	HDPE_NC_B	0.487	1.979	49.48	49.5
TRIAL 3	HDPE+CBA$_3$_NC_A	0.314	3.070	67.43	67.4
	HDPE+CBA$_3$_NC_B	**0.295**	**3.268**	69.40	**69.4**
TRIAL 1	HDPE+0.1wt%CNT_UV_A	0.876	1.100	9.13	9.1
	HDPE+0.1wt%CNT_UV_B	0.673	1.432	30.19	30.2
TRIAL 2	HDPE+0.1wt%CNT_NC_A	0.667	1.445	30.81	30.8
	HDPE+0.1wt%CNT_NC_B	0.639	1.509	33.71	33.7
TRIAL 3	HDPE+0.1wt%CNT+CBA$_3$_NC_A	0.453	2.128	53.01	53.0
	HDPE+0.1wt%CNT+CBA$_3$_NC_B	0.435	2.216	54.88	54.9
TRIAL 1	HDPE+0.5wt%CNT_UV_A	0.833	1.160	13.77	13.8
	HDPE+0.5wt%CNT_UV_B	0.745	1.297	22.88	22.9
TRIAL 2	HDPE+0.5wt%CNT_NC_A	0.642	1.505	33.54	33.5
	HDPE+0.5wt%CNT_NC_B	0.419	2.305	56.63	56.6
TRIAL 3	HDPE+0.5wt%CNT+CBA$_3$_NC_A	0.357	2.706	63.04	63.0
	HDPE+0.5wt%CNT+CBA$_3$_NC_B	0.323	2.991	66.56	66.6
TRIAL 1	HDPE+1wt%CNT_UV_A	0.705	1.373	27.17	27.2
	HDPE+1wt%CNT_UV_B	0.654	1.480	32.44	32.4
TRIAL 2	HDPE+1wt%CNT_NC_A	0.612	1.582	36.78	36.8
	HDPE+1wt%CNT_NC_B	0.502	1.928	48.14	48.1
TRIAL 3	HDPE+1wt%CNT+CBA$_3$_NC_A	0.457	2.118	52.79	52.8
	HDPE+1wt%CNT+CBA$_3$_NC_B	0.353	2.742	63.53	63.5

As is evident from values listed in Table 6.3, the use of SCF-CO_2 enabled the production of HDPE and HDPE-MWCNT composite foams with large weight reductions, higher expansion ratio and void fractions than those obtained via chemical foaming in previous (PART II) work and discussed in chapter 5. On average, an expansion ratio always > 1 and a void fraction > 36 % (i.e. highest value obtained from characterisation of foamed samples from previous work in PART II, see Table 5.10, chapter 5) was achieved in this study. The maximum expansion ratio of ca. 3.3, which is still classified this foam as a high-density foam (VER≤4), was obtained for HDPE+CBA$_3$_NC_B,

characterised by the highest void fraction (69.4 %) of all the samples produced by physically foaming.

The change of processing route from chemical to physical foaming was effective at increasing the void fraction in the samples, overcoming the major problems of high HDPE melt viscosity and stiffness. The MuCell aggregate system allowed the gas to overcome the attractive forces and entanglements and diffuse through the melt inducing foaming. The two different thicknesses of the surface of the mould with steps in plate thickness used in this study allowed for the production of two-layer plates, A and B, which led to different density values. As obvious from Table 6.3, samples cut from the thinner layer A (2 mm) was more dense than the samples cut from the thicker layers B (3 mm). The data reported in Table 6.3 also showed that by varying the approach to moulding these materials from under-volumetric (*TRIAL 1*) to negative compression moulding (*TRIALs 2* and *3*), differences in density along the flow path, in addition to the internal structure of the final microcellular was possible, see SEM images in section 6.1.2. In particular, lower reduction in density was attained in the samples made by filling the mould cavity in a sub-volumetric way, regardless of whether or not MWCNTs are added to the HDPE matrix, compared to the parts moulded by filling the cavity volumetrically in negative compression in which the dosage volume was varied. The significant reduction in density seen in foamed parts made using the latter process (see Table 6.3) is a consequence of the considerable gaseous phase developed within these structures and confirms that the tool with a decompression opening offers a critical advantage when a greater weight reduction is required compared to conventional moulds.

The MWCNTs clearly play a major role in determining the foamability of the polymer in addition to promoting the nucleation of cells and different foam morphology [16]. While the addition of 0.1 wt% MWCNTs resulted in a very small increase in the density of the foamed composites compared to the unfilled polymer, the trend in ρ_{foam} (Table 6.3) is in agreement with the theoretical predictions for microcellular foams, i.e. microcellular foaming processes lead to a reduction in the bulk density of microcellular composites by increasing size of the gas phase in the samples [17]. A decrease in the density of microcellular composites was in fact obtained with increasing MWCNT content (≤1 wt%) as the presence of the MWCNTs promoted the accumulation of gas at the polymer–particle interface [16, 18]. The higher foam expansion ratio in the composites resulted from some uptake of gas absorption which provided more heterogeneous nucleating sites. In equal measure, the MWCNT content and extent of dispersion resulted in an increase in the volume expansion ratio. In particular, of the three MWCNT loadings investigated in the MuCell trials, the use of 0.5 and 1 wt% MWCNTs proved to have a beneficial effect on the volume expansion ratio of the polymer. Of the composites, HDPE+0.5wt%CNT+CBA$_3$_NC_B had the highest foam expansion

ratio (ca. 3) and density reduction (66.6 %), followed by HDPE+1wt%CNT+CBA$_3$_NC_B (ρ_{foam}= 0.35 g cm^3, VER= 2.74, void fraction = 63.5%).

The density measurements performed on foamed parts prepared during *Trial 3*, confirmed that the use of an additional chemical blowing agent (CBA$_3$) in combination with the PBA helped to lower the density even further. As can be seen from the results reported in Table 6.3 for both unfilled and MWCNT filled HDPE foams, higher values of foam expansion ratio and void fraction were obtained when adding 1wt% CBA$_3$ to the system to assist foaming. The extra amount of CO$_2$ liberated from the decomposition of this CBA during moulding assisted with the formation of an appreciable fraction of voids inside the foamed structures and had a pronounced benefit on the volume expansion ratios of both unfilled and MWCNT filled HDPE foams.

6.3 Mechanical Compression Properties of foamed HDPE-MWCNT composites parts

In order to investigate the processing-structure-mechanical property performances of the IM foamed parts produced in this work, mechanical compression testing was conducted on the various foamed sample parts. The final morphology of the foams decisively affects their mechanical properties, which are significantly influenced by the integral foam structure inside the component [19]. How structural foams perform mechanically critically depends on the thickness of the skin layers as well as on the cell size distribution in the core [3]. Previous research has suggested that not only has the three-layer structure a significant effect on mechanical properties, but also that the mechanical properties of foamed composites are improved by fine bubbles [4]. In IM structural foams, the cell size distribution usually varies across the part thickness. In particular, in close proximity to the compact layers, the average cell size is rather small but increases steadily towards the centre of the part [3]. As a result, the compact skin layers dominate the mechanical behaviour, although the mechanical performance of the foam core critically affects the final properties depending on the density of the foam as well as the actual size and size distribution of the cells [12, 20].

Variations in the microstructure and cell wall properties of foams gives rise to variability in the mechanical properties. The micro-structures of most cellular solids are typically disordered and contain imperfections (e.g. wavy distortions of cell walls, variations in cell wall thickness, non-uniform cell shape, etc.) which affect the mechanical properties such as the stiffness of these solid foams [21]. Although the variations of cell shape and cell wall thickness do not impact remarkably the stiffness of cellular solids, the density is a determining factor. How the stiffness improves with density depends on cell morphology, and in particular on how cell walls or struts deform when the cell solid is deformed [21]. Especially with high weight reductions, the reduction of density leads to decreasing mechanical properties, which is why thermoplastic foamed parts are usually produced with a weight reduction of 8-15 % [19].

A minimum of five foamed specimens (27mm × 27mm square cut sample blocks) were tested under compression when applying a maximum force of 9000 N (<10,000 N which is the max value allowed by the machine). The test stopped once the max force of 9000 N was reached and the rupture point was never attained. The test allowed for the calculation of Young`s modulus in compression (elastic modulus), yield stress (compression strength) and compression at yield (strain at compression strength) derived from stress-strain curves. The average (from 5 replicates) values for the Young's modulus in compression and compression strength for the foamed composites are listed in Table 6.6. Additionally, the variation in the mechanical properties, under compression, of the foams tested can be seen in the representative stress-strain curves shown in Figure 6.26.
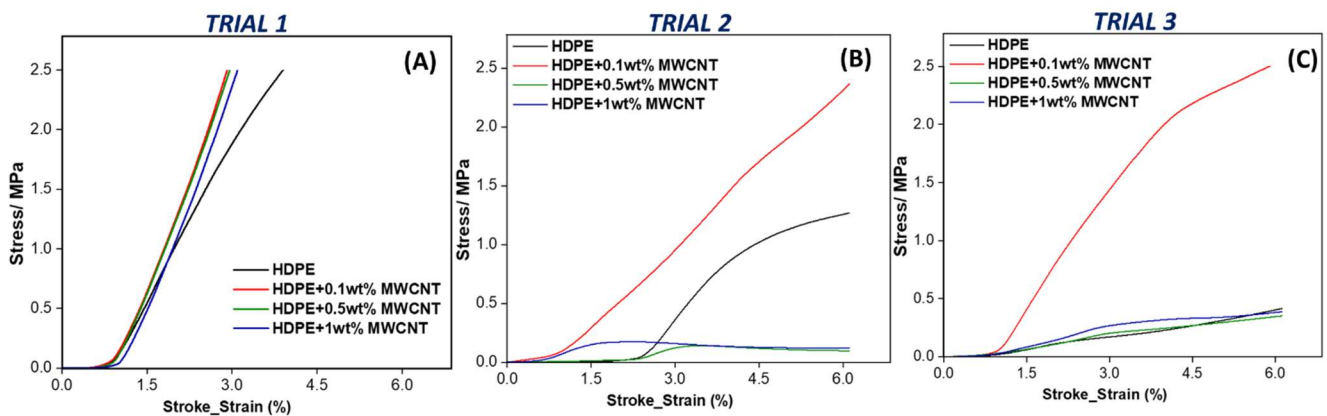
Figure 6.26. Variation of stress as function of strain for foamed parts prepared with Mucell technology by using the different moulding conditions of: (A) *TRIAL 1*; (B) *TRIAL 2*; (C) *TRIAL 3*.

The curves in Figure 6.26 reveal the different deformation behaviour of the various foamed samples under applied stress. Foam specimens tested in compression showed a relatively abrupt change in the initial slope of the loading curve following an initial plateau region (pre-loading region), after which the stress begins to increase. From the relationship of the stress and the strain of foamed HDPE and HDPE-MWCNT composites, it is evident that foams produced from *TRIAL 1* showed a different behaviour from the rest of the samples with only one region in the stress-strain curve of samples (see Figure 6.26(A)). In this case, the materials are in a non-linear elastic phase, namely the region where the stress increases with the increasing strain from the original state but none of the samples tested reached a yield point in which the stress would have been almost unchanged with the increasing strain as a result of large permanent changes in the original state with no extra load force. Similar behaviour was observed in our previous work with chemical foaming.

A totally different trend can be seen this time in figures 6.26(B-C), as a result of the increased porosity developed in the foamed parts when moulding in negative compression trials. The stress-strain curves overall indicate samples that showed much larger deformation (higher strains) at much lower stress than foams from *TRIAL 1*. The lower the foam density and the more inhomogeneous the cellular morphology, the higher is the probability that early failure of the material occurs at low

stresses [3]. Despite the part weight reduction, microcellular IM parts produced through MIM typically exhibit mechanical properties that are inferior to that of solid injection moulded parts (e.g. loss of ductility and toughness in the material) which is one of the common problems associated with polymer foams due to the generation of the cells [1]. As a result of the stresses applied during the compression test, the pore structure was significantly deformed even at low stresses. The compression stress is much lower in foams with open cells than in foams with closed cells [22]. This can be explained by the presence of air included in closed cells, which significantly influences the measured compression stresses and strains. Despite not all the foams reaching a breaking point or a yielding stage in which the pore structure was completely destroyed, residual irreversible strains are observed after unloading of curves in the plots (B-C). As the obtained foam structures are not in a microcellular range (not < 10 μm), the foam morphology acts as a defect in the part and as a stress concentrator increasing the brittleness of these integral foams, hence sacrificing severely their toughness [3].

Table 6.4. Changes in compression mechanical properties of foamed HDPE and HDPE-MWCNT composites prepared with Mucell technology at different moulding conditions.

	Sample	Young`s Modulus in Compression /MPa	Compression Strength /MPa	Strain at Compression Strength /%
TRIAL 1	HDPE_UV_A	69.01 ± 4.36	3.83 ± 0.00	5.37 ± 0.39
	HDPE_UV_B	83.63 ± 2.59	3.82 ± 0.00	4.42 ± 0.65
TRIAL 2	HDPE_NC_A	81.74 ± 3.31	1.64 ± 0.06	6.11 ± 0.00
	HDPE_NC_B	59.14 ± 3.40	1.30 ± 0.02	6.11 ± 0.01
TRIAL 3	HDPE+CBA$_3$_NC_A	23.92 ± 2.58	0.48 ± 0.00	6.11 ± 0.00
	HDPE+CBA$_3$_NC_B	9.61 ± 0.27	0.40 ± 0.02	6.11 ± 0.01
TRIAL 1	HDPE+0.1wt%CNT_UV_A	96.50 ± 2.59	3.83 ± 0.00	4.07 ± 0.00
	HDPE+0.1wt%CNT_UV_B	97.28 ± 4.64	3.83 ± 0.01	3.72 ± 0.09
TRIAL 2	HDPE+0.1wt%CNT_NC_A	87.49 ± 2.20	2.85 ± 0.01	6.11 ± 0.00
	HDPE+0.1wt%CNT_NC_B	43.03 ± 0.15	1.83 ± 0.76	6.11 ± 0.01
TRIAL 3	HDPE+0.1wt%CNT+CBA$_3$_NC_A	40.42 ± 7.41	1.68 ± 0.20	6.11 ± 0.00
	HDPE+0.1wt%CNT+CBA$_3$_NC_B	74.47 ± 7.75	2.25 ± 0.26	6.11 ± 0.01
TRIAL 1	HDPE+0.5wt%CNT_UV_A	109.76 ± 8.26	3.83 ± 0.00	4.38 ± 0.21
	HDPE+0.5wt%CNT_UV_B	105.98 ± 4.99	3.83 ± 0.01	3.38 ± 0.09
TRIAL 2	HDPE+0.5wt%CNT_NC_A	3.28 ± 0.52	0.03 ± 0.00	4.42 ± 1.95
	HDPE+0.5wt%CNT_NC_B	9.09 ± 1.49	0.12 ± 0.04	4.32 ± 1.55
TRIAL 3	HDPE+0.5wt%CNT+CBA$_3$_NC_A	1.25 ± 0.24	0.12 ± 0.02	5.69 ± 0.57
	HDPE+0.5wt%CNT+CBA$_3$_NC_B	2.21 ± 0.96	0.30 ± 0.08	6.11 ± 0.00
TRIAL 1	HDPE+1wt%CNT_UV_A	99.12 ± 0.25	3.83 ± 0.00	4.50 ± 0.01
	HDPE+1wt%CNT_UV_B	97.81 ± 4.96	3.83 ± 0.01	4.02 ± 0.03

TRIAL 2	HDPE+1wt%CNT_NC_A	3.04 ± 1.72	0.14 ± 0.05	3.62 ± 0.53
	HDPE+1wt%CNT_NC_B	5.09 ± 0.98	0.16 ± 0.20	4.20 ± 2.70
TRIAL 3	HDPE+1wt%CNT+CBA$_3$_NC_A	1.75 ± 1.50	0.13 ± 0.03	5.53 ± 1.00
	HDPE+1wt%CNT+CBA$_3$_NC_B	11.09 ± 1.50	0.38 ± 0.07	6.11 ± 0.00

From the mechanical properties listed in Table 6.4, it is evident that foaming of HDPE and HDPE-MWCNT composite using *TRIAL 1* did not result in a significant decrease in mechanical properties when compared with the foamed counterparts from Trials 2 and 3. In this case, the restoration of the deformation is nearly complete and only some negligible plastic deformation remains after unloading. Obviously, the still intact cells that are only deformed elastically are able to restore most of the deformation strain during unloading due to the mainly elastic deformation of struts by bending. The principal mechanism of linear-elastic deformation for foams was identified as cell wall bending [23].

The higher weight reductions and the porosity distribution of foams produced by trials 2 and 3 greatly lowered the compressive strength. The strength of materials, which is determined by the failure at their weakest point, in structural foams, is lowest in the cellular core region [3]. Therefore, foams with increased porosity displayed a decreased compressive strength. Both the modulus and the collapse stress (i.e. compressive strength) obtained for the cellular foams displayed in Table 6.4 are density dependent. In particular, the elastic moduli are related principally to the bending stiffness of the cellular structure (comprising the cell walls), which is related to the mechanical properties of the polymer material from which the cell struts are made, whereas the collapse is caused by the buckling of the cellular structure and therefore by the deformation mechanics of the cellular structure itself [23].

The presence of a filler phase in the host matrix was shown to influence the modulus of the foams. The modulus of the composite structures typically depends on the filler fraction and its modulus relative to that of the host matrix. While all the MWCNT contents employed in this study increased the Young`s moduli of the polymer foams produced from *TRIAL 1*, with the highest increase found for a MWCNT content of 0.5 wt%, the rest of the foams showed a beneficial effect in increasing overall the modulus only after additions of 0.1wt% (see *TRIALs* 2 and 3 in the first column of Table 6.4). Albeit with increasing amounts of filler, the modulus is expected to continue to increase relative to that of the unfilled foam caused by the reinforcing effect of the MWCNTs with high mechanical strength [4], additions ≥ 0.5 wt. % of MWCNT had no measurable effect on the modulus of the foam.

The effectiveness of the nucleating sites offered by the MWCNTs was predominant only in the composite foams, HDPE+0.1wt%CNT_NC and HDPE+0.1wt%CNT+CBA$_3$_NC, for which the improved compression modulus, strength and strain at compression strength (see red rectangle in Table 6.4) can be attributed to the decrease in cell size and increased cell density derived by the

MWCNTs nucleating as well as the high degree of MWCNT dispersion within the polymer. The corresponding trend shown graphically by the red curves in figures 6.26(B-C) confirmed that a 0.1 wt% MWCNT content or higher enhances the mechanical properties of the HDPE, preserving the destruction of the cells.

On examining this data, it can be seen that the trend obtained for the mechanical properties in compression is consistent with the observations made in previous sections, and can be attributed to the different degrees of foaming developed within each sample.

In order to limit the often encountered reduction in mechanical performance for a given mould technology, significant efforts has been directed towards obtaining structural injection moulded foams with a uniform cellular structure and a small average cell size even at low densities. In this work, significant advantages could be expected by adjusting the processing conditions as well as optimising the material rheological properties.

6.4 Acoustic Properties of foamed HDPE-MWCNT Composite parts

The acoustic properties of the unfilled and filled polymer foamed parts produced by physical blowing were evaluated via transmission of acoustic energy in water and across the sample, i.e. square cut sample blocks (27mm×27mm). Measurements were performed by comparing ultrasonic pulse transmissions in the time domain through each sample to the transmission in water without a sample present. A minimum of two specimens for each foam type were tested and the results are summarised in Table 6.5, which lists the ultrasonic velocities (longitudinal) and attenuation coefficients of ultrasound at 1 MHz, estimated based on the time shift measured between the reference and the measured signal in each sample (ToF technique) as a function of the sample thickness. No measurement percentage error (standard deviation) values are reported in the following tables 6.5 as using only two measurements resulted in errors of up to 0.05% which can be discarded.

The acoustic impedance was determined, a key factor of this project, by multiplying the measured densities of the foams (from Table 6.3) with the ultrasound velocity estimated for each sample. Additionally, a direct comparison of the acoustic properties of the foamed materials produced in this work with the benchmark materials (acquired instead by frequency-domain analysis measurements through ultrasonic pulse transmission in air) are made by comparing the data in Table 6.5 with Table 6.6.

Table 6.5. Acoustic properties obtained in water transmission for foamed HDPE and HDPE-MWCNT composite prepared by MIM.

Sample		Velocity of sound c /m s^{-1}	Measured Density ρ_{foam} /g cm^{-3}	Acoustic Impedence $Z = c \cdot \rho_{foam}$ /MRayl	Attenuation @ 1 MHz /Np m^{-1}
TRIAL 1	HDPE_UV_A	2066.86	0.841	1.74	1517.21
	HDPE_UV_B	1387.86	0.790	1.10	951.45
TRIAL 2	HDPE_NC_A	2244.94	0.543	1.22	381.56
	HDPE_NC_B	2119.55	0.487	1.03	450.66
TRIAL 3	HDPE+CBA$_3$_NC_A	**1247.36**	0.314	**0.39**	78.58
	HDPE+CBA$_3$_NC_B	**1179.90**	0.295	**0.35**	63.19
TRIAL 1	HDPE+0.1wt%CNT_UV_A	2120.39	0.876	1.86	549.52
	HDPE+0.1wt%CNT_UV_B	2218.97	0.673	1.49	365.69
TRIAL 2	HDPE+0.1wt%CNT_NC_A	2053.19	0.667	1.37	269.76
	HDPE+0.1wt%CNT_NC_B	2113.70	0.639	1.35	336.77
TRIAL 3	HDPE+0.1wt%CNT+CBA$_3$_NC_A	1557.59	0.453	0.70	120.94
	HDPE+0.1wt%CNT+CBA$_3$_NC_B	1467.46	0.435	**0.64**	74.71
TRIAL 1	HDPE+0.5wt%CNT_UV_A	1526.86	0.833	1.27	841.45
	HDPE+0.5wt%CNT_UV_B	1876.35	0.745	1.40	476.13
TRIAL 2	HDPE+0.5wt%CNT_NC_A	1942.43	0.642	1.25	602.55
	HDPE+0.5wt%CNT_NC_B	2058.98	0.419	0.86	142.92
TRIAL 3	HDPE+0.5wt%CNT+CBA$_3$_NC_A	1761.93	0.357	0.63	159.08
	HDPE+0.5wt%CNT+CBA$_3$_NC_B	1781.13	0.323	**0.57**	146.78
TRIAL 1	HDPE+1wt%CNT_UV_A	1816.61	0.705	1.28	1387.40
	HDPE+1wt%CNT_UV_B	1801.05	0.654	1.18	690.52
TRIAL 2	HDPE+1wt%CNT_NC_A	NA	0.612	NA	NA
	HDPE+1wt%CNT_NC_B	NA	0.502	NA	NA
TRIAL 3	HDPE+1wt%CNT+CBA$_3$_NC_A	NA	0.457	NA	NA
	HDPE+1wt%CNT+CBA$_3$_NC_B	NA	0.353	NA	NA

From the analysis of the acoustic properties, it emerged that the acoustic impedance was reduced by the one order of magnitude (<1 MRayl) necessary to ensure a significant improvement in sensor performance, confirming the high porosity achieved in such foams. Clearly, not all the samples listed in Table 6.5 have an appropriate acoustic impedance to make them useful candidates for matching layers in air-coupled ultrasonic sensors. For example, samples produced from under-volumetric moulding had acoustic impedances all above 1 MHz. On the other hand, the expanded parts moulded

by volumetrically filling the cavity under negative compression (*TRIALs 2* and *3*) displayed significant lower values of *c* following the introduction of a higher level of porosity (up to 80% as shown in Table 6.2) which has greatly expanded the range of acoustic properties of such materials. The required degree of porosity developed in these latter samples resulted in a low speed of sound and a low bulk density, when combined gives a low value of acoustic impedance.

In general, the lower values of ultrasound speed seen in samples foamed physically rather than chemically can be associated with the larger proportion of gas evolved inside the melt during manufacture. This explains why the highest gas content developed during *TRIAL 3* yielded the lowest values of *c* overall.

However, large porosity does not always favour a low speed of sound. If the pores are too large, ultrasonic waves simply travel through the foam without dissipating the acoustic energy efficiently. The characteristic porosity for an efficient acoustic absorber (directly related to the Knudsen numbers and flow regime in a porous solid) have been highlighted in chapter 2. As a rule of thumb, the wavelength (λ) must exceed the pore size at least by a factor of 10^3. Although an acoustic absorber must have an acceptable range of porosity that allows sound waves to penetrate far enough into the structure, the porosity must be neither too fine nor too coarse [24]. In fact, if the porosity is too coarse, sound waves that encounter a multitude of large pores pass through them penetrating into the foam but with minimal interaction/internal reflections with the structure [a].

Samples with coarse porosity, such as HDPE_NC_A, are not useful materials for matching layers in acoustic sensors as it is not possible to reduce the speed of sound and therefore the impedance, although very effective in reducing density (> 40%).

The presence of MWCNTs influenced the acoustic properties of the foams by slightly improving sound absorbing properties in the composite samples where the speed of sound was lowered compared to the neat polymer foam (e.g. HDPE+0.1wt%CNT_NC, HDPE+0.5wt%CNT_NC). However, it should be noted that the combination of a MWCNT content of 1 wt% with the negative compression moulding method (*TRIALs 2* and *3*) produced highly inhomogeneous parts which hindered measurement of certain acoustic parameters (velocity and attenuation). The *NA* values reported in Table 6.5 refer in fact to those cases in which the ultrasonic measurement was too noisy and compromised the measurement with an error so significant as to not make it reliable. The difficulty of evaluating some effective properties for these samples is directly related to their internal structure, very inhomogeneous and different throughout the bulk material. Regarding the latter, it is important to note that the use of water as coupling medium between the two transducers and the sample for water immersion measurements (i.e. transmission of ultrasonic pulses in water using the

---

[a] In contrast, a porosity that is too fine would allow most of the energy to be reflected back from the outer surface into the environment without ever entering the material deep enough to allow for multiple interactions with the structure.

pulse–echo technique) can result in an invasive test for open-cell foams (i.e. foamed samples with a large amount of open pores). In this case, since water can easily penetrate the open pores, it may cause permanent damage and/or undesired contamination to the cellular structure of the samples which could adversely affect the final properties of the materials. Nonetheless, sample HDPE+CBA$_3$_NC_B (porosity~75%) showed the lowest value of the speed of sound (1179.90 m/s), followed by HDPE+CBA$_3$_NC_A (1247.36 m/s) that is the same composite materials but cut from the thinner layer A of the moulded plate. It is important to emphasise again that the acoustic energy transmission through the matching layer in air-coupled ultrasonic sensors is at its maximum if the ML has an acoustic impedance which is the geometric mean of the acoustic impedances of the piezoelectric material and air ($Z_{ML}=(Z_{AIR} \cdot Z_{PIEZO})^{0.5}$~0.1 MRayl). For the foams produced in *TRIAL 3*, the acoustic impedance was lowered to below 0.4 MRayl for unfilled HDPE foams and to a minimum of 0.57 MRayl for the HDPE-MWCNT composite foams filled with 0.5 wt% MWCNTs, making these foams suitable for the targeted application and comparable (if not better) than the benchmarking samples, currently used as matching layers in industry, see Table 6.6.

Table 6.6. Acoustic properties obtained in air transmission for foamed benchmark samples.

Benchmark Sample	Velocity of sound c /m s^{-1}	Measured Density ρ_{foam} /g cm^{-3}	Acoustic Impedence $Z = c \cdot \rho_{foam}$ /MRayl	Attenuation @Resonance Frequency /Np m^{-1}
Syntactic Foam	2486.65	0.714	1.78	41.30 @ 0.80 MHz
ML-Trelleborg	1303.56	0.320	0.42	33.95 @ 0.90 MHz
Commercial ML	2188.60	0.441	0.97	21.99 @ 0.68 MHz

Unlike the syntactic foams which could be replaced in the sensors by the foamed composites produced by chemical foaming (PART II, chapter 5), the physical foaming method was required to produce highly foamed parts capable of achieving similar acoustic impedances to the corresponding commercial layers, *ML-Trelleborg* and *Commercial ML*, used in the sensor industry.

Clearly, how the materials behave inside the sensor construct is unknown at this stage. Other different factors will play a role in the final application where beam spread and dispersion of the acoustic energy will be inevitable. Material properties such as density, tortuosity, and porosity tackled in this work are certainly key features in impacting the absorption performance of a foam. However, there are additional features including the final thickness, the presence of layers, the geometrical accuracy and the surface of the product, which also contribute to the absorption of sound. In particular, any increase in density, thickness, porosity, and air flow at higher frequencies results in increased levels of absorption performance [25]. A suitable material with low attenuation

can still result in multiple reflections within the sensor and consequently a reduction of the signal-to-noise ratio and result in an impedance mismatch [26].

Furthermore, the nominal frequency at which the sensors work is crucial as it has a significant effect on sound dispersion and attenuation (i.e. frequency sound dependent behaviour). Reflection and attenuation of sound on the propagation route vary at various frequencies [24, 26]. This explains why the attenuation coefficients reported in the last column of Table 6.5, which refer to the loss of acoustic energy as the wave travels through the material in this case at the frequency of 1 MHz, are higher than the attenuation of the resonant frequency of each sample tested (all frequencies <1 MHz). Nevertheless, these values will be expected to be lowered at the lower value of nominal frequency of 200 KHz for the specific application of *Elster`s New Generation Ultrasonic Transducers*, as the attenuation coefficient varies linearly with frequency in these materials.

6.5 Implementation of candidate foams as ML in Sensor Assembly and Material Response

A non-destructive ultrasound testing method using an optical microphone was conducted at Honeywell`s facility of Mainz, Germany, to complete a preliminary feasibility of the most promising candidate ML materials developed in this EngD work (i.e. HDPE+CBA$_3$_NC_B, produced by MIM *TRIAL 3*) inside a new air-coupled ultrasonic transducer design. Details of the measurements performed in air and the 3D stage system setup employed so as to evaluate the output power of the new transducer, thus its effectiveness, can be found in the APPENDIX section (PART I).

Firstly, in order to meet the size specifications of MLs in the designed application, a number of small disks of 10mm diameter x 3mm thickness were cut from the inner core porous thick layer B of the selected moulded sample plate and only the discs with the best surface quality were considered for inclusion in the sensor construct. The fabrication of the new sensor (made by the industrial sponsor) took place by assembling gradually each component of the transducer to incorporate the polymer foams of HDPE identified as potential MLs. It should be noted that all interfaces within the sensor construct must have extremely good shear bonding for the acoustics to work properly [b]. For this reason, although an attempt was made to fabricating sensors incorporating HDPE-MWCNT composite foams produced by MIM *TRIAL 3*, the roughness and inhomogeneity encountered in most porous surfaces of such composite samples after the cutting step to produce the small discs were problematic.

The final selected (suitable) candidate ML disc was fully immersed in glue prior being attached to the piezoelectric layer and the rest of the sensor components as displayed in Figure 6.27.

---

[b] The bonding of a piezo-ceramic to another material influences its oscillation, as it decreases the maximum amplitude and shifts the resonance frequencies to higher values while decreasing resonance amplitude.
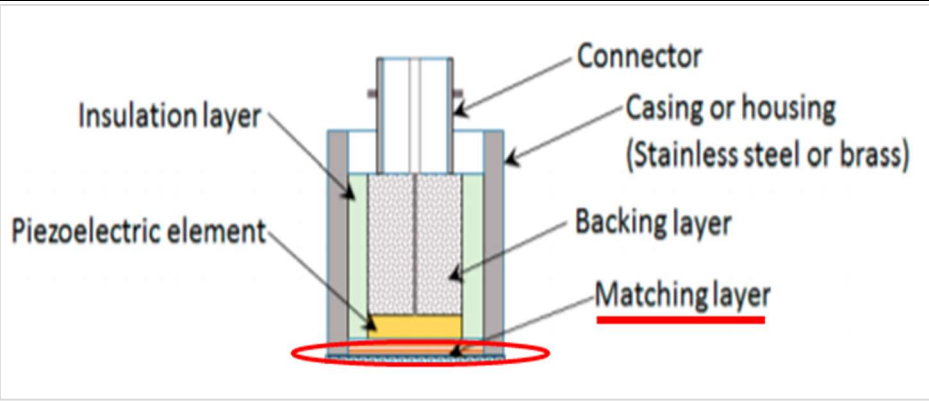
Figure 6.27. Schematic diagram of the cross-section of the piezoelectric ultrasonic transducer showing the various components, including the final candidate ML disc.

After completing the assembly of all components into the sensor, the sound field emission of the new air-coupled transducer was recorded by means of two-dimensional measurements performed in air with the optical microphone placed at a minimum distance (few mm) from the transducer. The characterization of the sound field generated by a transducer is a prerequisite for understanding acoustic signals emanating from it.

The sound field obtained from the measurements (i.e. a 2D plot of the energy emission resulted from the new sensor built with the sample HDPE+CBA$_3$_NC_B disc as ML) is shown in Figure 6.28.
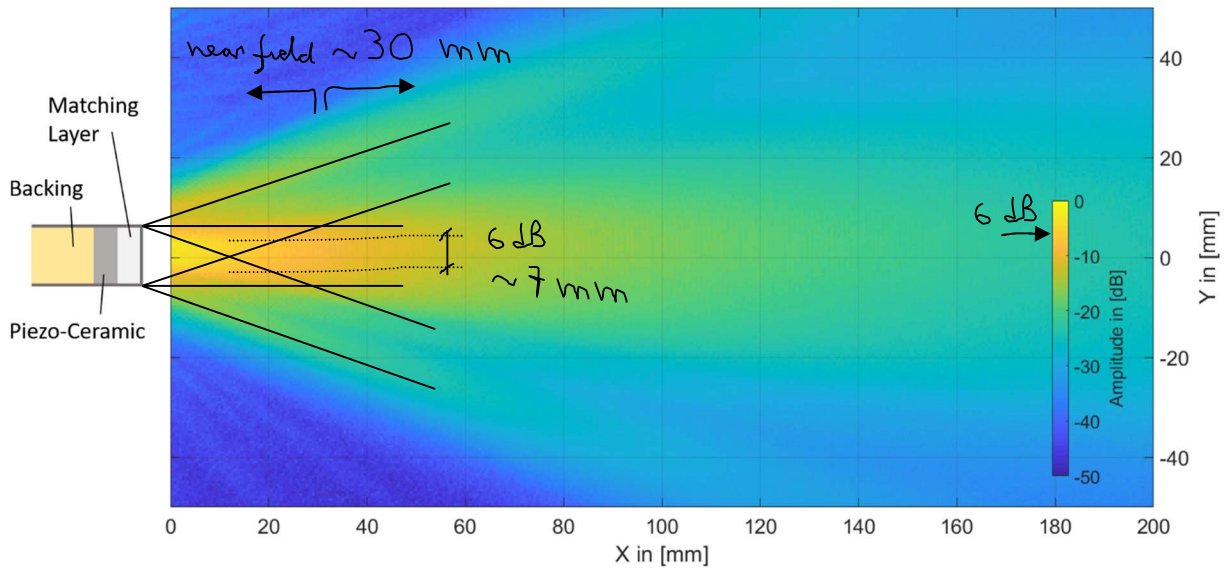
Figure 6.28. 2D sound field emission shape of the piezo-ceramic transducer assembled on the ML sample HDPE+CBA$_3$_NC_B. The axes XY indicate the respective distance to the centre of the transducer surface.

The intensity of the sound waves is indicated by colour, with lighter colours indicating higher intensity in the sound fields. The relative change in signal amplitude is commonly measured in decibels, namely the logarithmic value of the ratio of two signal amplitudes. The differences in the diameter of the sound beam visible in the plot are due to attenuation of the acoustic signals. The fact that the beam spread occurred and diverging fields are present in Figure 6.28 is the consequence of a partial transfer of acoustic energy in the direction of wave propagation due to reflections from

the lateral sides of the test object or other features outside the inspection area. The energy in the ultrasonic beam spreads out as it propagates through air to reach the microphone, resulting in a sensor energy output significantly reduced. Interpreting the signals in presence of beam spread can be difficult since it lowers the amplitude of sound signals making the sound field appearance less concentrated (weak). Since the ultrasound originates from a number of points along the transducer face, the ultrasound intensity along the beam is affected by constructive and destructive wave interference. The strongest reflections are likely to come from the area directly in front of the transducer, predominantly caused by attenuation of the signals in air or imperfections in the ML. The energy travelling in the wave direction of propagation is decreased by part of the wave sent in other directions. Most likely beam spread was caused by a problem of diffraction at the sensor aperture rather than a problem with the porosity of the ML material. The average pore size for this foamed sample was found to be around 60 μm (see previous sections 6.1.1 and 6.1.2) which is much smaller than the wavelength ($\lambda = \frac{c}{f} = \frac{1179.90 \text{m/s}}{200 \text{ KHz}} \approx 6\text{mm}$). Therefore, the size of the pores of the foamed ML sample is not the obstacle behind the partial transfer of acoustic energy. The vibrating particles of the ML material (through which the acoustic waves travel) are, in this case, able to transfer all their energy as confirmed by the low value of Z= 0.39 MRayl for this foamed sample (see Table 6.5), since the lower the acoustic impedance, the lower is the opposition to displacement of its particles by sound. Beam spread is largely determined by transducer diameter and centre frequency. When using a low frequency transducer such in this case (nominal frequency of 200 KHz), beam spread is greater than when using a high frequency transducer.

Nonetheless, a focusing effect can still be observed in Figure 6.28 [(c)]. The two side lobes emerged from the test (at about -10 dB below the central beam) are commonly also observed in an ideal piston transducer (ideal case of a flat transducer with max intensity of the amplitude at the focal zone of -6dB). Numerical comparisons should be made to evaluate how much the experimental beam diameter at the focal point (-6dB) differs from the ideal beam diameter at the focal point (-6dB). The quantified difference between magnitudes and measured sound fields from these measurements with expected theoretical values from conventional commercial matching layers of *Elster`s New Generation Ultrasonic Transducers* has not been confirmed by Honeywell yet. Likewise, additional data on the new sensors fabricated (e.g. sensitivity, natural focal point of *Elster`s New Generation Ultrasonic Transducers*, location of the transition from near to far field, output power of the new transducer) was not provided by Honeywell at this initial testing phase, but closing phase of the EngD project. The microphone was not fully calibrated as it is time and cost consuming at this early

---

[(c)] The focusing effect of a transducer is created by constructive interference of sound waves in air as a result of an increased efficiency of air-coupled ultrasound generation.

stage of development. It will be calibrated in the future and then the sensitivity values could be obtained from the measurements.

The sound field presented here is simply intended as proof of concept to validate the possibility that foams such as HDPE+CBA$_3$_NC_B produced by physical foaming have potential as MLs for air-coupled ultrasonic transducers. Normally, when testing the performance of a sensor, multiple measurements are carried out to increase the accuracy of the measurements but, in the present case, limited measurements were performed which, as a result, makes the uncertainty of these measurements very high, possibly as high as ± 50%. Although systematic errors will prevail most of the times, repeating measurements and averaging results can reduce statistical errors to negligible levels. In each measurement, every component involved in the signal flow process may alter the signal through inner and outer disturbances which can change over time. The use of models and statistical methods would greatly help to estimate the actual transmission through the ML material while performing error analysis, based on all accessible information.

The data obtained will be used as a basis for a following investigation of the sound fields with optimised material geometries. Overall, there are no significant asymmetries in the sound field, meaning that the ML is predominantly a homogeneous material and well bonded to the other components in the sensor. Measurements of the relative change in signal amplitude can be used in measuring the attenuation of the sound waves in a material as an indicator sample homogeneity. Nevertheless, an optimised homogeneity of the ML thickness is still needed and any additional post-processing steps (e.g. foam cutting to achieve the desired thickness of the target product) must be avoided. In this case, the post-processing cutting of the sample discs from the foamed sample plate may also have contributed to the performance of the sensor response, by causing possible tearing and collapse of individual pores in the foam which resulted in poor surface quality of the disc sample.

6.6 Concluding Remarks

The primary purpose of this study was to produce foams prepared using a physical blowing process based on MuCell technology (MIM), to increase the porosity of such novel composite foams in order to enhance their acoustic properties and examine their potential to act as passive layers in acoustic sensors. Compared to conventional moulding, the production of plastic injection moulded components produced by MIM results in an average cost reduction of 10% to 25 %. The microcellular foam process fundamentally changes the ultimate cost structure of injection moulded parts, providing significant economical benefits derived by four main sources. Operating costs are reduced through cycle time reductions of up to 50% as well as material costs through density reduction of the final products. The advantage of the purchase of fewer machines and mould tools

impacts and lowers the capital costs through. Finally, the ability to mold dimensionally improved thermoplastic parts may eliminate the extra costs involved in post-mould processes.

The use of MIM in this work enabled the production of HDPE and HDPE-MWCNT composites with a foamed core and a compact surface layer. Moulding parameters, thickness of the mould part and the amount of foaming agent played a critical role in determining the final degree of foaming achieved. The choice of the polymer has a big impact on the morphology and the properties of the foams obtained by MIM, in addition to the selection of the mould tool and processing parameters employed [3]. The high melt viscosity of HDPE was found to be the major obstacle encountered during chemical foaming of HDPE. Conversely, here the use of a fluid in the supercritical state (i.e. SCF-CO_2) greatly enabled a reduction in the melt viscosity of the HDPE which allowed cells to nucleate and expand.

A preliminary material screening was completed, assessing reductions in density, acoustic properties and morphology of the moulded samples produced by varying processing conditions and MWCNT loading (0.1%, 0.5% and 1%, by weight). The use of a special mould tool (with steps in plate thickness) and adopting a negative compression moulding process was effective in the production of HDPE and HDPE-MWCNT composite foams with very high porosity (> 80%), high cell densities (order of 10^6 cells/cm^3) and the target expansion ratios (> 3 %), especially when prepared using *TRIAL 3*. Density measurements performed on foamed parts prepared with *TRIAL 3*, confirmed that the use of an additional chemical blowing agent (1 wt % CBA_3) in combination with the PBA lowered the density of the foam even further for both unfilled and MWCNT filled HDPE foams. The thicker plate layer (B) provided sufficient room for foaming resulting in greater weight reduction, although the thinner layer parts (A) tended to have better surface appearance than thick-layered parts.

The porous structure of the foams was studied using two complementary and independent characterization techniques, scanning electron microscopy (SEM) and X-ray micro-tomography. The pore structure is a key characteristic which must be determined especially when a homogeneous foamed structure is required. The observations from both techniques performed (coupled with image analysis), demonstrated great variability in the microcellular structures obtained with wide cell size distributions ranging from fine- to macro- cellular in size. Inclusion of MWCNTs clearly played a major role in determining the foamability of the polymer during the foaming process in addition to promoting the nucleation of cells and governing foam morphology. From the characterization of the MWCNT loaded composite foams, the function of the MWCNTs is to reinforce the cell microstructure as well as induce heterogeneous nucleation. A more porous structure was obtained on inclusion of the MWCNTs which resulted in increased cell interconnectivity, resulting in more porous foams and hence reductions in weight. The addition of 0.1 wt% MWCNT to HDPE and

foaming using *TRIAL 3* made it possible to significantly decrease the size of the cells while increasing the number of pores and therefore the cell density. The addition of CBA$_3$ to assist foaming resulted in a relatively more uniform cell distribution than without it.

The high degree of porosity developed in these last samples yielded a low speed of sound as well as a low bulk density and, when combined gave a low value for acoustic impedance. The unfilled polymer sample, HDPE+CBA$_3$_NC_B (porosity~75%) had the lowest value of the speed of sound (1179.90 m/s) of all the foams produced during this project, followed by HDPE+CBA$_3$_NC_A (1247.36 m/s), i.e. the same composite but the sample is cut from the thinner layer A of the moulded plate.

The acoustic energy transmission through the matching layer in air-coupled ultrasonic sensors is at its maximum if the ML has an acoustic impedance of ca. 0.1 MRayl. For the foams produced in *TRIAL 3*, Z was lowered to below 0.4 MRayl for unfilled HDPE foams and to a minimum of 0.57 MRayl for the HDPE-MWCNT composite foams for a MWCNT content of 0.5 wt%. By comparing the values of acoustic impedance of these foams with benchmarking samples, it can be concluded that these MWCNT filled polymer foams are suitable for the application and comparable (if not better). Physical foaming produced highly foamed parts capable of achieving similar acoustic impedances to materials used currently as commercial layers, from *ML-Trelleborg* and *Commercial ML*, used in the sensor industry.

The first attempt at fabricating a new sensor based on the foam sample HDPE+CBA$_3$_NC_B (i.e. the best candidate among the many foams produced in this EngD work) selected as suitable for MLs was overall successful and the new sensor sound field emission profile was qualitatively evaluated through ultrasonic testing protocols by means of an optical microphone in air.

Although further work is required for the optimisation of the HDPE foam system (e.g. geometry and surface finishing) to ensure a significant improvement in the *Elster`s New Generation Ultrasonic Transducer* in measuring gas flow rate in large gas pipelines, the major output from this work is that it has been proven that thermoplastic foams can be used in this application area.

References

[1] X. Sun, H. Kharbas, J. Peng, L-S. Turng, A novel method of producing lightweight microcellular injection molded parts with improved ductility and toughness, Polymer, 56, 2015, pp. 102-110.
[2] J.W.S. Lee, J. Wang, J.D. Yoon, C.B. Park, Strategies to Achieve a Uniform Cell Structure with a High Void Fraction in Advanced Structural Foam Molding, Industrial & Engineering Chemistry Research, 47(23), 2008, pp. 9457-9464.
[3] A.N.J. Spörrer, V. Altstädt, Controlling Morphology of Injection Molded Structural Foams by Mold Design and Processing Parameters, Journal of Cellular Plastics, 43(4-5), 2007, pp. 313-330.
[4] R. Nobe, J. Qiu, M. Kudo, K. Ito, M. Kaneko, Effects of SCF content, injection speed, and CF content on the morphology and tensile properties of microcellular injection-molded CF/PP composites, Polymer Engineering & Science, 59(7), 2019, pp. 1371-1380.

[5] M. Kozlowski, Lightweight Plastic Materials, in: Thermoplastic Elastomers, InTech, chapter 14, 2012, pp. 291-318.

[6] C. Timpano, H. Abdoli, S.N. Leung, G.W. Melenka, Characterization of open-cellular polymeric foams using micro-computed tomography, Polymer, 202, 2020, pp. 122628_1-12.

[7] M. Rohleder, F. Jakob, Foam Injection Molding, in: Specialized Injection Molding Techniques, William Andrew Publishing, chapter 2, 2016, pp. 53-106.

[8] C. C. Ibeh, M. Bubacz, Current Trends in Nanocomposite Foams, Journal of Cellular Plastics, 44(6), 2008, pp. 493-515.

[9] J. Xu, Microcellular injection molding, John Wiley & Sons, Inc., 2010, pp. 1-618.

[10] S.S. Ray, M. Okamoto, Polymer/layered silicate nanocomposites: a review from preparation to processing, Progress in Polymer Science, 28, 2003, pp. 1539–1641.

[11] A. Léonard, C. Calberg, G. Kerckhofs, M. Wevers, R. Jérôme, J-P. Pirard, A. Germain, S. Blacher, Characterization of the porous structure of biodegradable scaffolds obtained with supercritical CO2 as foaming agent, Journal of Porous Materials, 15(4), 2008, pp. 397-403.

[12] R. Der Chien, S-C. Chen, P-H. Lee, J-S. Huang Study on the Molding Characteristics and Mechanical Properties of Injection-molded Foaming Polypropylene Parts, Journal of Reinforced Plastics and Composites, 23(4), 2004, pp. 429-444.

[13] Y. Zhang, Polyolefin Formulations for Improved Foaming: Effects of Molecular Structure and Material Properties, Doctoral Thesis, Department of Chemical Engineering, Queen's University, Kingston, Canada, 2013, pp. 1-133.

[14] A.H Behravesh, C.B. Park, L.K. Cheung, R.D. Venter, Extrusion of polypropylene foams with hydrocerol and isopentane, Journal of Vinyl and Additive Technology, 2(4), 1996, pp. 349-357.

[15] D. Eaves, Handbook of Polymer Foams, Rapra Technology Limited, 2004, pp. 1-277.

[16] M.M. Khorasani, S.R. Ghaffarian, A. Babaie, N. Mohammadi, Foaming Behavior and Cellular Structure of Microcellular HDPE Nanocomposites Prepared by a High Temperature Process, Journal of Cellular Plastics, 46(2), 2010, pp. 173-190.

[17] M.M. Khorasani, S.R. Ghaffarian, S.H. Goldansaz, N. Mohammadi, A. Babaie, Solid-state microcellular foaming of PE/PE composite systems, investigation on cellular structure and crystalline morphology, Composites Science and Technology, 70(13), 2010, pp. 1942-1949.

[18] L.J. Lee, C.C. Zeng, X. Cao, X. Han, J. Shen, G. Xu, Polymer nanocomposite foams, Composites Science and Technology, 65(15-16), 2005, pp. 2344-2363.

[19] C. Hopmann, Y. Zhang, Investigation of the foamability and resulting mechanical properties of foamed thermoplastic elastomers, Antec Proceedings 2019, RWTH-2019-10776, Detroit, USA, 2019, pp. 1-5.

[20] P. Rachtanapun, S.E.M. Selke, L.M. Matuana, Relationship between cell morphology and impact strength of microcellular foamed high-density polyethylene/polypropylene blends, Polymer Engineering & Science, 44(8), 2004, pp. 1551-1560.

[21] J.L. Grenestedt, Influence of Imperfections on Effective Properties of Cellular Solids, Porous and Cellular Materials for Structural Applications Conference, Materials Research Society Symposium Proceedings, San Francisco, California, U.S.A., vol.521, 1998, pp. 3-13.

[22] F. Ramsteiner, N. Fell, S. Forster, Testing the deformation behaviour of polymer foams, Polymer Testing, 20(6), 2001, pp. 661–670.

[23] S.H. Goods, C.L. Neuschwanger, L.L. Whinnery, Mechanical properties of a structural polyurethane foam and the effect of particulate loading, Porous and Cellular Materials for Structural Applications Conference, Materials Research Society Symposium Proceedings, San Francisco, California, U.S.A., vol.521, 1998, pp. 15-20.

[24] M.A. Kuczmarski, J.C. Johnston, Acoustic Absorption in Porous Materials, NASA/TM, Conference Paper, NASA Glenn Research Center, Cleveland, US, March 2011, pp. 1-20.

[25] C. Skinner, J. Peters, J. Vandenbroeck, Acoustic Absorbers: A third way for the management of sound in automobiles, Paper for UTECH Europe, 2006, pp.1-15.

[26] M. Sinha, D.J. Buckley, Acoustic Properties of Polymers, in: Physical Properties of Polymers Handbook, Springer, Chapter 60, second edition, 2007, pp. 1021-1031.

CHAPTER 7: CONCLUSIONS AND FUTURE PERSPECTIVES

In this EngD project, the study of new acoustic materials as alternatives to conventional materials used for matching layer/s within ultrasonic transducer assembly was addressed. The large impedance mismatch of about five orders of magnitude between the active piezo-ceramic material and air is the major issue that currently limits the efficiency of air-coupled ultrasonic transducers as it causes reflection losses at the interface of the two media and thus lowering the total amount of acoustic energy transmitted and converted. A quarter-wavelength matching layer (ML) made of a material having an appropriate acoustic impedance and attenuation coefficient as low as possible can significantly improve the sensitivity and thus the performance of these sensors. Materials comprising bubbles, perhaps provided through the introduction of gas, having low density are needed for use as MLs.

The selection of materials for passive matching layers (MLs) with the aim of enhancing the acoustic energy transfer in air-coupled ultrasonic transducers, specifically *Elster`s new generation transducers* fabricated by Honeywell, led to the choice of using lightweight polymer and composite foams based on high-density polyethylene (HDPE) and non-functionalised multi-walled carbon nanotubes (MWCNTs). Thermoplastics are favoured over other materials in numerous applications due to their relatively low cost and wide range of properties, as well as their ease of processing and reprocessing when molten and ability to be shaped to conform to a curved surface (e.g. specific transducer design) and recycled. The introduction of porosity can greatly expand the range of acoustic properties of these polymer materials. The foaming of commodity thermoplastics usually takes place by means of BAs that take part in the production of porous parts in processes commonly used in industry such as extrusion and IM of polymers. CBAs or alternatively PBAs are a source of gas developed via chemical reaction (or thermal decomposition) or through irreversible physical changes, respectively. Once the gas has developed, it creates the cellular structure (bubbles) by diffusing only into the amorphous phase of the polymer, which is the reason behind the technical challenge of foaming a highly crystalline matrix and high melt viscosity polymer like HDPE. Nevertheless, under certain processing conditions and for a given polymer formulation, it is possible to create a foamed structures even for a high melt viscosity polymer like HDPE which is also high crystalline (>75%). The uniqueness of the system investigated, very different to existing MLs, is highly novel and provides a route to low cost, low weight, stiff and durable materials, while offering an optimal balance of desired acoustic properties (high transmission/absorption and low acoustic impedance and attenuation), strength, suitable size and shape with reduced density.

In this work, firstly, the choice of a chemical foaming method in a conventional two-step foaming process was pursued using endothermic CBAs added to the extruder prior to foaming during

IM. Since the use of CBAs does not require any modifications to the extruder, chemical foaming is the favourite route when it is necessary to maintain low levels of capital expenditure on equipment and machinery. The careful selection of the amount (i.e. 4 wt%) and type of CBAs (i.e. mixtures of citric acid and sodium bicarbonate) in combination with favourable and optimised process conditions for foaming in both the extruder and mini-IM machines produced a foam structure, having desired physical and acoustic properties. As a result, foamed parts of HDPE and HDPE-MWCNT composites produced with this approach proved to possess the basic property requirements (mainly low vales of density, speed of sound and acoustic attenuation) to be considered potential candidate materials for passive MLs in acoustic sensors. The chemical foaming of the HDPE polymer with 4 wt% *Hydrocerol Compound* (i.e. CBA$_1$) yielded foams characterised by void contents up to ca.36%, expansion ratios up to ca.1.6 and low values of speed of sound ($c \leq 1700$ m/s) and density ($\rho \leq 0.70$ g cm^{-3}). Accordingly, the combination of $c \times \rho$ in these foams resulted in a much lower acoustic impedance (i.e., Z = [1.0- 1.3 MRayl]) than the impedances showed by benchmarked *syntactic foams* (i.e., $c \approx 2490$ m/s, Z= [1.75- 2.22 MRayl]), currently in use in the sensor industry. Hence, novel HDPE based foams with better acoustic characteristics, including impedance matching and absorbing properties than the syntactic foams have been developed from this study, proving the possibility of replacing existing MLs already in use, to attain higher frequencies in the sensors. Albeit ensuring a significant performance improvement for the target *Elster/Honeywell's new generation transducers*, Z still needs to be lowered by a further order of magnitude (i.e. the maximum acoustic energy transmission through the ML is provided at $Z_{ML} = \sqrt{Z_{AIR} \cdot Z_{PIEZO}} \approx 0.1$ MRayl), these new materials can still be applied for matching different propagating media (e.g. water, human tissues). Matching different propagating media such as water and/or human tissues (Z$\approx$ 1.5 MRayl), is definitely less problematic than air (Z$\approx$ 0.000420 MRayl), in terms of acoustic mismatch with most sound generating piezo-electric materials (active layers). The variety of types of sensors available on the market extends the alternatives for these polymer foams (economically viable, repeatable and can be manufactured in high volumes) to be applied in a multitude of other industrial applications and engineering fields (e.g. medical field, where ultrasound is used for diagnostic evaluation of human bodies).

The second approach using MuCell technology (i.e. using PBAs during IM) allowed for a much higher degree of foaming than the chemical foaming method, thus achieving greater reductions in material density in the final moulded foamed parts. The final goal of increasing the porosity of such novel composite foams to enhance acoustic properties was successfully accomplished in this study. The use of supercritical carbon dioxide, SCF-CO$_2$, in microcellular foaming processes has proven to be beneficial for handling highly viscous polymer melts such as HDPE. The processing benefits derived by utilising a supercritical fluid in a compressed state resulted in high gas diffusivity

and a good plasticizing of the polymer with dissolved CO_2 gas, which significantly reduced the polymer melt viscosity, improving melt flow and generating polymer foams with much higher void content (up to ca. 70%).

The use of a special mould tool (with steps in plate thickness) while adopting a negative compression moulding process was effective in the production of HDPE and HDPE-MWCNT composite foams characterised by a compact skin layer and a foamed core with very high porosity (> 80%), high cell densities (in the order of 10^6 cells/cm^3) and target expansion ratios (> 3 %). The thicker plate layer (B) provided sufficient room for foaming resulting in greater weight reduction, although the thinner layer (A) tended to have better surface appearance than the thick-layers. Furthermore, the use of an additional 1wt % CBA_3 in combination with ca. 2wt% $SCF-CO_2$, lowered the density of final foams even further for both unfilled and MWCNT filled HDPE foams. The high degree of porosity developed in the unfilled polymer sample, $HDPE+CBA_3\_NC\_B$ (porosity~75%) yielded the lowest bulk density (~ 0.30 g cm^{-3}) and the lowest value of the speed of sound (1179.90 m/s), which combined gave the lowest acoustic impedance (Z=0.35 MRayl) among all the foams produced in this project.

The highly foamed parts produced in this work have great potential to act as passive layers in acoustic sensors as they have similar acoustic impedances (if not better) to commercial materials (e.g. *ML-Trelleborg* with Z=0.42 MRayl and *Commercial ML* with Z= 0.97 MRayl) used already as MLs for air-coupled ultrasonic transducers in the sensor industry. Initial trials using real world sensors, at Elster-Honeywell factory (Mainz, Germany), demonstrated that the replacement of existing MLs with the novel foams developed in this study can be function in air-coupled transducers. However, further work is required to improve the quality of the sample in terms of homogeneity and external surface quality (e.g. removal of pits or holes in the surface).

The role and the importance of the addition of MWCNTs to the HDPE has been demonstrated. The MWCNTs are efficient nucleating agents for HDPE able to enhance the physical, mechanical and acoustic absorbing properties of HDPE.

The presence of MWCNTs in HDPE-MWCNT composites in the solid-state (i.e. not foamed) affected significantly the crystallization behaviour of the HDPE, particularly at a low loading (up to 0.1 wt%) where a shish-kebab structure formed. The presence of MWCNTs was highly influential on the foaming process as well. The role of MWCNTs in polymer foaming is not merely limited to the nucleation of cells, they also promote foam morphologies and play a major role in determining the foamability of the polymer of interest. The MWCNT content was varied to tailor the microstructure as MWCNTs were found to act as heterogeneous nucleating agents during foaming also. The use of MWCNTs as nucleation agents during the foaming process increased the cell nucleation rate while narrowing the cell size distribution. Furthermore, the addition of MWCNTs

was shown to reinforce the cell walls, thus achieving macroscopic enhancement of sound absorbing properties in the foam by increasing tortuosity (at MWCNT loadings $\leq$ 1wt%). From the characterization of the MWCNT loaded composite foams, the number of cells in the foamed polymer melt was increased by means of small MWCNT addition, resulting in cellular structures with higher cell densities than the unfilled HDPE. A MWCNT content of 0.1wt% appeared to be the optimal loading in both physical and chemical foaming resulting in a reduction in density and speed of sound in the moulded composite foam. A more uniform cell distribution was obtained after inclusion of MWCNTs in the HDPE matrix. This is in agreement with other studies found in literature focused on foaming polyolefin-filler mixtures and may have resulted from the heterogeneous nature of the semi-crystalline polymer as well as from the fact that the gas did not distribute uniformly in the polymer since it does not dissolve in the crystalline phase.

The low values for acoustic velocity and impedance resulted from the MWCNT addition to the HDPE matrix and extends greatly the range of applications for these cellular composite materials in other industrial fields. The acoustic impedance determined for the composite foams (Z~[1.1-1.7 MRayl] for composites foamed chemically; Z~[0.6-1.8 MRayl] for composites foamed physically), is very close to that of water and human tissues (Z~[1.2-1.8 MRayl]), therefore these materials could be applied as MLs in ultrasonic transducers for biomedical applications.

A summary of the main properties of interest of the novel materials produced in this work when compared to the benchmark materials is provided in table 7.1.

Table 7.1. Summary of the acoustic properties obtained for foamed HDPE and HDPE-MWCNT composite fabricated in this research against the benchmark materials.

Material Sample	Velocity of sound c	Measured Density ρ_{foam}	Acoustic Impedance $Z = c \cdot \rho_{foam}$	Attenuation @Resonance Frequency
	/m s^{-1}	/g cm^{-3}	/MRayl	/Np m^{-1}
BENCHMARK MATERIALS				
Syntactic Foam	2486.65	0.714	1.78	41.30 @ 0.80MHz
ML-Trelleborg	1303.56	0.320	0.42	33.95 @ 0.90MHz
Commercial ML	2188.60	0.441	0.97	21.99 @ 0.68MHz
RESEARCH MATERIALS (from chemical foaming with Profile 1 and Method 8)				
HDPE+4wt%CBA_1	2084.30	0.72	1.50	N/A
HDPE+0.01wt%MWCNT+4wt%CBA_1	1589.90	0.70	1.11	N/A
HDPE+0.1wt%MWCNT+4wt%CBA_1	1842.99	0.65	1.20	N/A
HDPE+0.3wt%MWCNT+4wt%CBA_1	1833.51	0.72	1.32	N/A
HDPE+0.5wt%MWCNT+4wt%CBA_1	1973.17	0.76	1.50	N/A
HDPE+1wt%MWCNT+4wt%CBA_1	1860.91	0.71	1.32	N/A
RESEARCH MATERIALS (from chemical foaming with Profile 1 and Method 9)				
HDPE+4wt%CBA_1	1692.75	0.62	1.05	N/A
HDPE+0.01wt%MWCNT+4wt%CBA_1	1773.14	0.69	1.22	N/A
HDPE+0.1wt%MWCNT+4wt%CBA_1	1931.32	0.62	1.20	N/A
HDPE+0.3wt%MWCNT+4wt%CBA_1	1723.78	0.72	1.24	N/A
HDPE+0.5wt%MWCNT+4wt%CBA_1	1866.34	0.70	1.31	N/A
HDPE+1wt%MWCNT+4wt%CBA_1	1947.46	0.67	1.30	N/A
RESEARCH MATERIALS (from physical foaming with TRIAL 3 in MuCell technology)				
HDPE+CBA$_3$_NC_A	**1247.36**	0.314	**0.39**	78.58 @ 1 MHz
HDPE+CBA$_3$_NC_B	**1179.90**	0.295	**0.35**	63.19 @ 1 MHz
HDPE+0.1wt%CNT+CBA$_3$_NC_A	1557.59	0.453	0.70	120.94 @ 1 MHz
HDPE+0.1wt%CNT+CBA$_3$_NC_B	1467.46	0.435	**0.64**	74.71 @ 1 MHz
HDPE+0.5wt%CNT+CBA$_3$_NC_A	1761.93	0.357	0.63	159.08 @ 1 MHz
HDPE+0.5wt%CNT+CBA$_3$_NC_B	1781.13	0.323	**0.57**	146.78@ 1 MHz

In summary, given the data obtained the newly developed polymeric foams outperformed the reference MLs with respect to having superior acoustic absorbing properties and acoustic impedance. The innovative approach of using a PBA during IM for the production of MLs is highly promising and confirms they are economically viable, repeatable and can be manufactured at high scale and in large volumes. This is a suitable route to optimizing ultrasonic transducers for use in

UFM applications. Moreover, the use of a commodity thermoplastic polymers, such as HDPE, is a route to generating valuable and low-cost cellular products, for many other applications.

Physical foaming is generally the preferred method to produce polymeric foams, primarily because of the lack of hazardous chemical solvents used and no issues in the removal of side-products. When using inert gases such as carbon dioxide (CO_2), the physical properties of the polymer remain unaffected, unlike in the case of CBAs which react to generate decomposition products and often residues that can affect the material properties negatively (e.g. embrittlement). Besides being more expensive, the use of CBAs may leave residues of these chemicals in the polymer after expansion. Conversely, supercritical CO_2 is known to be chemically inert and is a non-toxic gas that is also relatively low in cost. The main disadvantages of using PBAs to foam in IM processes is the need for a relatively expensive gas metering station to pressurize and meter the blowing agent. However, any initial capital expenditure would be recovered as the foams can be produced at scale and in high volumes.

The main factors that decide for the ultimate cost of the moulded ML disks are the size and intricacy of the parts, besides the material used and the number of parts being produced. In terms of total mass of material used for the final product, the research materials would potentially allow for savings more than half of the costs of production considering the much lower density values (ca. 320 $Kg·m^{-3}$) compared to the commercial ML materials currently used in the target application (ca. 660 $Kg·m^{-3}$). Nevertheless, for such small parts, the cost of the material has a very small effect on the unit price, especially in a production size of 10,000 units of MLs fabricated per year (i.e. current usage status for Honeywell). Increased production rates of the parts could significantly reduce the overall costs, since the production rate has a much larger effect than the material cost if considering the total cost formula (*Total cost = (Average fixed cost × average variable cost) × Number of units produced*). High volume manufacturing of MLs will be required for sectors currently being explored by Honeywell.

In conclusion:

➢ the *innovation* of the work described in this thesis is the production of novel materials via industrially relevant and cost-effective manufacturing methods for use as improved passive layers in ultrasonic transducers.

➢ the *novelty* of this work is the concept of using such a new polymer foam system for sound absorption in ultrasonic flow metering (UFM) applications and described in the present work for the first time.

➢ the *impact* of this research project, both academic and applied are considerable. Firstly, Honeywell nor none of their industrial competitors in the sensor industry have previously employed filled HDPE foams as MLs. Not only have HDPE-MWCNT composite foams not

been used in sensors before, but the degree of porosity developed in the moulded parts in this work enabled the production of highly expanded materials with significant potential for other application areas, as they have similar (if not better) acoustic impedances of existing commercial ML materials. The introduction of such new materials combined with the relative ease of manufacture for an established industrial sector such as that of ultrasonic transducers, could provide Honeywell with new business opportunities leading to increased sales and revenues in what is the global market for sensors and related technologies.

7.1 Recommendations for Future Work

i.   The most promising porous HDPE and HDPE-MWCNT composite foams produced should be incorporated and tested in new sensor devices (not air-coupled transducers) to study and eventually improve their potential of replacing standard MLs in current use. The acoustic performance of the new devices should be tested and optimised accordingly.

ii.   Increase the homogeneity of the porosity in the samples. As was demonstrated processing is critical in determining the final morphology and characteristics of a foam. Further optimisation of the parameter settings during the MuCell process is required for the production of more regular cell morphologies (cell geometry) with minimal warpage and shrinkage of moulded parts (surface appearance), especially for the MWCNT filled HDPE composite foams.

iii. A more in-depth study should be carried out through DSC analysis to investigate how the polymer crystalline content was impacted by the highly porous structure.

iv.   As porous parts generally show a reduced fatigue strength, the fatigue behaviour and fracture mechanisms of foamed specimens could be further topics of investigation for the assessment of fatigue life so that an early failure of the material product in harsh in-service conditions can be prevented.

v.   The use of a mould tool with the same thickness of the final product requirements is highly recommended. It would help to avoid any disadvantages caused by the post-processing cutting of material samples, although this aspect is likely to be automated for production.

vi.   The texture (structure) characterization of highly porous materials is a major issue in relation to their potential applications. There is still limited knowledge about the structure and properties (primarily acoustic properties) of nanocomposite foams. The pore size and pore distribution within the microstructures have undefined correlations with acoustic properties, including the velocity of sound and acoustic impedance. The use of statistical models and methods based on accessible information provided by experimental data would greatly help to fill this gap. Therefore, new modelling studies to find correlations between foam morphology and acoustic properties of polymer and composite foams could be an important step towards adjusting the microcellular structure to

optimize their acoustical performance. The quantitative information on porosity, pore size and MWCNT distribution obtained in this research work can provide a new direction for the choice of secondary processing routes and help modelling of the acoustic performance of HDPE-MWCNT composite foams.

vii. Polymer foams are widely used in all kinds of different applications because they can be manufactured from many different types of polymers and there are plenty of different blowing agents available to customize the foam to specific requirements. Exploration of new polymer foam systems, perhaps with lower melt viscosity than HDPE, rigid or flexible, and studying the control of porosity during foaming would be helpful.

viii. The influence of the molecular architecture of on foam morphology is a well-established phenomenon. Replacing a linear chain polymer with little or no branching like HDPE, with a long chain highly branched polymer (e.g. LDPE) could be perhaps be an effective way of altering melt viscosity, demonstrated in this work to be the principal cause for the significant rupture of cell walls during the foam expansion process. Furthermore, the use of a non semicrystalline polymer, with low melt viscosity and less difficult to foam would be an advantage. Selecting an amorphous polymer, for example, would avoid many of the technical challenges faced in trying to foam a highly viscous polymer like HDPE. Most likely, using only CBAs on a different polymer matrix would have allowed for more uniform foams.

ix. The MWCNTs were shown to have a nucleating effect on HDPE and a reinforcement role and combined with good chemical resistance are highly desirable in aggressive environments such as those of the designed application in the oil and gas industry. Nonetheless, the effect of heterogeneous nucleation is poorly understood and irregular, so further work is necessary to better understand why the same filler can promote nucleation in one polymer, but not in another. Considering the addition of different nucleating agents during foaming (e.g. other 0D/1D/2D materials) would be fundamentally be of great interest in polymer science.

x. Sensor designers frequently face difficulties in finding suitable materials that meet the multitude of application requirements in various engineering fields. One of the most common ways to enhance the properties of a sensor is the use of porous structures instead of bulk materials with the same compositions to both reduce density, thus the cost, and improve sensing performance. Compared to existing methodologies employed to fabricate commercial MLs, the technology and polymer system presented in this work not only allow for the production of MLs, but potentially the whole sensor device itself inclusive of the passive backing layer and the active layer. Piezocomposite transducers, in which piezoelectric composites replace piezo-ceramics as the active layer, have been recently developed to overcome several drawbacks of piezo-ceramics such as the brittleness of the piezoelectric ceramic. The possibility of producing sensors with good performance by developing

a combination of composite foams for each sensor component, while adopting the high volume manufacturing methods employed in this work would be very advantageous. The concept of fabricating high porosity thermoplastic composite foams based on using SCF-CO_2 in combination with, or alternatively to, CBAs may be suitable for further applications can overcome some drawbacks of conventional fabrication methods (e.g. high cost, long processing time, environmental impact, limited material, sample shaping due to the size limitations of the sensor itself).

xi. The use of an over-moulding system in which each single layer component of the inside sensor construct would be directly moulded on top of each other for a glue free assembling could greatly improve the quality of the layer bonding which affects sensor efficiency (i.e. improved bonding can provide a higher transducer output power).

xii. Many applications of ultrasound fall within the scope of measurement science, where ultrasonic transducers are considered key components in sensors for distance, flow and level measurement. However, other ultrasonic fields of considerable practical interest such as medical and biomedical (e.g. ultrasonic transducers, probes, for use in making cross-sectional images of various parts of the body) should be further scope of exploration.

APPENDIX : METHODS AND PROCEDURES

A1. Morphological Analysis by X-Ray micro-tomography

X-ray tomography studies were performed using a Zeiss Versa 520 at WMG, University of Warwick, UK. In order to determine the porosity and the pore size distribution of the foams, image analysis was performed on 3D images obtained by X-ray micro-tomography at low magnification. In order to observe the internal pore structure, foams were cut with a razor blade. Each sample was scanned at an energy of 80 kV and a power of 7 W using the x 4 objective at a source/detector distance of 57 mm. No filtration was required. The exposure was 5s with 1 frame per projection, with a total of 4500 frames being acquired for reconstruction, resulting in a scan duration of 6 hr:15m per sample. Each scan was then reconstructed separately using Zeiss Reconstructor, which utilises the standard filtered back projection (FBP) method common to most lab-base CT systems (Feldkamp, 1984). The scans required no beam hardening correction or any other corrections. This resulted in volume consisting of a cylinder of material with a diameter of 1.75 mm and a length of 1.79 mm, with a resolution of 0.896 μm. The 3D images were obtained by stacking a series of 2D binary cross section images using the Zeiss software. The 3D volumes were then imported into Avizo 2020 (Thermo-Fisher Scientific) for segmentation and analysis. The reconstructed 3D volume was segmented utilizing a label marked technique to separate matrix material and voids so that the segmented volumes were divided into two different label fields, one for the pores, and the other for the foam material (i.e. volume that is occupied by closed cells, cell walls, and unfoamed solid polymer). Specifically, manual segmentation was carried out to isolate the voids and foam material, selecting pores from the background foam using a threshold-based selection method and filling holes in the pores. This was followed by manual correction of the resultant porosity to resolve any errors. The remaining voxels were then segmented, excluding those of the pores, to obtain the foam. The different segments were then statistically analysed and represented in 3D to demonstrate their distribution and interference. The total volume of each cylinder of material analyses covered ~ 4.28mm^3 of material. The achieved resolution from these voxel datasets provided the required statistics information of pore size, volume fractions and pore position. Table A1 presents the XCT machine details, software, and optimum scanning parameters used in the present study.

Table A1. Machine, software packages, and XCT scanning parameters used in this study.

Machine and software used	Name	
X-ray CT scanner	Zeiss Versa 520	
CT scanning software	Zeiss Scout and Scan Control System	
CT reconstruction software	Zeiss Scout and Scan Reconstructor	
Analysis software	Avizo 2020	
XCT scanning parameters		
Conditions	Exposure Voltage (kV)	80
	Exposure Power (W)	7
	Exposure time (ms)	5000
	Duration of Test for each sample (h)	6h:15min
Information about the scan	Voxel size (µm)	0.896
	Number of Projections	4500
	SDD (mm)	57
	Frame per Projection	1
Filters	Material	none
	Thickness	-

A2. Measurement system for air-coupled ultrasound testing with optical microphone

Last phase of completion of this EngD study was based on the fabrication of a new transducer assembled with the best ML candidate identified among the multitude of foamed thermoplastic foams produced in this work. All components of the acoustic transducer and its assembly process are standard and follow industrial, well established procedures. The disc of ML foam candidate was glued in to an active layer made of *Navy-II type piezo-ceramic*. After functional testing assessing the proper shear bonding between the crucial parts of the transducer assembly (i.e. the piezo element, ML and front-face/enclosure), the performance of the new air-coupled transducer was characterized regarding the sound field recorded from its emitted sound beam.

In an attempt to evaluate the output power of the new transducer, two-dimensional measurements to determine the sound field of the new air-coupled transducer were performed at the Elster-Honeywell facility, Mainz, Germany. The experimental 3D stage system set-up employed in this work (see Figure A1) allowed to evaluate the new sensor through air-coupled ultrasound (ACU) testing protocols conducted in air by means of an optical microphone.
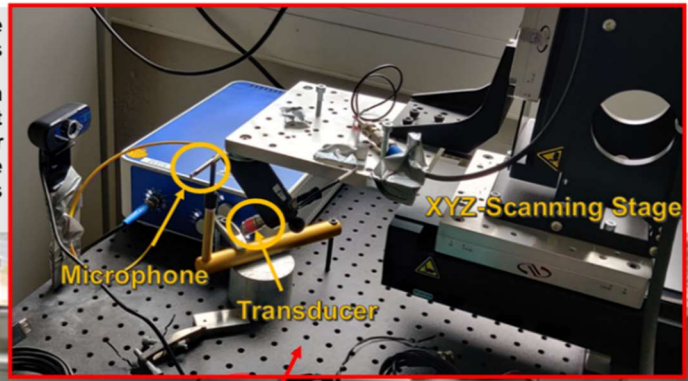
EXPERIMENTAL SET-UP

The Signal generator generated sound pulse signals used for excitation of the transducers

The Amplifier provides an output for a given voltage, observable by directly connecting it to an oscilloscope. It provides a trigger signal which is highly synchronized to the transducer excitation output, and that acts as one input of the oscilloscopes.

The Oscilloscopes record analog signals and either display them directly to the user or convert them to a digital signal for data processing and storage. All signals coming from the transducer excitation need to be recorded. The voltage range of the oscilloscope varies depending on the experimental setup.

Figure A1. Experimental setup employed for the evaluation of the new sensors (located in the Elster-Honeywell facilities, Mainz, Germany).

The use of optical microphones is a known measurement approach in the ultrasonic field for recording transducer sound fields at frequencies over 200 kHz. These devices are based on interferometers to detect certain changes in the optical path of a laser due to sound pressure waves. Without moving mechanical components, the optical microphone detects and measure the sound pressure changes directly in air with a laser beam. It can receive ultrasound over a wide frequency spectrum, allowing the testing of various materials without significant frequency-dependent sensitivity (with high resolution). In this work, measurements were conducted with a scanning optical microphone (XARION Eta-250 Ultra) mounted on a XYZ-scanning system (see Figure A2). The Microphone was programmed to record the maximum emitted sound pressure by the new transducer on a 2-dimensional grid either parallel or perpendicular to the emission direction. The use of a software for data processing enabled the visualization process.
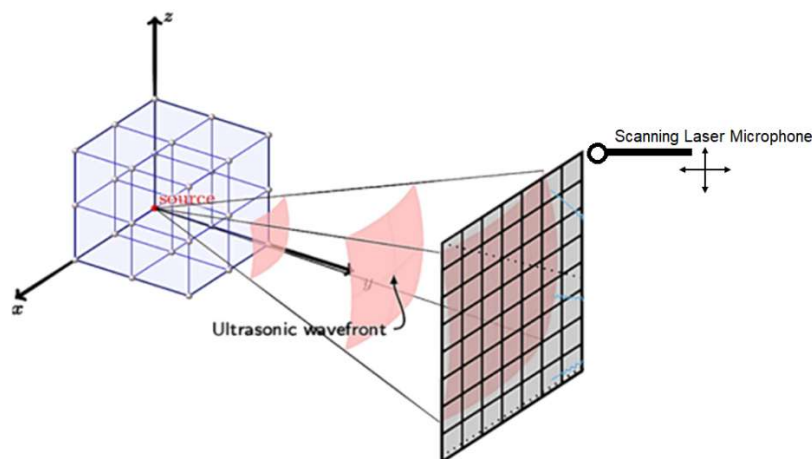
Figure A2: Schematic of the experimental setup: A "scanning laser microphone" was used to characterize the 2-D emission characteristics of assembled ultrasonic transducer in the XZ- and YZ-plane.

The optical microphone was placed at a minimum distance of few mm from the transducer (see enlargement in Figure A2). The transducer was excited with a predetermined pulse in periodic intervals, and the recording of the measurement started together with the excitation pulse.

Operating principle → For each measuring point where the transducer is excited, the complete response signal is recorded (i.e. the optical microphone records the transducer sound field). During the measurements, multiple consecutive scans are processed and visualized in a 2D image that allows to visualize ultrasonic signals in spatial representations. The acoustic signal is sent through time and space and is visible in space as energy concentrated in one point. A time-domain energy analysis is first conducted to analyse the peaks of the waveforms in the amplitude envelope spectrum where each peak corresponds to the maximum acoustic energy content as a function of time. Each point detected in the x-y plane is then analysed to determine the amplitude of the ultrasound wave. All the point measurements recorded in the area scan are then arranged to yield a coloured two-dimensional image, in which each pixel represents one point in space. A multitude of processing methods exist to obtain the final image. The choice is generally made on the basis of the fraction of the measurement information needed. The color-coding strongly influences the information obtainable from a scan as small differences in data can be highlighted through abrupt changes in the colour-map.

In this work, the amplitude was the main parameter to investigate and thus plotted in the 2-dimensional color-coded image (see 2D emission profile of the transducer in chapter 6, Figure 6.28) derived from encoding each signal amplitude recorded for the new transducer with a colour. The chosen method of data representation visualized the received signal power in one image (i.e. all the signal amplitude values were mapped in the x-y plane). In this case, the color-coding was used to determine the colour of a pixel from its signal amplitude and the absolute energy was evaluated based on each pixel corresponding to a whole waveform.

Non-destructive testing methods such as ultrasound are commonly used for quality control during production processes. To counter the main challenge of the air-coupled ultrasound (ACU) testing methods (i.e. the large acoustic impedance differences at the solid-air interface, which causes large sound intensity losses), measurements require powerful ultrasound sources and sufficiently sensitive receivers, as well as optimised measurement data processing algorithms, in combination with optimised measurement chain components and arrangements of these.